Atomic-Scale Analysis of Plasma-Surface Interactions and Formation Mechanisms of Profile Anomalies and Surface Roughness during Plasma Etching of Silicon

Hirotaka Tsuda

2013

Abstract

This thesis presents an atomic-scale analysis of plasma-surface interactions and feature profile evolutions during Si etching in Cl_2 and Cl_2/O_2 plasmas to investigate the formation mechanisms of profile anomalies and surface roughness. In Si etching for the semiconductor fabrication processes of gate electrodes and shallow trench isolation, chlorine-based O_2-containing plasmas are widely used owing to their productively, reproducibility, and controllability of etched profiles. As the dimensions of devices continue to be scaled down to sub-micrometer/nanometer scale, however, increasingly strict requirements are being imposed on plasma etching technology. Recently, in advanced three-dimensional (3D) device structures such as a fin-type field-effect transistors (FinFETs), 3D measurement and prediction of atomic-scale surface roughness on etched features become increasingly important for the analysis of line edge roughness (LER) and line width roughness (LWR) on feature sidewalls during etching; however, the feature profiles are too small and/or too complex to measure the surface roughness on bottom surfaces and sidewalls of the etched features. To control etched feature profiles and to predict the surface roughness on atomic/nanometer scale, in this thesis we presents a Monte Carlo-based semi-empirical model or an atomic-scale cellular model (ASCeM) at an intermediate scale between continuum models and a molecular dynamics (MD) simulation. Moreover, we introduce a new 3D feature profile simulator or a three-dimensional atomic-scale cellular model (ASCeM-3D) for analyzing the formation mechanisms of atomic-scale surface roughening during plasma etching.

This thesis consists of seven chapters. In Chapter 1, the requirements and the challenges for plasma etching technologies in the fabrication of advanced ultra-large-scale integrated (ULSI) circuit devices are presented. The plasma-surface interactions during etching processes are then explained along with their effects on the formation of various undesired profile anomalies. The scope of this thesis is given after introducing the previous experimental and numerical studies of the formation mechanisms of such profile anomalies and surface roughness.

In Chapter 2, we focus on the analysis of formation mechanisms of profile anomalies and microscopic uniformity during Si etching in Cl_2 plasmas, using the ASCeM and feature profile simulation. The synergistic effects between neutral particle transport and fraction of surface coverage are analyzed by comparing the feature profiles and surface conditions for different

neutral-to-ion flux ratios and spaces of the pattern. The ASCeM investigate that not only ion scattering on sidewalls but also neutral shadowing in microstructural features would strongly affect on the formation of profile anomalies such as microtrenching, tapering, and reactive ion etching (RIE) lag.

In Chapter 3, we focus on the formation mechanisms for profile anomalies such as surface roughness and residue during Si etching in Cl_2/O_2 plasmas by numerical and experimental approaches. The ASCeM can reproduce the feature profile evolution experimentally observed during etching at increased O_2 concentrations. A comparison between simulation and experiment also indicates that synergistic effects between surface oxidation and ion scattering in microstructural features on roughened surfaces increase the surface roughness, then causing residues or micropillars on bottom surfaces of etched features.

In Chapter 4, we investigate the mechanisms of the initial-stage formation of micromasks causing surface roughness and micropillars during Si etching in Cl_2/O_2 plasmas by employing a MD simulation. Numerical results indicate that there were several differences between the behavior of Cl and O atoms on and in surface reaction layers, owing to the reactivity of O radicals with substrate Si atoms and Cl atoms. The nanometer-scale micromasks caused by oxygen addition significantly affect the formation of roughened surfaces and evolution of micropillars.

In Chapter 5, we developed a 3D model for feature profile simulation (ASCeM-3D) to reproduce the 3D structure of etched feature surfaces during Si etching in Cl_2 plasmas. The ASCeM-3D would be useful for predicting and analyzing the atomic-/nanometer-scale surface roughness in 3D during Si etching. Numerical results indicate that nanometer-scale convex roughened features appeared on the surface soon after the start of etching, which caused the formation of a larger surface roughness, and that the surface roughness tended to be saturated after several seconds.

In Chapter 6, we focus on the prediction of the atomic-scale surface roughness on feature bottom and sidewalls, by using ASCeM-3D and feature profile simulation. Emphasis is placed on a better understanding of the formation mechanisms of nanoscale surface roughening and rippling during plasma etching and sputtering of Si with different ion incident angles. Numerical results indicated that surfaces are randomly roughened in the case of Cl_2 plasma etching for normal incidence of ions. For increased incident angles, ripples are formed perpendicular to the direction of ion incidence, while parallel to that of ion incidence for further

increased incident angle. Numerical results also implied that the spatial dispersion of ion scattering/focusing on etched surfaces triggers the local difference in etch yield, and leads to the surface roughening and rippling during plasma etching and sputtering.

Chapter 7 concludes this study and discusses remaining challenges for the future works.

Acknowledgments

This study was carried out in Kyoto University (Propulsion Engineering Laboratory, Department of Aeronautics and Astronautics, Graduate School of Engineering) from April 2009 to March 2013.

I would like to acknowledge Research Fellowships of the Japan Society for the Promotion of Science for Young Scientists for the financial support from April 2011.

I would like to express my cordial gratitude to Professor Kouichi Ono for his continuous guidance and encouragement throughout this work. In particular, his knowledge and experience have always helped and motivated me. I would also like to sincerely thank Professor Takaji Inamuro and Professor Kazuo Aoki for their careful review of this thesis and their valuable comments and advices.

I gratefully acknowledge Associate Prof. Koji Eriguchi, Assistant Prof. Yoshinori Takao, and the former assistant Prof. Hiroaki Ohta for giving me useful knowledge and valuable suggestions on my research and for teaching me basic manner and knowledge for my earlier research.

Many thanks go out to the members of the Propulsion Engineering Lab. for sharing with me the great times in the lab. To Mr. Shoki Irie, thank you very much for teaching me about profile simulation. Thanks must go to Mr. Masahito Mori for realizing the collaboration and giving continuous assistance. I would like to Mr. Takumi Saegusa and Mr. Asahiko Matsuda for giving me fruitful advices and nice experiences. To Mr. Akira Iwakawa, Mr. Toshikazu Yamaguchi, Mr. Yoshinori Ueda, Mr. Masahiro Yoshida, Mr. Eri Kujiraoka, Mr. Tatsuya Nagaoka, Mr. Ken Taniguchi, Mr. Hiroki Miyata, Mr. Shota Sato, Mr. Fukushima Daisuke, and Mr. Nobuya Nakazaki, thank you for sharing interesting numerical and experimental results. In particular, thanks must go to Dr. Takeshi Takahashi for their preparation of my computing environments. It would not have been possible to write this thesis without member in the lab.

Finally, I would like to thank my family, mother, father, and sister, and all my friends for supporting me to fulfill my goal.

Contents

Chapter 1
Introduction

1.1 Semiconductor Devices

The semiconductor industry is one of the most important and fundamental industries for an advanced information society.[1)] Semiconductor devices are necessary to the development of the information society, and are installed in a lot of electronic products such as a desktop or laptop computers, a flat panel television, a digital camera, and an automobile for the control of their systems. In particular, a smartphone and a tablet computer as new communication tools, with more advanced computing capability and connectivity than a feature phone, have become popular in the past several years. The growth of electronic devices has been powered mainly by the development of semiconductor devices and the improvement of the process of semiconductor manufacturing.

Semiconductor devices have made progress on their performance for decades now. The number of transistors on an integrated circuits (IC) chip has been doubling approximately every 18 months (and increasing tenfold every 5 years), and this long-term prediction for the miniaturization of semiconductor devices is well known as 'Moore's Law'.[2)] Figure 1.1 shows the recently technology innovations of semiconductor devices given the International Technology Roadmap for Semiconductors (ITRS),[3)] which is the assessment of the semiconductor industry's future technology requirements. Beginning in 1990, the semiconductor industry has entered the ultra-large-scale integration (ULSI) era with 10 million or more devices per IC chip,[4)] and the modern integration device has over one billion transistors on a chip. Since its first demonstration in 1960,[5)] the metal-oxide-semiconductor field-effect transistor (MOSFET), as shown in Fig. 1.2, is one of the most important building block in ULSI devices, because of its advantages of low-power dissipation in miniaturization or simple mechanism compared to all other semiconductor devices.[4,6)] The complementary metal oxide semiconductor (CMOS), the dynamics random access memory (DRAM), and the static random access memory (SRAM) are derived from MOS transistors, and they are the most widely used for digital logic circuits or semiconductor memories. Another important building block in ULSI devices is the nonvolatile semiconductor memory (NVSM), which can be electrically erased and reprogrammed, and is primarily used in memory cards, USB flash drives, solid-state drives, and similar products, for general storage and transfer of data. The ITRS defines the

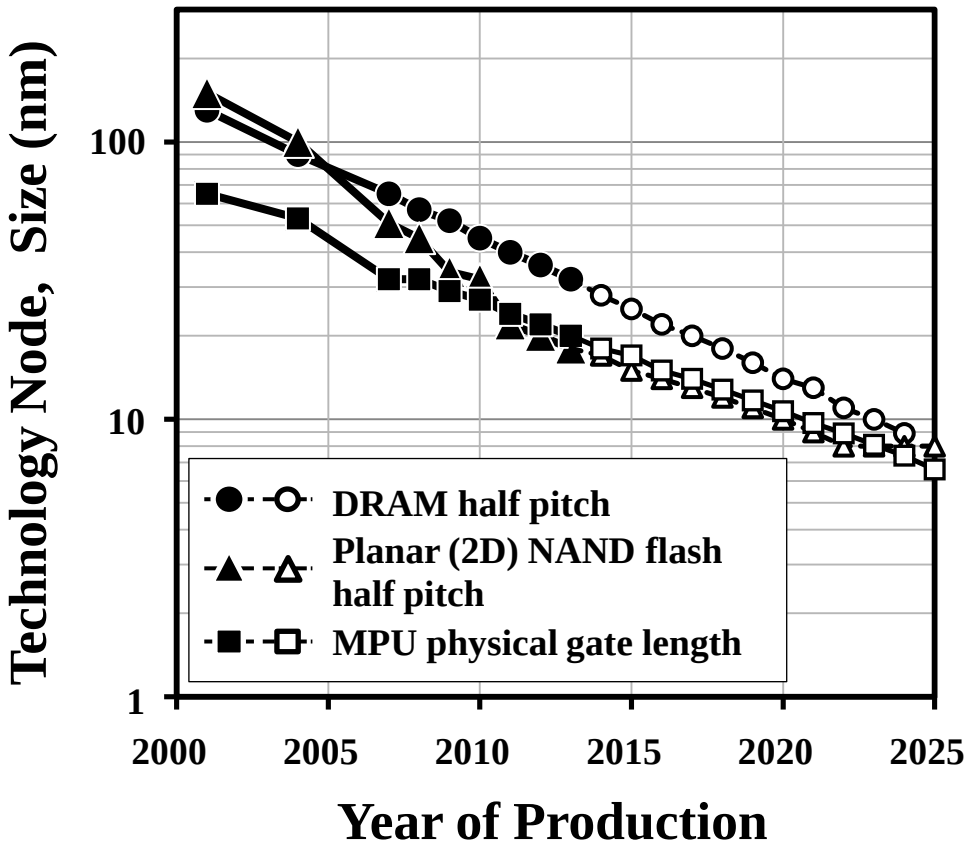

Fig. 1.1. Transfer scaling of the technology node or the size of the critical dimension of several devices given the International Technology Roadmap for Semiconductors (ITRS).

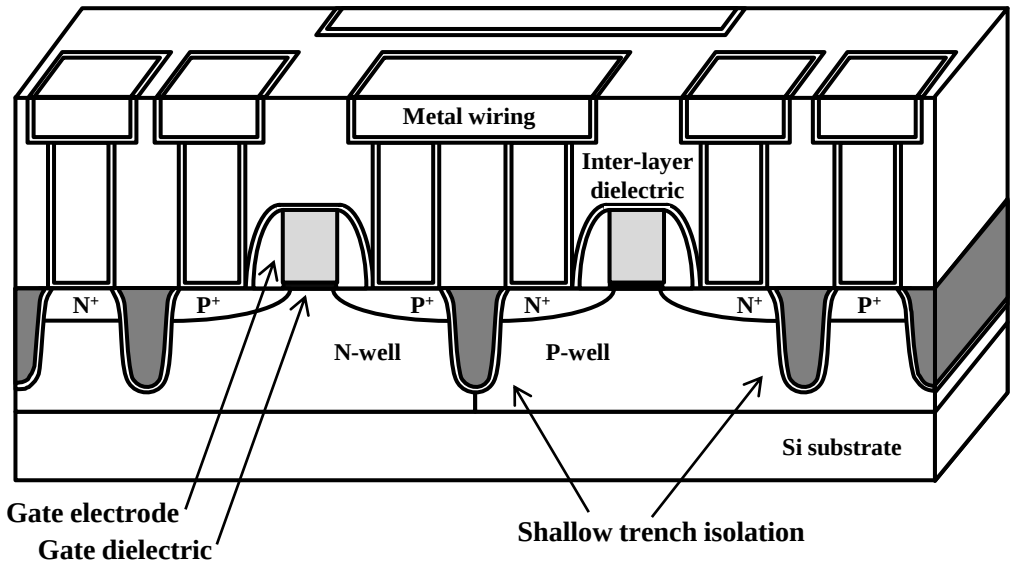

Fig. 1.2. Cross-section view of a typical complementary metal–oxide–semiconductor (CMOS) logic device. The metal-oxide-semiconductor field-effect transistor (MOSFET) is used in digital CMOS logic device, which uses p- and n-channel MOSFETs as building blocks.

'technology node', which is the smallest half-pitch of contacted metal lines on any product (mainly on DRAM cells), as an indicator of device miniaturization. Figure 1.1 shows that the technology node or the size of the critical dimension (CD) in devices currently reaches 32 nm and is being reduced to beyond sub-20 nm.[3] Thus, it has become more difficult to manufacture such very small elements of semiconductor devices.

1.2 Challenges for Miniaturization of Devices

Figure 1.3(a) shows a schematic of a classical bulk *n*-channel MOSFET (or NMOS device). An *n*-channel MOSFET is a three-terminal device and consists of a *p*-type semiconductor substrate in which two *n*-type regions, are called the source and the drain, are formed. A gate stack composed of an insulator (called the gate dielectric) and a metal gate electrode (or a heavily doped polysilicon) is placed above the *p*-type substrate between the source and the drain. The distance between the source and the drain is called the channel length L, is nearly equal to the gate length L_g. Under typical bias condition in *n*-channel MOSFET, the source and the *p*-type substrate are grounded, and a positive voltage is applied to the drain. In this case, there is no current flowing from the drain to the source, because both *p*-*n* junctions of the source and the drain are not under forward bias and the wide depletion regions are formed. When a large enough positive voltage is applied to the gate, electrons from the n-type semiconductor source and drain regions are attracted by the gate. After that, an electron-rich layer underneath the gate is formed, which is called the channel; the channel connects the source to the drain, and current can flow from the drain to the source. In this way, the transistor can be controlled according to the biases on the gate and the drain, and behave as a switching device. Therefore, the controlling of basic device parameters which are the channel length, the channel width (or the gate width W_g), the gate dielectric thickness, the junction depth, and the substitute doping density, strongly affect performance characteristic of the MOSFET.

From a technical perspective, miniaturization of the MOS transistors has been conformed to the Dennard's scaling theory.[4,7,8] Table I reproduced from this scaling theory summarizes transistor or circuit parameter changes under ideal scaling conditions, where α is the dimensionless scaling factor. As transistors get smaller, smaller device size can achieve higher device density in an IC chip, and smaller channel length improves the driving current of the transistor. Miniaturization followed the scaling theory enables both high performance and low operating power, thus preserving the electrostatic behavior of semiconductor devices.

Table I. Technology Scaling Rules*.

Physical Parameter	Constant Electric Field Scaling Factor	Generalized Scaling Factor
Channel length, Insulator thickness	$1/\alpha$	$1/\alpha$
Wiring width, Channel width	$1/\alpha$	$1/\alpha$
Electric field in device	1	ε
Voltage	$1/\alpha$	ε/α
Doping	α	$\varepsilon\alpha$
Area	$1/\alpha^2$	$1/\alpha^2$
Capacitance	$1/\alpha$	$1/\alpha$
Gate delay	$1/\alpha$	$1/\alpha$
Power dissipation	$1/\alpha^2$	ε^2/α^2
Power density	1	ε^2

*α is the dimensional scaling parameter, ε is the electric field scaling parameter.

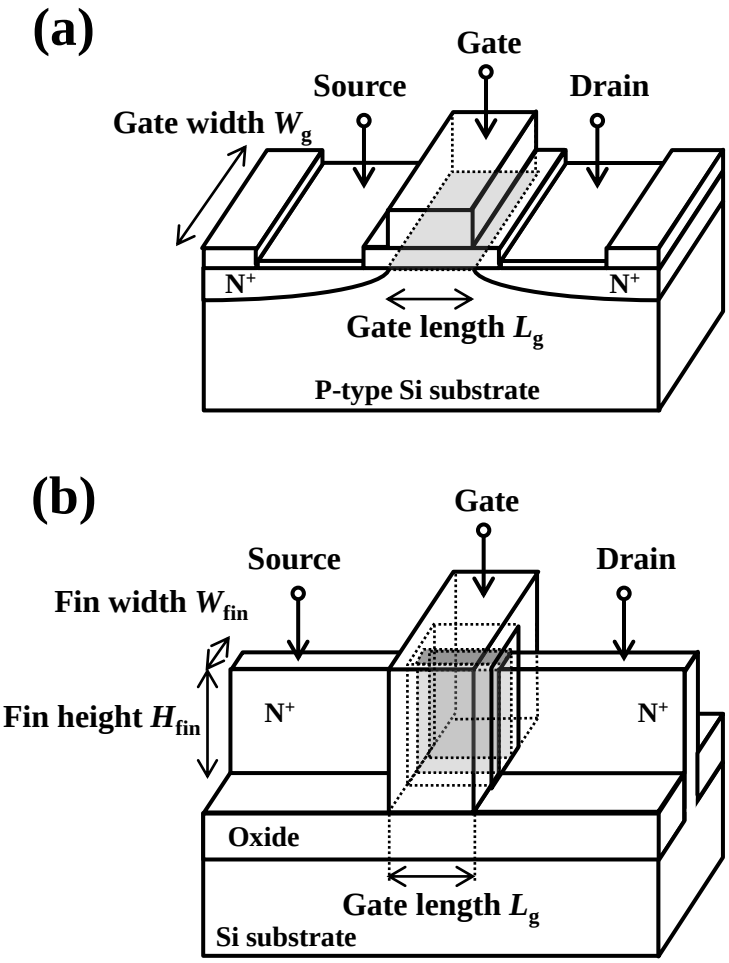

Fig. 1.3. Schematic of (a) a classical n-channel MOSFET (or NMOS) and (b) a fin field-effect transistor (FinFET). The FinFET has a thin silicon "fin" structure, and the electrode is wrapped around several sides of the channel region.

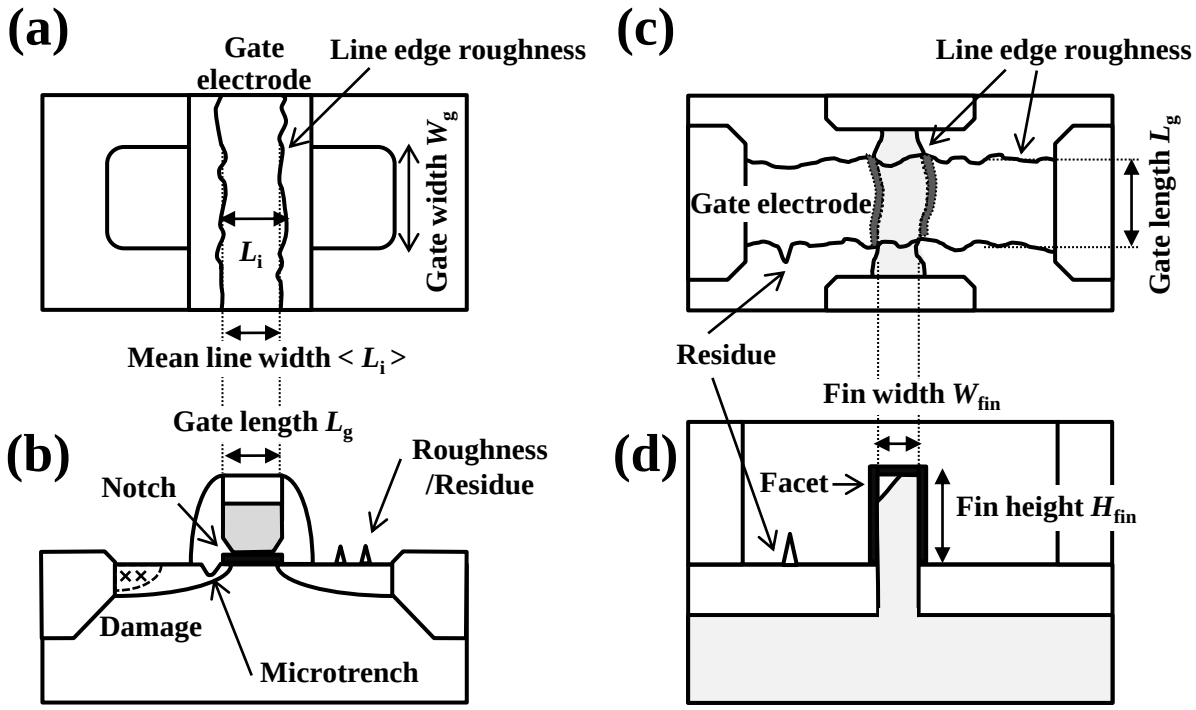

Fig. 1.4. Schematic of the nanomether-scale transistor, showing various profile anomalies and the roughness that often occurs on top/bottom surfaces and sidewalls of the etched feature, where $L_g \approx 10$ nm and $W_g \approx 30$ nm for 10-nm scale devices. Note that the line edge roughness (LER) is the fluctuation of the line edge about its mean value for the left and right edges of the line, and that the line width roughness (LWR) is the fluctuation of a linewidth L_i about its mean value $< L_i >$ averaged over the width W_g.

As the dimensions of the MOSFETs are reduced to sub-micrometer/nanometer scale, however, the fabricating of the semiconductor devices becomes more difficult. For the fabrication of the classical bulk MOSFETs (in such a configuration, the device is the planar and essentially two dimensional), the precise manufacturing processes of the gate electrodes and the gate dielectrics of MOSFETs are especially required, because the characteristics of the channels depend on the gate lengths and widths, as shown in Figs. 1.3(a) and 1.4(a). Moreover, as channel length is reduced, the electric fields derived from the source and drain regions begin to influence on electron drift characteristics in the channel, and then, the device performance become worse. These physical phenomena are called the short-channel effects; especially the off-state leakage current increases the stand-by power of semiconductor devices.

Recently, to avoid the short-channel effects and improve the device performance, three-dimensional MOSFET devices[9,10] such as a fin field-effect transistor (FinFET)[11–13] with a new gate structure are proposed, as shown in Fig. 1.3(b). These new types of MOSFETs have multi-gate structures,[9–16] where the electrodes are wrapped around several sides of the channel regions. Therefore, multiple gates allow enhanced drive current in the on-state. Compared with classical planar transistors, however, there are more difficulties in fabricating processes required to form these structures without structural damages or anomalies.

1.3 Fabrication of Semiconductors

To achieve these technical challenges of fabricating semiconductor devices, the technical innovation of semiconductor processes has been made.[17–19] In the fabricating semiconductor devices, there are many process steps to produce the desired ICs. The process steps can be generally divided into two major parts: the front-end-of-line (FEOL) and back-end-of-line (BEOL) processing. The FEOL is the first portion of IC fabrication wherein the individual devices (such as MOSFETs and memory devices) are patterned and formed on the wafer, and the BEOL is the second portion of IC fabrication wherein the individual devices are interconnected with wiring on the wafer for achieving chip-to-package connections.

Now, we focus on the FEOL process, there are also many manufacturing steps in the process: the modification of electrical properties, planarization, deposition, lithography, etching, and cleaning processes. Figure 1.5 shows a schematic flow of the FEOL process in fabricating semiconductor devices. Devices are built from a number of different layer materials deposited sequentially. In the deposition process, a thin film is grown or deposited on the substrate (Figs.

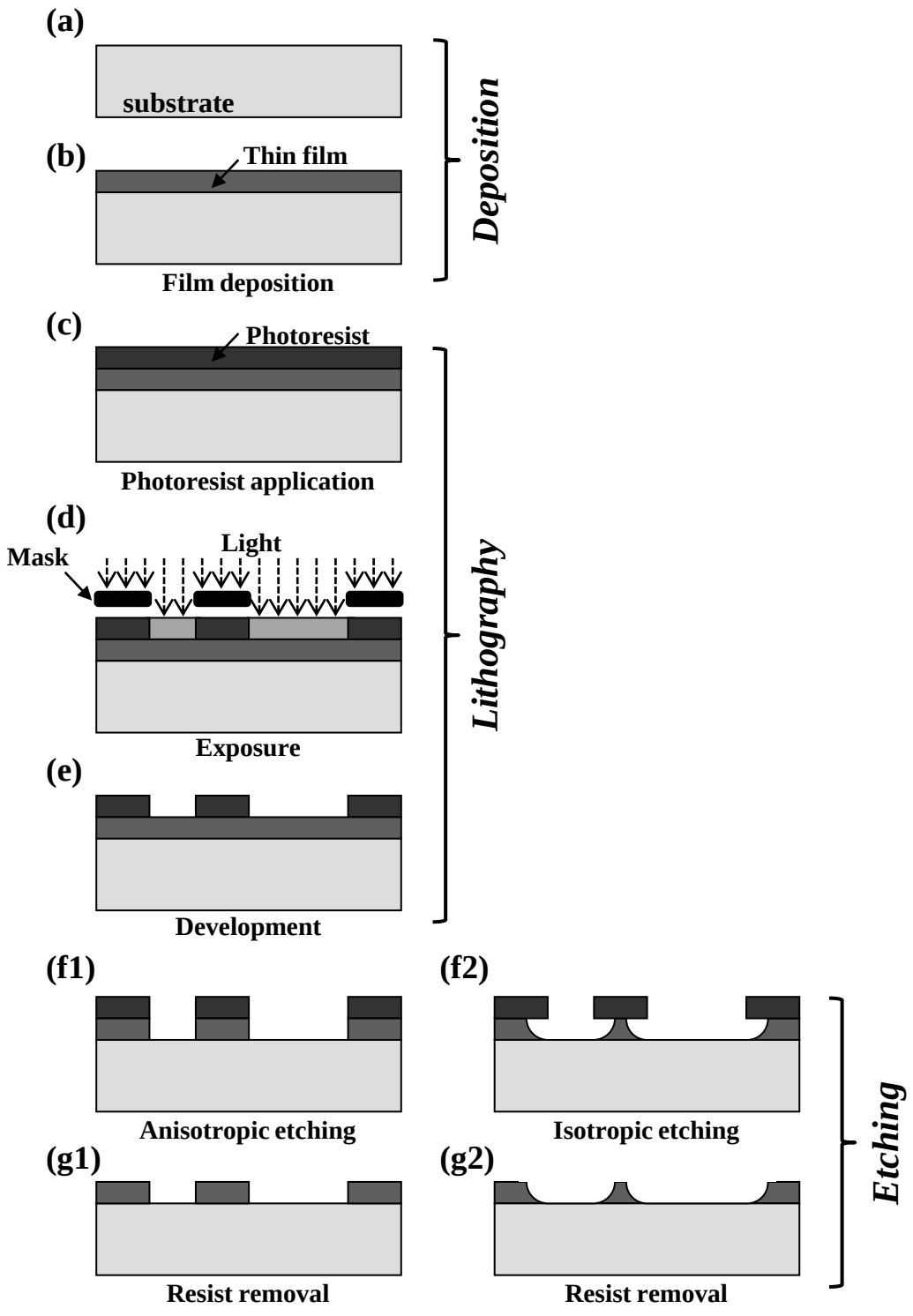

Fig. 1.5. Schematic flow of front-end-of line (FEOL) processes in fabricating semiconductor devices: (a) prepare the wafer, (b) file to be deposited on the substrate, (c) photoresist is coated over the film, (d) the photoresist is exposed to radiation through the patterned mask, (e) the exposed part of the resist is removed, (f1) the unprotected part of the underlying film is etched (anisotropic etching), (f2) the film is etched (isotropic etching), and (g1) and (g2) the photoresist is removed.

1.5(a) and 1.5(b)). In the lithography process, the light-sensitive material called a photoresist is coated over the surface of the wafer (Fig. 1.5(c)). After that, a mask containing the circuit patterns is positioned over the photoresist and is irradiated with ultraviolet light for producing a pattern in the photoresist layer (Figs. 1.5(d) and 1.5(e)). In the next step, the unprotected part of the underlying film is removed by the etching techniques (Figs. 1.5(f1) and 1.5(f2)), and the circuit patterns can be transferred on the wafer (Figs. 1.5(g1) and 1.5(g2)).

Historically, lithography and etching techniques make a significant role for the progress of recent semiconductor manufacturing processes, because they are used repeatedly in manufacturing process. These days, the minimum feature size of fabricating devices, which is also called the critical dimension (CD), is being smaller than the wavelength of the UV light used in the lithography process. To compensate for these issues, etching process combining with several techniques for enhancing resolution, e.g. multiple patterning methods, has been developed. However, etching processes faced more difficulties to increase the process steps and to reduce the feature scale. It is necessary to deeply understand etching mechanisms for the progress of semiconductor industry for the future, because the precise control of profiles determines the device dimensions, which affect not only the device's quality but also its product amount and manufacturing cost.

1.4 Plasma Etching

Etching techniques consist of dry and wet etching methods. Dry etching uses gas-phase etchants, and could achieve anisotropic etched profiles as shown in Fig. 1.5(f1). Dry etching is generally synonymous with plasma etching. By contrast, wet etching uses liquid-phase etchants, and the wafer is immersed in a bath of etchant. Therefore, wet chemical etching results in isotropic etching, where both vertical and lateral etch rates (*ER*s) are comparable as shown in Fig. 1.5(f2). The recent fabrication for semiconductor devices frequently requires anisotropic etched profiles; that is, plasma processing using plasma etching techniques is of great importance for today's semiconductor manufacturing because of their potential for very-high-accuracy transfer of resist patterns.

Figures 1.6(a)-1.6(c) show images of an inductively coupled plasma (ICP) reactor and schematic of reaction processes in the plasma reactor during etching, respectively. In plasma processing for the fabrication of microelectronics, high-frequency (100 kHz ~ a few tens of MHz) and/or microwave (typically 2.45 GHz) glow discharges are mainly used to etch, because

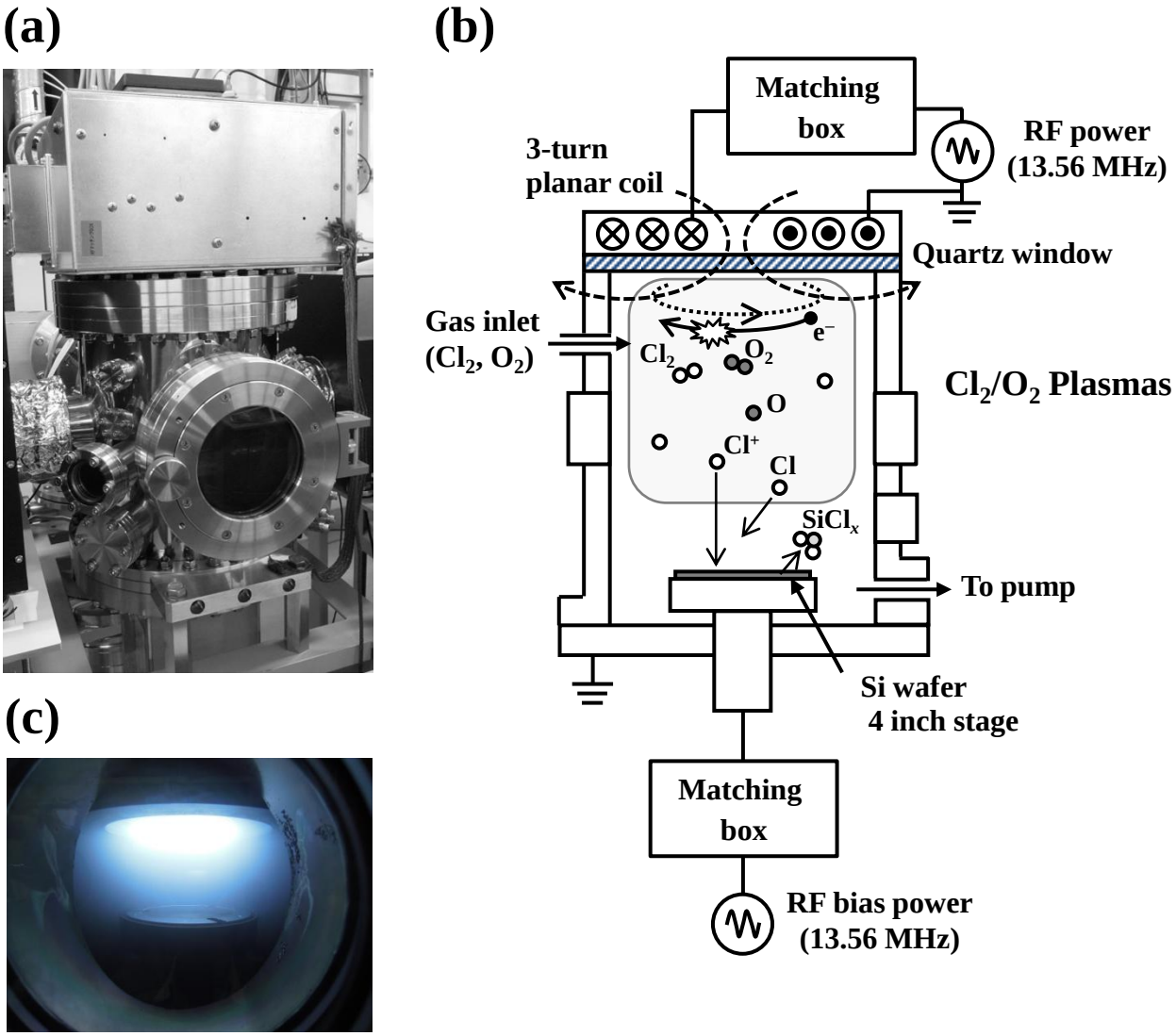

Fig. 1.6. (a) An image of a inductive coupled plasma (ICP) reactor, (b) schematic of ICP chamber set up and (c) a photograph of Cl_2 plasma generated in an ICP reactor.

higher frequency discharges can be generated even if the electrodes are covered with the dielectric materials; therefore, these discharges can achieve the etching of insulator materials such as oxide film.

In etching process, plasma is used as a source of both highly reactive neutrals (e.g. atomic chlorine) that react with the surface to produce volatile species and ions that bombard the surface being etched. In high-frequency discharges, electrons accept the energies from the oscillating electric field, and then induce ionization, dissociation, and excitation of gas molecules. High-frequency discharges can produce ions and reactive neutral species at lower pressure (10^{-4} ~ 1 Torr) than that in dc glow discharge. In plasma discharges, plasma sheath, where a dark space between plasma and the electrodes or reactor walls is observed, is developed due to the different mobility of electrons and ions. Since electrons have relatively lower mass and move faster than ions, the surfaces exposed to plasma quickly charge negatively, thus developing a negative potential (a sheath potential) with respect to the plasma. The resulting electric field attracts and accelerates the ions and repels the electrons to remain a net zero flux of charges to the surface. Therefore, ions are injected vertically into substrate surface trough the sheath with the energy approximately equal to the sheath potential. On the other hand, neutrals and gas molecules have an isotropic distribution and are injected with thermal velocities without effects of the electric field of the sheath.

In the fabricating semiconductor devices, silicon (Si) is mainly used for the semiconductor material, because of its availability and quality performance of a silicon/silicon oxide (Si/SiO_2) interface, which can get easily by thermal oxidation at low cost.[20] Thus, halogen-based plasmas such as fluorine- (F),[21] chlorine- (Cl),[22] and bromine (Br)-based[23] plasmas are widely used in Si etching, which have a high reactivity with Si substrates.[18,24,25] F-based chemistry, therefore, gives low selectivity to silicon oxide and isotropic profiles, while Cl-based chemistry tends to provide high selectivity and better profiles. Furthermore, using Br-based chemistry, much higher selectivity and anisotropic profiles can be achieved. Sometimes small amount of other gases, such as H_2, N_2, O_2, and Ar are also added for the stabilization of plasma discharge, the improvement of productivity (the enhancement of etch rates), and the controllability of etched profiles. A schematic of etching a Si film in Cl_2/O_2 plasmas is shown in Fig. 1.7. A small amount of oxygen is often added into Cl_2 plasma to improve the etched profiles and the selectivity over thin gate oxides. A part of the ions and neutrals is transported onto etched substrate through the sheath, and cause the etching reaction thereon. Etch products desorbed

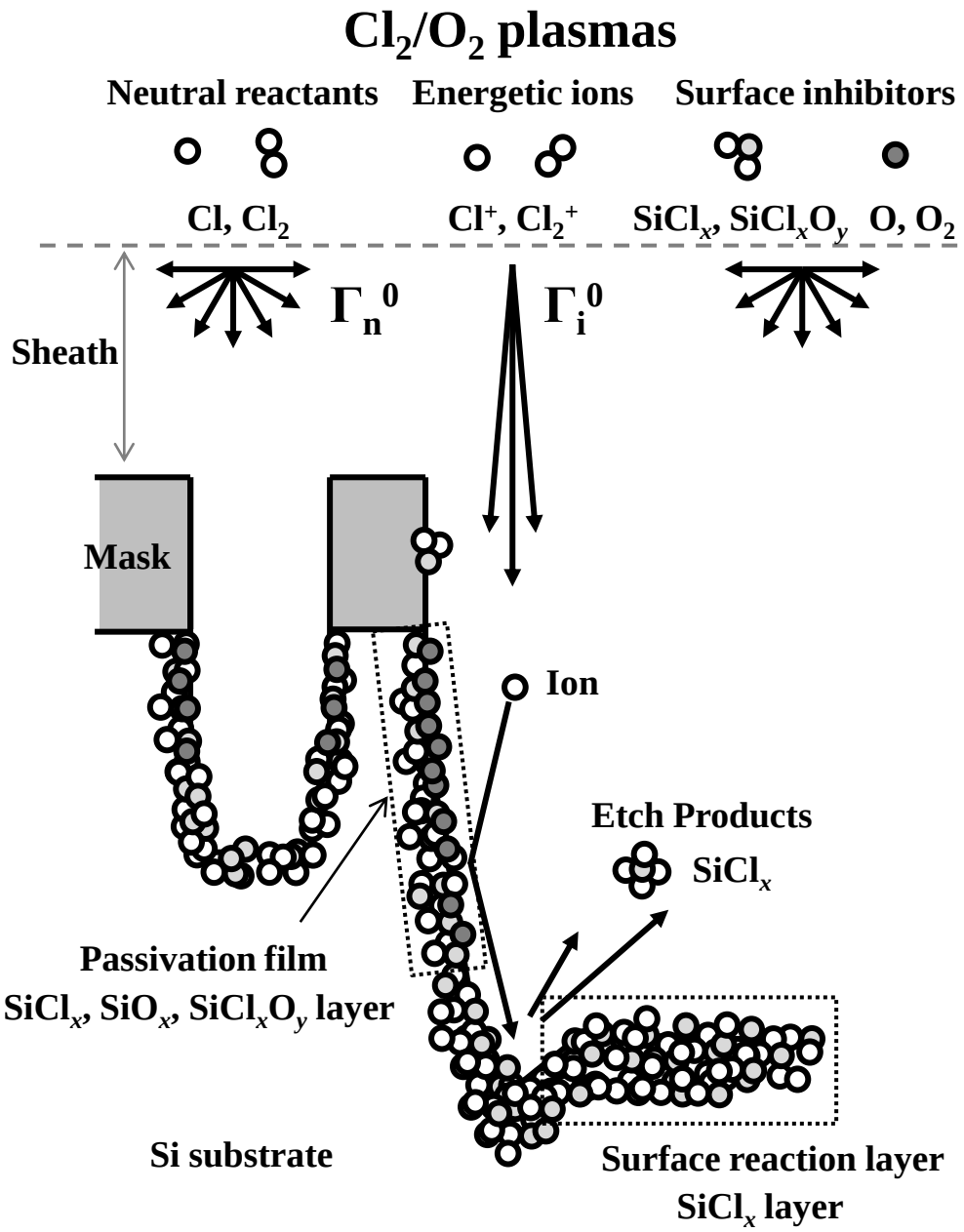

Fig. 1.7. Schematic of plasma-surface interactions in microstructures during Si etching in Cl_2/O_2 plasmas. Directional pr anisotropic etching is achieved owing to the ion-enhanced etching at the feature bottom and the formation of passivation layers or inhibitor deposition on feature sidewalls.

from substrate surfaces are also involved in ionization, dissociation, and oxidation either in the gas phase or on the reactor walls.[23,24] Furthermore, a part of the etch/etch-by products returns and deposit onto substrate surfaces and influences the surface reaction processes.

Figures 1.8(a)-1.8(d) show a schematic of surface reactions during plasma etching, which includes chemical etching, ion-enhanced etching, spattering, and deposition or passivation. In chemical etching, reactive neutral species transported from the plasma interact with the surface materials to form volatile etch products. Chemical etching occurs isotropically due to the isotropic angular distribution of the neutral species injected from plasma. Selectivity, which is defined the ratio of the *ER* of the target material being etched to the *ER* of other materials, is relatively high in chemical etching. In physical sputtering, energetic positive ions bombard the surface at high speed and knock-on the surface atoms. Physical etching can yield anisotropic profiles; however, it is associated with low etch selectivity and high bombardment-induced damage. Ion-enhanced etching is caused by a combination of the chemical and physical reactions. The etch profiles in ion-enhanced etching are anisotropic as in physical etching, with a higher *ER* and reasonably better selectivity; however, ion bombardments often cause some physical damage to the surface, while they enhance *ER*s at the damaged areas. In deposition and passivation, particles in gas phase are condensed on the surface or the etch/etch-by products reattach with the surfaces, and then thin films are formed. When thin films including etch inhibitors are deposited on surfaces, chemical etching is inhibited either by physical blocking against chemical etch species or by reacting with and depleting these species. These various physical and chemical reactions have been widely applied to plasma processing for the fabrication of IC devices. For example, an ion-enhanced etching process is necessary to achieve a high selectivity and anisotropic profiles for high-aspect-ratio-contact (HARC) formation.[20] In addition, a passivation process combining etching and deposition is aggressively utilized in the fabricating of polysilicon gates of MOSFET in $HBr/Cl_2/O_2$ plasmas.[28]

1.5 Profile Anomalies

In the fabrication of IC devices, an ideal plasma etching process mainly requires perfect pattern transfer by anisotropic etching of polysilicon (the unprotected part of the underlying film by the photoresist) without etching of photoresist by ion bombardment (infinite selectivity). However, a perfect pattern transfer is very difficult. As the dimensions of the semiconductor

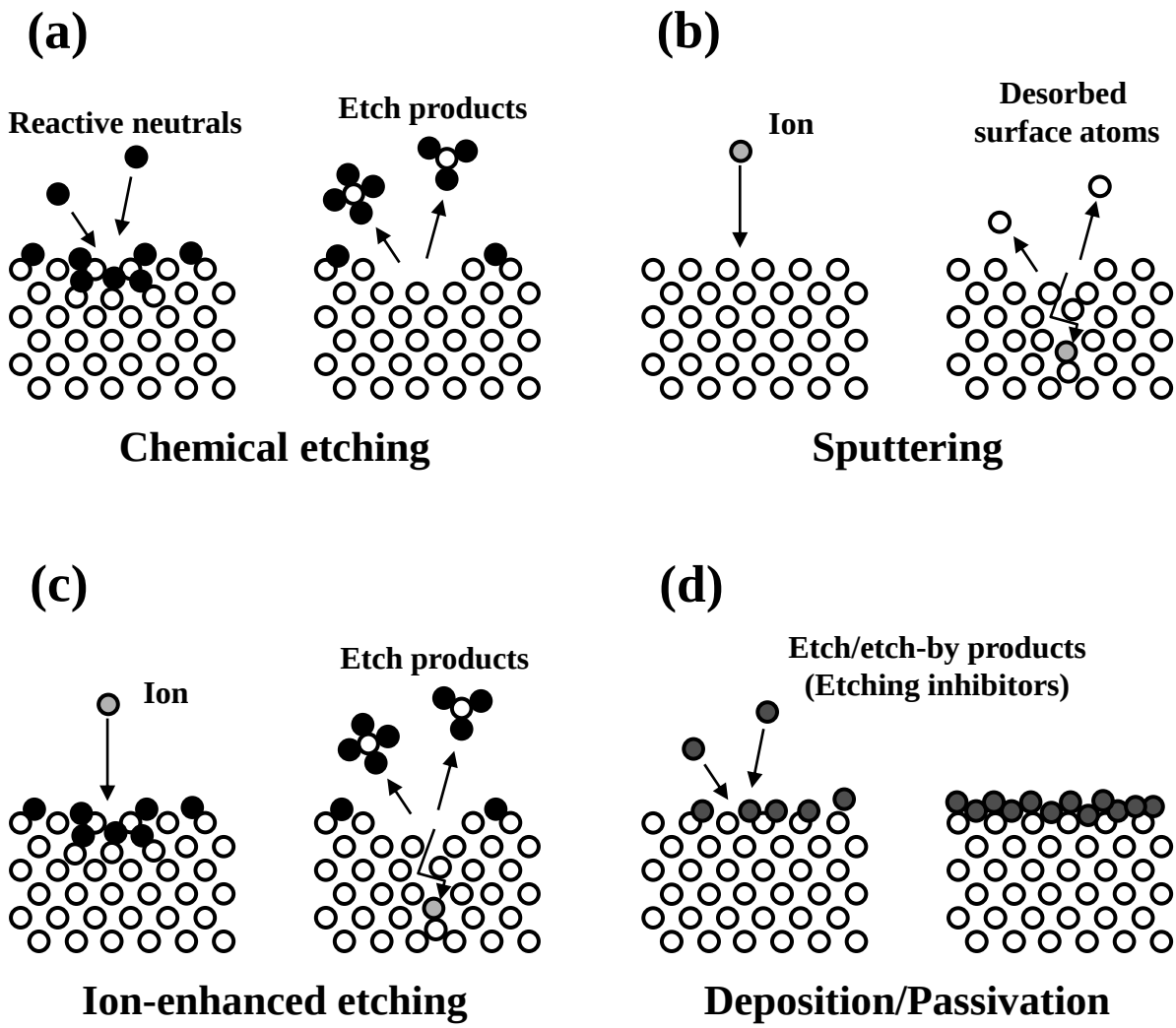

Fig. 1.8. Schematic of plasma-surface interactions: (a) chemical etching, (b) sputtering, (c) ion-enhanced etching, and (d) deposition/passivation.

devices are scaled down, increasingly strict requirements are imposed on dimensional precision of the feature profiles in microstructure devices to prevent a decrease of device performance; therefore, several issues regarding feature profile evolution during plasma etching have attracted attention recently.

As shown in Figs. 1.9(a)-1.9(l), various undesired profile anomalies such as undercutting, bowing, tapering/inverse tapering, faceting, notching, microtrenching, residues/micropillar, and microloading including RIE lag and inverse RIE lag are often observed during a typical plasma etching. There are general assumptions to explain the mechanisms for the formation of these feature anomalies as follows.

1.5.1 Undercutting

Firstly, undercutting[21,29–31] or the lateral etching beneath the mask, as shown in Fig. 1.9(a), occurs at the interface of two materials where one material is resistant towards etching and another is not. It is often observed in the reactive ion etching of Si using high reactive halogen-based plasma such as SF_6,[21] and caused by isotropic spontaneous etching (e.g. chemical etching and wet etching) at higher substrate temperatures[27,30] or by ion scattering under the mask.[31]

1.5.2 Bowing

Local bowing is a lateral etching located on the sidewalls,[32] resulting in profile destruction as shown in Fig. 1.9(b). Bowing may cause voids during the trench-refilling step, leading to degradation in the mechanical performance of the component.[33] The challenge is to achieve deep anisotropic trenches without local bowing. Sidewall passivation layers are key to achieving etch directionality without undercutting or bowing. Without oxygen in the feed gas the protective sidewall film cannot be formed and the etch profile is nearly isotropic.[21]

1.5.3 Tapering/Inverse Tapering

The etched profile becomes tapered, when redeposition of etch products increases and surface oxidation or inhibitor deposition suppresses the lateral etching on the sidewalls,[34] as shown in Fig. 1.9(c). In contrast, the absence of sidewall passivation sometimes leads to inversely tapered etched profiles,[35] as shown in Fig. 1.9(d). In general, anisotropic etching patterns are required for the fabrication of devices; however, several plasma processes

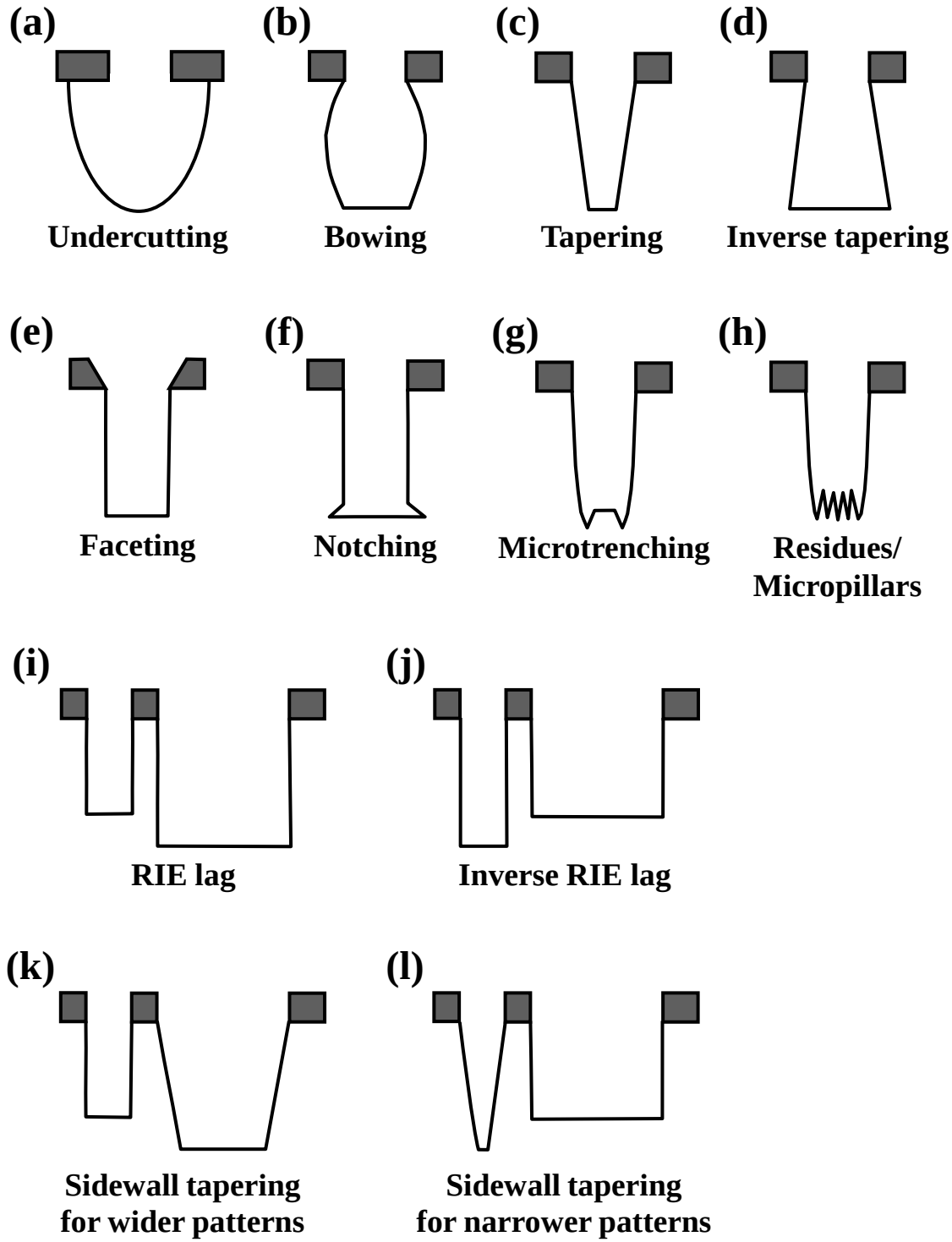

Fig. 1.9. Schematics of various feature profile anomalies: (a) undercutting, (b) bowing, (c) tapering, (d) inverse tapering, (e) faceting, (f) notching, (g) microtrenching, (h) residues or micropillars, (i) reactive ion etching (RIE) lag, (j) inverse RIE lag, (k) sidewall tapering for wider patterns, and (l) sidewall tapering for narrower patterns.

proactively taking advantage of such tapering phenomena also exist. In the shallow trench isolation (STI) processes which are used for isolation between IC elements, microscopic trench structures need to be often filled with suitable dielectric or conductive materials after forming trenches into substrates. Therefore, trench formation processes require the controllability and reproducibility of shapes, which include width or depth of trench and taper angle of sidewalls.

1.5.4 Faceting

Faceting is due to the large variation of sputter yield as a function of angle of ion incidence, and the facet structures are formed by the sputtering of the corners of the mask during the etching process,[36,37] as shown in Fig. 1.9(e). These facets may affect the further etching of the surfaces by altering the trajectory of the ions scattered from the facet.[31,38]

1.5.5 Notching and Charging

Notching has been observed during overetching of conductive films (polysilicon and aluminum) at its interface with an underlying insulating film (SiO_2),[39–43] as shown in Fig. 1.9(f). It typically forms at the inner sidewall foot of the outermost feature in a line-and-space pattern neighboring an open area. Notching has been generally attributed to the feature-charging-induced ion trajectory distortion and the subsequent etching of polysilicon by ion induced etching.[44] Charging of the silicon dioxide surface within a feature is caused by the difference in the directionality of ions and electrons; i.e., the isotropically directed electrons charge the photoresist sidewalls negatively and the anisotropically directed ions charge the underlying oxide positively during overetching.[40,41] This surface charging leads to ion deflection due to local electric fields in the trench space, because the trajectories of incoming charged ions are deflected by the Coulomb force. However, the high electrical field necessary to deflect injected energetic ions to form notches causes surface leakage, reducing the field, and thereby, preventing the deflection of ions to the extent needed to form notches by this mechanism alone. Thus, other (non-electrostatic) mechanisms to explain notching have been investigated.[45]

1.5.6 Microtrenching

Microtrenching describes the appearance of narrow grooves at the feet of sidewalls in the direction of ion bombardment,[44,46–50] as shown in Fig. 1.9(g). In the contact etching, the

microtrench profile is very important to determine the step coverage of subsequent deposition materials, which can cause some issues on contact resistance and leakage current. Microtrenching is chiefly attributed to forward scattering of ions at the sidewalls (of the mask or the material being etched).[48–50] When sidewalls are inclined or bowed with respect to the direction of ion incident, forward scattering causes a focusing of the ion energy flux at the sidewall feet.[50] Note that even when sidewalls are perfectly straight, microtrenching can occur due to the charging effect of the upper mask sidewalls. Interestingly, microtrenching have been found to occur during etching of dielectrics, semiconductors, and metals. Moreover, the formation of microtrenching also depends on the type of plasma chemistry involved. For example, while microtrenching is absent in HBr-based plasma, it is always observed in Cl-based plasma etching.[49]

1.5.7 Residues/Micropillars

Using Br-based chemistry, much higher selectivity and anisotropic profiles can be achieved. Hence, to satisfy the above requirements, trench etching using Br-based plasmas is very attractive. Such highly selective etching, however, causes a severe problem, i.e., the occurrence of silicon residues, well-known as microscopic silicon needles, grass or black silicon,[51] as shown in Fig. 1.9(h). In particular, these phenomena are often observed during Si etching in O_2-containig plasmas such as Cl_2/O_2 plasmas. This is due to the residue formation caused by the protection of Si surfaces from etching by small micromasks, which consist of different materials such as silicon oxide. The development of those surface structures is only possible if the etching process shows a much higher etching rate of Si than that of the micromasking material. As a source of the micromask, the following have been proposed: native oxide on the Si surface,[52] sputtered involatile masking material,[51] sputtered involatile electrode or chamber wall material,[53] silicon oxide formed by the reaction of etch products with oxygen,[54] and interstitial oxygen precipitates in the Si substrate, which are incorporated into the Si for wafer directly from the silica crucible in the Czochralski (Cz) growth process (Si wafer manufacturing process).[55]

1.5.8 Microloading

Some issues in achieving microscopic uniformity may occur because *ER*s and profiles depend on feature size and line-and-space pattern density. Reactive ion etching (RIE) lag, as

shown in Fig. 1.9(i), describes the difference in *ER*s between open and density patterned areas. Such microscopic uniformity problems can be grouped into two categories: aspect-ratio-dependent etching (ARDE) and pattern-dependent etching, known as microloading.[56] Based on the observed dependences, four mechanisms responsible for such microscopic nonuniformities have been proposed[44,56–65] : the Knudsen transport of neutrals,[57] ion shadowing,[58–61] neutral shadowing,[62–64] and differential charging of insulating microstructure.[44,65,66] In contrast, the *ER* is reduced for lower-aspect-ratio features or wider-space patterns in the presence of oxygen or etch inhibitor, being called an inverse RIE lag,[62,67] as shown in Fig. 1.9(j). The control of simultaneous deposition have been proposed as a solution for overcoming the RIE lag problem encountered in low-pressure, high-density plasma etching.[62,67] However, it still remains a question whether the inhibitor deposition results in microscopically uniform *ER*s without sidewall tapering or line-space narrowing.[34] Figures 1.9(k) and 1.9(l) show schematics of sidewall tapering for wider patterns and for narrower patterns, respectively. In such cases, overetching must be continued until the tapered sidewalls become straight, and thereby, notching sometimes occurs due to the continued bombardment of the deflected ions at the inner sidewall foot.[45]

1.5.9 Damage

As the feature size of devices is reduced down to sub-100 nm, the plasma-induced damages (PIDs) also become a significant problem.[68] The feature charging can lead to tunneling current damage to thin dielectrics.[69] Moreover, energetic ions penetrating into substrates cause the defects or lattice damage in Si substrates, for example as shown in Fig. 1.4(b).[70] High energy photons radiated from plasma also cause the bond-breaking in substrate materials.[71] These PIDs result in degradation of device performance.

1.5.10 Roughness

Although etching uniformity is generally able to be achieved in plasma etching, surface roughness is caused by the local fluctuations in the complex interactions between plasma and etched feature surfaces. Surface roughness is significant in nanometer-scale devices or structures because it does not scale down with the dimensions of the devices; i.e., as device dimensions go down, surface roughness may remain the same, thus, its importance is increasing.[72] In the gate fabrication, surface roughness causes the dispersion of device

characteristics because the edges of the gate are not straight but rough lines, thereby the gate does not have a constant length or width, as shown in Figs. 1.4(a) and 1.4(b). The deviation of the line edge from a straight line is termed line edge roughness (LER), while the deviation from the mean line length is termed line width roughness (LWR). Indeed, it has been shown that degradation of the line width accuracy directly impacts the electrical performances of the transistor off-state leakage and device drive currents.[73,74] According to the ITRS 2011, the gate critical dimension (or the physical gate length) will be 18 nm at the 28 nm technological node and requirements for LWR will be of sub-2 nm (3σ).[3] Moreover, in advanced three-dimensional (3D) device structures such as FinFETs, the effects of LER and LWR of the fin as well as those of the gate become significant,[75] because the conducting channels of FinFETs are formed on the top and two vertical sidewalls of the fin, as shown in Figs. 1.4(c) and 1.4(d). The top and sidewall roughness of the fin generated by the dry etch process[76,77] causes the degradation of electron mobility and decreases device performance.[78]

In order to measure the vertical characteristics of the surface deviations and to quantify roughness, the following amplitude parameters are widely used for characterizing surface topography: first conventional roughness parameter is the arithmetic average height parameter (R_a) and second is the root mean square (*RMS*) of the standard deviation of the distribution of surface heights.[79] R_a is defined as the average absolute deviation of the roughness irregularities from the mean line over one sampling length. Although this parameter is easy to define, easy to measure, and gives a good general description of height variations, it does not give any information about the wavelength and it is not sensitive to small changes in profile. By contrast, *RMS* is an important parameter to describe the surface roughness by statistical methods. This parameter is more sensitive than the arithmetic average height (R_a) to large deviation from the mean line. In fact, a common technique used to quantitatively measure surface roughness is a surface profilometer, such as an atomic force microscopy (AFM).[80] A surface profilometer determines the surface roughness by measuring the vertical deflection tip, or stylus, which rides over the surface as the sample is scanned below the tip. An AFM has been widely used to investigate the surface morphology, because it easily provides high-resolution images and characterizes the surface roughness. As device dimensions continue to be scaled down, however, the feature profiles become too small and/or too complex to measure the roughness on the top, bottom and sidewall surfaces of the etched features. In particular, such currently used tools to measure LER have limitations or difficulties[81–83] and

may not be able to meet the LER measurement requirement of the semiconductor industry. This is because recent semiconductor devices have 3D complex structures with vertical surfaces and the available instruments are not optimized for such measurement.[84)]

The formation of surface roughness is stochastic as well as 3D, being affected by a number of factors during processing including plasma etching. Therefore, modeling and simulation of the formation of surface roughness and profile anomalies during etching is becoming increasingly important for the fabrication of next-generation nanoscale devices,[85,86)] to predict and control the atomic-scale roughness on etched feature surfaces, and to gain a better understanding of the mechanisms underlying the phenomena observed.

1.6 Feature Profile Simulation

A number of experimental and numerical studies have been made for Si etching in halogen-based plasmas for advanced FEOL etching processes in nanometer-scale ICs device fabrication.[87)] Thus, the numerical simulation for Si/halogen systems may be available and helpful for a better understanding of the etch mechanisms concerned, and also for a process design with less experimental efforts.[86)]

Regarding etched profiles, various continuum models have been developed using different algorithms such as string method, method of characteristics, level set method, and cell-removal method. Recently, not only two-dimensional (2D) but also three-dimensional (3D) models have been developed using a number of representation and solution algorithms.

1.6.1 String Method

The string method was introduced by Jewett *et al*. and was initially used to describe photoresist development.[88)] The surface is represented by a set of nodes connected by straight line segments moving according to the local etch or deposition rate thereat, as shown in Fig. 1.10(a). The advantages of this method are that the surface propagation is straightforward, and the simple algorithm requires little memory and computation. However, some difficulties lie in the treatment of edge segments at sharp corners, and then this method requires the efficient delooping algorithms to prevent unrealistic feature profiles. Oldham *et al*. have applied this method in modeling the lithography and etching.[89)] Tuda *et al*. simulated Si etching in Cl_2/O_2 plasmas, to analyze the effects of neutral-to-ion flux ratios and additional oxygen on the lateral etching, sidewall tapering, and microscopic uniformity of the etching.[34,35,90)] Vyvoda *et al*.

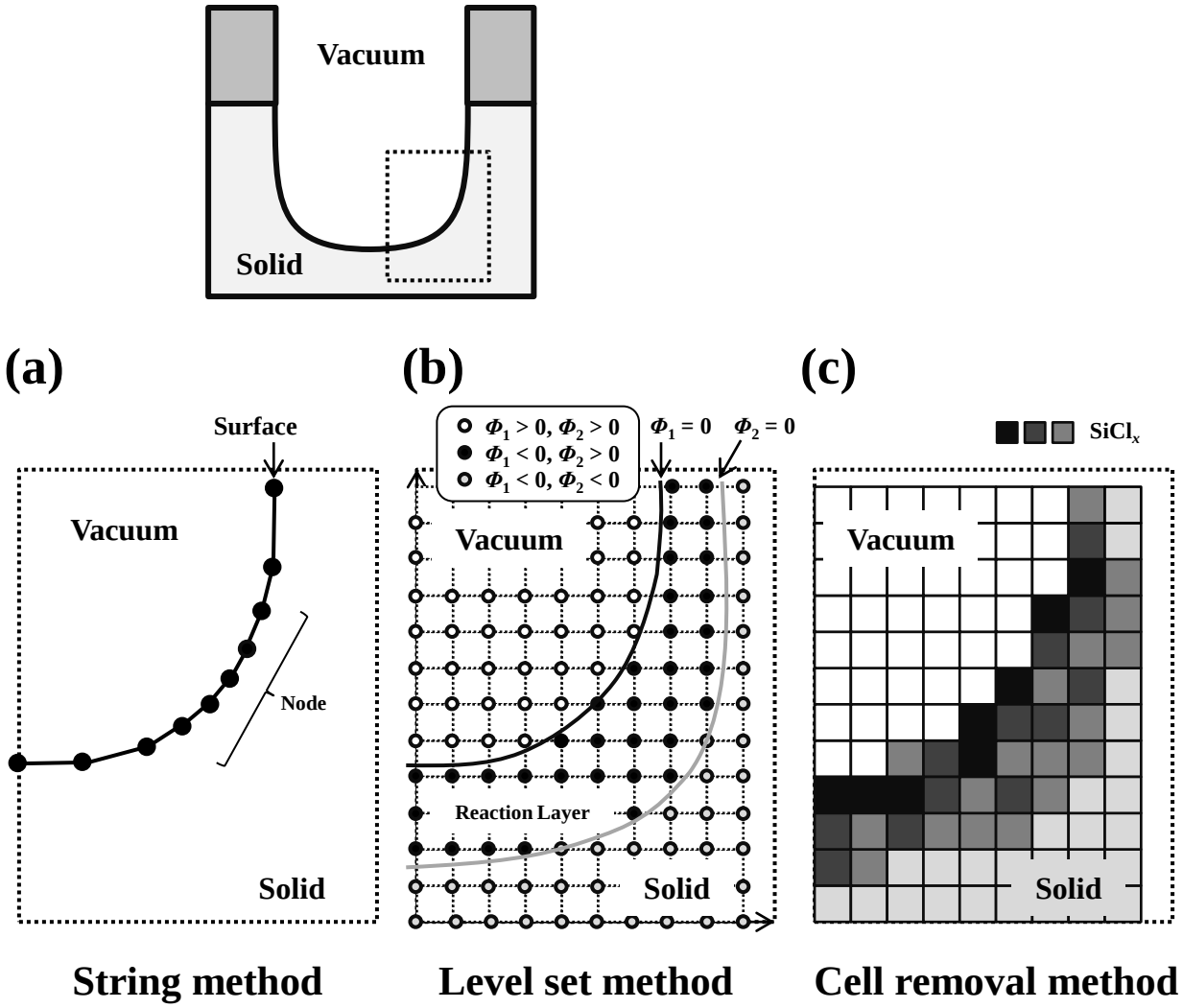

Fig. 1.10. Schematic of continuum models for feature profile evolution: (a) string method, (b) level set method, and (c) cell removal method.

discussed microtrench formation due to ion scattering on sidewalls of feature profiles during Si etching in Cl_2 and HBr plasmas.[91)]

1.6.2 Method of Characteristics

By improving the string method, the method of characteristic has been developed.[92)] In this method, the evolution of the interface is defined by a system of ordinary differential equations that are solved numerically to obtain the profile feature. Shaqfeh and Jurgensen investigated the effects of trench aspect-ratio in low-pressure reactive ion etching.[59)] Method of characteristics have been also used to model reactive ion etching,[93)] rectangular trench etching,[94)] and aluminum etching in a Cl_2/BCl_3 plasmas.[95)] Both methods of string method and method of characteristics, however, become complex in 3D simulations to prevent loop formation of the string network. Moreover, it is also difficult to consider surface composition.

1.6.3 Level Set Method

Level set method was introduced by Osher and Sethian.[96)] They presented the level set representation of the time-dependent evolving interface, of which the essential idea of the method is to represent the interface as a level set of a smooth function Φ, for example the set of points where $\Phi = 0$, as shown in Fig. 1.10(b). The principle advantage of the level set method is the ease of handling topological changes and incorporation into 3D. The level set method has been widely used due to its robustness. Adalsteinsson and Sethian applied a level set formulation to the problem of surface advancement in a 2D topography simulation of deposition, etching, and lithography process in IC fabrication.[97,98)] Hsiau *et al*. incorporated the level set method into the SPEEDIE code to simulate etching and deposition.[99)] Kokkoris *et al*. applied this method in SiO_2 feature etching to simulate RIE lag and inverse RIE lag, and in etching of high-aspect-ratio Si trenches using the Bosch process.[100)] In addition, the level set method can also incorporate the surface composition and the charging effects. Simada *et al*. investigated the relationship between local wall charging and the feature profile in a SiO_2 trench pattern by storing data (or physical quantities) of the charge storage and the surface composition on a fixed, regular spatial grid.[101)] However, this method cannot reproduce the sharp discontinuities or profile anomalies on a nanometer scale.

1.6.4 Cell Removal Method

In cell removal method, the calculation domain is divided into a set of cells which contain volume fractions of different materials, as shown in Fig. 1.10(c). The feature profile is defined by the solid cells adjacent to the unfilled cells and the evolving surfaces are described by removing cells from the surface in this method; the deposition is described by allocating cells at the surface. The solid cells are filled with either a number of particles[42,48,50,102–109] or density.[110] Cell sizes vary from atomic scale[107–109] up to tens of nanometers.[42,110] Cell structure is usually rectangular in 2D[50,105–109] and cubic in 3D,[85,110–114] with the exception of spherical with close-packed arrangement.[115] Surface reactions are usually determined by probabilistic representations of rates for surface physics and chemistries including scattering, sticking of neutrals, ion-induced reactions, etc; thus, a feature profile simulations developed by combining models for the particle transport in microstructures and the surface kinetics are often called dynamic Monte Carlo (MC) simulations. For large-scale MC simulations, an efficient method to create random numbers is essential. In this thesis, we introduced a pseudorandom number generator, called the *Mersenne Twister* (MT19937ar) proposed by Matsumoto and Nishimura,[116] which has a long period $2^{19937} - 1$ and a 623-dimensional equidistribution property.

The advantages of this method are that it can easily handle topological changes including the formation of the sharp discontinuities or profile anomalies on a nanometer scale and that it can be extended to 3D. In addition, cell removal method can easily treat surface composition and various interactions between a particle and surfaces, including the adsorption, deposition, thermal reflection of particles, forward reflection of energetic ions, and desorption of etch products, which are important factors in the characterization and understanding of surface processes, as shown in Fig. 1.10(c). However, there are also negative aspects to this method. Cell-based method generally cannot obtain oblique surfaces or smooth surfaces and thus it has a somewhat less mathematically-rigorous. Moreover, this method requires a large amount of CPU and memory resources (approximately over 1 Gbytes of memory in 3D simulation) than other methods, because etch cell has a data structure which must be stored during simulation.[85] As the current computers become high-performance, such computational resources become relatively reasonable.

In 1975, Dill *et al*. applied a cell removal method to modeling projection exposure and development of the photoresist film. Hwang *et al*. simulated the topography evolution during neutral beam etching of Si and revealed the importance of scattering dynamics in etching.[48]

Moreover, Hwang and Giapis developed a precise model to clarify the mechanisms for notching during overetch step for gate electrode etching, resulting from charging on insulating masks and SiO_2 films underlying polysilicon.[42,102] Mahorowala *et al*. took into account surface oxidation, deposition of etch products desorbed from surfaces, deposition of carbon sputtered from photoresist masks, and forward reflection of ions, to simulate Si etching in Cl_2 plasmas[31,50,105] as well as Cl_2/HBr plasmas.[118] For the investigation of atomic-scale surface reactions, Osano *et al*. introduced the ion penetration scheme like Stopping and Range of Ions in Matter (SRIM),[119] which is a group of computer programs and can calculate interaction of ions with matter, into surface reactions of a cell removal method, and developed an atomic-scale cellular model (ASCeM) for simulating plasma-surface interactions during Si etching in Cl_2 and Cl_2/O_2 plasmas.[107–109] The ASCeM is a MC-based semi-empirical model at an intermediate between continuum models and molecular dynamics simulation, as shown in Fig. 1.11; in practice, it gives a nanometer-scale representation of the feature profile evolution, along with that of surface reaction and passivation multilayers, their chemical constituents, and roughness.

1.6.5 3D Hybrid Methods and Other Methods

To meet the requirements of analysis profiles evolution in 3D, several 3D simulation including hybrid models have been developed. Fujinaga *et al*. combined the concepts of string and cell-based algorithms to develop a 3D topography simulator called a MUlti Layer Shape Simulator (3-D MULSS).[110] Hoekstra *et al*. developed a 3D profile simulator for the purpose of comparing profiles for innately 3D features to results obtained from a 2D profile simulation.[104] Kawai *et al*. developed an algorithm for cell removal/addition in 3D simulation, and investigated surface roughening during polysilicon etching in Ar^+ ion sputtering and Cl_2 gas plasma.[85,111–114] Zhou *et al*. presented a new 2D simulator with a string–cell hybrid method and simulated the etching polymerization alternation in the Bosch process for an infinite trench.[120] Ertl and Selberherr developed an advanced Monte Carlo method with multiple level sets method, which is possible to describe accurately the different material layers which are involved in the process.[121] They also simulated the etching of holes in the Bosch process and investigated the influence of passivation/etching cycle times and hole diameters on the final profile.

To give fundamental etching characteristics such as etch yield, product stoichiometry, and atomistic surface structures, molecular dynamics (MD) simulations have been developed to

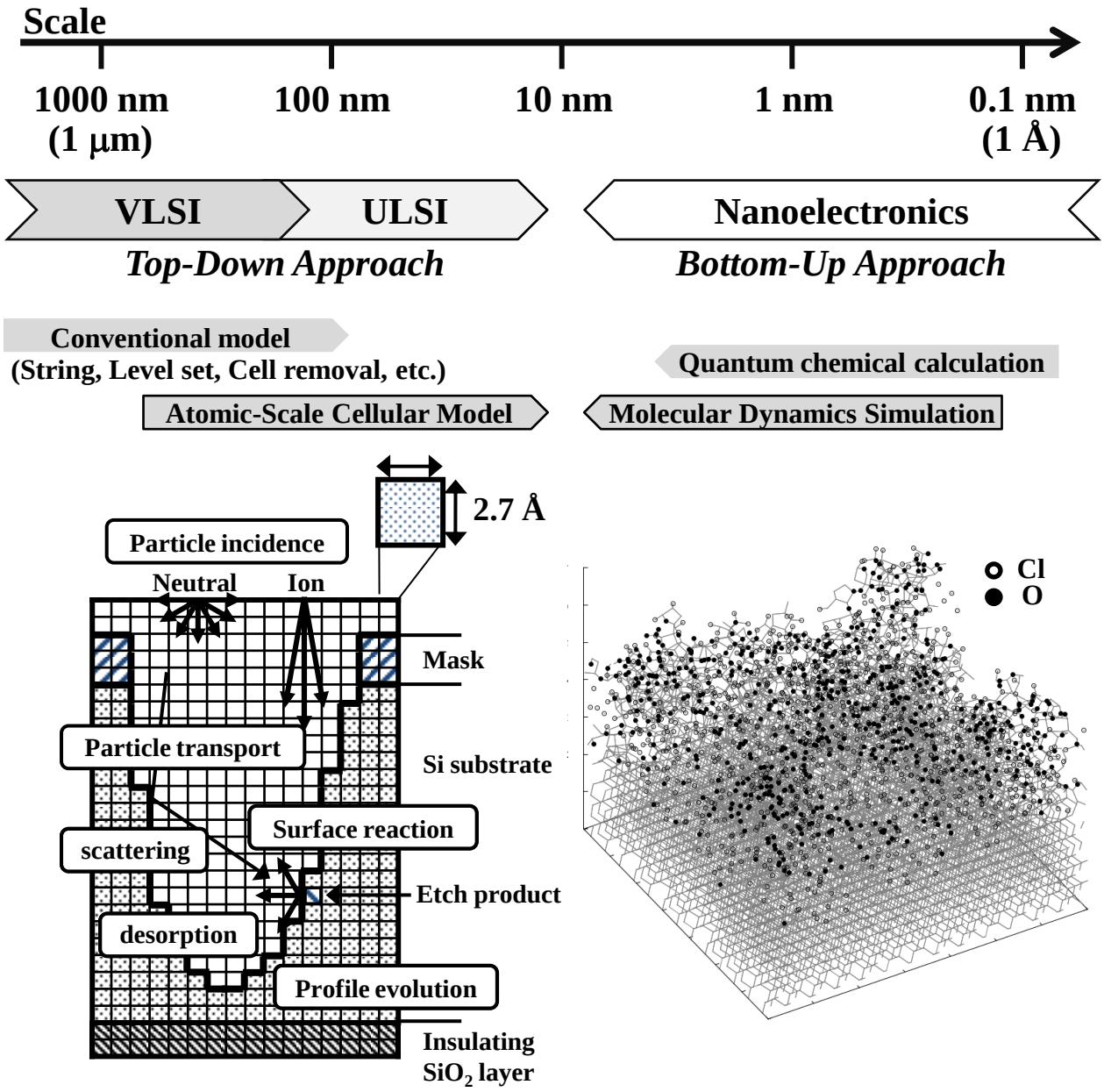

Fig. 1.11. Computer modeling and simulation methods of the plasma-surface interactions during plasma etching for developing next-generation devices.

clarify surface reaction kinetics on atomic scale.[86,122] The MD simulation is usually performed for the etching reaction, where the movements of atoms are analyzed by integrating the Newton's equation of motion using the interatomic potentials defined for each combination of atom species. The MD simulation has a prominent feature to gain atomistic analysis of surface reaction processes. Ohta *et al*. developed MD simulations for Si/Br and Si/HBr as well as Si/Cl systems,[123,124] together with an improved interatomic potential model for Si/halogen interactions,[125] because of a poor understanding of plasma-surface interactions for Br-based plasma etching of Si in experiments as well as simulations. Tsuda *et al.* applied MD simulation to feature profile evolution during Si etching in F, Cl, and Br mono-energetic beams.[126] However, it is difficult for the MD simulation to represent the feature profile evolution during etching, because a long time scale calculation (or a large amount of particle injection) is needed for the analysis of feature profile evolution[126] and the definition of the outermost surface is uncertain in the MD simulation.[127]

1.7 Structure of the Thesis

This thesis presents a Monte Carlo-based semi-empirical model at an intermediate scale between continuum models and the MD simulation as shown in Fig. 1.11, to simulate the feature profile evolution during etching of Si in Cl_2 and Cl_2/O_2 plasmas. An atomic-scale cellular model (ASCeM) is developed to describe the nanometer scale feature geometry, including the multilayer surface reactions and the ion scattering/reflection on the feature surface and penetration into substrates with a binary collision model. The main scheme of the ASCeM has been developed by Osano *et al*.[107–109] In this thesis, we investigate the formation mechanisms of profile anomalies such as bowing, tapering, microtrenching, RIE lag, inverse RIE lag, and residues/micropillars during Si trench etching in Cl_2 and Cl_2/O_2 plasmas, by comparing numerical results of both MC and MD approaches. In addition, we introduce an extended ASCeM model or three-dimensional atomic-scale cellular model (ASCeM-3D) and a simulation of plasma-surface interactions and feature profile evolution during Si etching in Cl_2 plasma. By using the new 3D simulator, we also analyze the formation mechanisms of atomic-scale surface roughening in 3D.

In Chapter 2, we focus on the analysis of formation mechanisms of profile anomalies and microscopic uniformity during plasma etching of Si in Cl_2 plasmas, using our own ASCeM and feature profile simulation. Nanometer-scale control of etched profiles is being increasingly

required for plasma etching technology, as the device feature size continues to be scaled down. Correspondingly, a better understanding of plasma-surface interactions is necessary to clarify dynamics of surface reactions. In fact, RIE has been used in the manufacture of semiconductor devices such as the gate formation and shallow trench isolation. However, the formation mechanisms of profile anomalies and microscopic uniformity have been poorly understood until now. The numerical results indicate that the synergistic effects between ion-enhanced etching and neutral shadowing in microstructural features play a significant role in the formation of profile anomalies.

In Chapter 3, we investigate the formation mechanisms for profile anomalies such as surface roughness and residue for Si etching in Cl_2/O_2 plasmas by numerical and experimental approaches. The ASCeM can reproduce the feature profile evolution experimentally observed during etching at increased O_2 concentrations. A comparison between simulation and experiment also indicates that the local surface oxidation induces surface roughness at the bottom of the feature during etching; then, synergistic effects between surface oxidation and ion scattering in microstructural features on roughened surfaces increase the surface roughness, which in turn cause a number of significant residues or micropillars on bottom surfaces of the feature.

In Chapter 4, we focus on the mechanism underlying local surface oxidation during Si etching in Cl_2/O_2 plasmas, and analyze the relationship between local surface oxidation and surface roughness on the nanometer scale, by a classical MD simulation. Addition of oxygen to Cl_2 discharge is widely used in Si etching for the fabrication of gate electrodes and shallow trench isolation. As the control of etching processes becomes more critical, a deeper understanding of plasma-surface interactions is required for the formation of roughened surfaces during etching. In particular, a small amount of O_2 often leads to profile anomalies such as residues, micropillars, and roughened surfaces. The numerical results indicate that O radicals tend to break Si–Si bonds and distort the Si lattice structure; thus, nanometer-scale micromasks tend to be formed on convex roughened surfaces, owing to the reactivity of O radicals with substrate Si atoms and Cl atoms.

In Chapter 5, we introduce the ASCeM-3D and feature profile simulation, with emphasis being placed on the formation of surface roughness on the atomic scale soon after the start of Si etching in Cl_2 plasmas, in order to predict the surface roughness on an atomic or nanometer scale. Three-dimensional measurement and prediction of atomic-scale surface roughness on

etched features become increasingly important for the fabrication of next-generation devices; however, the feature profiles are too small or too complex to measure the surface roughness on bottom surfaces and sidewalls of the etched features. The ASCeM-3D indicates that nanometer-scale convex roughened features appear on the surface soon after the start of etching, which causes the formation of a larger surface roughness, and that the surface roughness tends to be saturated after several seconds. A comparison is also made between numerical results and experiments.

In Chapter 6, we investigate the evolution of nanoscale surface features and roughness during Si etching in Cl_2 plasmas, with further attention being given to that of ripple structures on etched surfaces by using the ASCeM-3D. Numerical results indicate that as the ion incident angle is increased, nanoscale concavo-convex features drastically change and ripple structures occur on etched surfaces. Analysis of ion trajectories also implies that the ion reflection and concentration on microscopically roughened surfaces largely affect the surface roughening and rippling during plasma etching. These numerical approaches would become important to predict the nanoscale surface features and roughness, especially the line edge roughness (LER) formed on feature sidewalls, because experiments of oblique incidence of ions on surfaces are difficult in plasma environments.

Chapter 7 concludes this study and discusses recommendation for future works and challenges.

References

1) H. Abe, M. Yoneda, and N. Fujiwara: Jpn. J. Appl. Phys. **47** (2008) 1435.
2) G. E. Moore: Electronics **38** (1965) 114.
3) International Technology Roadmap for Semiconductors, ITRS 2011 Edition [http://www.itrs.net].
4) C. Y. Chang and S. M. Sze: *ULSI Devices* (John Willy & Sons, New York, 2000).
5) D. Kahng and M. M. Atalla: IRE-AIEE Solid-State Device Res. Conf., 1960.
6) S. M. Sze: *Semiconductor Devices, Physics and Technology, 2nd Edition* (John Willy & Sons, New York, 2002).
7) R. H. Dennard, F. H. Gaensslen, H. -N. Yu, V. L. Rideout, E. Bassous, and A. R. LeBlanc: IEEE. J. Solid-State Circuits **SC-9** (1974) 256.
8) G. Baccarani, M. R. Wordeman, and R. H. Dennard: IEEE Trans. Electron Devices **ED-31** (1984) 452.
9) T. Sekigawa and Y. Hayashi: Solid-State Electron. **27** (1984) 827.
10) D. Hisamoto, T. Kaga, Y. Kawamoto, and E. Takeda: IEEE Electron Device Lett. **11** (1990) 36.
11) D. Hisamoto, W. -C. Lee, J. Kedzierski, H. Takeuchi, K. Asano, C. Kuo, E. Anderson, T. -J. King, J. Bokor, and C. Hu: IEEE Trans. Electron Devices **47** (2000) 2320.
12) X. Huang, W. -C. Lee, C. Kuo, D. Hisamoto, L. Chang, J. Kedzierski, E. Anderson, H. Takeuchi, Y. -K. Choi, K. Asano, V. Subramanian, T. -J. King, J. Bokor, and C. Hu: IEDM Tech. Dig., 1990, p. 67.
13) X. Huang, W. -C. Lee, C. Kuo, D. Hisamoto, L. Chang, J. Kedzierski, E. Anderson, H. Takeuchi, Y. -K. Choi, K. Asano, V. Subramanian, T. -J. King, J. Bokor, and C. Hu: IEEE Trans. Electron Devices **48** (2001) 880.
14) J. P. Colinge, M. H. Gao, A. Romano-Rodríguez, H. Maes, and C. Claeys: IEDM Tech. Dig., 1990, p. 595.
15) B. S. Doyle, S. Datta, M. Doczy, S. Hareland, B. Jin, J. Kavalieros, T. Linton, A. Murthy, R. Rios, and R. Chau: IEEE Electron Device Lett. **24** (2003) 263.
16) I. Ferain, C. A. Colinge, and J. -P. Colinge: Nature **479** (2011) 310.
17) S. M. Sze: *VLSI Technology, 2nd Edition* (McGram-Hill, New York, 1988).
18) C. Y. Chang and S. M. Sze: *ULSI Technology, International Editions* (McGram-Hill, New York, 1996).

19) M. A. Lieberman and A. J. Lichtenberg: *Principles of Plasma Discharges and Materials Processing, 2nd Edition* (Wiley, NewYork, 2005).
20) M. C. Elwenspoek and H. V. Jansen: *Silicon Micromachining* (Cambridge University Press, UK, 1998).
21) G. S. Oehrlein, K. K. Chan, M. A. Jaso, and G. W. Rubloff: J. Vac. Sci. Technol. A **7** (1989) 1030.
22) M. Sato and Y. Arita: J. Electrochem. Soc. **134** (1987) 2856.
23) T. D. Bestwick and G. S. Oehrlein: J. Vac. Sci. Technol. A **8** (1990) 1696.
24) J. D. Plummer, M. D. Deal, and P. B. Griffin: *Silicon VLSI Technology: Fundamentals, Practice and Modeling* (Prentice Hall, Upper Saddle River, New Jersey, 2000).
25) K. Nishikawa, T. Oomori, and K. Ono: J. Vac. Sci. Technol. B **17** (1999) 127.
26) C. Lee, D. B. Graves, and M. A. Lieberman: Plasma Chem. Plasma Proc. **16** (1996) 99.
27) D. L. Flamm: Pure Appl. Chem. **62** (1990) 1709.
28) E. Pargon, M. Darnon, O. Joubert, T. Chevolleau, L. Vallier, L. Mollard, and T. Lill: J. Vac. Sci. Technol. B **23** (2005) 1913.
29) M. Oda and K. Hirata: Jpn. J. Appl. Phys. **19** (1980) L405.
30) E. A. Ogryzlo, D. E. Ibbotson, D. L. Flamm, and J. A. Mucha: J. Appl. Phys. **67** (1990) 3115.
31) W. Jin and H. H. Sawin: J. Vac. Sci. Technol. A **21** (2003) 911.
32) S. A. Vitale, H. Chae, and H. H. Sawin: J. Vac. Sci. Technol. A **19** (2001) 2197.
33) M. Boufnichel, S. Aachboun, P. Lefaucheux, and P. Ranson: J. Vac. Sci, Technol. B **21** (2003) 267.
34) M. Tuda and K. Ono: Jpn. J. Appl. Phys. **36** (1997) 2482.
35) M. Tuda, K. Ono, and K. Nishikawa: J. Vac. Sci. Technol. B **14** (1996) 3291.
36) A. D. G. Stewart and M. W. Thompson: J. Mater. Sci. **4** (1969) 56.
37) R. Smith: *Atomic and Ion Collisions in Solids and at Surfaces - Theory, Simulation and Applications* (Cambrige University Press, UK, 1997) Chap. 9, p. 284.
38) S. Ohki, M. Oda, H. Akiya, and T. Shibata: J. Vac. Sci. Technol. B **5** (1987) 1611.
39) T. Nozawa, T. Kinoshita, T. Nishizuka, A. Narai, T. Inoue, and A. Nakaue: Jpn. J. Appl. Phys. **34** (1995) 2017.
40) N. Fujiwara, T. Maruyama, and M. Yoneda: Jpn. J. Appl. Phys. **34** (1995) 2095; **35** (1996) 2450.

41) T. Kinoshita, M. Hane, and J. P. McVittie: J. Vac. Sci. Technol. B **14** (1996) 560.
42) G. S. Hwang and K. P. Giapis: J. Vac. Sci. Technol B **15** (1997) 70.
43) K. P. Cheung: *Plasma Charging Damage* (Springer, London, 2000) Chap. 3, p. 99.
44) J. C. Arnold and H. H. Sawin: J. Appl. Phys. **70** (1991) 5314.
45) R. J. Shul and S. J. Pearton: *Handbook of Advanced Plasma Processing Techniques* (Springer, Berlin, 2000).
46) T. J. Dalton, J. C. Arnold, H. H. Sawin, S, Swan, and D. Corliss: J. Electrochem. Soc. **140** (1993) 2395.
47) A. C. Westerheim, A. H. Labun, J. H. Dubash, J. C. Arnord, H. H. Sawin, and V. Y. Wang: J. Vac. Sci. Technol. A **13** (1995) 853.
48) G. S. Hwang, C. M. Anderson, M. J. Gordon, T. A. Moore, T. K. Minton, and K. P. Giapis: Phys. Rev. Lett. **77** (1996) 3049.
49) A. P. Mahorowala, H. H. Sawin, R. Jones, and A. H. Labun: J. Vac. Sci. Technol. B **20** (2002) 1055.
50) A. P. Mahorowala and H. H. Sawin: J. Vac. Sci. Technol. B **20** (2002) 1077.
51) G. S. Oehrlein, J. F. Rembetski, and E. H. Payne: J. Vac. Sci. Technol. B **8** (1990) 1199.
52) H. Jansen, H. Gardeniers, M. de Boer, M. Elwenspoek, and J. Fluitman: J. Micromech. Microeng. **6** (1996) 14.
53) G. S. Oehrlein, R. G. Schad, and M. A. Jaso: Surf. Interface Analysis **8** (1986) 243
54) C. F. Carlström, R. van der Heijden, F. Karouta, R. W. van der Heijden, H. W. M. Salemink, and E. van der Drift: J. Vac. Sci. Technol. B **24** (2006) L6.
55) T. Hayakawa, T. Suzuki, T. Uesugi, and Y. Mitsushima: Jpn. J. Appl. Phys. **37** (1998) 5.
56) R. A. Gottscho, C. W. Jurgensen and D. J. Vitkavage: J. Vac. Sci. Technol. B **10** (1992) 2133.
57) J. W. Coburn and H. F. Winters: Appl. Phys. Lett. **55** (1989) 2730.
58) T. Arikado, K. Horioka, M. Sekine, H. Okano and Y. Horiike: Jpn. J. Appl. Phys. **27** (1988) 95.
59) E. S. G. Shaqfeh and C. W.Jurgensen: J. Appl. Phys. **66** (1989) 4644.
60) N. Fujiwara, T. Shibano, K. Nishioka, and T. Katoz: Jpn. J. Appl. Phys. **28** (1989) 2147.
61) Y. Gotoh, T. Kure, and S. Tachi: Jpn. J. Appl. Phys. **32** (1993) 3035.
62) A. D. Bailey III, M. C. M. van de Sanden, J. A. Gregus, and R. A. Gottscho: J. Vac. Sci. Technol. B **13** (1995) 92.

63) K. P. Giapis, G. R. Scheller, R. A. Gottscho, W. S. Hobson, and Y. H. Lee: Appl. Phys. Lett. **57** (1990) 983.
64) D. L. Olynick, J. A. Liddle, and I. W. Rangelow: J. Vac. Sci. Technol. B **23** (2005) 2073.
65) S. G. Ingram: J. Appl. Phys. **68** (1990) 500.
66) H. Ootera, T. Oomori, M. Tuda, and K. Namba: Jpn. J. Appl. Phys. **33** (1994) 4276.
67) A. D. Bailey III and R. A. Gottscho: Jpn. J. Appl. Phys. **34** (1995) 2083.
68) K. Eriguchi and K. Ono: J. Phys. D **41** (2008) 024002.
69) K. P. Cheung: *Plasma Charging Damage* (Springer, Heidelberg, 2001).
70) K. Eriguchi, Y. Nakakubo, A. Matsuda, M. Kamei, H. Ohta, H. Nakagawa, S. Hayashi, S. Noda, K. Ishikawa, M. Yoshimaru, and K. Ono: IEDM Tech. Dig., 2008, p. 443.
71) T Yunogami and T. Mizutani: J. Appl. Phys. **73** (1993) 8184.
72) E. Gogolides, V. Constantoudis, G. P. Patsis, and A. Tserepi: Microelectron. Eng. **83** (2006) 1067.
73) J. A. Croon, G. Storms, S. Winkelmeier, I. Pollentier, M. Ercken, S. Decoutere, W. Sansen, and H. E. Maes: IEDM Tech. Dig., 2002, p. 307.
74) H. -W. Kim, J. -Y. Lee, J. Shin, S. -G. Woo, H. -K. Cho, and J. -T. Moon: IEEE Trans. Electron Devices **51** (2004) 1984.
75) K. Patel, T. -J. K. Liu, and C. J. Spanos: IEEE Trans. Electron Devices **56** (2009) 3055.
76) E. Altamirano-Sánchez, V. Paraschiv, M. Demand, and W. Boullart: Microelectron. Eng. **88** (2011) 2871.
77) K. J. Kanarik, G. Kamarthy, and R. A. Gottscho: Solid State Technol. **55** (2012) 15.
78) Y. -K. Choi, N. Lindert, P. Xuan, S. Tang, D. Ha, E. Anderson, T. -J. King, J. Bokor, and C. Hu: IEDM Tech. Dig., 2001, p. 421.
79) E. S. Gadelmawla, M. M. Koura, T. M. A. Maksoud, I. M. Elewa, and H. H. Soliman: J. Mater. Proc. Technol. **123** (2002) 133.
80) G. Binnig, C. F. Quate, and C. Gerber: Phys. Rev. Lett. **56** (1986) 930.
81) A. Yahata, S. Urano, and T. Inoue: J. Vac. Sci. Technol. A **36** (1997) 6722.
82) D. L. Goldfarb, A. P. Mahorolawa, G. M. Gallatin, K. E. Petrillo, K. Temple, M. Angelopoulos, S. Rasgon, H. H. Sawin, S. D. Allen, M. C. Lawson, and R. W. Kwong: J. Vac. Sci. Technol. B **22** (2004) 647.
83) K. L. Westra and D. J. Thomson: J. Vac. Sci. Technol. B **13** (1995) 344.
84) N. G. Orji, T. V. Vorburger, J. Fu, R. G. Dixson, C. V. Nguyen, and J. Raja: Meas. Sci.

Technol. **16** (2005) 2147.

85) W. Guo and H. H. Sawin: J. Phys. D **42** (2009) 194014.

86) K. Ono, H. Ohta, and K. Eriguchi: Thin Solid Films **518** (2010) 3461.

87) K. Ono, *et al*., J. Plasma Fusion Res. **85** (2009) 163 [in Japanese], and references therein.

88) R. E. Jewett, P. I. Hagouel, A. R. Neureuther, and T. van Duzer: Polymer Eng. Sci. **17** (1977) 381.

89) W. G. Oldham, A. R. Neureuther, C. Sung, J. L. Reynolds, and S. N. Nandgaonkar: IEEE Trans. Electron Devices **27** (1980) 1455.

90) M. Tuda, K. Nishikawa, and K. Ono: J. Appl. Phys. **81** (1997) 960.

91) M. A. Vyvoda, M. Li, D. B. Graves, H. Lee, M. V. Malyshev, F. P. Klemens, J. T. C. Lee, and V. M. Donnelly: J. Vac. Sci. Technol. B **18** (2000) 820.

92) D. S. Ross: J. Electrochem. Soc. **135** (1988) 1260.

93) S. Hamaguchi, M. Dalvie, R. T. Farouki, and S. Sethuraman: J. Appl. Phys. **74** (1993) 5172.

94) B. Abraham-Shrauner: IEEE Trans. Plasma Sci. **25** (1997) 433.

95) D. J. Cooperberg, V. Vahedi, and R. A. Gottscho: J. Vac. Sic. Technol. A **20** (2002) 1536.

96) S. Osher and J. A. Sethian: J. Comput. Phys. **79** (1988) 12.

97) D. Adalsteinsson and J. A. Sethian: J. Comp. Phys. **120** (1995) 128.

98) D. Adalsteinsson and J. A. Sethian: J. Comp. Phys. **122** (1995) 348.

99) Z. -K. Hsiau, E. C. Kan, J. P. McVittie, and R. W. Dutton: IEEE Trans. Electron Devices **44** (1997) 1375.

100) G. Kokkoris, A. Tserepi, A. G. Boudouvis, and E. Gogolides: J. Vac. Sci. Technol. A **22** (2004) 1896.

101) T. Shimada, T. Yagisawa, and T. Makabe: Jpn. J. Appl. Phys. **45** (2006) L132.

102) G. S. Hwang and K. P. Giapis: J. Vac. Sci. Technol. B **15** (1997) 1839.

103) R. J. Hoekstra, M. J. Grapperhaus, and M. J. Kushner: J. Vac. Sci. Technol. A **15** (1997) 1913.

104) R. J. Hoekstra, M. J. Grapperhaus, and M. J. Kushner: J. Vac. Sci. Technol. A **16** (1998) 3274.

105) A. P. Mahorowala and H. H. Sawin: J. Vac. Sci. Technol. B **20** (2002) 1064.

106) A. P. Mahorowala and H. H. Sawin: J. Vac. Sci. Technol. B **20** (2002) 1084.

107) Y. Osano and K. Ono: Jpn. J. Appl. Phys. **44** (2005) 8650.

108) Y. Osano, M. Mori, N. Itabashi, K. Takahashi, K. Eriguchi, and K. Ono: Jpn. J. Appl. Phys. **45** (2006) 8157.
109) Y. Osano and K. Ono: Jpn. J. Vac. Sci. Technol. B **26** (2008) 1425.
110) M. Fujinaga and N. Kotani: IEEE Trans. Electron Devices **44** (1997) 226.
111) H. Kawai: Ph. D. Thesis, Dept. of Chemical Engineering, Massachusetts Institute of Technology, MA, 2008.
112) W. Guo, B. Bai, and H. H. Sawin: J. Vac. Sci. Technol. A **27** (2009) 388.
113) W. Guo and H. H. Sawin: J. Vac. Sci. Technol. A **28** (2010) 250.
114) W. Guo and H. H. Sawin: J. Vac. Sci. Technol. A **28** (2010) 259.
115) V. Arunachalam, S. Rauf, D. G. Coronell, and P. L. G. Ventzek: J. Appl. Phys. **90** (2001) 64.
116) M. Matsumoto and T. Nishimura: ACM Trans. Model. Comput. Simul. **8** (1998) 3.
117) F. H. Dill, A. R. Neureuther, J. A. Tuttle, and E. J. Walker: IEEE Trans. Electron Devices **ED-22** (1975) 456.
118) W. Jin, S. A. Vitale, and H. H. Sawin: J. Vac. Sci. Technol. A **20** (2002) 2106.
119) J. F. Ziegler, J. P Biersack, and M. D. Ziegler: *SRIM – The Stopping and Range of Ions in Matter* (SRIM, Chester, MD, 2008), the program is down loadable from the world wide web at http://www.srim.org/.
120) R. Zhou, H. Zhang, Y. Hao, and Y. Wang: J. Micromech. Microeng. **14** (2004) 851.
121) O. Ertl and S. Selberherr: Microelectron. Eng. **87** (2010) 20.
122) D. B. Graves and P. Brault: J. Phys. D **42** (2009) 194011.
123) H. Ohta, A. Iwakawa, K. Eriguchi, and K. Ono: J. Appl. Phys. **104** (2008) 073302.
124) T. Nagaoka, K. Eriguchi, K. Ono, and H. Ohta: J. Appl. Phys. **105** (2009) 023302.
125) H. Ohta, T. Nagaoka, K. Eriguchi, and K. Ono: Jpn. J. Appl. Phys. **48** (2009) 020225.
126) H. Tsuda, K. Eriguchi, K. Ono, and H. Ohta: Appl. Phys. Express **2** (2009) 116501.
127) C. F. Abrams and D. B. Graves: J. Vac. Sci. Technol. A **16** (1998) 3006.

Chapter 2
Analysis of Profile Anomalies and Microscopic Uniformity

2.1 Introduction

Plasma etching or reactive ion etching (RIE) has been used in the manufacture of semiconductor integrated circuit devices since the late 1970s.[1)] In Si etching for the fabrication of gate electrodes and shallow trench isolation (STI), chlorine-based plasmas are widely used because of the controllability of etching profiles. As device dimensions continue to be scaled down, the precise or nanometer-scale control of profiles is increasingly required during plasma etching. For example, gate electrode etching requires vertical sidewalls with high dimensional accuracy (no footing, notch, microtrench, and residue) and high selectivity over thin gate dielectrics and substrates. On the other hand, STI requires tapered sidewalls, round corners of top and bottom surfaces, and uniform etched depths. In addition, feature sizes below 1 μm with high aspect ratios (depth/width) cause several problems of microscopic uniformity, such as RIE lag and inverse RIE lag.[2,3)]

To meet these requirements and control the etched profiles accurately, it is necessary to understand the interactions between chemically reactive plasmas and substrate surfaces, and to clarify the formation mechanisms of profile anomalies such as microtrench and RIE lag during plasma etching.[4)] Although a number of numerical[5-8)] and experimental[9-17)] studies have been reported, fundamental cause-and-effect relationships for these phenomena are still poorly understood. In this paper, we focus on the formation mechanisms of profile anomalies and surface roughness during plasma etching of Si in Cl_2 plasmas, using our own atomic-scale cellular model (ASCeM).[18-21)] Emphasis is placed on the synergistic effects between ion-enhanced etching and neutral shadowing in microstructural features, and we analyze the microscopic uniformity induced, with attention being given to the effects of incident ion energy and neutral-to-ion flux ratio on the pattern dependence of etched profiles.

2.2 Modeling and Simulation

Figure 2.1 shows a schematic of the ASCeM model.[18–21)] The model represents the etching of infinitely long trenches in Si substrates with Cl_2 plasma chemistries. The simulation domain is divided into a number of small square cells of 2.7 Å atomic sizes, corresponding to the interatomic distance in Si substrates. Energetic ions, neutrals, and etch by-products are

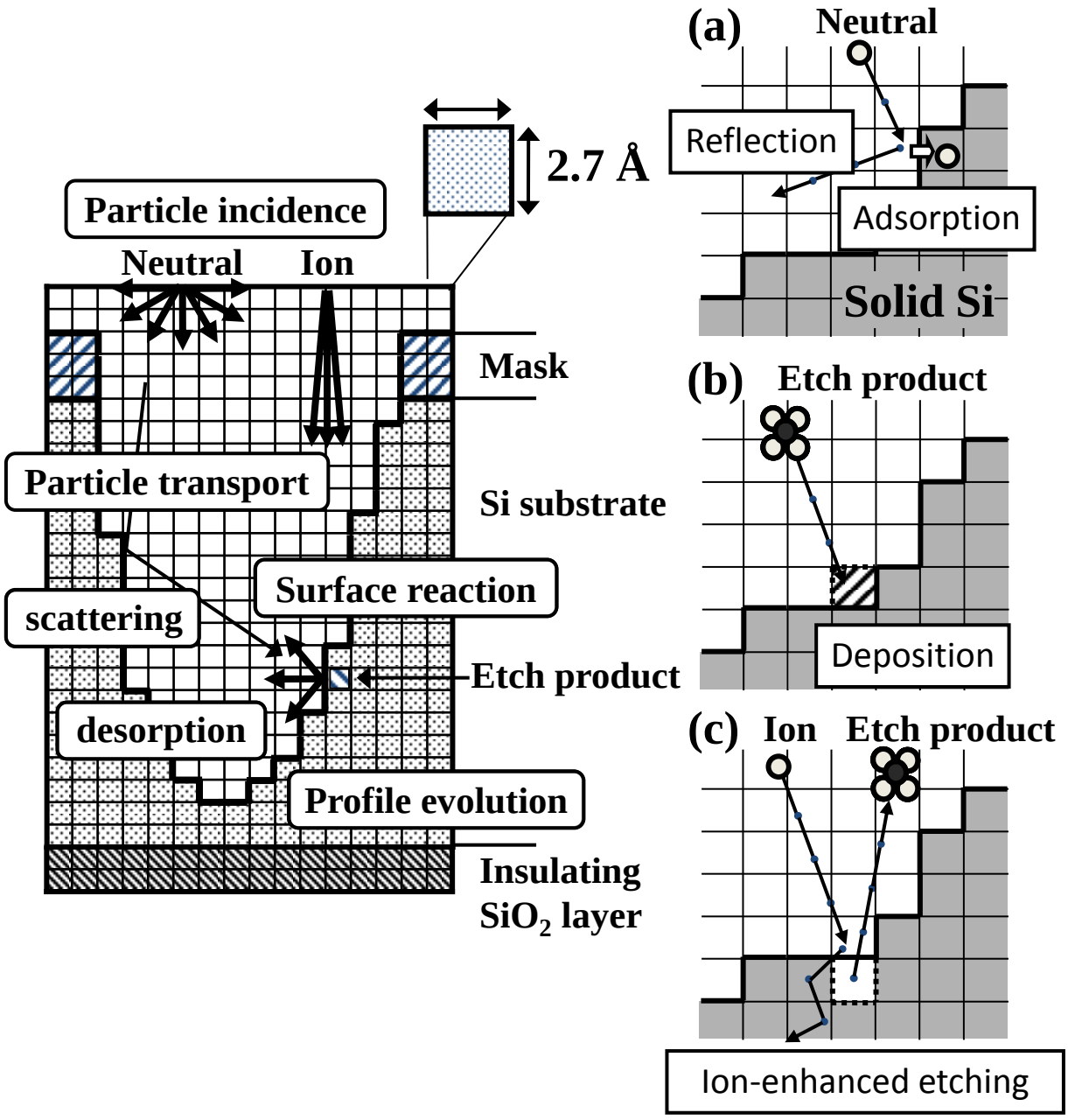

Fig. 2.1. Schematic of the ASCeM model, where Cl^+ ions, Cl neutrals, O neutrals, and etch by-products [$SiCl_x$ (x = 1 ~ 4)] are injected from the top of the simulation domain, and etch products are desorbed from etching surfaces into microstructural features. The particle transport is analyzed using the Monte Carlo (MC) algorithm with three velocity components. The simulation domain is divided into a number of small square cells of 2.7 Å atomic sizes, and Si atoms are allocated at the center of square lattices. The model also takes into account surface chemistries based on the MC algorithm: (a) adsorption and reemission of neutrals, (b) deposition of etch products and by-products, and (c) ion-enhanced etching.

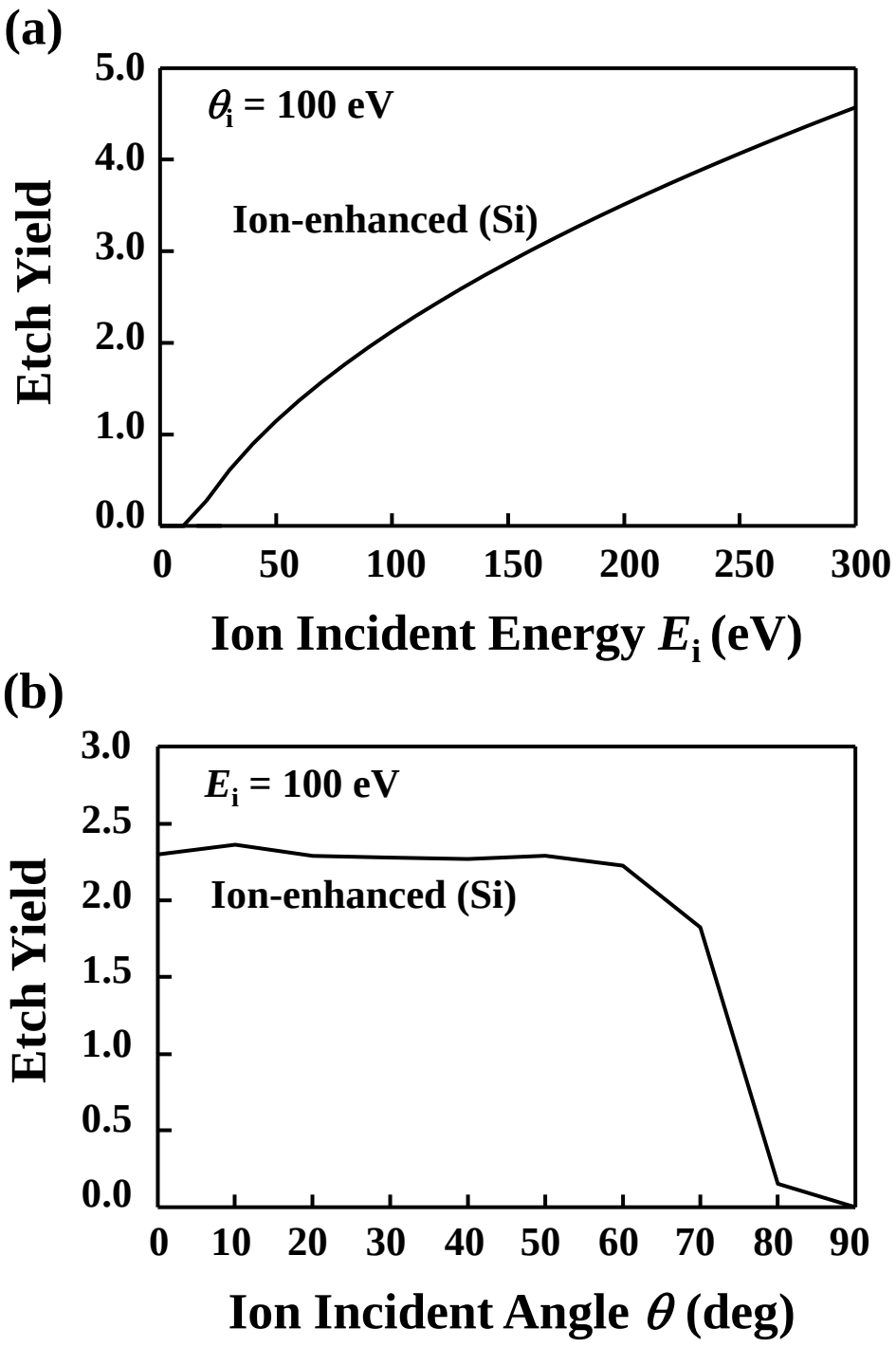

Fig. 2.2. Etch yield for Cl^+ ions on Si surfaces as a function of (a) incident ion energy E_i (θ_i = 0° or normal incidence) and (b) incident angle θ (E_i = 100 eV).

introduced from the top of the simulation domain, and etch products are desorbed from etching surfaces into microstructural features. The particle transport is analyzed using the two-dimensional Monte Carlo (MC) algorithm with three velocity components.[19,22–24)]

To analyze the interactions between energetic ions and substrates, the model includes two-body elastic collision processes between incident ions and substrate atoms with the Stillinger-Weber interaction potential for the Cl–Si system.[25–27)] The model also takes into account surface chemistries based on the MC algorithm,[20,28,29)] including ion-enhanced etching, chemical etching, reemission of neutrals, and redeposition of etch products from the feature surface. Note that in this study, passivation layer formation is not taken into account through surface oxidation and deposition of etch by-products coming from the plasma. Figures 2.2(a) and 2.2(b) show the etch yield for Cl^+ ions on Si surfaces as a function of incident energy and incident angle, respectively. The etch yield depending on the ion incident angle is obtained automatically in the calculation of collision process between Cl^+ ions and Si substrate atoms.[29,30)]

The feature profile evolution during Si etching in Cl_2 plasma is simulated for line-and-space patterns separated by different spaces. The initial surface profile is a hard mask pattern of line-and-space structure on poly-Si films of thickness H_{Si} = 200 nm; the mask pattern has a linewidth L_{mask} = 100 nm and a height H_{mask} = 50 nm, each separated by six different spaces of W = 30, 50, 70, 100, 200, and 500 nm. There is an insulating SiO_2 layer under the poly-Si, and the mask and SiO_2 layer are assumed not to be eroded during etching.

More detail of the ASCeM will be mentioned in Appendix A.

2.3 Results and Discussion

2.3.1 Formation of RIE Lag

Figures 2.3(a)-2.3(c) show the etched profile evolution of line-and-space patterns of Si, simulated for different incident ion energies of E_i = 50, 100, and 200 eV. Here, the incident ion energy is E_i = 100 eV, the ion temperature kT_i = 0.5 eV, the ion flux $\Gamma_i^0 = 1.0 \times 10^{16}$ $cm^{-2}s^{-1}$, the neutral flux ratio $\Gamma_n^0 = 1.0 \times 10^{17}$ $cm^{-2}s^{-1}$, the neutral-to-ion flux ratios of $\Gamma_n^0/\Gamma_i^0 = 10$, the gas temperature T_g = 500 K, the substrate temperature T_s = 300 K, the sticking probability S_n = 1 for Cl neutrals on unsaturated surface sites of Si, and the sticking probability S_q = 0.05 for etch products ($SiCl_4$) desorbed from feature surfaces being etched. The incident angle of energetic ions is obtained by random sampling from the expression for the angular distribution of ion

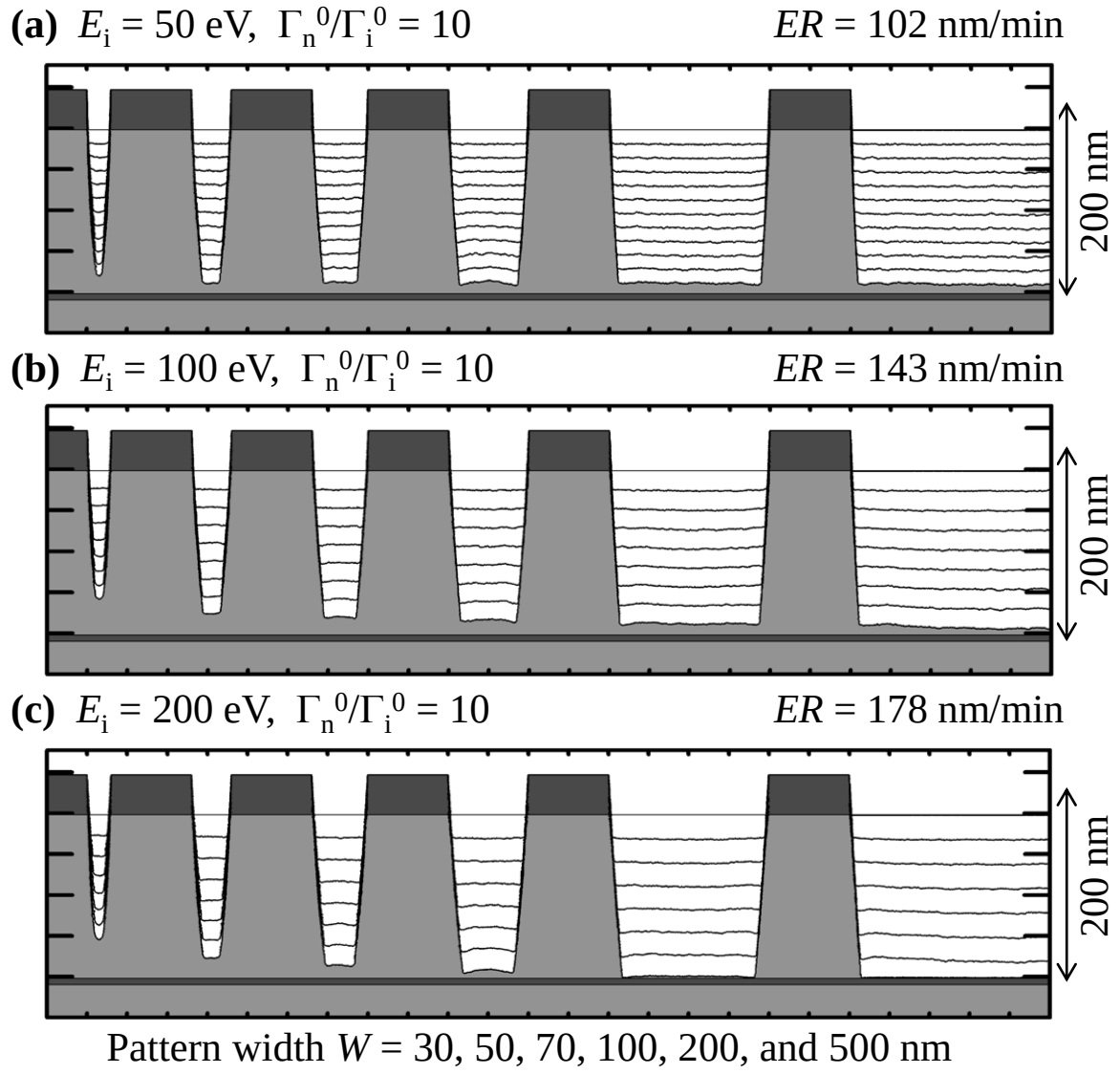

Fig. 2.3. Etched profile evolution of line-and-space patterns of Si, simulated for different incident ion energies of E_i = (a) 50, (b) 100, and (c) 200 eV. Calculations were made with an ion temperature kT_i = 0.5 eV, an ion flux $\Gamma_i^0 = 1.0 \times 10^{16}$ cm^{-2} s^{-1}, a neutral-to-ion flux ratio Γ_n^0/Γ_i^0 = 10, and a sticking probability S_q = 0.05 for etch products ($SiCl_4$) desorbed from feature surfaces being etched. Each curve represents the evolving interfaces every 10 s, and the insets are the vertical etch rates (*ER*s) at the center of the W = 500 nm feature bottom. The initial surface profile is a hard mask pattern of lines and spaces on poly-Si films of thickness H_{Si} = 200 nm; the mask pattern has a linewidth L_{mask} = 100 nm and a height H_{mask} = 50 nm, each separated by six different spaces of W = 30, 50, 70, 100, 200, and 500 nm. There is an insulating SiO_2 layer under the poly-Si, and the mask and the SiO_2 layer are assumed not to be eroded during etching.

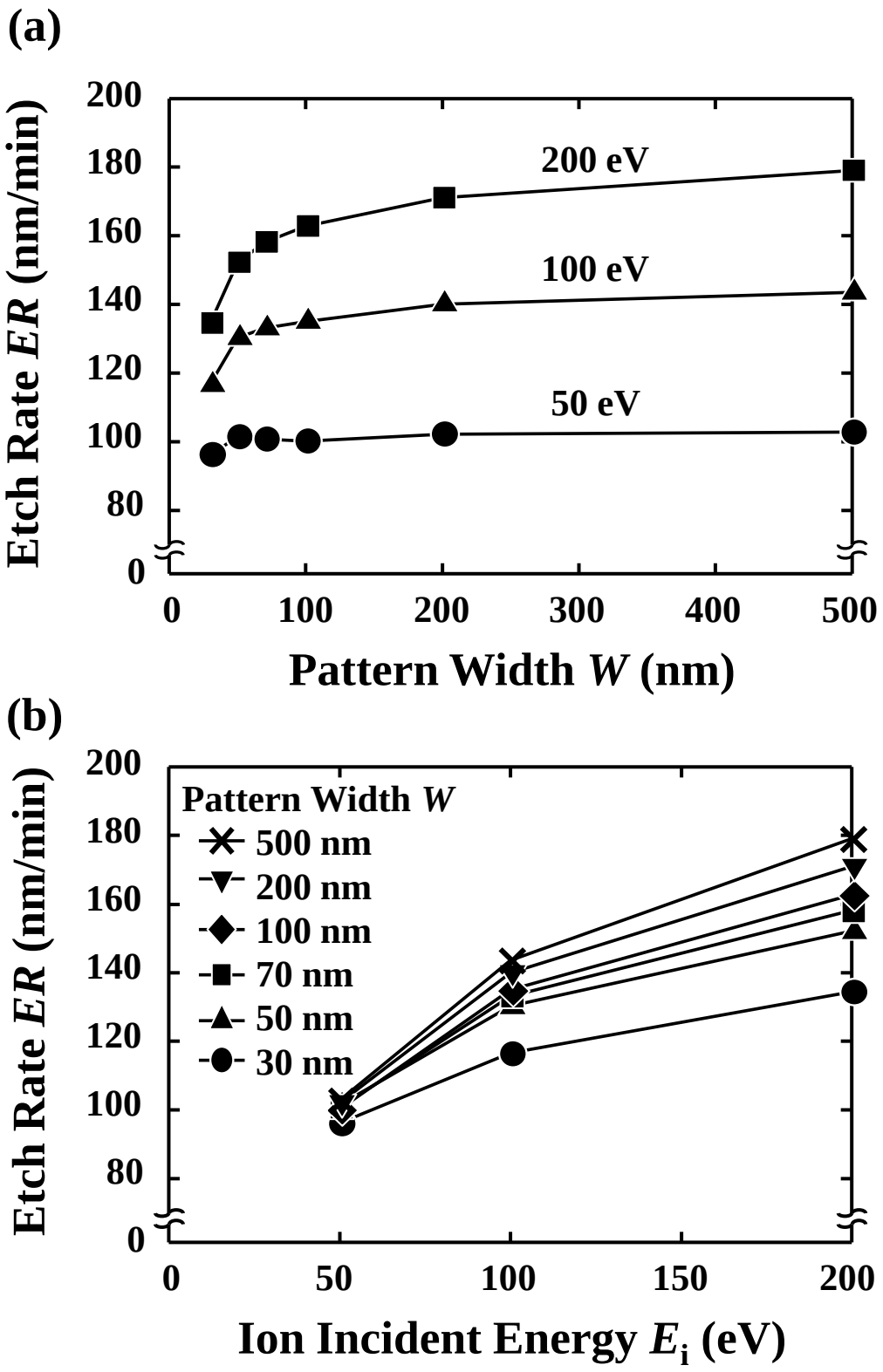

Fig. 2.4. Etch rates or *ER*s as a function of (a) pattern width *W* and (b) Incident Energy E_i, taken from the data of Figs. 2.3(a)-2.3(c).

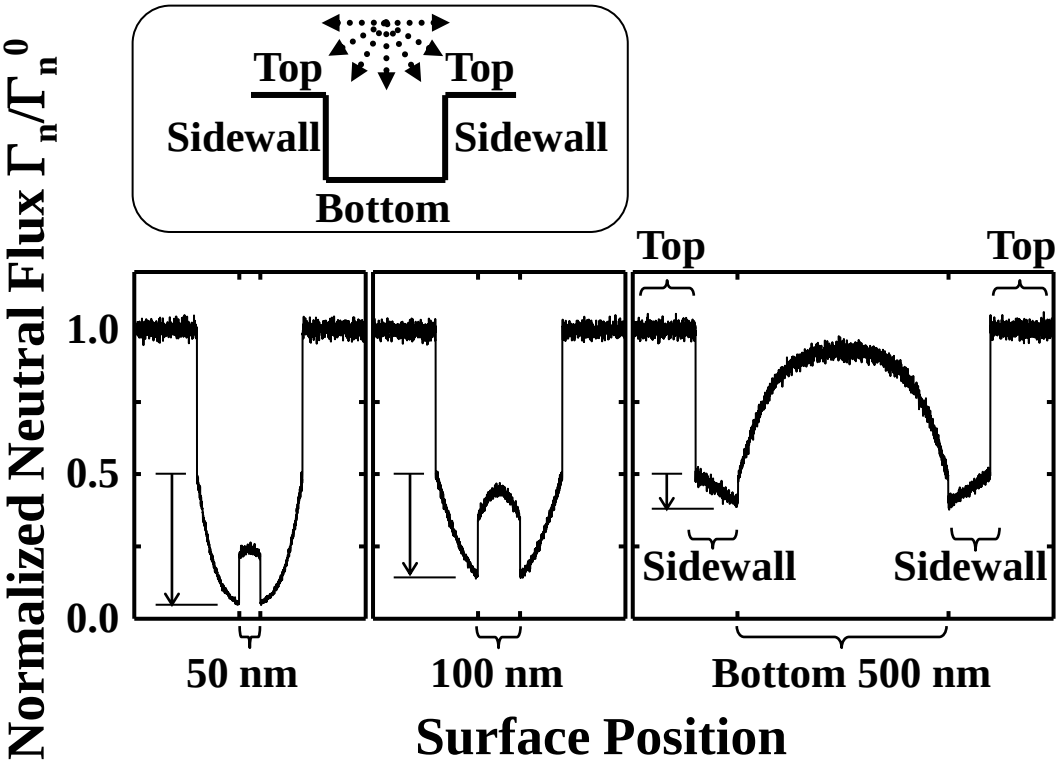

Fig. 2.5. Distribution of the neutral flux Γ_n/Γ_n^0 incident on sidewall and bottom surfaces of a rigid rectangular trench of 100 nm depth and different spaces of W = 50, 100, and 500 nm. Here, Γ_n is an incident neutral flux at each point on feature surfaces of the trench, and Γ_n^0 is an incident neutral flux on the top of the trench.

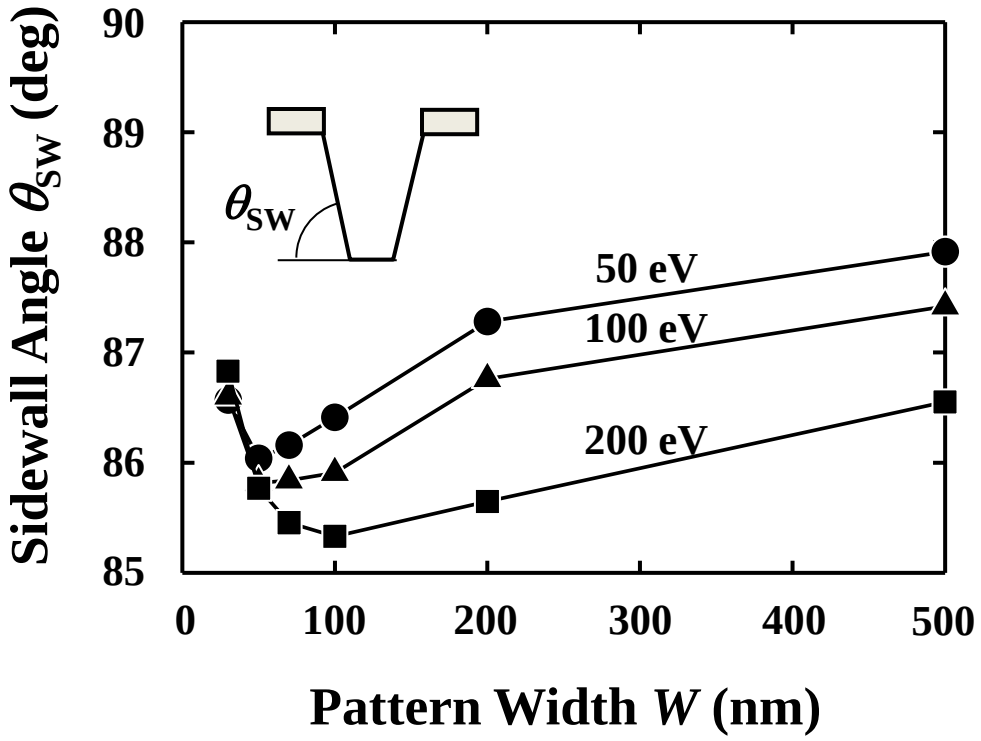

Fig. 2.6. Sidewall angle θ_{SW} as a function of pattern width W for different incident ion energies of E_i = 50, 100, and 200 eV with a neutral-to-ion flux ratio Γ_n^0/Γ_i^0 = 10, taken from the data of Figs. 2.3(a)-2.3(c). Here, θ_{SW} = 90° indicates vertical sidewalls, and θ_{SW} < 90° indicates tapered sidewalls.

fluxes through the sheath onto substrate surfaces, and these ion particles are assumed to move straight towards the feature surfaces in microstructures without collision with other particles therein. Here, angular distribution of ion fluxes calculated for incident ion energy E_i (~100 eV) gained in sheath field to ion temperature kT_i (~0.5 eV in this study) obtained in the corresponding experiments or other studies.[22,24,31,32] These conditions are typical in low-pressure and high-density plasmas such as electron cyclotron resonance (ECR) and inductively coupled (ICP) plasmas.[22,23] Each curve represents the evolving interfaces every 10 s, and the insets are the vertical etch rates (*ER*s) at the center of the W = 500 nm feature bottom.

As shown in Figs. 2.3(a)-2.3(c), RIE lag occurs at lower Γ_n^0/Γ_i^0, where the narrow features are etched slower than wider ones. Figure 2.4(a) and 2.4(b) show the *ER*s as a function of pattern width W and incident ion energy E_i, respectively, indicating that *ER*s tend to increase with increasing E_i in whole patterns. In particular, *ER*s tends to be gradually accelerated in wider patterns with increasing E_i, which in turn results in RIE lag. Figure 2.5 shows the distribution of the neutral flux Γ_n/Γ_n^0 incident on sidewall and bottom surfaces of a rigid rectangular trench of 100 nm depth, where Γ_n is the local incident flux of neutrals on feature surfaces of the trench, and Γ_n^0 is the neutral flux incident on the top of the trench. Figure 2.5 indicates that the neutral flux incident on the bottom of the trench tends to decrease with narrowing pattern width, owing to the so-called neutral shadowing effect, which in turn results in decreased *ER*s in narrower patterns through ion-enhanced etching, and thus results in RIE lag.

Figure 2.6 shows the sidewall angle θ_{SW} as a function of pattern width W for different E_i = 50, 100, and 200 eV with Γ_n^0/Γ_i^0 = 10, where θ_{SW} = 90° indicates vertical sidewalls and θ_{SW} < 90° indicates tapered sidewalls. In Fig. 2.6, the wider patterns tend to be less tapered for W > 100 nm. This may be ascribed in part to an increase in the amount of chemically active neutrals in wide patterns, which induce lateral etching of sidewalls, owing to neutral shadowing effects as shown in Fig. 2.5. Moreover, Fig. 2.6 shows that θ_{SW} tends to decrease with increasing E_i. At high E_i, the etching time is generally shorter than at low E_i, owing to increased vertical *ER*s. Thus, the amount of lateral etching of sidewalls tends to decrease, and so θ_{SW} tends to decrease at high E_i. In narrow patterns (W < 100 nm), the sidewall-angle dependence on E_i tends to become small, implying that other effects such as ion scattering on sidewalls would have a much greater effect on the sidewall angle in narrow patterns.

2.3.2 Formation of Microtrenches

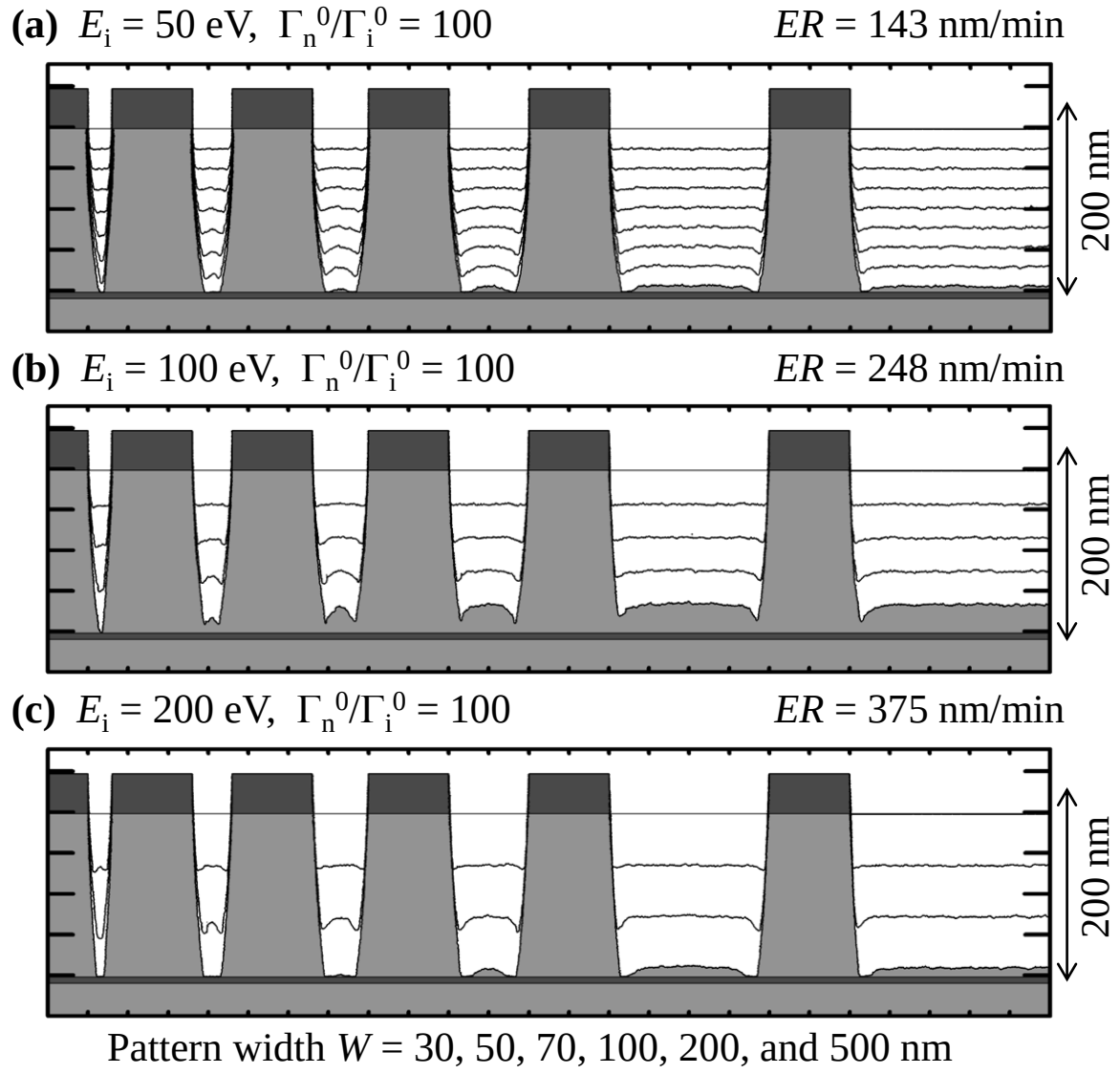

Fig. 2.7. Etched profile evolution of line-and-space patterns of Si, simulated for different incident ion energies of E_i = (a) 50, (b) 100, and (c) 200 eV. Calculations were made with an ion temperature kT_i = 0.5 eV, an ion flux $\Gamma_i^0 = 1.0 \times 10^{16}$ cm^{-2} s^{-1}, a neutral-to-ion flux ratio Γ_n^0/Γ_i^0 = 100, and a sticking probability S_q = 0.05 for etch products $SiCl_4$. Each curve represents the evolving interfaces every 10 s, and the insets are the vertical etch rates (*ER*s) at the center of the W = 500 nm feature bottom. Figure properties are the same as those of Figs. 2.3, along with the mask pattern and the mask and SiO_2 layer condition during etching.

Figures 2.7(a)-2.7(c) show the etched profile evolution of line-and-space patterns of Si, simulated for different incident ion energies of E_i = 50, 100, and 200 eV with E_i = 100 eV, kT_i = 0.5 eV, $\Gamma_i^0 = 1.0 \times 10^{16}$ cm^{-2}s^{-1}, $\Gamma_n^0 = 1.0 \times 10^{18}$ cm^{-2}s^{-1}, $\Gamma_n^0/\Gamma_i^0 = 100$, and S_q = 0.05. As shown in Figs. 2.7(a)-2.7(c), *ER*s are increased in all the patterns at increased Γ_n^0/Γ_i^0, where microtrenches occur clearly at the bottom corner of the trench. Comparing Figs. 2.7(a)-2.3(c) with Figs. 2.3(a)-2.3(c) indicates that the increase in neutral supply in microstructural features enhances the microtrenching significantly. Mahorowala *et al.* indicated in their numerical and experimental studies that the microtrench is caused in part by ion scattering from curved sidewalls of the feature.[33,34] Moreover, they also showed that the microtrenching was more significant for narrower patterns than for wider ones.[33] It should be concluded that the synergistic effects between neutral supply and ion-enhanced etching strongly affect the microtrench formation during etching.

2.3.3 Formation of Inverse RIE Lag

Figures 2.8(a)-2.8(f) show the etched profile evolution of line-and-space patterns of Si, simulated for different Γ_n^0/Γ_i^0 = 1, 10, 20, 50, 100, and 200 with E_i = 100 eV, kT_i = 0.5 eV, $\Gamma_i^0 = 1.0 \times 10^{16}$ cm^{-2}s^{-1}, and S_q = 0.05. Each curve represents the evolving interfaces every 10 s, and the insets are the vertical *ER*s at the center of the W = 500 nm feature bottom, indicating that *ER*s increase with increasing Γ_n^0/Γ_i^0. As shown in Figs. 2.8(a)-2.8(c), RIE lag occurs at low Γ_n^0/Γ_i^0, whereas microtrenches and inverse RIE lag (larger etched depth for narrower W) occur clearly at higher Γ_n^0/Γ_i^0 as in Figs. 2.8(d)-2.8(f).

Figures 2.9(a) and 2.9(b) show the *ER*s as a function of pattern width W and neutral-to-ion flux ratio Γ_n^0/Γ_i^0, respectively, indicating that *ER*s tend to increase with increasing Γ_n^0/Γ_i^0, and that feature profiles shift from RIE lag to inverse RIE lag. Moreover, *ER*s tend to be saturated in wider patterns, while *ER*s in narrow patterns (W < 70 nm) increase with increasing Γ_n^0/Γ_i^0. These results imply that the synergistic effects between neutral supply and ion-enhanced etching induce the inverse RIE lag; in other words, if neutral species are fully supplied in narrow patterns, the ion-enhanced etching tends to be accelerated therein, owing to the effect of ion scattering on sidewalls.

2.3.4 Surface Coverage

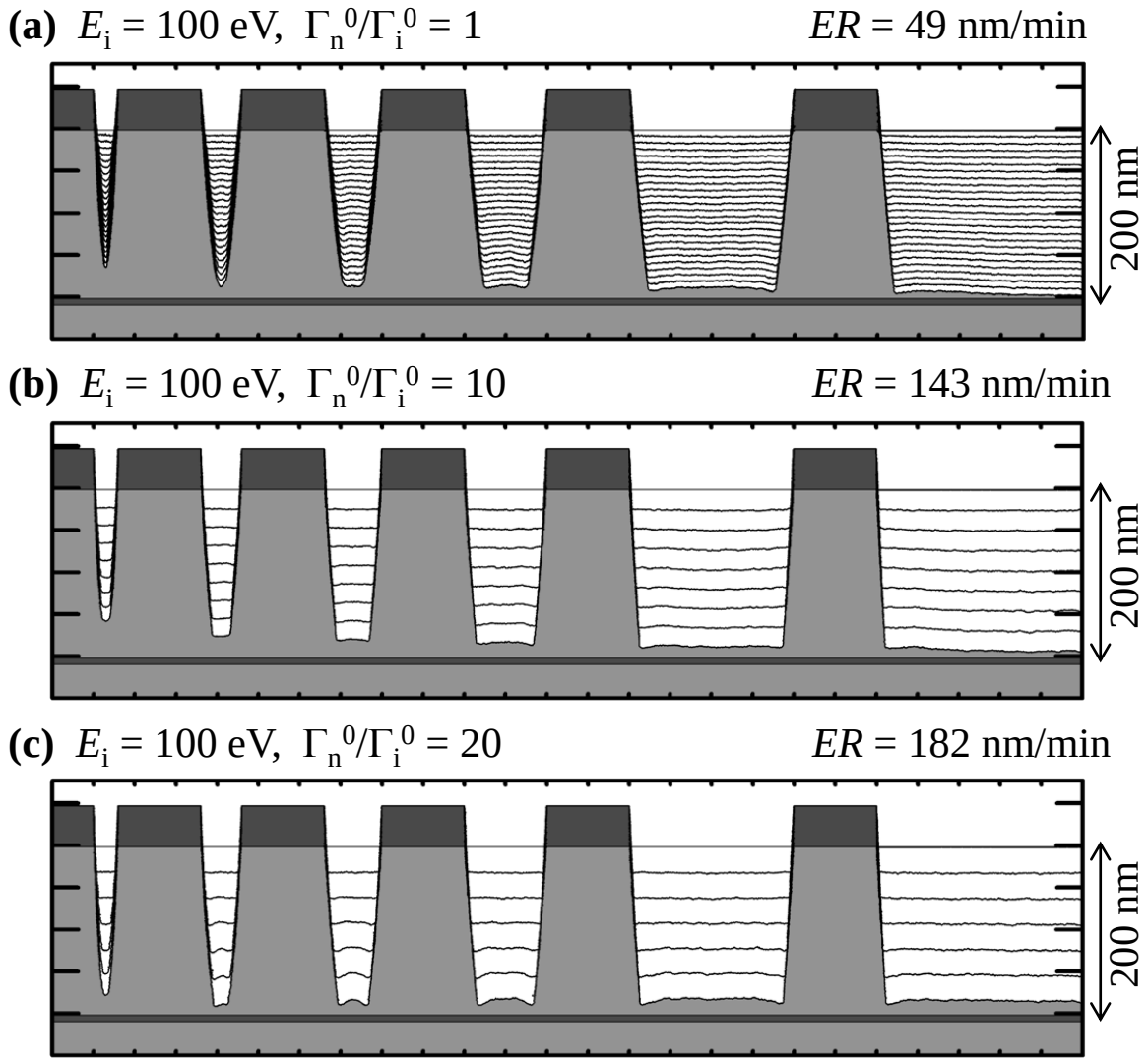

Fig. 2.8. Etched profile evolution of line-and-space patterns of Si, simulated for different neutral-to-ion flux ratios of Γ_n^0/Γ_i^0 = 1, 10, 20, 50, 100, and 200. Calculations were made with an incident ion energy E_i = 100 eV, an ion temperature kT_i = 0.5 eV, an ion flux Γ_i^0 = 1.0 × 10^{16} cm^{-2} s^{-1}, and a sticking probability S_q = 0.05 for etch products $SiCl_4$. Figure properties are the same as those of Figs. 2.3, along with the mask pattern and the mask and SiO_2 layer condition during etching.

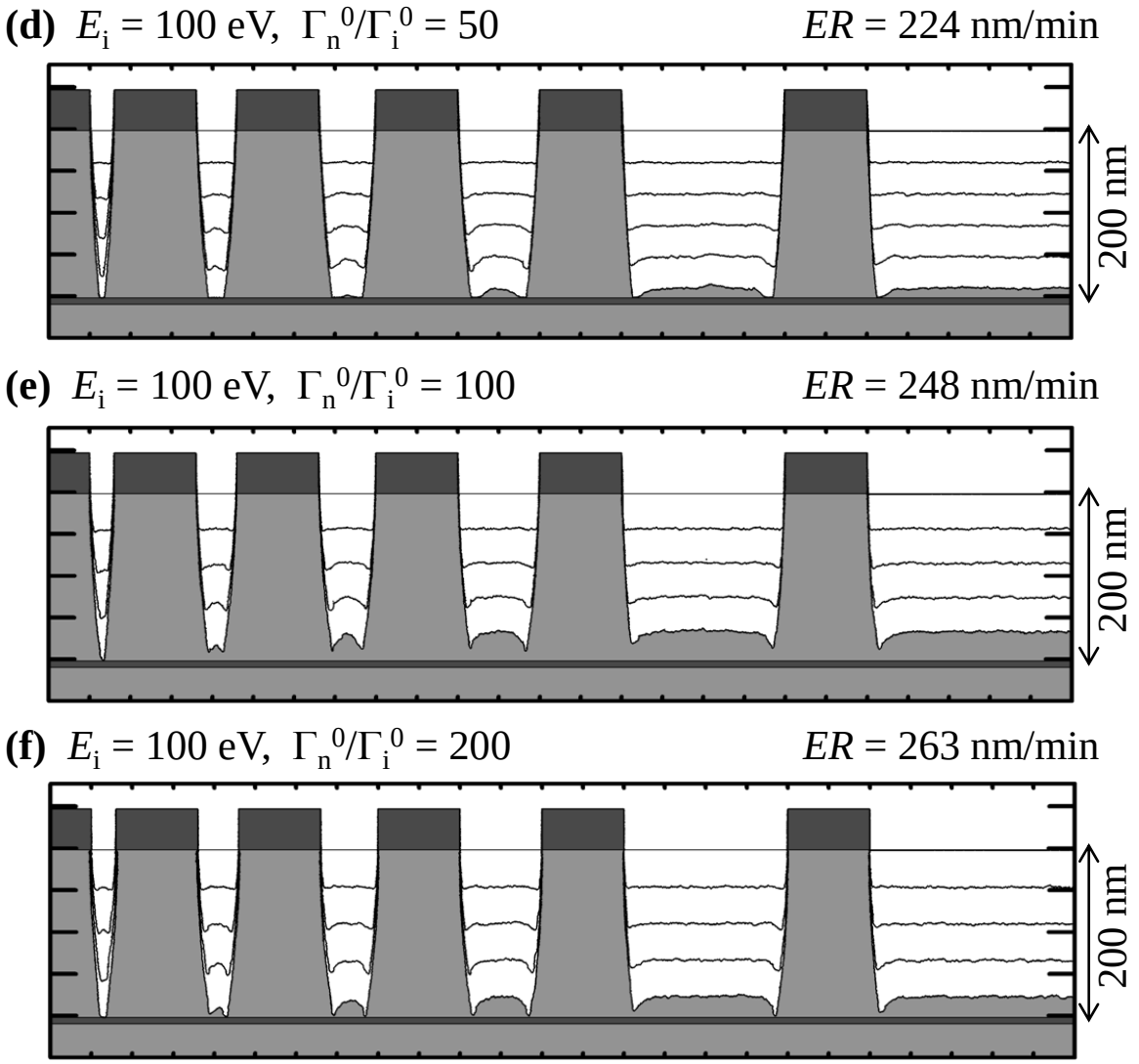

Fig. 2.8. (Continued)

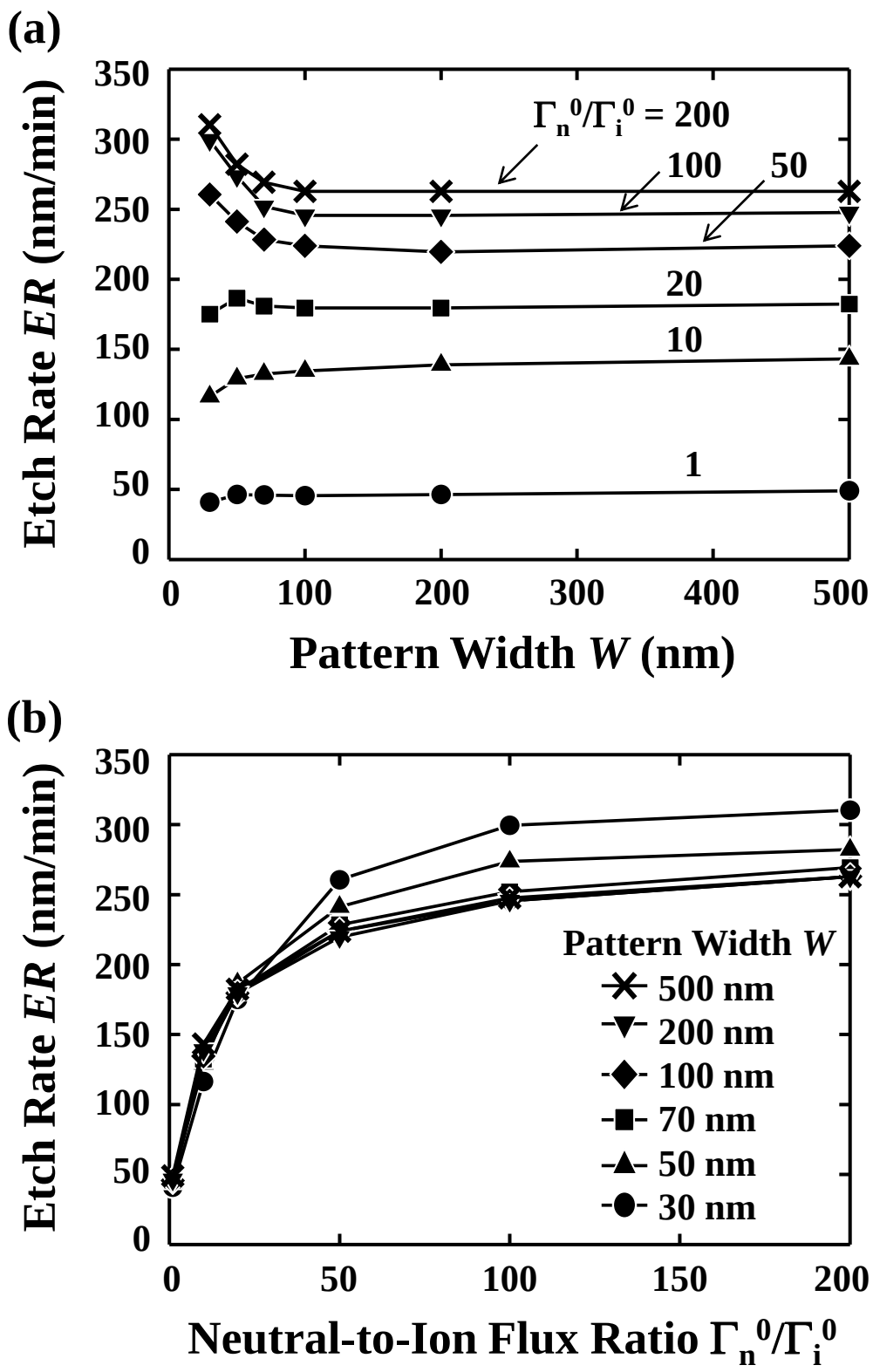

Fig. 2.9. Etch rates or *ER*s as a function of (a) pattern width *W* and (b) neutral-to-ion flux ratio Γ_n^0/Γ_i^0, taken from the data of Figs. 2.8(a)-2.8(f).

To analyze synergistic effects between ion and neutral particle transports, we focus on the feature profile evolution and the surface coverage for different neutral-to-ion flux ratios and different spaces of the line-and-space pattern. Figures 2.10(a) and 2.10(b) show the profile evolution of Si etched in Cl_2 plasmas, simulated for neutral-to-ion flux ratios of Γ_n^0/Γ_i^0 = 10 and 100 and spaces of W = 30 and 500 nm, with the other parameters being the same as in Figs. 2.8(b) and 2.8(e).

Figure 2.11 shows the surface coverage Θ at the bottom of etched features of Si as a function of neutral-to-ion flux ratio Γ_n^0/Γ_i^0 and space width W, analyzed from the simulation of Figs. 2.10(a) and 2.10(b). Surface saturation process of particles depends strongly on a neutral flux and a sticking probability of neutral particles on etched surfaces.[21] At Γ_n^0/Γ_i^0 = 10, the surface coverage Θ for W = 500 nm tends to be larger than that for W = 30 nm, owing to the so-called neutral shadowing effect. On the other hand, at higher Γ_n^0/Γ_i^0 = 100, Θ in narrower space tends to be larger than that in wider one. At lower flux, neutral particles tend to easily come into microstructure features in wider space, owing to neutral shadowing effects. And the etch rate tends to increase with widening a pattern width and a RIE lag tends to occur. However, at higher flux the etched surfaces become nearly saturated in narrow or wide space, and then a lot of incident neutral particles which are reflected on the etched surfaces tend to easily go out microstructural features, while neutral particles at high Γ_n^0/Γ_i^0 tend to increase chances to contact feature surfaces in narrower space. This is because a solid angle of an open-mask area with origin at a bottom surface or sidewalls is large in wider space. These results imply that at high Γ_n^0/Γ_i^0, the etched surface in narrow space tend to be easily saturated with neutral species, which leads to inverse RIE lag that occurs therein.

2.3.5 Distribution of Cl atoms in Surface Reaction Layers

Control of neutral supply is important to suppress RIE lag and microtrenches, but lower Γ_n^0/Γ_i^0 causes another problem. Figures 2.12(a) and 2.12(b) show the distributions of Cl atoms in surface reaction layers at the bottom of etched features of Si. The *ER* and surface roughness tend to decrease and the total etching time increases with decreasing Γ_n^0/Γ_i^0. Moreover, the number of Cl atoms penetrated into Si substrates tends to increase with decreasing Γ_n^0/Γ_i^0. These residual particles may often break down the structure of Si substrate lattice and thus induce plasma damages.[35]

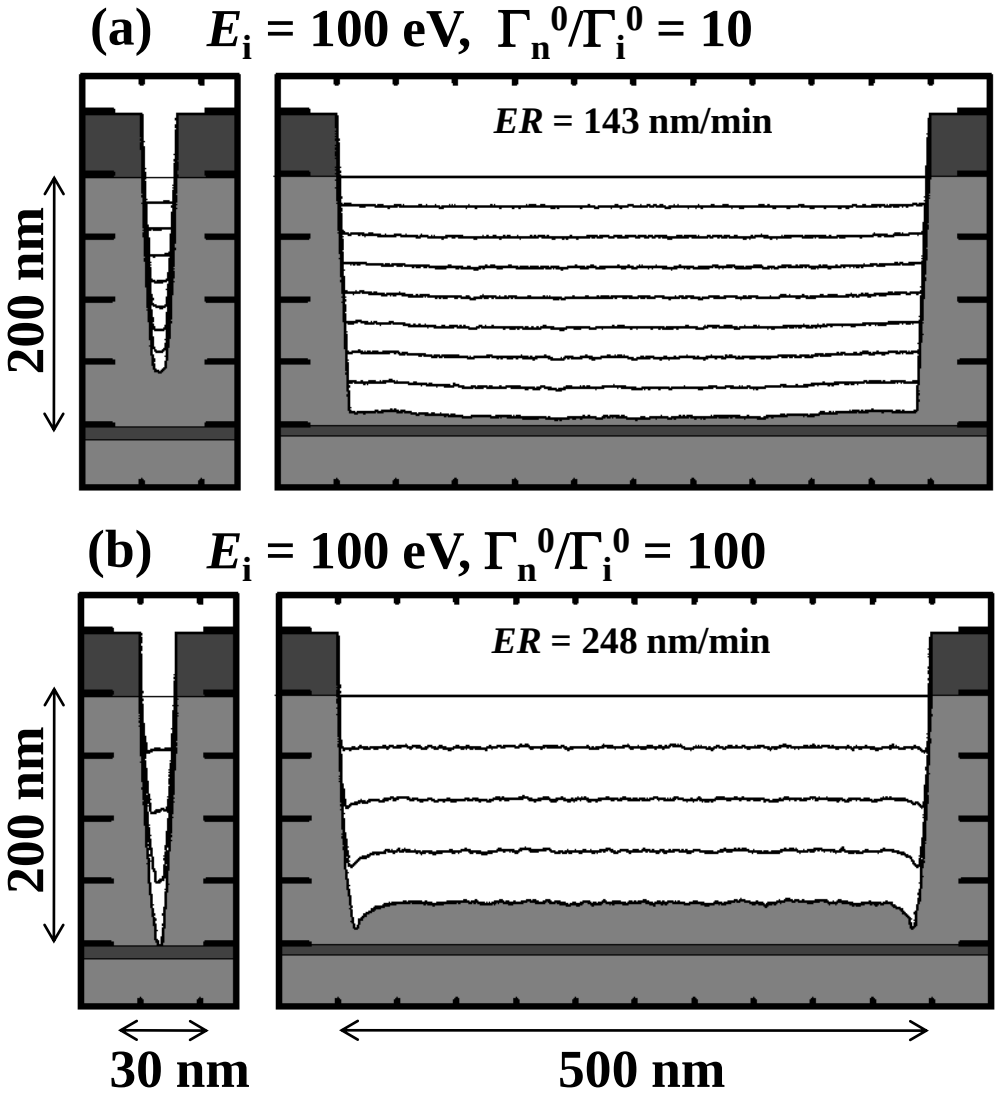

Fig. 2.10. Profile evolution of Si etched in Cl_2 plasmas, simulated for neutral-to-ion flux ratios of Γ_n^0/Γ_i^0 = 10 and 100 and spaces of W = 30 and 500 nm, with the other parameters being the same as in Figs. 2.8(b) and 2.8(e). Each curve represents the evolving interfaces every 10 s, and the insets are the vertical etch rates (*ER*s) at the center of the W = 500 nm feature bottom. The initial surface profile is a hard mask pattern of lines and spaces on poly-Si films of thickness H_{Si} = 200 nm, where the mask pattern has a height H_{mask} = 50 nm. There is an insulating SiO_2 layer under poly-Si, and the mask and the SiO_2 layer are assumed not to be eroded during etching.

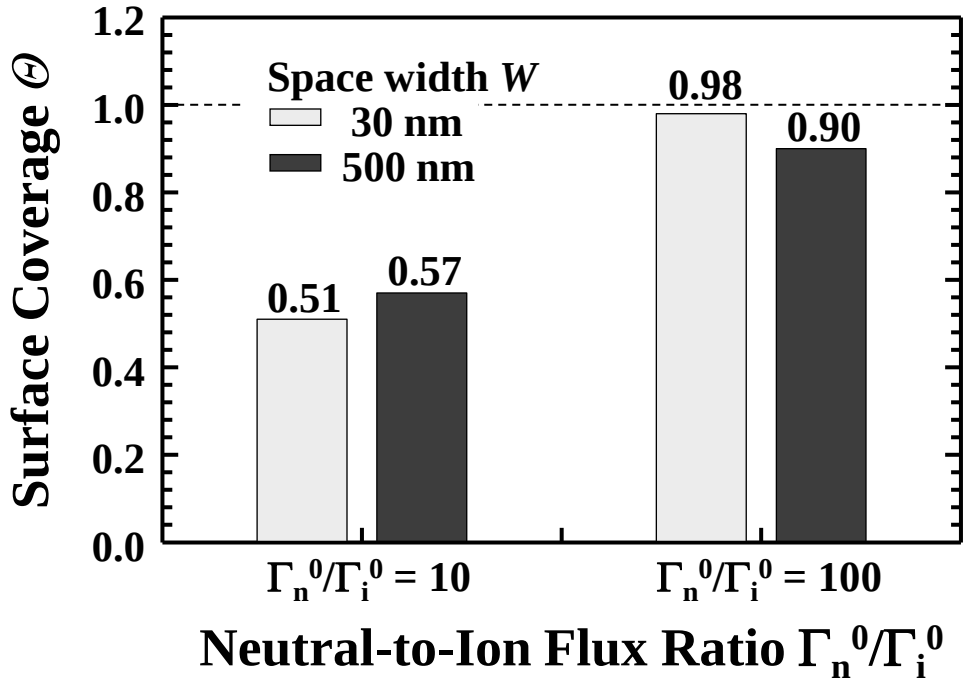

Fig. 2.11. Surface coverage Θ at the bottom of etched features of Si as a function of neutral-to-ion flux ratio Γ_n^0/Γ_i^0 and space width W.

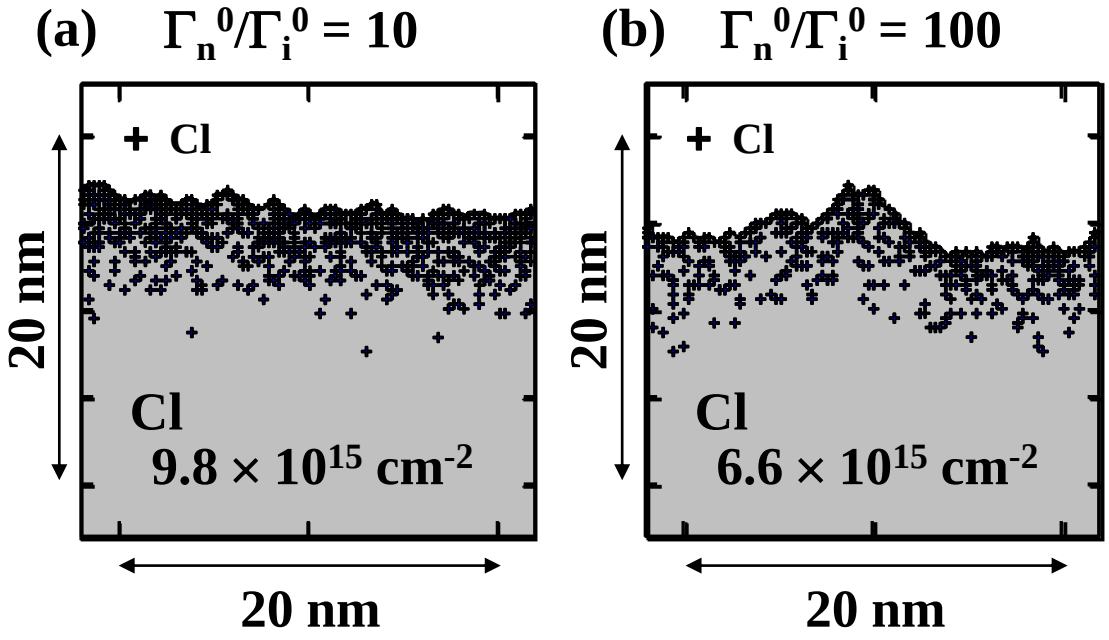

Fig. 2.12. Distributions of Cl atoms in surface reaction layers at the bottom of etched features of Si.

2.4 Conclusions

The formation mechanisms of profile anomalies and microscopic uniformity during plasma etching of Si in Cl_2 plasmas have been analyzed using our own atomic-scale cellular model (ASCeM), which reproduced the feature profile evolution experimentally observed, including microtrenches, tapered profiles, RIE lag, and inverse RIE lag. At low neutral-to-ion flux ratios, neutral shadowing effects are dominant to determine the feature profile evolution during etching, and RIE lag tends to occur. In particular, *ER*s tends to be accelerated in wider patterns with increasing E_i. On the other hand, at high neutral-to-ion flux ratios, neutral species are fully supplied even in narrow patterns, and *ER*s tend to increase in whole patterns. In particular, the ion-enhanced etching tends to accelerate *ER*s in narrow patterns (W < 70 nm), owing to the effect of ion scattering on feature sidewalls, which in turn results in inverse RIE lag. In addition, the effects of not only ion scattering on sidewalls but also neutral supply would be important in microtrench formation at the bottom corner of trenches. Moreover, sidewalls tend to be tapered with decreasing pattern width, except for narrow patterns of W < 100 nm, owing to neutral shadowing effects and the resultingly decreased chemical etching of sidewalls. Sidewalls also tend to be tapered with increasing E_i, owing to increased vertical *ER*s and the resultingly decreased lateral etching of sidewalls. In narrow patterns (W < 100 nm), the effects of ion scattering on sidewalls would have a much greater effect on the sidewall angle, owing to the decreased effects of lateral etching. The numerical results also indicated that low neutral-to-ion flux ratio would cause RIE lag and ion-induced damage, while it would reduce microtrench and surface roughness. Thus, it can be concluded that the control of neutral supply in microstructural features affects the microscopic uniformity. In particular, the synergistic effects between ion-enhanced etching and neutral shadowing in microstructural features play a significant role in the formation of profile anomalies; in other words, geometrical effects for ions and neutrals would be more important to control the microscopic uniformity.

References

1) H. Abe, M. Yoneda, and N. Fujiwara: Jpn. J. Appl. Phys. **47** (2008) 1435.
2) R. A. Gottscho, C. W. Jurgensen, and D. J. Vitkavage: J. Vac. Sci. Technol. B **10** (1992) 2133.
3) H. Jansen, H. Gardeniers, M. de Boer, M. Elwenspoek, and J. Fluitman: J. Micromech. Microeng. **6** (1996) 14.
4) K. Ono, H. Ohta, and K. Eriguchi: Thin Solid Films **518** (2010) 3461.
5) M. Tuda and K. Ono: Jpn. J. Appl. Phys. **36** (1997) 2482.
6) K. Ono and M. Tuda: Jpn. J. Appl. Phys. **36** (1997) 4854.
7) K. Ono and M. Tuda: Thin Solid Films **374** (2000) 208.
8) R. Kinzikevičius: Vacuum **72** (2004) 53.
9) H. Jansen, M. de Boer, R. Wiegerink, N. Tas, E. Smulder, C. Neagu, and M. Elwenspoek: Microelectron. Eng. **35** (1997) 45.
10) M. F. Doemling, N. R. Rueger, and G. S. Oehrlein: Appl. Phys. Lett. **68** (1996) 10.
11) H. H. Doh, C. K. Yeon, and K. W. Whang: J. Vac. Sci. Technol. A **15** (1997) 664.
12) S. L. Li, D. Johnson, and R. Westerman: J. Vac. Sci. Technol. A **24** (2006) 1283.
13) C. K. Chung and H. N. Chiang: NSTI-Nanotech, 2004, p. 481.
14) A. C. Westerheim, A. H. Labun, J. H. Dubash, J. C. Arnold, H. H. Sawin, and V. Y. Wang: J. Vac. Sci. Technol. A **13** (1995) 853.
15) S. Samukawa and T. Tsukada: Appl. Phys. Lett. **69** (1996) 1056.
16) K. Tsujimoto, T. Kumihashi, N. Kofuji, and S. Tachi: J. Vac. Sci. Technol. A **12** (1994) 1209.
17) O. Joubert, G. S. Oehrlein, and Y. Zhang: J. Vac. Sci. Technol. A **12** (1994) 658.
18) Y. Osano and K. Ono: Jpn. J. Appl. Phys. **44** (2005) 8650.
19) Y. Osano, M. Mori, N. Itabashi, K. Takahashi, K. Eriguchi, and K. Ono: Jpn. J. Appl. Phys. **45** (2006) 8157.
20) Y. Osano and K. Ono: J. Vac. Sci. Technol. B **26** (2008) 1425.
21) H. Tsuda, M. Mori, Y. Takao, K. Eriguchi, and K. Ono: Thin Solid Films **518** (2010) 3475.
22) M. Tuda, K. Ono, and K. Nishikawa: J. Vac. Sci. Technol. B **14** (1996) 3291.
23) M. Tuda, K. Nishikawa, and K. Ono: J. Appl. Phys. **81** (1997) 960.
24) R. A. Gottscho: J. Vac. Sci. Technol. B **11** (1993) 1884.
25) F. H. Stillinger and T. A. Weber: Phys. Rev. B **31** (1985) 5262.

26) H. Feil, J. Dieleman, and B. J. Garrison: J. Appl. Phys. **74** (1993) 1303.
27) C. F. Abrams and D. B. Graves: J. Vac. Sci. Technol. A **16** (1998) 3006.
28) A. P. Mahorowala and H. H. Sawin: J. Vac. Sci. Technol. B **20** (2002) 1064.
29) W. Jin, S. A. Vitale, and H. H. Sawin: J. Vac. Sci. Technol. A **20** (2002) 2106.
30) C. Steinbrüchel: Appl. Phys. Lett. **55** (1989) 1960.
31) T. Nakano, N. Sadeghi, and R. A. Gottscho: Appl. Phys. Lett. **58** (1991) 458.
32) K. H. A. Bogart, F. P. Klemens, M. V. Malyshev, J. I. Colonell, V. M. Donnelly, J. T. C. Lee, and J. M. Lane: J. Vac. Sci. Technol. A **18** (2000) 197.
33) A. P. Mahorowala and H. H. Sawin: J. Vac. Sci. Technol. B **20** (2002) 1077.
34) A. P. Mahorowala, H. H. Sawin, R. Jones, and A. H. Labun: J. Vac. Sci Technol. B **20** (2002) 1055.
35) K. Eriguchi and K. Ono: J. Phys. D. **41** (2008) 024002.

Chapter 3
Formation of Surface Roughness and Residue

3.1 Introduction

As semiconductor integrated circuit devices continue to offer technical advantages, the precise or nanometer-scale control of profiles is increasingly indispensable during plasma etching of Si. To meet these requirements, it is necessary to have an atomic-scale understanding of interactions between chemically reactive plasmas and substrate surfaces. In Si etching for the fabrication of gate electrodes and shallow trench isolation (STI), chlorine-based plasmas are widely used, where a small amount of oxygen is often added to improve the etched profiles and the selectivity over thin gate oxides, and a severe surface evolution problem of residues or micropillars is often observed to achieve high etch selectivity.[1–3] To analyze the formation mechanisms of profile anomalies such as notch,[4–7] microtrench,[8] roughness,[9] and residue,[10] a number of feature profile simulations have been made until now. A string model[11–13] and a level set method,[14] for example, are widely used as the simulation model for feature profile evolution. However, it is still difficult for these conventional profile simulations to reproduce etched profiles containing significant residues or micropillars, because these models confront computational difficulties when reproduce sharp-pointed features. On the other hands, a cell removal model is easy to understand intuitively, and can easily represent intricately-shaped surfaces. This paper focuses on formation mechanisms of surface roughness and residues during plasma etching of Si in Cl_2/O_2 plasmas, by using our atomic-scale cellular model (ASCeM)[15–17] which can simulate effects of surface oxidation on feature profile evolution.

3.2 Modeling and Simulation

Figure 3.1 shows a schematic illustration of the ASCeM model and four-point surface normal technique.[15] The model represents the etching of infinitely long trenches in Si substrates with Cl_2/O_2 plasma chemistries.[15–17] The simulation domain is divided into a number of small square cells of atomic size of 2.7 Å, corresponding to the interatomic distance in Si substrates. The incidence angle for ion-enhanced etching, sputtering, and ion scattering species on feature surfaces is calculated by using the four-point surface normal,[18] while the scattering of neutrals from surfaces is assumed to be isotropic. Energetic ions, neutrals, and

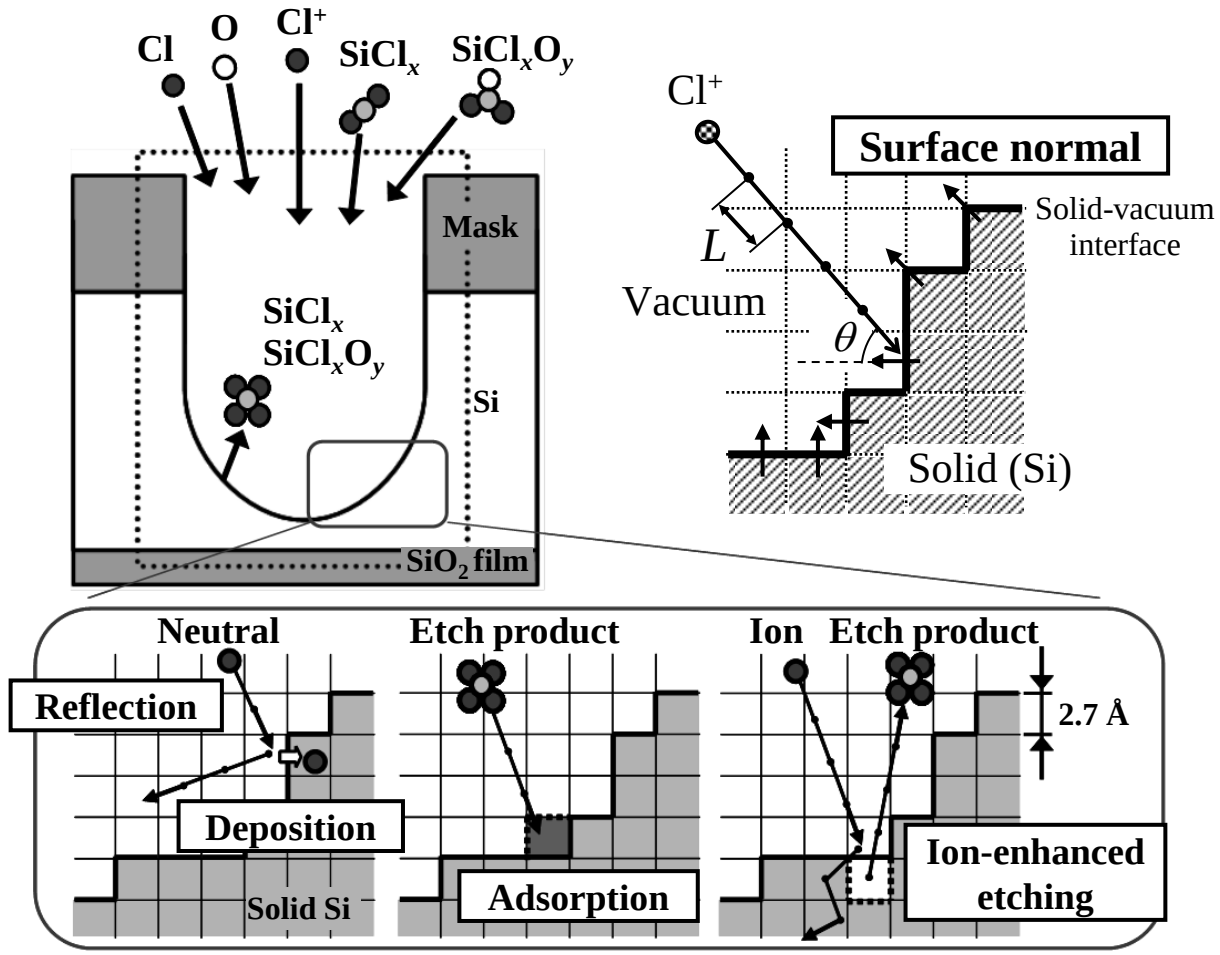

Fig. 3.1. Schematic illustrations of the ASCeM model and four-point surface normal technique, where Cl^+ ions, Cl neutrals, O neutrals, etch products $SiCl_x$, and etch by-products $SiCl_xO_y$ are injected from the top of the simulation domain with three velocity components. The simulation domain is divided into a number of small square cells of atomic size of L = 2.7 Å, and Si atoms are allocated at the center of square lattices. The surface normal is determined by the presence or absence of four cells neighboring to the top, bottom, left, and right.

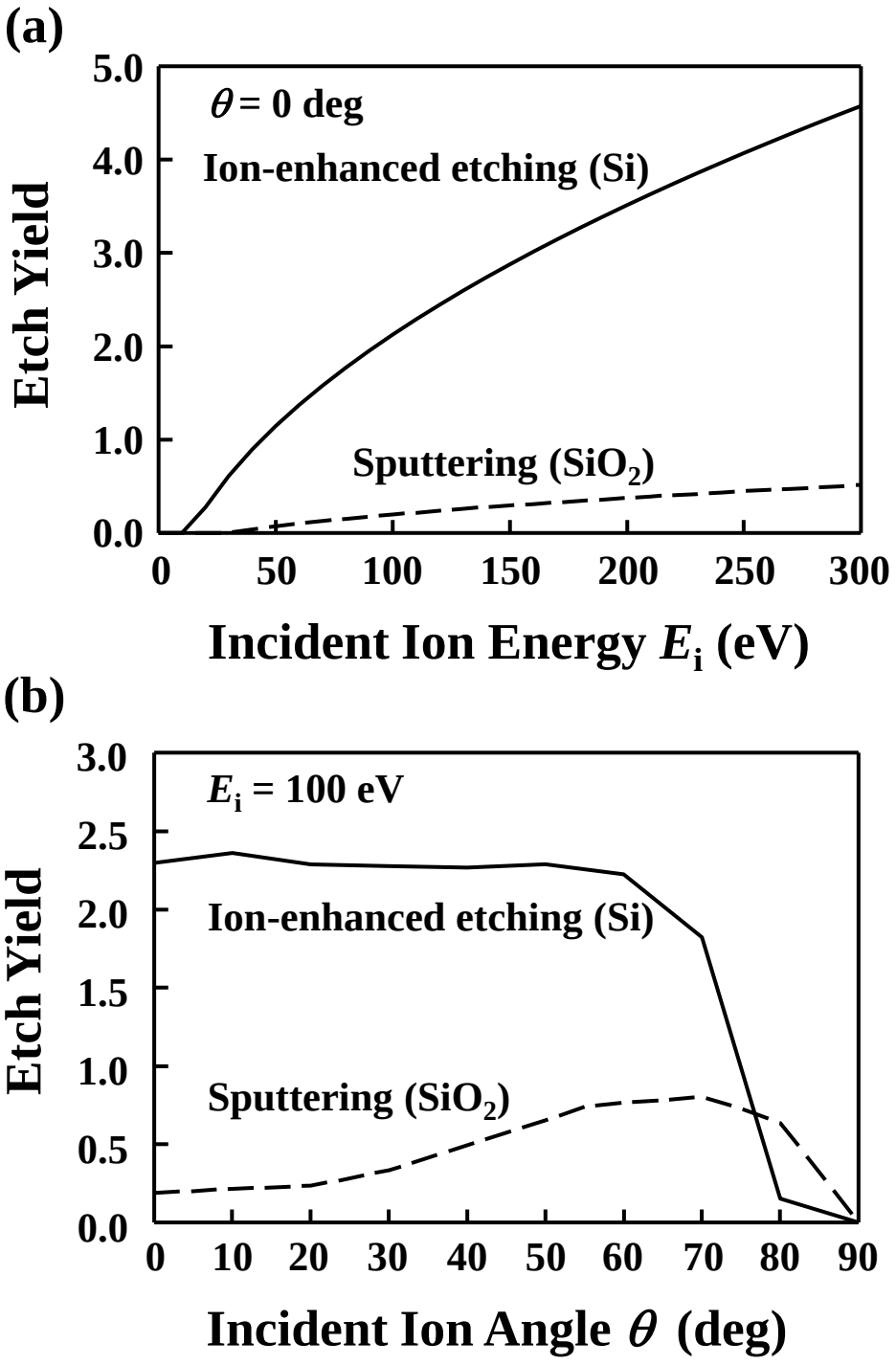

Fig. 3.2. Etching and sputtering yields for Cl^+ ions on Si and SiO_2 surfaces, as a function of (a) incident energy E_i (θ = 0 deg or normal incidence) and (b) incident angle θ (E_i = 100 eV).

etch by-products are introduced from the top of the simulation domain into microstructural features, and the particle transport is analyzed by using the two-dimensional Monte Carlo (MC) algorithm with three velocity components.[11,12,16,19)]

To analyze interactions between energetic ions and substrates, the model includes two-body elastic collision processes between incident ions and substrate atoms with the Stillinger-Weber interaction potential for the Cl–Si system.[20–22)] The model also takes into account surface chemistries by using the MC algorithm,[17,18,23)] including ion-enhanced etching, chemical etching, surface remission of neutrals, surface oxidation, deposition of etch products and by-products, and sputtering of deposited layers and oxidized surfaces. Figures 3.2(a) and 3.2(b) show the ion incident energy and angle dependences of the etching and sputtering yields for Cl^+ ions on Si and SiO_2 surfaces in the model, where the dependence of the etching and sputtering yields on ion incident angle is obtained automatically in the MC procedure.

3.3 Experiment

To compare numerical results with the actual process, etching experiments were performed using an ultrahigh-frequency electron cyclotron resonance (UHF-ECR) plasma etching reactor, where pure Cl_2 and Cl_2/O_2 gas mixtures were introduced into the reactor at a total gas flow rate of 100 sccm and a pressure of 1 Pa. The discharges were established by 450 MHz UHF waves at an incident power of 500 W. A 400 kHz rf bias was supplied to the wafer stage at a power of 50 W, and the stage temperature was maintained at ~ 300 K during etching. Under these conditions, the ion incident energy E_i was assumed to be ~ 1/3 of the rf amplitude, which was estimated to be ~ 100 eV; moreover, the ion flux Γ_i^0 onto the surface was measured to be ~ 1.0×10^{16} $cm^{-2}s^{-1}$ by using small planar Langmuir probes. The neutral-to-ion flux ratio Γ_n^0/Γ_i^0, the oxygen-to-ion flux ratio Γ_o^0/Γ_i^0, and the sticking probability S_q were chosen to fit the numerical results to the etch rates (*ER*s) and feature profiles measured in experiments. In addition, the ion temperature kT_i was assumed to be 0.5 eV, which is typical conditions in low-pressure, high-density plasmas such as ECR.[11,12)]

3.4 Results and Discussion

3.4.1 Effects of Oxygen Addition

Figures 3.3(a)-3.3(e) show the etched profile evolution of 200-nm space during 40 s from the start of etching, simulated for different oxygen-to-ion flux ratios of Γ_o^0/Γ_i^0 = 0, 0.1, 0.5, 2.0,

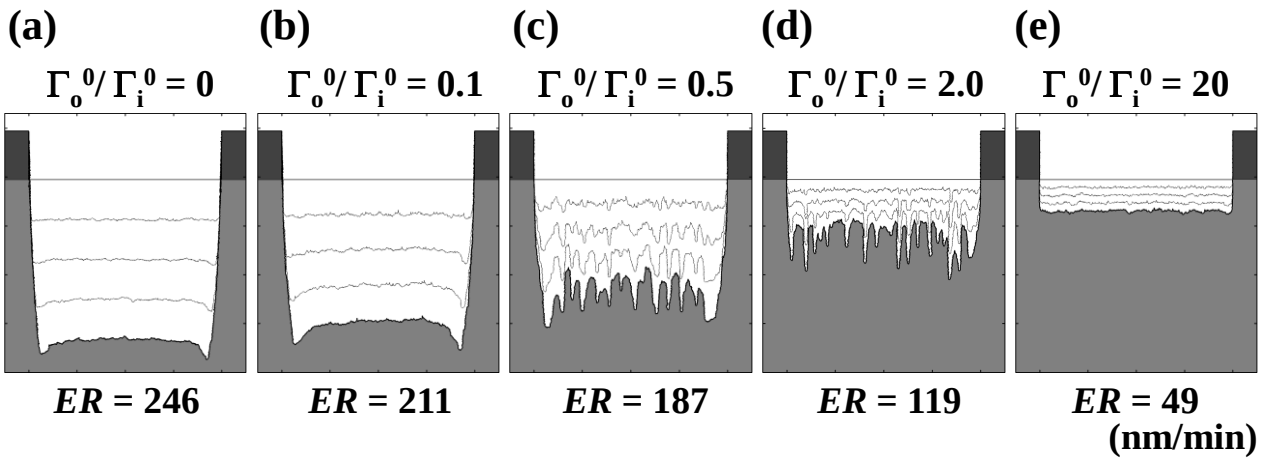

Fig. 3.3. Etched profile evolution of 200-nm space during 40 s from the start of etching, simulated for different oxygen-to-ion flux ratios of Γ_o^0/Γ_i^0 = (a) 0, (b) 0.1, (c) 0.5, (d) 2.0, and (e) 20.0. Each curve represents the evolving interfaces obtained every 10 s. Calculations were made with E_i = 100 eV, kT_i = 0.5 eV, $\Gamma_i^0 = 1.0 \times 10^{16}$ cm^{-2}s^{-1}, Γ_n^0/Γ_i^0 = 100, and S_q = 0.05.

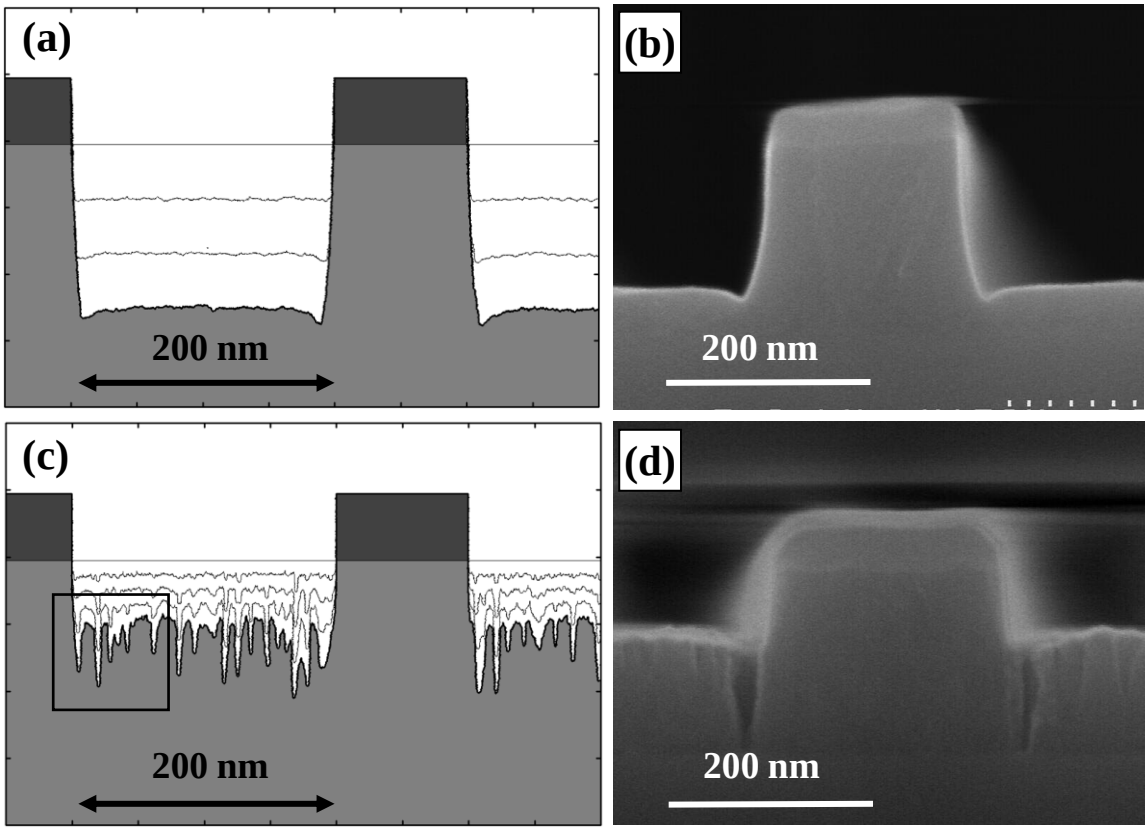

Fig. 3.4. Comparison between numerical and experimental results of the etched profile evolution of 200-nm space. Profile evolutions for (a) $\Gamma_o^0/\Gamma_i^0 = 0$ and (c) $\Gamma_o^0/\Gamma_i^0 = 2.0$, simulated with the other parameters being the same as in Fig. 3.3, and the corresponding SEM micrographs of the etched profile experimentally obtained in (b) Cl_2 and (d) Cl_2/30%-O_2 plasmas.

and 20.0. Here, the incident ion energy is E_i = 100 eV, the ion temperature kT_i = 0.5 eV, the ion flux $\Gamma_i^0 = 1.0 \times 10^{16}$ $cm^{-2}s^{-1}$, the neutral-to-ion flux ratio Γ_n^0/Γ_i^0 = 100, and the sticking probability S_q = 0.05 for etch products $SiCl_4$ desorbed from feature surfaces being etched. The initial surface profile is a hard mask pattern of lines and space on Si films of thickness H_{Si} = 200 nm, and the mask pattern has a linewidth L_{mask} = 100 nm and a height H_{mask} = 50 nm. The mask is assumed not to be eroded during etching. The *ER* tends to decrease with increasing O_2 flux, and a number of residues or micropillars tend to occur. Moreover, the roughness of bottom surfaces tends to be decreased at high O_2 flux, owing to increased surface oxidation.

Figures 3.4(a)-3.4(d) show a comparison between numerical and experimental results of the etched profile evolution of 200-nm space. Figure 3.4(a) shows a numerical result of the profile evolution in Cl_2 plasma, simulated for $\Gamma_o^0/\Gamma_i^0 = 0$ with the other parameters being the same as in Fig. 3.3. Figure 3.4(b) shows a scanning electron microscope (SEM) image of the etched profile experimentally obtained in Cl_2 plasma. Under these conditions, the microtrench was observed at bottom surfaces, together with tapered sidewalls. On the other hand, Fig. 3.4(c) shows a numerical result of the etched profile evolution in Cl_2/O_2 plasma, simulated for Γ_o^0/Γ_i^0 = 2.0 with the other parameters being the same as in Fig. 3.3. Figure 3.4(d) shows an SEM image of the etched profile, experimentally obtained in Cl_2/O_2 plasma with a gas flow rate ratio of Cl_2:O_2 = 70:30 sccm. These clearly show that effects of oxygen addition cause a number of residues or micropillars on bottom surfaces of the feature.

Figures 3.5(a) and 3.5(b) show an enlarged view of the 80-nm-square area of Fig. 3.4(c) for etching in Cl_2/O_2 plasma, showing the distribution of adsorbed and penetrated Cl and O on locally roughened feature surfaces of residues or micropillars, together with the trajectories of energetic Cl^+ ions in local microstructures. A large amount of oxygen adsorbs at around the top of rough surfaces, while there is few oxygen on the bottom of rough surfaces, owing to local geometrical shadowing effects for neutral oxygen. It should be further noted that on sidewalls of rough surfaces, the scattering of incident ions become pronounced on sidewalls of rough surfaces.

3.4.2 Effects of Ion Scattering

Figures 3.6(a) and 3.6(b) show a comparison of the etched profile evolution of 200-nm space between in the presence and absence of ion scattering on feature surfaces, simulated with the other parameters being the same as in Fig. 3.3(d) for Γ_o^0/Γ_i^0 = 2.0. These clearly show that

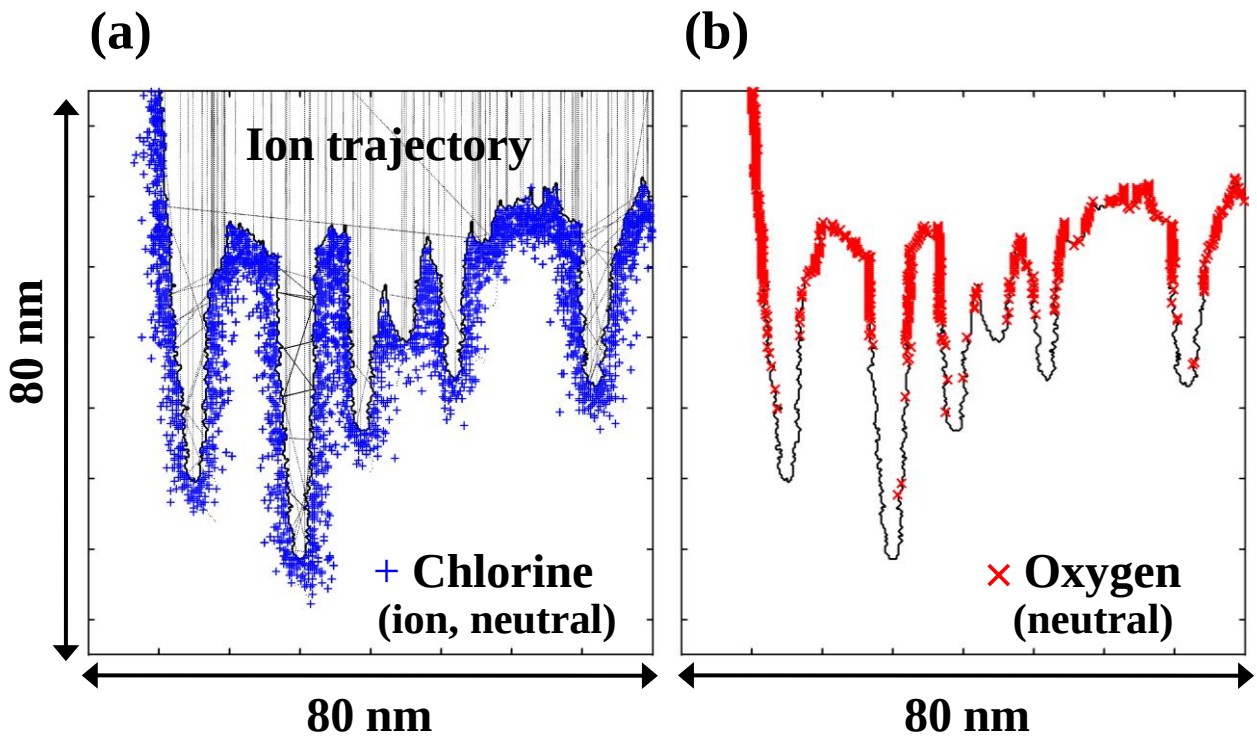

Fig. 3.5. Enlarged views of the 80-nm-square area of Fig. 3.4(c) for etching in Cl_2/O_2 plasma, showing the distributions of adsorbed and penetrated (a) Cl and (b) O on locally rough feature surfaces, together with the trajectories of energetic Cl^+ ions in local microstructures.

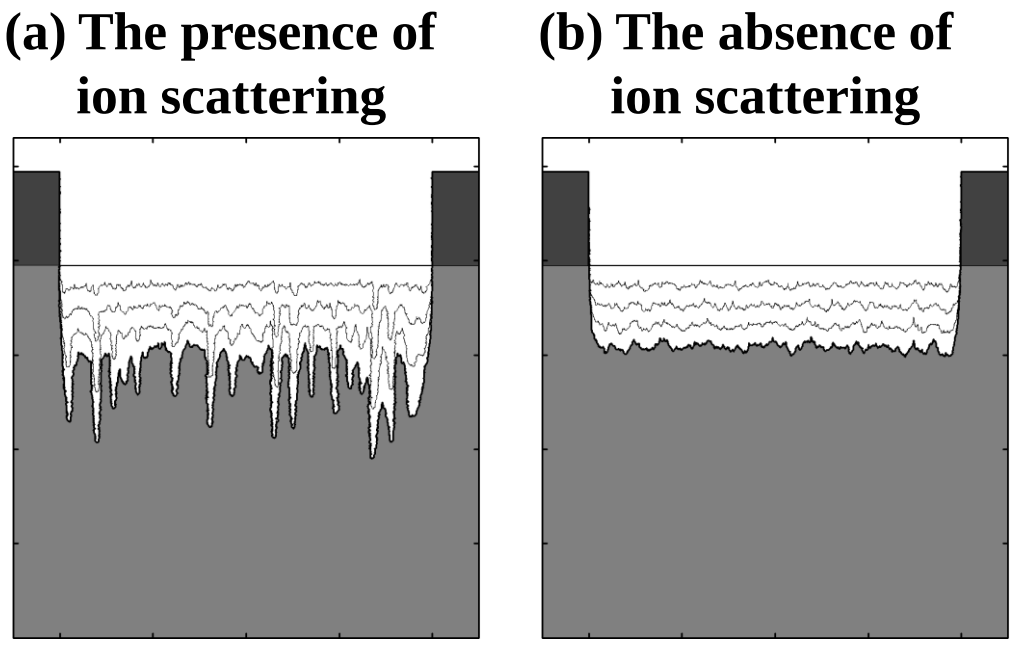

Fig. 3.6. Etched profile evolution of 200-nm space in the (a) presence and (b) absence of ion scattering on feature surfaces, simulated with the other parameters being the same as in Fig. 3.3(d) for $\Gamma_o^0/\Gamma_i^0 = 2.0$.

the etching reactions induced by scattered ions cause the local feature profile evolution or the formation of residues or micropillars on bottom surfaces of the feature.

Figures 3.7(a) and 3.7(b) show the normalized number of ions having different incident angles on feature surfaces of 200-nm space, analyzed every 10 s from the simulation of Fig. 3.4. The number of ions having an incident angles of 40 to 50 deg increases after 10 s from the start of etching, owing to the initial growth of microscopic surface roughness both in the presence and absence of oxygen. However, without oxygen, the number of ions having different angles remains almost unchanged thereafter during etching, while that having large incident angles over 50 deg increases with time in the presence of oxygen. This implies that synergistic effects between surface oxidation and ion scattering on microstructural feature surfaces increase with time, which results in increased roughness and then in the formation of significant residues or micropillars during etching in the presence of oxygen.

3.4.3 Effects of Si over SiO_2 Selectivity

Figures 3.8(a) and 3.8(b) show the ion incident energy and angle dependences of the etch selectivity of Si/SiO_2 for Cl^+ ions, obtained from the data as shown in Fig. 3.2. The Si/SiO_2 selectivity decreases with increasing ion energy, where the selectivity is higher at smaller angles of incidence. Moreover, the Si/SiO_2 selectivity decreases with increasing angle of incidence, where the selectivity is higher at lower ion energies. Therefore, scattered ions, which enter microstructural feature surfaces with larger angles of incidence, tend to etch oxidized surfaces at similar or higher rates as compared to Si, which would also be responsible for the increased roughness and then significant residues or micropillars in the presence of oxygen.

3.5 Conclusions

Atomic-scale cellular model ASCeM reproduced the feature profile evolution experimentally observed during Si etching at increased O_2 concentrations in Cl_2/O_2 plasmas, including decreased etch rates, and also increased roughness and residues on bottom surfaces of the feature. Numerical results indicated that the local surface oxidation induces the surface roughness at the bottom of the feature. Moreover, the other numerical results also indicated that the ion scattering in microstructural features on roughened surface increases the surface roughness, which in turn cause a number of significant residues or micropillars on bottom surfaces of the feature during etching. Thus, it should be concluded that synergistic effects

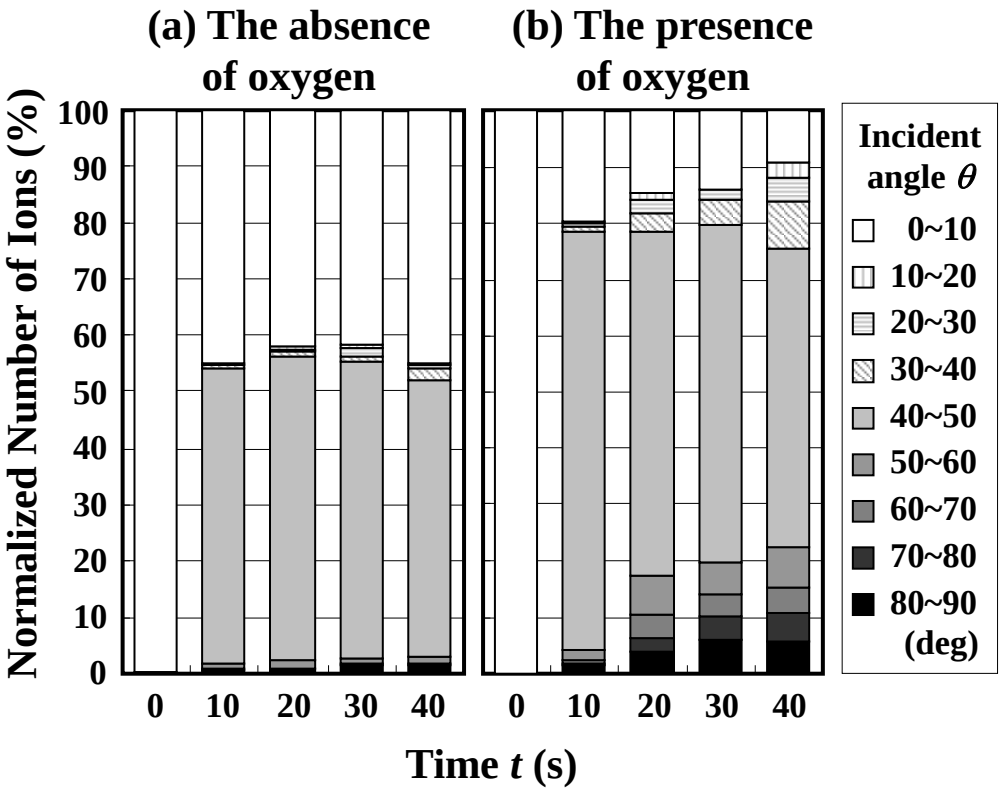

Fig. 3.7. Normalized number of ions having different incident angles on feature surfaces of 200-nm space, analyzed every 10 s from the simulation of Fig. 3.4.

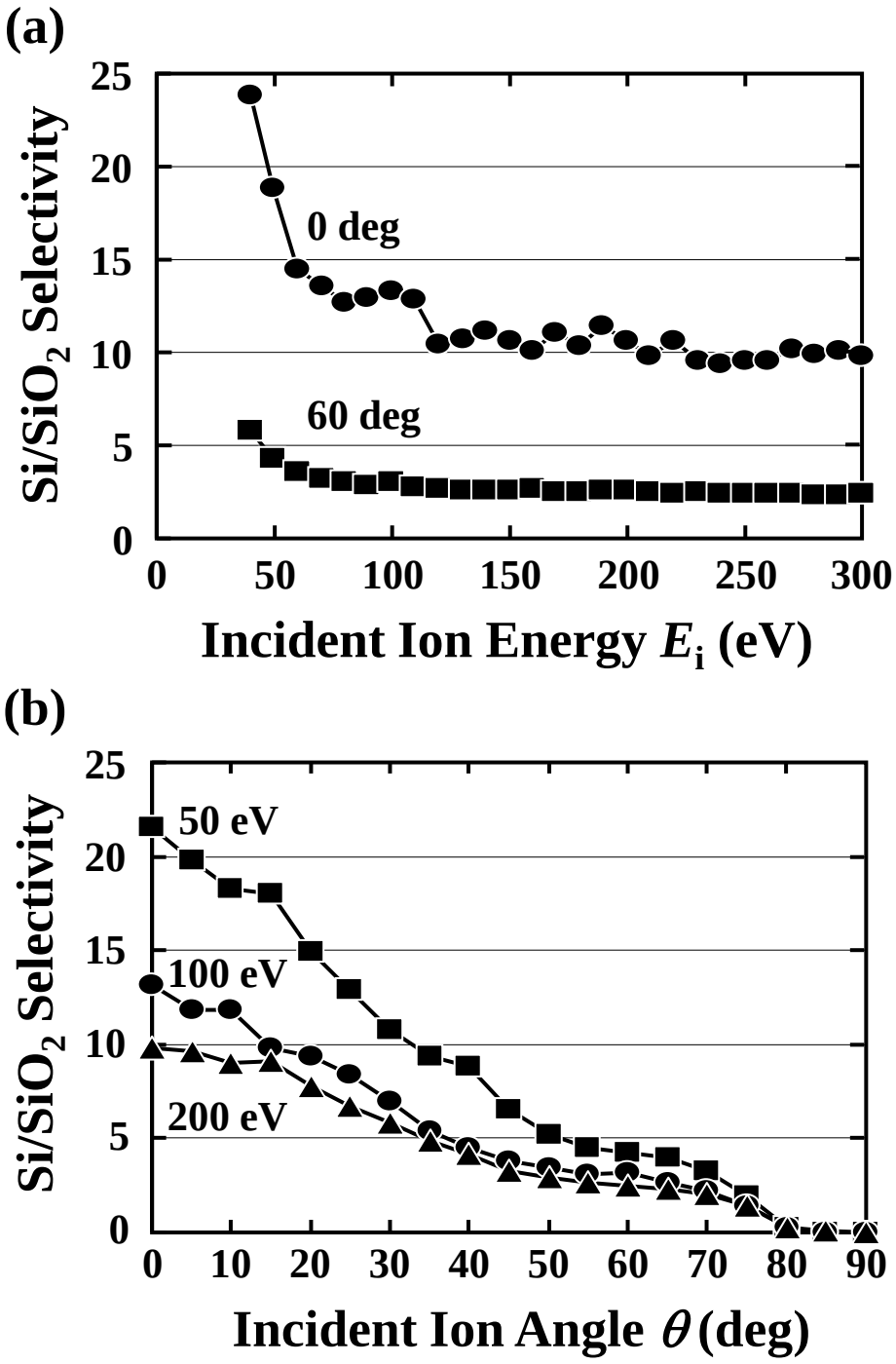

Fig. 3.8. Etch selectivity of Si/SiO_2 for Cl^+ ions, as a function of (a) incident energy E_i (θ = 0, 60 deg) and (b) incident angle θ (E_i = 50, 100, 200 eV), obtained from the data as shown in Fig. 3.2.

between surface oxidation and ion scattering in microstructural features on roughened surfaces play a significant role in the formation of surface roughness and residue. In practice, in roughened microstructural features, geometrical shadowing effects for neutral oxygen suppress the surface oxidation at the local feature bottom; consequently, the difference between etch rates through ion-assisted reactions on top surfaces (with significant oxidation) and bottom surfaces (with less oxidation) of the local feature further increases the roughness, and causes significant residues. Further studies are now in progress to control the roughness, together with a quantitative analysis of the correlation between numerical and experimental results of its spatial dependence.

References

1) G. S. Oehrlein, J. F. Rembetski, and E. H. Payne: J. Vac. Sci. Technol. B **8** (1990) 1199.
2) G. S. Oehrlein and Y. Kurogi: Mater. Sci. Eng. **24** (1998) 153.
3) T. P. Chow, P. A. Maciel, and G. M. Fanelli: J. Electrochem. Soc. **134** (1987) 1281.
4) H. Jansen, H. Gardeniers, M. De Boer, M. Elwenspoek, and J. Fluitman: J. Micromech. Microeng. **6** (1996) 14.
5) G. S. Hwang and K. P. Giapis: J. Vac. Sci. Technol. B **15** (1997) 70.
6) G. S. Hwang and K. P. Giapis: Appl. Phys. Lett. **70** (1997) 2377.
7) G. S. Hwang and K. P. Giapis: J. Vac. Sci. Technol. B **15** (1997) 1741.
8) W. Jin and H. H. Sawin: J. Vac. Sci. Technol. A **21** (2003) 911.
9) G. S. Oehrlein, R. G. Schad, and M. A. Jaso: Surf. Interf. Anal. **8** (1986) 243.
10) T. Hayakawa, T. Suzuki, T. Uesugi, and Y. Mitsushima: Jpn. J. Appl. Phys. **37** (1998) 5.
11) M. Tuda, K. Ono, and K. Nishikawa: J. Vac. Sci. Technol. B **14** (1996) 3291.
12) M. Tuda, K. Nishikawa, and K. Ono: J. Appl. Phys. **81** (1997) 960.
13) M. A. Vyvoda, M. Li, D. B. Graves, H. Lee, M. V. Malyshev, F. P. Klemens, J. T. C. Lee, and V. M. Donnelly: J. Vac. Sci. Technol. B **18** (2000) 820.
14) H. H. Hwang, M. Meyyappan, G. S. Mathad, and R. Ranade: J. Vac. Sci. Technol. B **20** (2002) 2199.
15) Y. Osano and K. Ono: Jpn. J. Appl. phys. **44** (2005) 8650.
16) Y. Osano, M. Mori, N. Itabashi, K. Takahashi, K. Eriguchi, and K. Ono: Jpn. J. Appl. phys. **45** (2006) 8157.
17) Y. Osano and K. Ono: J. Vac. Sci. Technol. B **26** (2008) 1425.
18) A. P. Mahorowala and H. H. Sawin: J. Vac. Sci. Technol. B **20** (2002) 1064.
19) R. A. Gottscho: J. Vac. Sci. Technol. B **11** (1993) 1884.
20) F. H. Stillinger and T. A. Weber: Phys. Rev. B **31** (1985) 5262.
21) H. Feil, J. Dieleman, and B. J. Garrison: J. Appl. Phys. **74** (1993) 1303.
22) C. F. Abrams and D. B. Graves: J. Vac. Sci. Technol. A **16** (1998) 3006.
23) W. Jin, S. A. Vitale, and H. H. Sawin: J. Vac. Sci. Technol. A **20** (2002) 2106.

Chapter 4
Molecular Dynamics Analysis of Surface Roughening

4.1 Introduction

Plasma processing for the pattern etching of thin films is essential for fabricating microelectronic devices.[1)] Since the dimensions of ultralarge-scale integrated (ULSI) circuit devices are approaching the sub-40 nm regime at the transistor gate level, the control of etching processes becomes more critical. Thus, it becomes important to determine how surface reactions occur during plasma etching, and thus a better understanding of interactions between plasmas and surfaces is more essential for next-generation devices. In Si etching for the fabrication of gate electrodes and shallow trench isolation, chlorine-based plasmas are widely used owing to their productivity, and the reproducibility and controllability of etched profiles, where passivation layers are formed on feature sidewalls by adding small amounts of O_2.[2–4)] However, O_2 addition often causes several problems such as the formation of residues, micropillars, and roughened surfaces, and the mechanism underlying the formation of roughened surfaces is less well understood.[5,6)]

We have developed a Monte Carlo (MC)-based etching profile simulation using a semiempirical model (atomic-scale cellular model, ASCeM), which can reproduce the feature profile evolution down to < 50 nm scale, including bowing, tapering, microtrenching, reactive ion etching (RIE) lag, inverse RIE lag, and micropillar during Si trench etching in Cl_2 and Cl_2/O_2 plasmas.[7–13)] In particular, we demonstrated that synergistic effects between surface oxidation and ion scattering in microstructural features on roughened surfaces play a significant role in the formation of residues or micropillars.[10,12,13)] However, the mechanisms of the initial-stage formation of micromasks soon after the start of etching are still poorly understood. This study focuses on the formation of roughened surfaces on the atomic scale during Si etching in Cl_2 and Cl_2/O_2 plasmas, and on the relationship between local surface oxidation and surface roughness on the nanometer scale, using a classical molecular dynamics (MD) approach.[14)]

4.2 Modeling and Simulation

Figure 4.1 shows a schematic of our classical MD simulation for Si etching in Cl_2/O_2 plasmas. The surface area of Si(100) substrates of interest is a square 70 Å on one side (or an area of 4900 $Å^2$), and the simulation cell initially contains 6700 Si atoms at a depth of 27 Å.

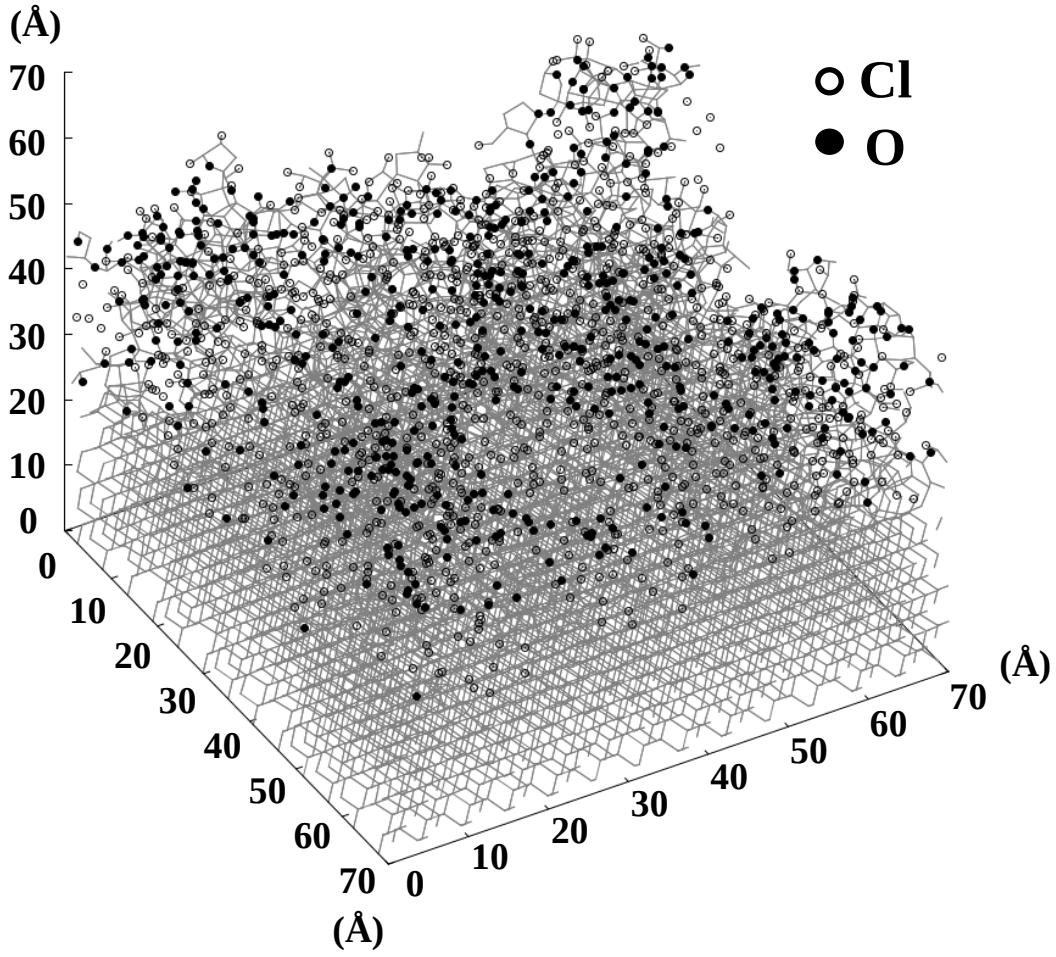

Fig. 4.1. Schematic of the classical MD simulation of etching. Substrate or target Si atoms are placed in the simulation cell, which has a square 70 Å on one side and initially contains 6700 Si target atoms at a depth of 27 Å. Note that Si atoms themselves are not depicted in the simulation results.

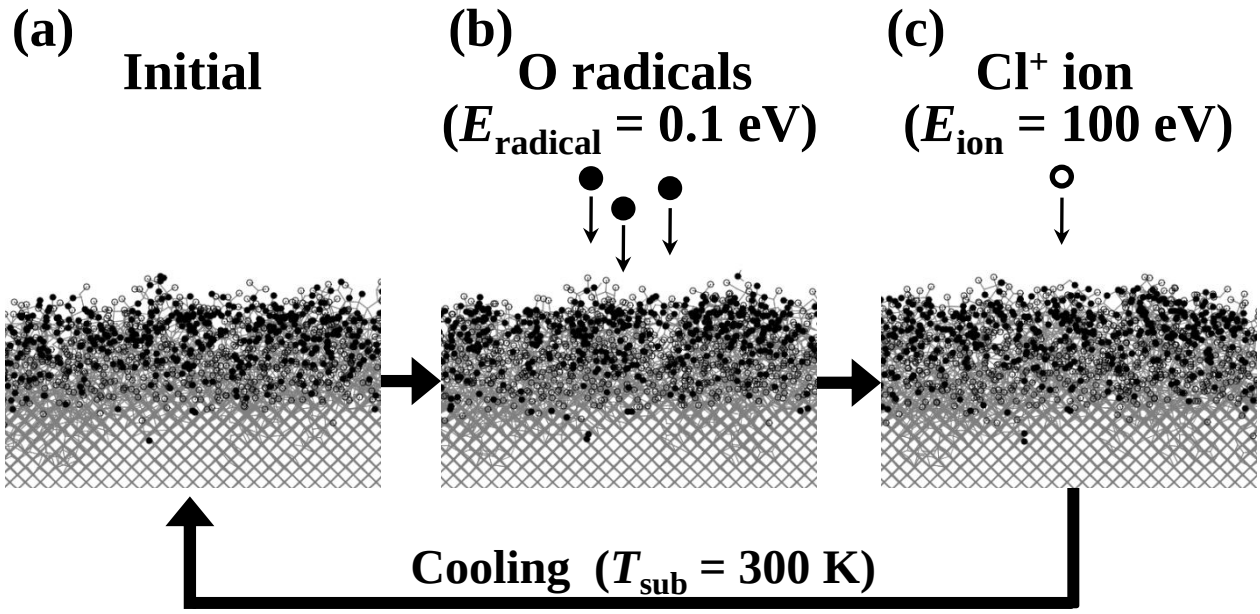

Fig. 4.2. Schematic of the MD simulation flow of plasma etching. Low-energy O radicals are supplied onto surfaces every Cl^+ ion bombardment, where the incident ion energy is E_{ion} = 100 eV and that of neutral radicals is $E_{radical}$ = 0.1 eV.

Target atoms in the bottom layer are fixed during the simulation, while periodical boundaries are imposed in the horizontal direction. To simulate surface reactions during Cl_2/O_2 plasma etching, high-energy Cl^+ ions (E_{ion} = 100 eV) and low-energy O radicals ($E_{radical}$ = 0.1 eV) are alternately injected normal to the surface, as shown in Fig. 4.2. Every after injection of several low-energy particles (O radicals) and a single high-energetic particle (Cl^+ ion) onto surfaces, we let the system evolve for 0.7 ps with the total energy being constant, and then artificially cool the system for 0.3 ps down to the initial temperature (T_{sub} = 300 K) of substrate atoms.[15] We use the improved Stillinger-Weber (SW)[16] interatomic potentials for Si/Cl,[17] Si/O,[18] and Si/Cl/O systems,[19] which involve a correction term for the three-body potential function, to predict surface reaction kinetics more accurately without overestimation of the repulsive interaction in the original SW model.[20] It is noted here that the effects of Cl radicals need to be considered in the analysis of plasma-surface interactions during Si etching in Cl_2/O_2 plasmas; however, in this study, we treat only Cl^+ ions and O radicals in order to reduce the calculation cost of our simulations. In addition, impinging particles are assumed to be charge-neutral with high translational energies.

4.3 Results and Discussion

4.3.1 Surface Roughness

To analyze the relationship between neutral oxygen flux and surface roughness, the feature profiles during Si etching in Cl_2/O_2 plasmas are simulated for different neutral oxygen fluxes. Figures 4.3(a)-4.3(e) show side views of the etched surface of Si(100) during Cl_2/O_2 plasma etching, simulated with 3500 ion bombardments for different of Γ_o^0/Γ_i^0 = 0, 1, 2, 5, and 10. The results indicated that many Cl and O atoms are located in surface reaction layers, and the amount of O atoms in surface reaction layers tends to increase with increasing Γ_o^0/Γ_i^0. However, increasing the O flux does not make a marked difference in the thickness of surface reaction layers and surface roughness.

Figure 4.4 shows the roughness parameter R_a of the etched surface as a function of Γ_o^0/Γ_i^0 after 3500 ion bombardments. Note that R_a is the arithmetic average of the absolute values of the profile height deviations from the mean height, or the roughness average of a surface calculated from microscopic peaks and valleys. In this study, R_a is given by

$$R_a = \frac{1}{N}\sum_{i=1}^{N}\left(z(i)-\bar{z}\right) , \qquad (4.1)$$

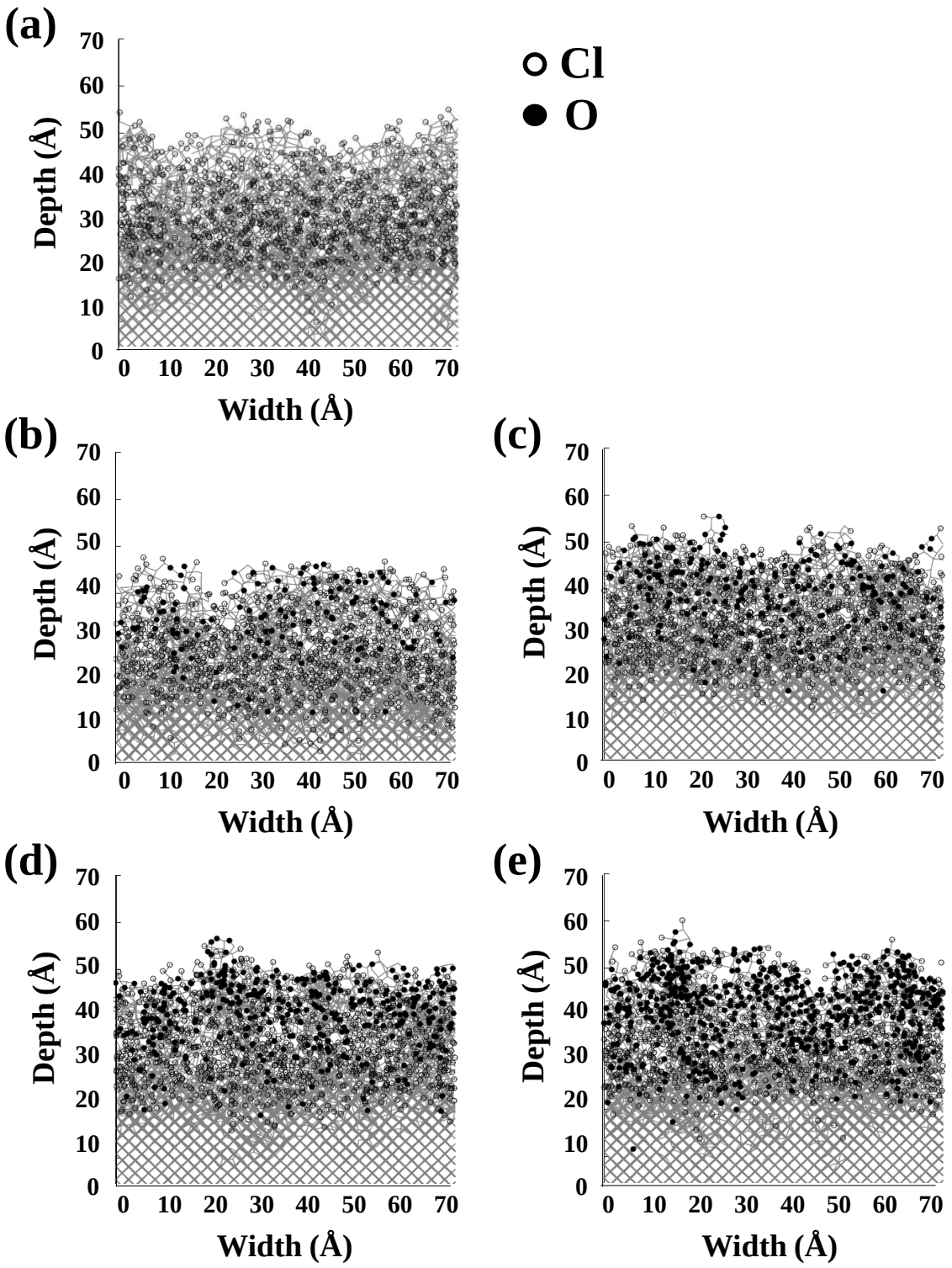

Fig. 4.3. Side views of the etched surface of Si(100) during Cl_2/O_2 plasma etching, simulated with 3500 ion bombardments for different neutral-oxygen-to-ion flux ratios of Γ_o^0/Γ_i^0 = (a) 0, (b) 1, (c) 2, (d) 5, and (e) 10.

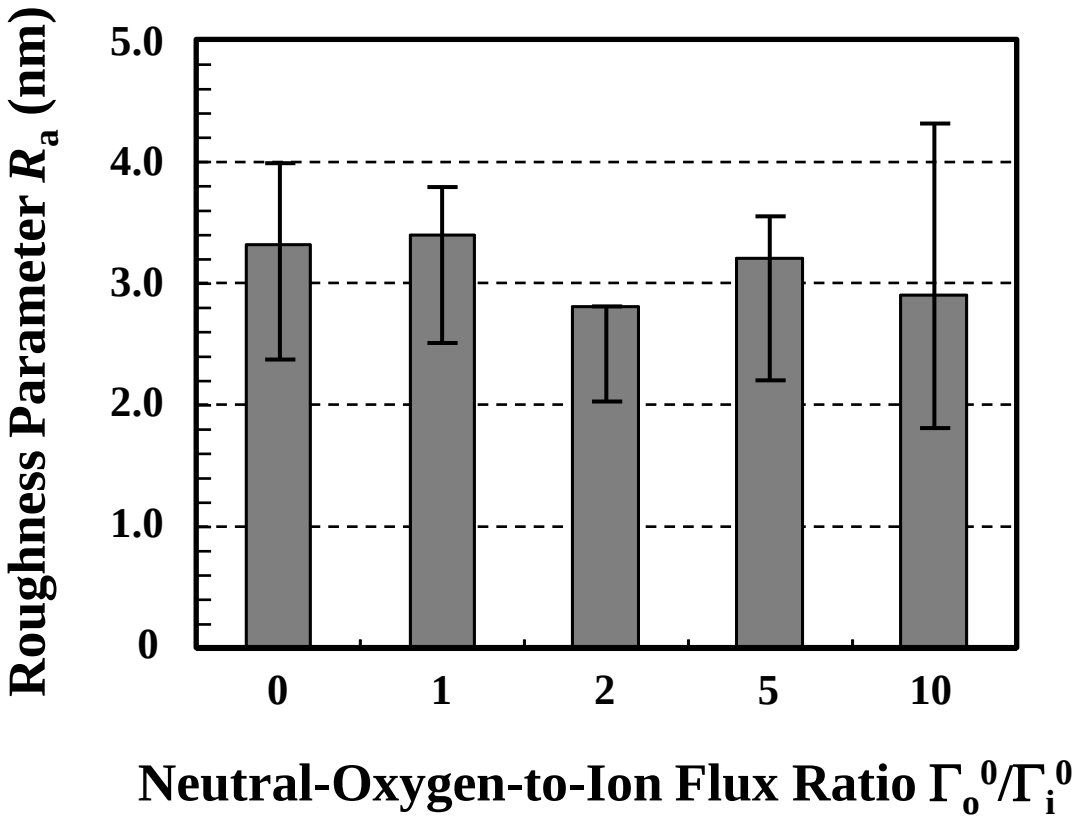

Fig. 4.4. Roughness parameter R_a as a function of neutral-oxygen-to-ion flux ratio Γ_o^0/Γ_i^0, where R_a means the arithmetic average of the profile height deviations from the mean height.

where N is the sampling number or data points of the Si atoms located at the outermost surface and $z(i)$ denotes the ordinate at the sampling outermost Si atoms. The mean height $\bar{z} = (1/N)\sum_{i=1}^{N} z(i)$ of etched surfaces is calculated from the locations of the Si atoms constituting the outermost etched surfaces. The results indicate that the etched surfaces tend to be roughened with increasing amount of ion injection or decreasing amount of O neutrals. It follows that in the present MD simulation, increasing the O flux does not make a marked difference in R_a, possibly because the simulation cell might be too small to reproduce the evolution of surface roughness of sub-100 nm scale.

4.3.2 Distribution of O and Cl Atoms on Surfaces

Figures 4.5(a) and 4.5(b) show the side views of the etched surface of Si(100), together with the depth profiles of Si, Cl, and O atoms therein, simulated with 3500 ion impacts for different neutral-oxygen-to-ion flux ratios of Γ_o^0/Γ_i^0 = 1 and 10. The results indicate that Cl atoms tend to be distributed widely in surface reaction layers, while O atoms are located preferentially in the upper part of surface reaction layers. It is noted here that surface diffusion of O atoms is little observed at T_{sub} = 300 K except that a few O atoms are pushed into the substrate by the impact of incident energetic ions, even if we lengthen the evolve time (noncooling time) of the MD calculation. In particular, the distribution of O atoms relies on the energy of incident ions and radicals. Figures 4.6(a) and 4.6(b) show the top views of the etched surfaces of Figs. 4.5(a) and 4.5(b), indicating that Cl atoms tend to be distributed randomly or uniformly on etched surfaces, while O atoms are located selectively on surface areas where the Si–Si bonds are broken or distorted.

On the bases of the MD simulations shown in Figs. 4.5 and 4.6, we depict a three-dimensional (3D) surface plot of the location of Si atoms constituting the outermost etched surfaces, and then plot the distribution of the outermost O atoms thereon, as shown in Figs. 4.7(a) and 4.7(b). The results indicate that O atoms tend to be located on nanometer-scale convex surfaces; thus, the broken or distorted bond structures are formed preferentially on nanometer-scale convex surfaces roughened during plasma etching.

The bond energies and lengths for the Si/Cl/O system are listed in Table II. Here, the bond energy and length are the depth and position of the potential minimum, respectively, calculated from the corresponding two-body interatomic potentials.[17–19] The results shown in

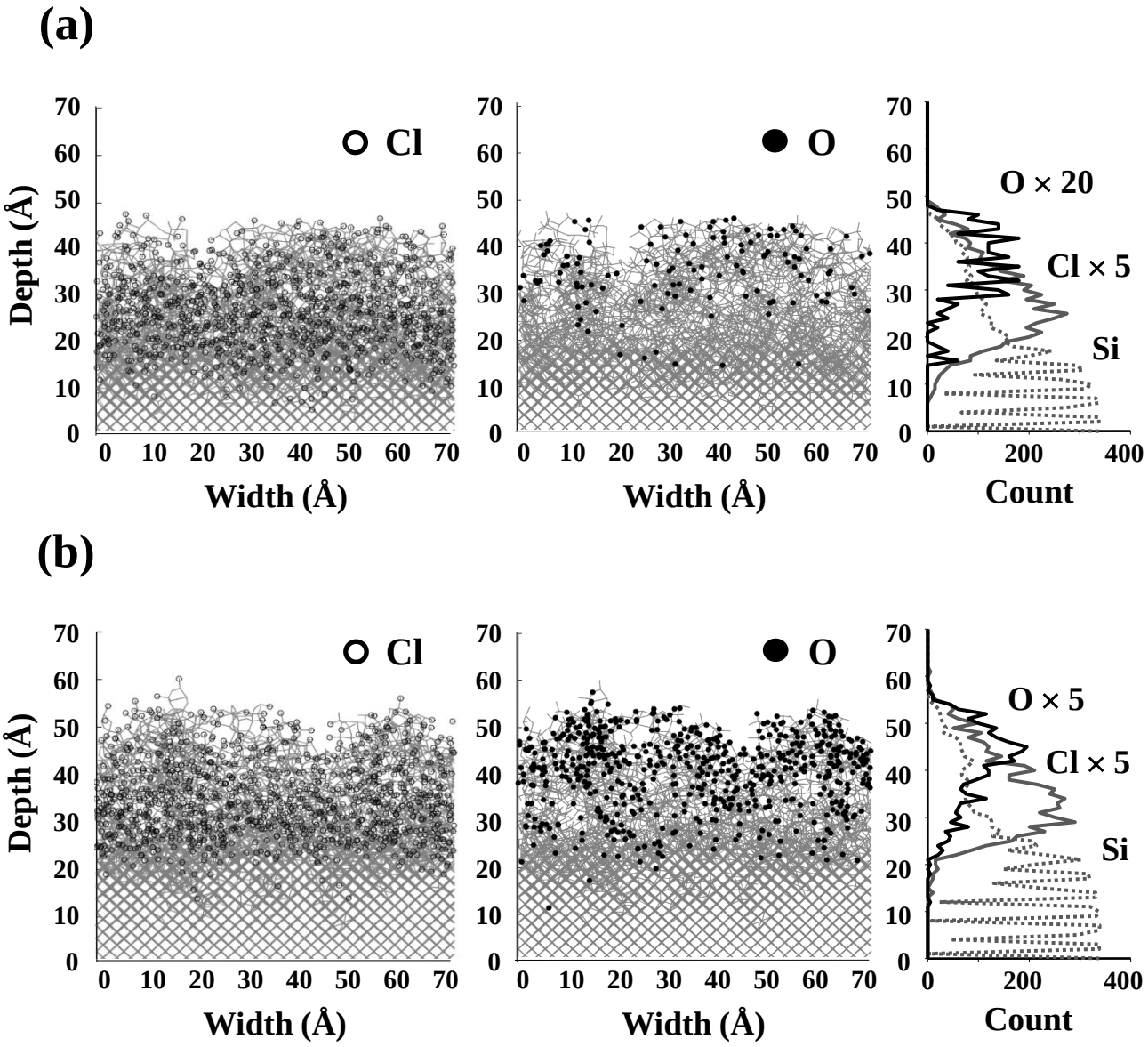

Fig. 4.5. Side views of the etched surface of Si(100), together with the depth profiles of Si, Cl, and O atoms therein, simulated with 3500 ion bombardments for different neutral-oxygen-to-ion flux ratios of Γ_o^0/Γ_i^0 = (a) 1 and (b) 10.

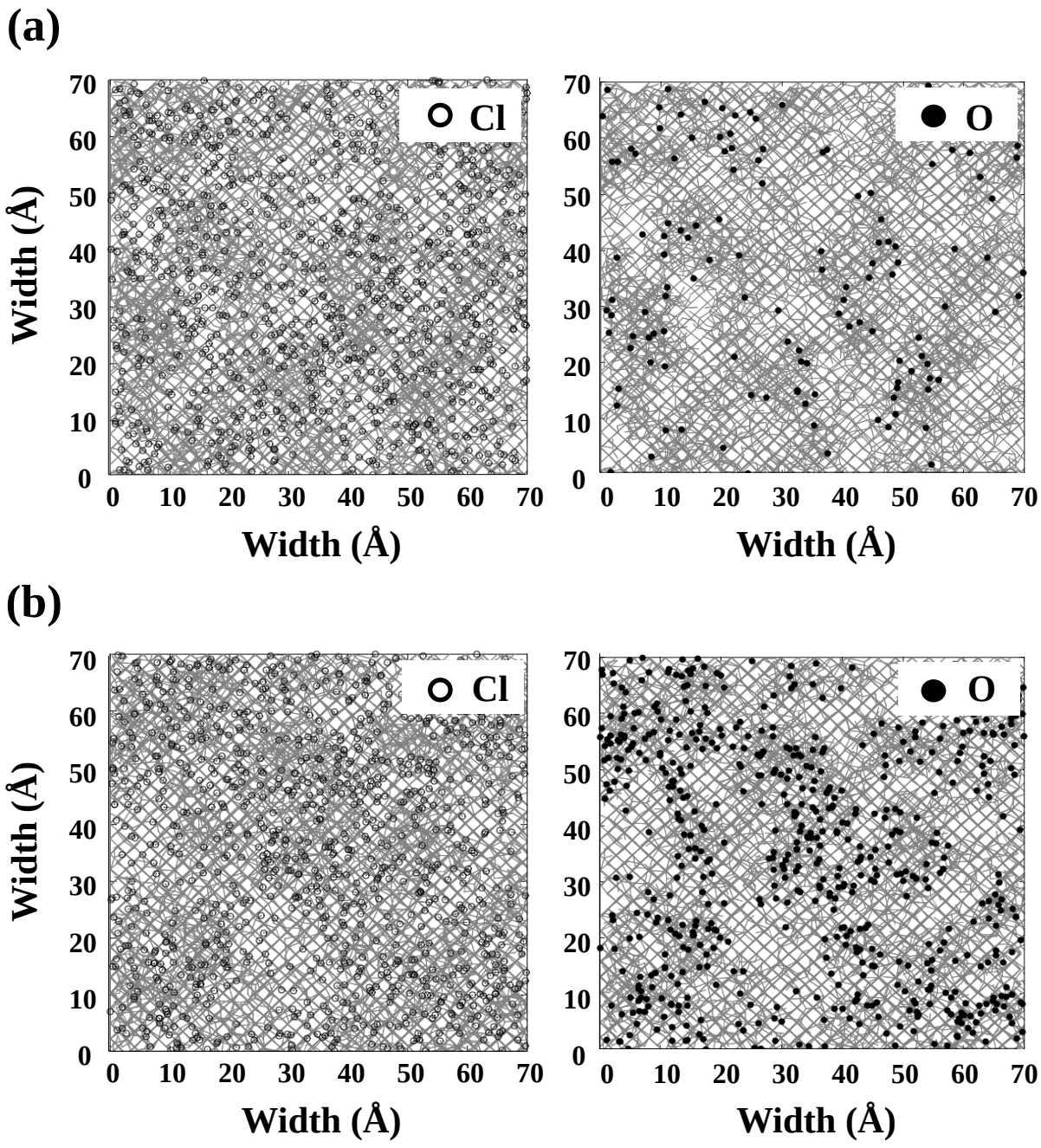

Fig. 4.6. Top views of the etched surfaces of Figs. 4.5(a) and 4.5(b), together with the distribution of the outermost Cl and O atoms thereon, simulated for different ratios of Γ_o^0/Γ_i^0 = (a) 1 and (b) 10.

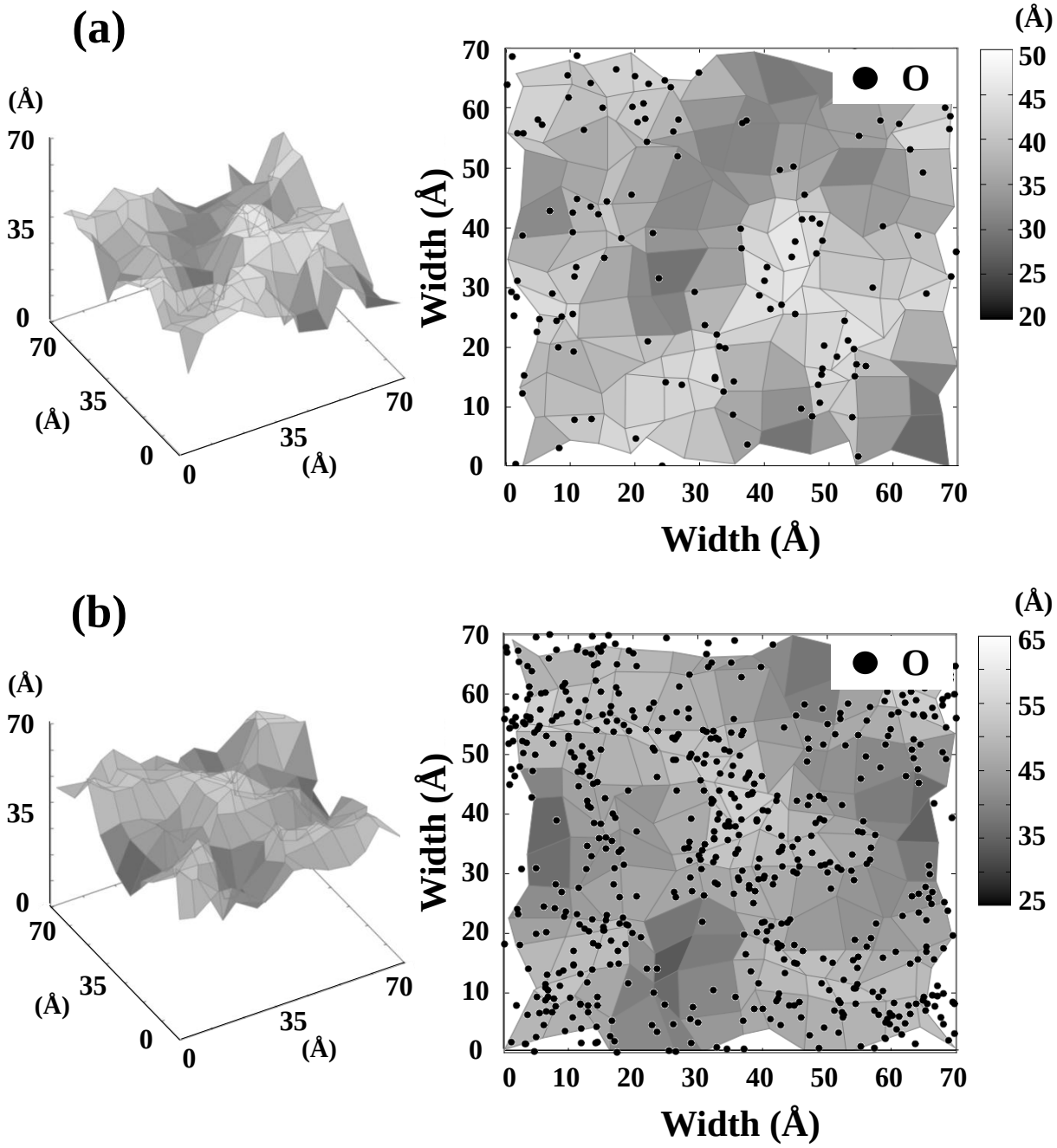

Fig. 4.7. Three-dimensional (3D) surface plots of the location of Si atoms constituting the outermost etched surfaces, together with the distribution of the outermost O atoms thereon, simulated with 3500 bombardments for different oxygen-neutral-to-ion flux ratios of Γ_o^0/Γ_i^0 = (a) 1 and (b) 10.

Table II. Bond energies and lengths for Si/Cl/O system.

Bond	Bond energy (eV)	Bond length (Å)
Si–Si	2.17	2.35
Si–O	4.14	1.61
Si–Cl	3.96	2.06
Cl–Cl	2.47	1.96
Cl–O	2.09	1.62

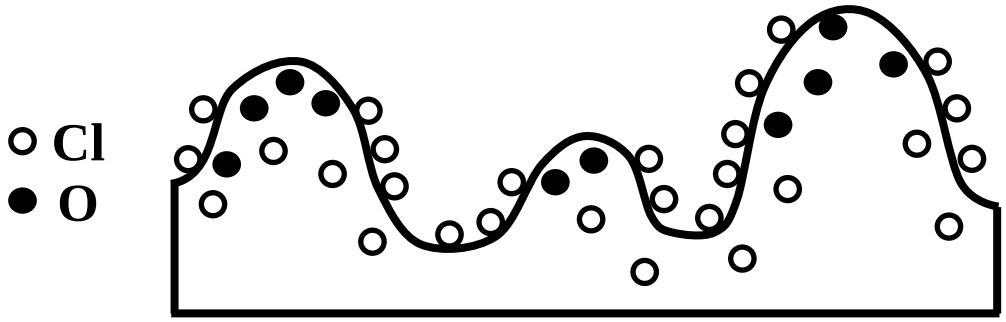

Fig. 4.8. Schematic of the formation nanometer-scale micromasks at around the top of roughened surfaces, where O atoms tend to adsorb on convex surfaces roughened during etching.

Table II imply that O atoms tend to break the Si–Si bonds and distort the Si lattice structure, because the Si–O bonds are stronger and shorter than the Si–Si bonds. In addition, the Si–O bonds are also stronger and shorter than the Si–Cl bonds, implying that O atoms tend to bond to Si atoms in place of Cl atoms bonded. Thus, it follows that O atoms tend to be adsorbed on convex surfaces roughened during etching, which leads to the formation of nanometer-scale micromasks at around the top of roughened surfaces, as depicted in Fig. 4.8, where Cl atoms tend to be distributed uniformly around O atoms on roughened surfaces. It is noted here that the O atoms incident and adsorbed on nanometer-scale concave surfaces tend to be removed, possibly by incident energetic ions that are reflected on local feature sidewalls and then focused at around the bottom of concave surfaces, which results in the absence of O atoms on nanometer-scale concave surfaces roughened during etching.

4.3.3 Comparison between Numerical and Experimental Results

To compare between numerical and experimental results, etching experiments were performed using an inductively coupled plasma (ICP) reactor, where pure Cl_2 and 98%-Cl_2/2%-O_2 gases were introduced into the reactor at a total gas flow rate of 40 sccm and a pressure of 20 mTorr. The source ICP power was P_{ICP} = 450 W at 13.56 MHz, and the RF bias power was P_{RF} = 30 W at 13.56 MHz. Under these conditions, Si(100) samples were exposed to the plasma for 2 min, where the dc self-bias voltage at the wafer stage was measured to be V_{dc} = 87 and 71 V in Cl_2 and Cl_2/O_2 plasmas, respectively.

Figures 4.9(a) and 4.9(b) show atomic force microscopy (AFM) and scanning electron microscopy (SEM) images of the Si surface etched in pure Cl_2 and Cl_2/O_2 plasmas, respectively, exhibiting that sub-10-nm-scale roughness occurs on surfaces in Cl_2 plasma, while over-100-nm-high micropillars or roughened structures occur on surfaces in Cl_2/O_2 plasma. The roughness parameter R_a values measured from AFM images are 1.17 and 8.03 nm for Si surfaces etched in Cl_2 and Cl_2/O_2 plasmas, respectively. The R_a value in Cl_2/O_2 plasma etching is significantly larger than that shown in Fig. 4.4 obtained from the MD simulation, and so the present MD simulation might be insufficient to reproduce the formation of surfaces with a large roughness in the presence of surface oxidation, as mentioned earlier in §4.3.1. However, the present MD simulations suggest that O radicals coming from the plasma tend to induce local surface oxidation on convex roughened surfaces during etching, and that the resulting nanometer-scale micromasks on etched surfaces significantly affect the formation of roughened

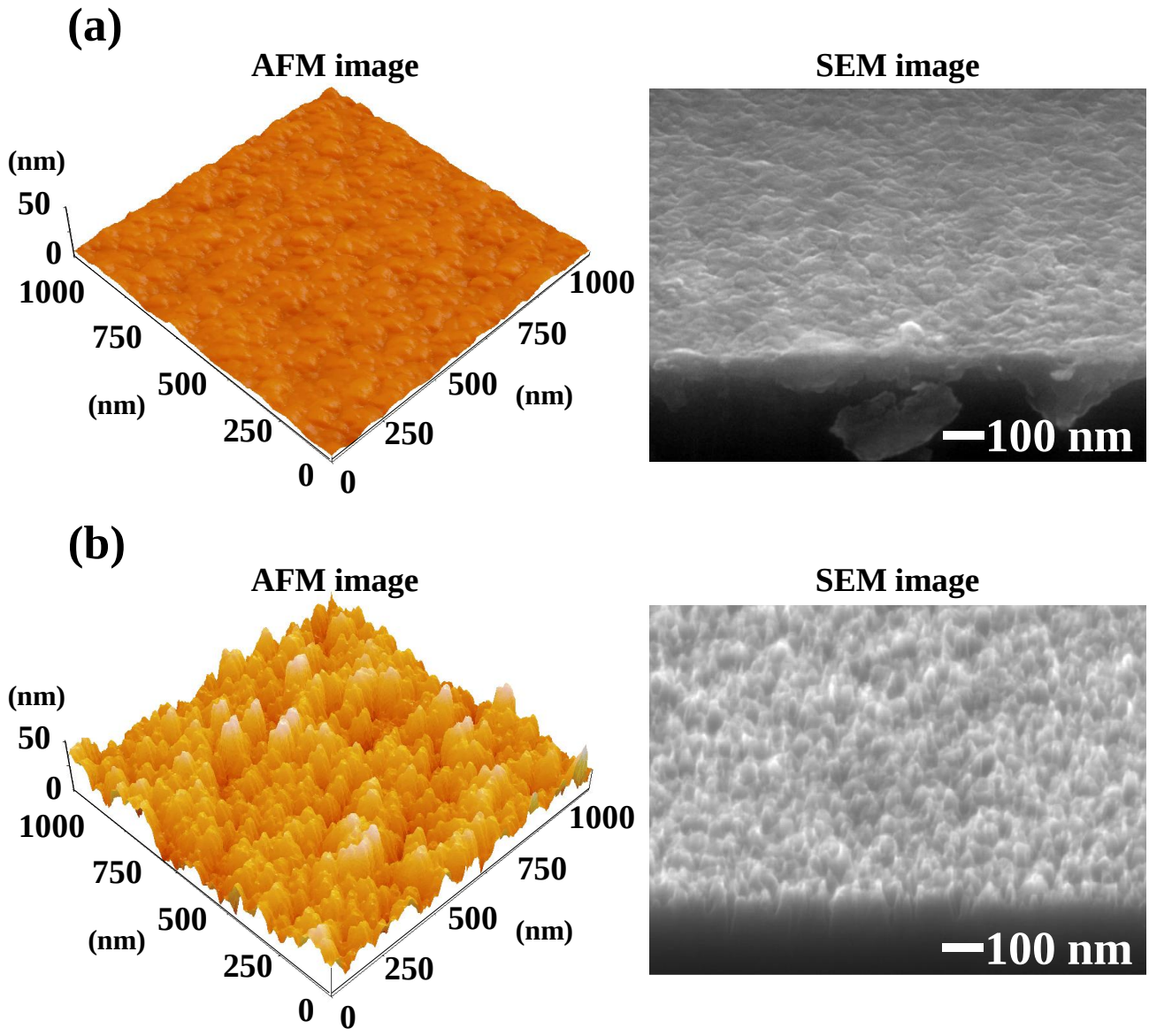

Fig. 4.9. Atomic force microscopy (AFM) and scanning electron microscopy (SEM) images of the Si surface etched in (a) pure Cl_2 and (b) Cl_2/O_2 plasmas. The roughness parameter R_a values measured from AFM images are 1.17 and 8.03 nm for Si surfaces etched in Cl_2 and Cl_2/O_2 plasmas, respectively.

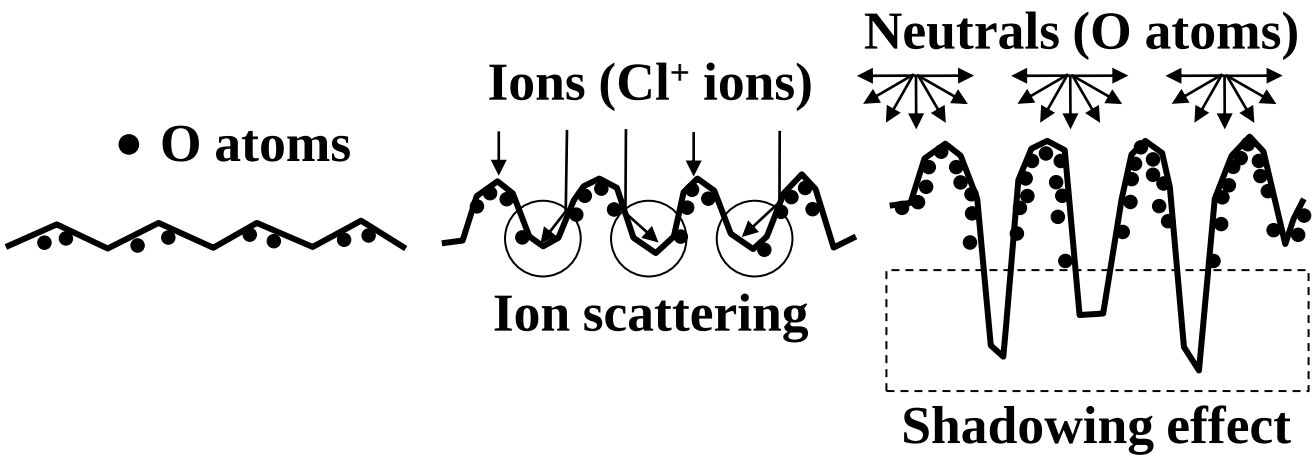

Fig. 4.10. Schematic of the formation of roughened surfaces and micropillars during Si etching in Cl_2/O_2 plasmas. Synergistic effects between surface oxidation and ion scattering in microstructural features on roughened surfaces play a significant role in the formation of roughened surfaces or development of micropillars.

surfaces or development of micropillars, as depicted in Fig. 4.10.

4.4 Conclusions

We have investigated the mechanisms of the initial-stage formation of roughened surfaces and micropillars during Si etching in Cl_2 and Cl_2/O_2 plasmas by employing the MD approach. Numerical results indicated that there are several differences between the behavior of Cl and O atoms on and in surface reaction layers. Cl atoms tend to be distributed uniformly in surface reaction layers, while O atoms tend to be located on convex surfaces where the bond structures are broken or distorted. It follows that nanometer-scale micromasks are formed owing to local oxidation on the top of roughened surfaces, and O atoms would have a large effect on the bond structure of etched surfaces. Experiments showed that over-100-nm-high micropillars are formed on the Si surface etched in Cl_2/O_2 plasmas, while only sub-10-nm-scale roughness occurs on the surface etched in pure Cl_2 plasma. It is clear that oxygen addition would affect etched profiles, especially the formation of roughened surfaces.

A comparison between numerical and experimental results implies that the MD simulation might not be sufficient to reproduce the formation of surface roughness that is often observed in experiments. The mechanisms of local surface oxidation, and formation of micromasks, roughened surfaces, and micropillars may be revealed by employing two approaches, namely, nanometer-scale MC and atomic-scale MD simulations. In practice multiscale modeling and comparison with experiments are more important for understanding complex phenomena of plasma-surface interactions on the nanometer scale.

References

1) H. Abe, M. Yoneda, and N. Fujiwara: Jpn. J. Appl. Phys. **47** (2008) 1435.
2) F. H. Bell, O. Joubert, and L. Vallier: J. Vac. Sci. Technol. B **14** (1996) 96.
3) E. Pargon, M. Darnon, O. Joubert, T. Chevolleau, L. Vallier, L. Mollard, and T. Lill: J. Vac. Sci. Technol. B **23** (2005) 1913.
4) E. Pargon, O. Joubert, T. Chevolleau, G. Cunge, S. Xu, and T. Lill: J. Vac. Sci. Technol. B **23** (2005) 103.
5) G. S. Oehrlein, J. F. Rembetski, and E. H. Payne: J. Vac. Sci. Technol. B **8** (1990) 1199.
6) G. S. Oehrlein and Y. Kurogi: Mater. Sci. Eng. **24** (1998) 153.
7) Y. Osano and K. Ono: Jpn. J. Appl. Phys. **44** (2005) 8650.
8) Y. Osano, M. Mori, N. Itabashi, K. Takahashi, K. Eriguchi, and K. Ono: Jpn. J. Appl. Phys. **45** (2006) 8157.
9) Y. Osano and K. Ono: J. Vac. Sci. Technol. B **26** (2008) 1425.
10) H. Tsuda, M. Mori, Y. Takao, K. Eriguchi, and K. Ono: Thin Solid Films **518** (2010) 3475.
11) H. Tsuda, M. Mori. Y. Takao, K. Eriguchi, and K. Ono: Jpn. J. Appl. Phys. **49** (2010) 08JE01.
12) K. Ono, H. Ohta, and K. Eriguchi: Thin Solid Films **518** (2010) 3461.
13) K. Ono, H. Ohta, and K. Eriguchi: Plasma Kaku Yugo Gakkaishi **85** (2009) 163 [in Japanese].
14) H. Tsuda, K. Eriguchi, K. Ono, and H. Ohta: Appl. Phys. Express **2** (2009) 116501.
15) H. J. C. Berendsen, J. P. M. Postma, W. F. van Gunsteren, A. DiNola, and J. R. Haak: J. Chem. Phys. **81** (1984) 3684.
16) H. Ohta, T. Nagaoka, K. Eriguchi, and K. Ono: Jpn. J. Appl. Phys. **48** (2009) 020225.
17) H. Feil, J. Dieleman, and B. J. Garrison: J. Appl. Phys. **74** (1993) 1303.
18) T. Watanabe, H. Fujiwara, and H. Noguchi: Jpn. J. Appl. Phys. **38** (1999) L366.
19) H. Ohta and S. Hamaguchi: J. Chem. Phys. **115** (2001) 6679.
20) F. H. Stillinger and T. A. Weber: Phys. Rev. B **31** (1985) 5262.

Chapter 5
Three-Dimensional Atomic-Scale Cellular Model: Analysis of Profile Anomalies and Surface Roughness

5.1 Introduction

Since the dimensions of metal-oxide-semiconductor (MOS) devices in ultralarge-scale integration (ULSI) are approaching the sub-40 nm regime at the transistor gate level, the control of etching processes becomes more critical.[1,2] In particular, the three-dimensional measurement and prediction of atomic-scale surface roughness on etched feature profiles become more significant for the fabrication of next-generation devices;[3] however, the measurement is difficult, simply because the target feature profiles are too small or too complex to measure the surface roughness on bottom surfaces and sidewalls of the etched feature profiles. Therefore, the atomic-scale prediction of the surface roughness by numerical approaches becomes of great importance.[4]

In Si etching for the fabrication of gate electrodes and shallow trench isolation, chlorine-based plasmas are widely used owing to their productivity, reproducibility, and controllability of etched profiles, and several complex phenomena during plasma etching have been revealed up to now. However, phenomena such as the formation of surface roughness are still poorly understood, where the scale required for the fabrication of next-generation devices is entering into the atomic-scale area, and thus these phenomena cannot be explained by only the knowledge accumulated in the past several decades.

To understand plasma-surface interactions during etching on the atomic or nanometer-scale, several numerical models or methods, such as the sting model[5–7] and level set method,[8] have been developed for the feature profile simulations until now; however, there is no definite one, and it is still important to select adequate models or methods when we use them to analyze the phenomena concerned. We have developed a two-dimensional Monte Carlo-based etching profile simulation with a semi-empirical cell removal model (atomic-scale cellular model, ASCeM),[9–15] that can reproduce the feature profile evolution on the nanometer scale, including bowing, tapering, microtrenching, reactive ion etching (RIE) lag, inverse RIE lag, and micropillar, during Si trench etching in Cl_2 and Cl_2/O_2 plasmas. In this study, we present an extended ASCeM model or a three-dimensional atomic-scale cellular model (ASCeM-3D) and a simulation of plasma-surface interactions and feature profile evolution during Si etching in Cl_2

plasmas. The ASCeM-3D can analyze the three-dimensional structures of etched surfaces and the evolution of atomic-scale surface roughness, and represent profile anomalies such as intricately shaped and sharp-pointed features, which could not be reproduced in detail by the two-dimensional model. Emphasis is placed on the structure and the evolution of surface roughness soon after the start of etching. A comparison is also made between numerical results and experiments.

5.2 Modeling and Simulation

Figure 5.1 shows a schematic of the ASCeM-3D model for Si etching in Cl_2 plasmas, and Fig. 5.2 shows a flow chart of the simulation. The simulation domain is 50 nm square with a 230 nm depth, and is divided into a number of small cubic cells of $L = \rho_{Si}^{-1/3} = 2.7$ Å, where $\rho_{Si} = 5.0 \times 10^{22}$ cm^{-3} is the atomic density of Si substrates. The 184 × 184 × 847 atomic-scale cells (about 3×10^7 cells in total) are located initially with periodical boundaries in the horizontal direction. The feature profile evolution during Si etching in Cl_2 plasma is simulated for line-and-space patterns separated by different spaces. The initial surface profile is a poly-Si films of thickness $H_{Si} = 200$ nm with an insulating SiO_2 layer (10 nm) and the undermost Si layer (10 nm) under the poly-Si films. The present ASCeM-3D calculation requires approximately 1–3 Gbytes of memory, which is reasonable in current computer environments.

Ions and neutrals are injected from the top of the simulation domain with a Gaussian-like anisotropic angular distribution[9,10,16] and an isotropic distribution, respectively, and etch and/or sputter products are assumed to be desorbed from etching surfaces into microstructural features thermally or isotropically with a cosine distribution. The particle transport is analyzed using the three-dimensional Monte Carlo (MC) algorithm, and the surface normal is calculated by the four-point technique[17] for 5 × 5 × 5 neighboring cells (125 cells in total) at around the substrate surface cell that the ion reaches from the plasma. The ASCeM-3D takes into account surface chemistries based on the MC algorithm, including adsorption and reemission of neutrals, chemical etching, ion-enhanced etching, physical sputtering, and redeposition of etch products on feature surfaces, as summarized in Table III. Note that the deposition of etch products/by-products coming from the plasma is not taken into account in this study.

We assume the sticking probability of neutral reactants or Cl atoms to be $S_n = 1 - x/4$ on Si substrate surfaces unsaturated ($SiCl_x$, $x = 0 \sim 3$). The spontaneous chemical etching is taken to occur on saturated surfaces ($SiCl_x$, $x = 4$), where the reaction probability $\alpha_{chem} = \rho_{Si} ER_{chem}/\Gamma_n$

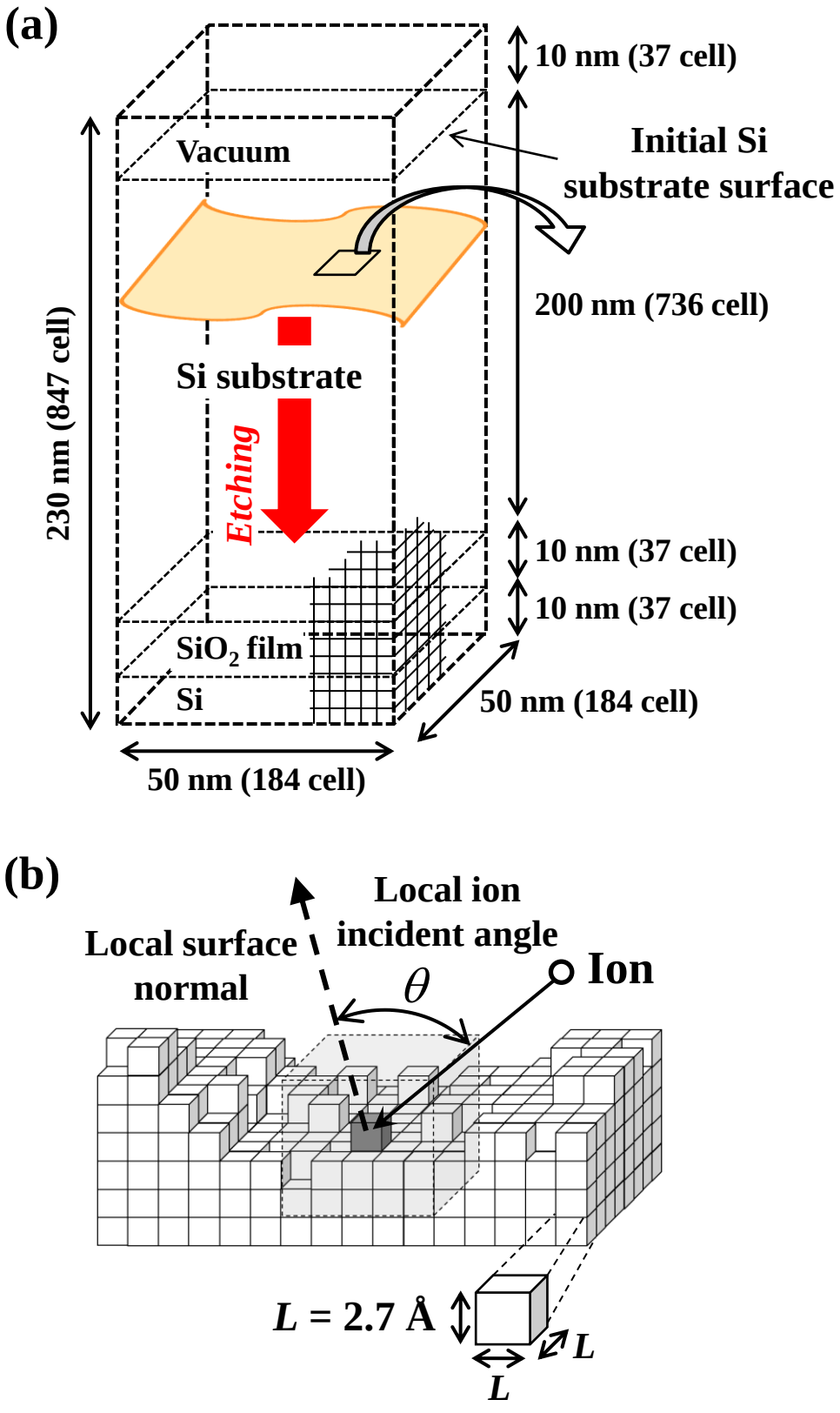

Fig. 5.1. Schematic of the three-dimensional atomic-scale cellular model (ASCeM-3D) and feature profile simulation. In the model, the surface normal is calculated by the so-called four-point technique for 5 × 5 × 5 neighboring cells (125 cells in total) at around the substrate surface cell that the ion reaches from the plasma.

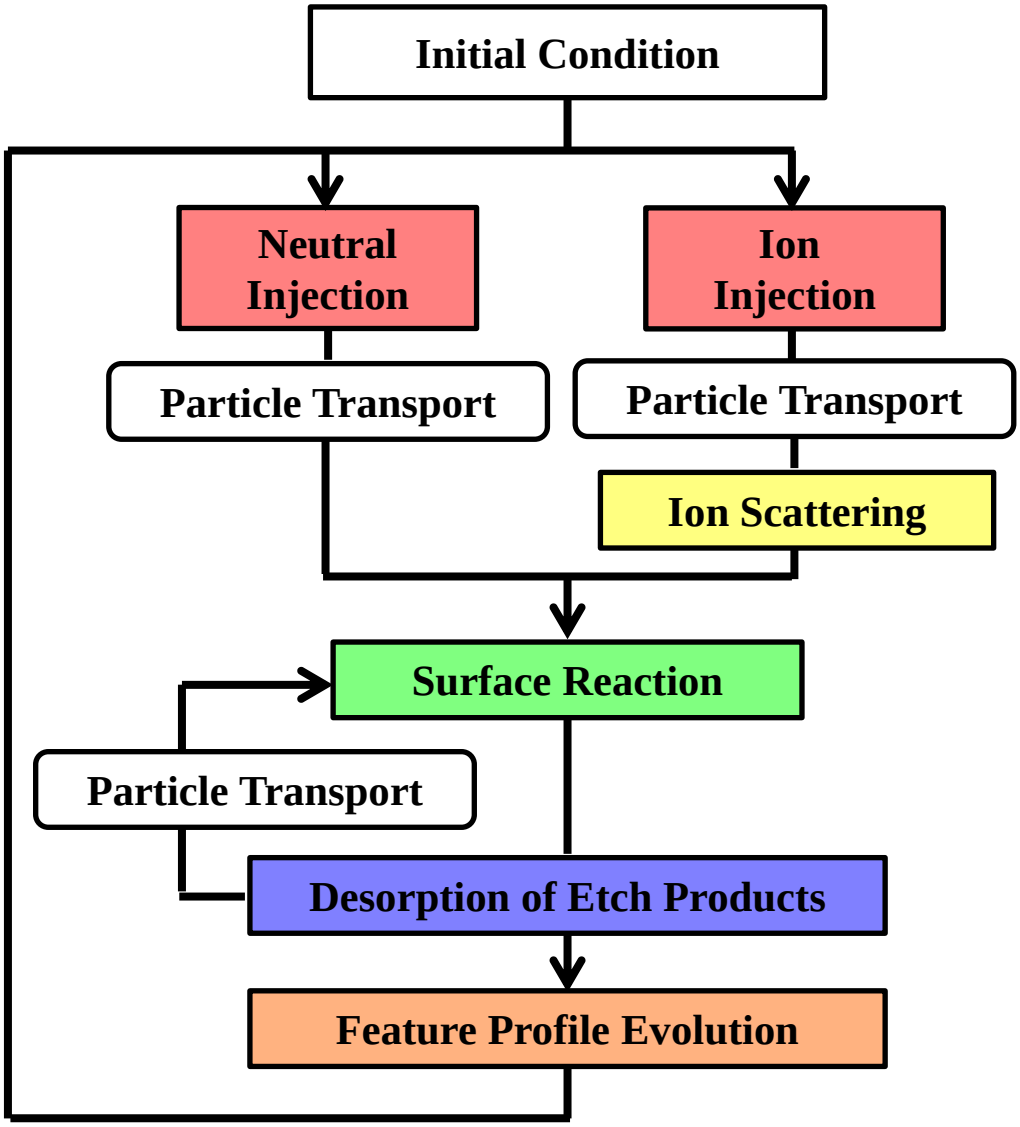

Fig. 5.2. Flow chart of the ASCeM-3D simulation. The particle transport and surface reaction processes are analyzed using the 3D Monte Carlo (MC) algorithm.

Table III. Surface kinetics model for Si etching in Cl_2 plasmas.

Reaction	Process		Coefficient
Neutral adsorption	$SiCl_x(s) + Cl(g) \rightarrow SiCl_{x+1}(s)$	$(x = 0 \sim 3)$	$S_n = 1 - x/4$
Chemical etching	$SiCl_3(s) + Cl(g) \rightarrow SiCl_4(g)$		α_{chem}
Ion-enhanced etching	$SiCl_x(s) \xrightarrow{Cl^+} SiCl_x(g)$	$(x = 1 \sim 4)$	$Y_{Si/Cl+} = (x/4)\, Y_{SiCl4}(E_i, \theta)$
Physical sputtering	$Si(s) \xrightarrow{Cl^+} Si(g)$		$Y_{Si/Cl+} = Y_{Si}(E_i, \theta)$
Redeposition	$SiCl_x(g) \rightarrow SiCl_x(s)$	$(x = 0 \sim 4)$	$S_q = 0.05$

(the number of substrate atoms etched per incident reactant on saturated surfaces) is calculated from the experimental etch rate ER_{chem} reported by Ogryzlo *et al.*,[18] where Γ_n denotes the flux of neutral Cl incident on surfaces. The etch yield $Y_{Si/Cl+} = Y_{SiCl4}$ for Cl^+ ions on saturated or fully chlorinated Si surfaces (the number of substrate atoms etched per incident ion on saturated surfaces) is taken from the model of Guo and Sawin,[19] as expressed by

$$Y_{SiCl_4} = A \cdot \left(\sqrt{E_i} - \sqrt{E_{th}}\right) \cdot f(\theta) \quad , \tag{5.1}$$

where

$$A = 0.353 \quad ,$$

$$E_{th} = 25.2 \cdot \left(M_t / M_p\right)^{-0.6} + 0.928 \cdot \left(M_t / M_p\right) \quad ,$$

$$f(\theta) = \begin{cases} 1 & (0° < \theta \le 25°) \, , \\ \dfrac{(90-\theta)}{65} - \dfrac{(\theta-25)(\theta-90)}{5000} & (25° < \theta \le 90°) \, . \end{cases}$$

Here, A is the coefficient, E_i is the ion incident energy, E_{th} is the threshold energy, and $f(\theta)$ is the angular dependence. Note that the ion incident angle θ is measured from the surface normal. The etch yield $Y_{Si/Cl+} = Y_{SiCl4}$ depends on the ion incident energy E_i and angle θ on surfaces; in addition, ion-enhanced etching is also assumed to occur on the surfaces unsaturated with the yield $Y'_{Si/Cl+} = (x/4)Y_{SiCl4}$. The sputtering of Si substrate atoms through energetic Cl^+ ion bombardment on unchlorinated surfaces is also assumed to occur in this study, as expressed by

$$Y_{Si} = A \cdot \left(\sqrt{E_i} - \sqrt{E_{th}}\right) \cdot g(\theta) \quad , \tag{5.2}$$

where

$$A = 0.0054 \cdot \left(Z_p Z_t\right)^{0.5} \cdot \sqrt{\left(\frac{M_t}{M_p + M_t}\right)} - 0.0198 \quad ,$$

$$E_{th} = 25.2 \cdot \left(M_t / M_p\right)^{-0.6} + 0.928 \cdot \left(M_t / M_p\right) \quad ,$$

$$g(\theta) = -81.70 \cdot (\cos\theta)^5 + 244.03 \cdot (\cos\theta)^4 - 208.19 \cdot (\cos\theta)^3 + 67.569 \cdot (\cos\theta)^2 - 0.711 \cdot \cos\theta - 0.0242 \quad .$$

The sputter yield $Y_{Si/Cl+} = Y_{Si}$ is taken from the model of Guo *et al.*[20] Here, Z_p denotes the

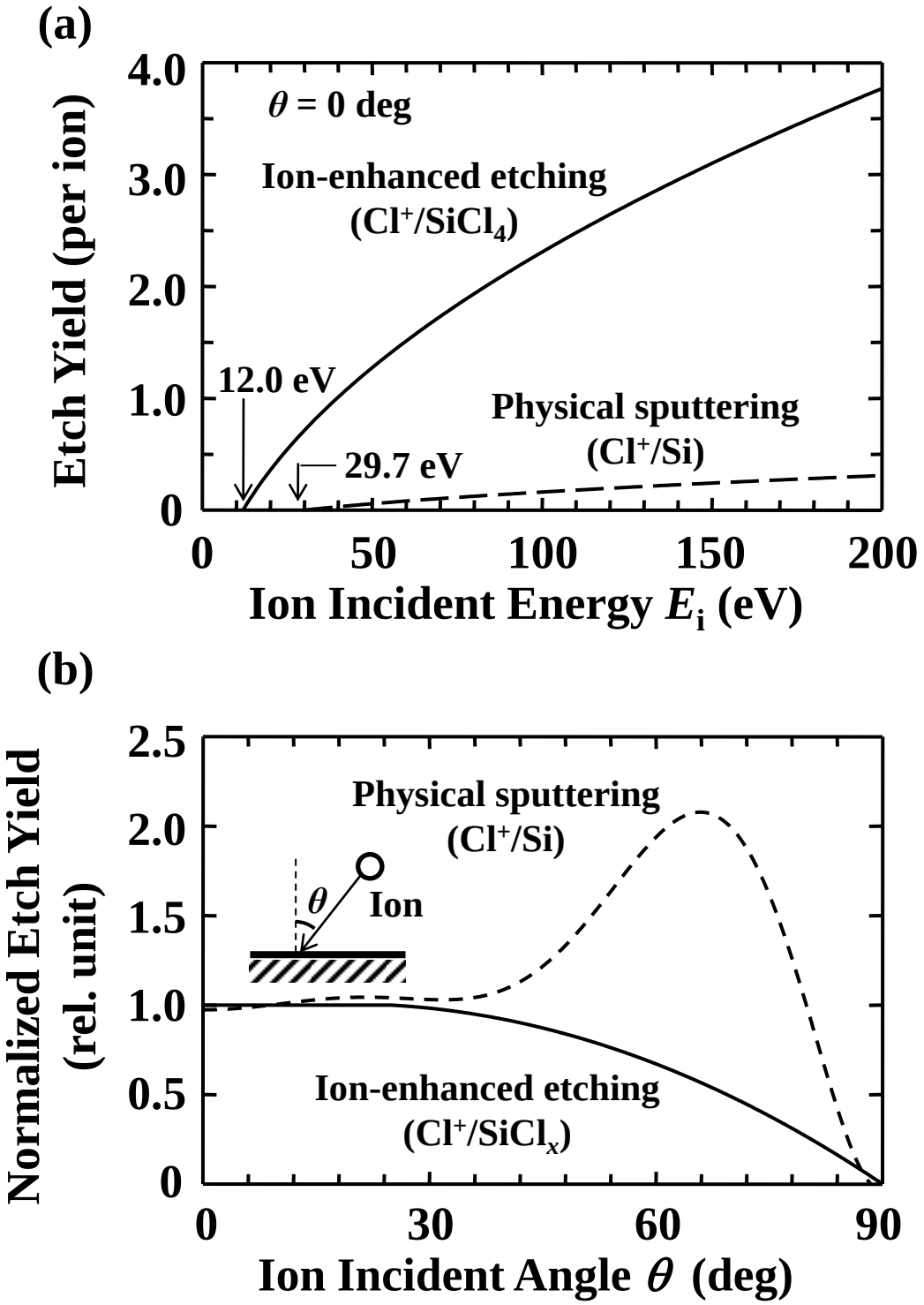

Fig. 5.3. Etch yields for ion-enhanced etching Y_{SiCl4} and physical sputtering Y_{Si} for Cl^+ ions on Si surfaces, as a function of ion incident (a) energy E_i and (b) angle θ, where the incident ion angle θ is measured from the surface normal.

atomic number of the projectile ion, Z_t the atomic number of the target atom, M_p the mass of the projectile ion, and M_t the mass of the target atom. The function $g(\theta)$ is the angular dependence for sputtering. The E_i and θ dependences of Y_{SiCl4} and Y_{Si} are shown in Fig. 5.3, where the respective threshold energies E_{th} = 12.0 and 29.7 eV are taken from the experimental data.[21–25] Moreover, the sticking probability of etch and sputter products $SiCl_x$ (x = 0 ~ 4) desorbed from feature surfaces being etched is assumed to be S_q = 0.05 on saturated as well as unsaturated substrate surfaces, which was determined from a comparison between numerical and experimental etched profiles.[10] It is further noted that to analyze the interactions between energetic incident ions and substrates, such as ion reflection on and penetration into substrates, the ASCeM-3D also takes into account two-body elastic collision processes between incident ions and substrate atoms with the Ziegler-Biersack-Littmark (ZBL) potential for the Si/Cl system,[26,27] as shown in Fig. 5.4.

5.3 Results and Discussion

5.3.1 Evolution of Surface Roughness and Etch Rate

Figure 5.5 shows the time evolution of three-dimensional plots of the location of the outermost Si atoms or substrate cells on etched surfaces during Si etching in Cl_2 plasmas, simulated for incident ion energy E_i = 100 eV, ion temperature kT_i = 0.5 eV, ion flux $\Gamma_i^0 = 1.0 \times 10^{16}$ $cm^{-2}s^{-1}$, and neutral-to-ion flux ratio Γ_n^0/Γ_i^0 = 100. These conditions are typical in low-pressure, high-density plasmas such as electron cyclotron resonance (ECR) and inductively coupled (ICP) plasmas,[5,6] where ion-enhanced etching is assumed to be the dominant mechanism for etching. Numerical results indicate that nanometer-scale convex roughened surface features occur soon after the start of etching, and then the surfaces tend to be roughened with increasing etching or plasma exposure time. This implies that nanometer-scale convex features cause the occurrence of higher surface roughness, by increasing in size with time, and new nanoscale convex features continue to occur on top of the enlarged convex ones during etching, thus resulting in concavo-convex features superimposed on the roughened surface.

Figure 5.6 shows the etch rate (*ER*) and surface roughness parameters (*RMS*, R_p, and R_v) as a function of etching or plasma exposure time, derived from the numerical simulation results in Fig. 5.5. Note that *RMS* is the root mean square roughness, which is calculated from the rms average or standard deviation of the surface feature ordinates from their mean value:

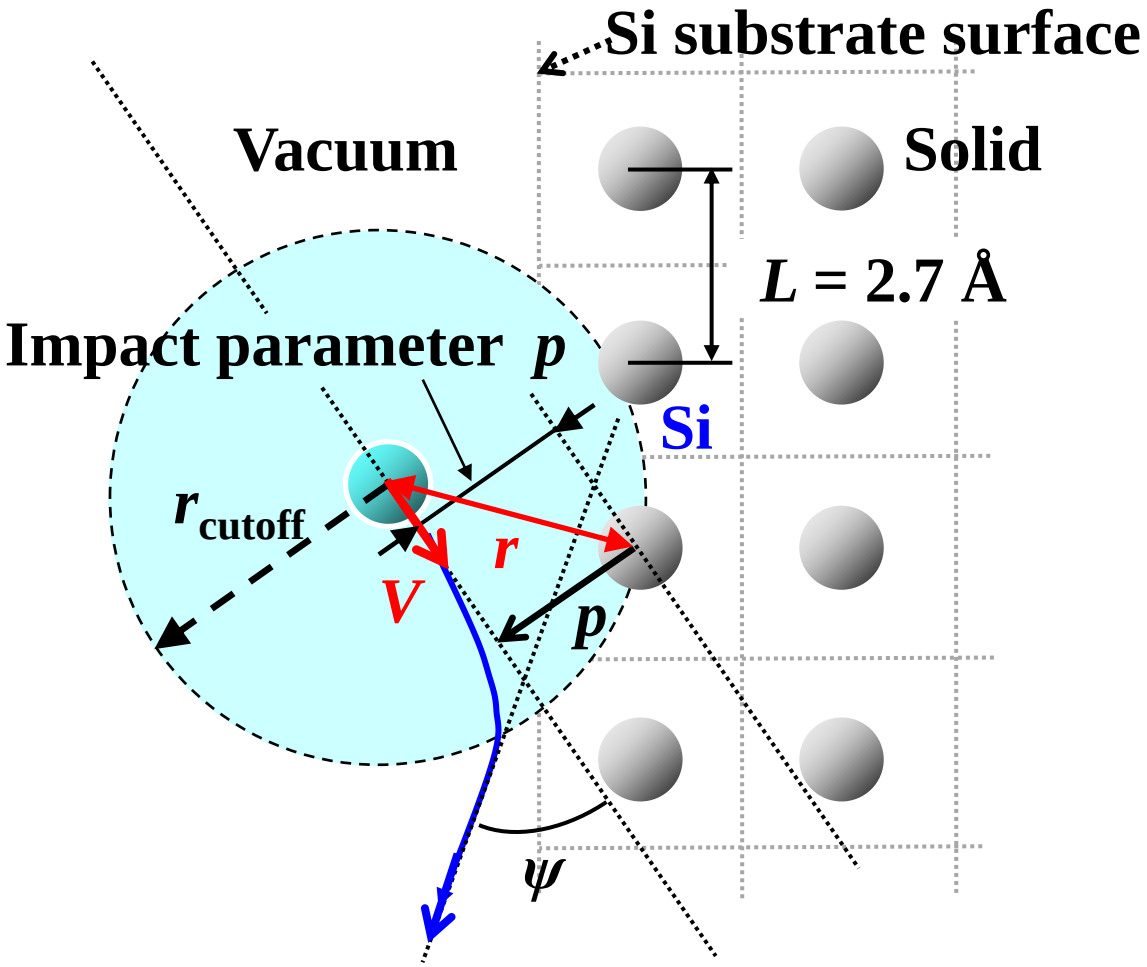

Fig. 5.4. Schematic of two-body elastic collision processes between incident Cl^+ ions and substrate Si atoms. We employed the Ziegler-Biersack-Littmark (ZBL) interatomic potential function for the Si/Cl system in this study.

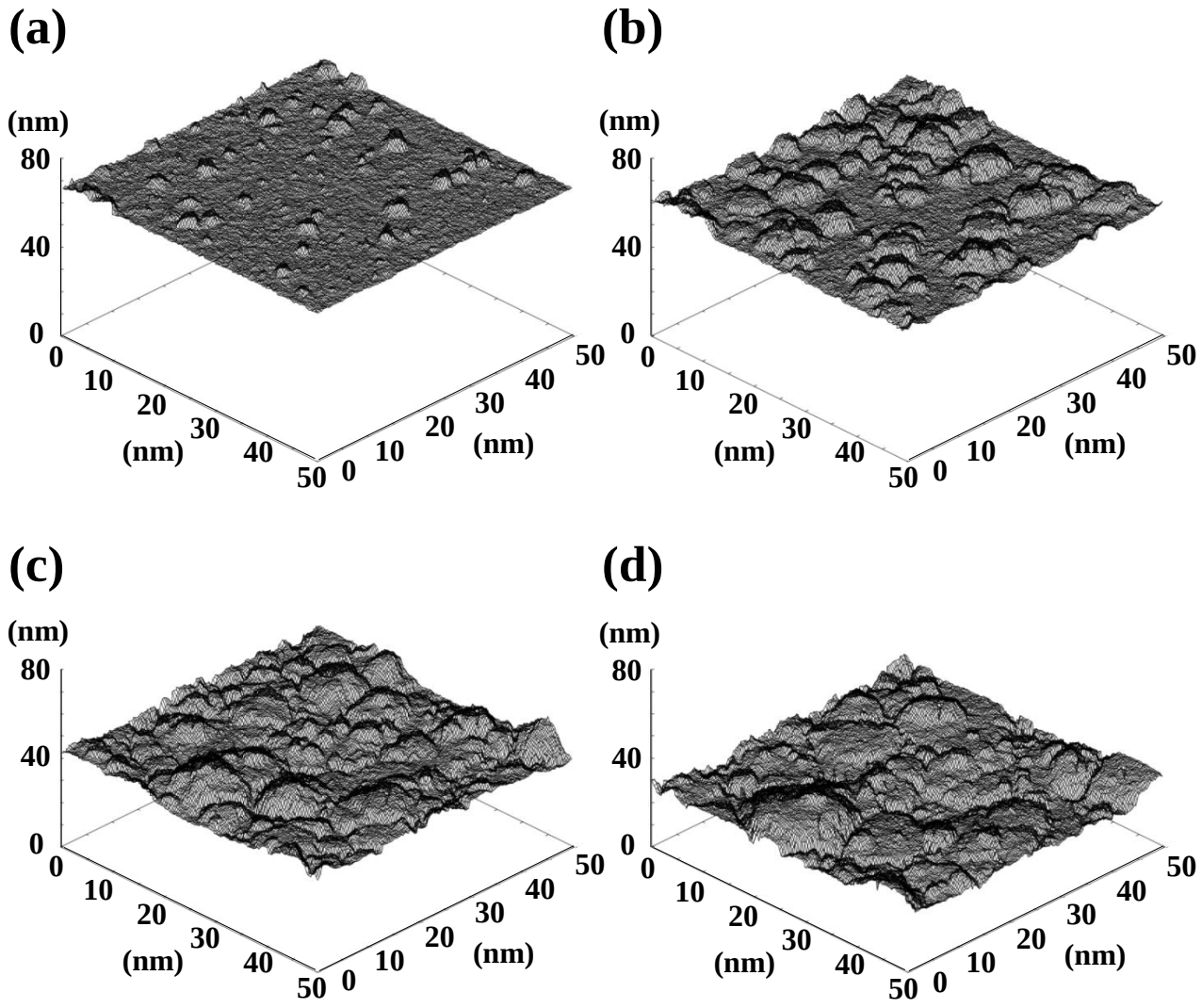

Fig. 5.5. Evolution of three-dimensional plots of the location of the outermost Si atoms or substrate cells on etched surfaces at t = (a) 3, (b) 5, (c) 10, and (d) 15 s after the start of etching during Si etching in Cl_2 plasmas, simulated using ASCeM-3D with incident ion energy E_i = 100 eV, ion temperature kT_i = 0.5 eV, ion flux $\Gamma_i^0 = 1.0 \times 10^{16}$ cm^{-2}s^{-1}, and neutral-to-ion flux ratio $\Gamma_n^0/\Gamma_i^0 = 100$.

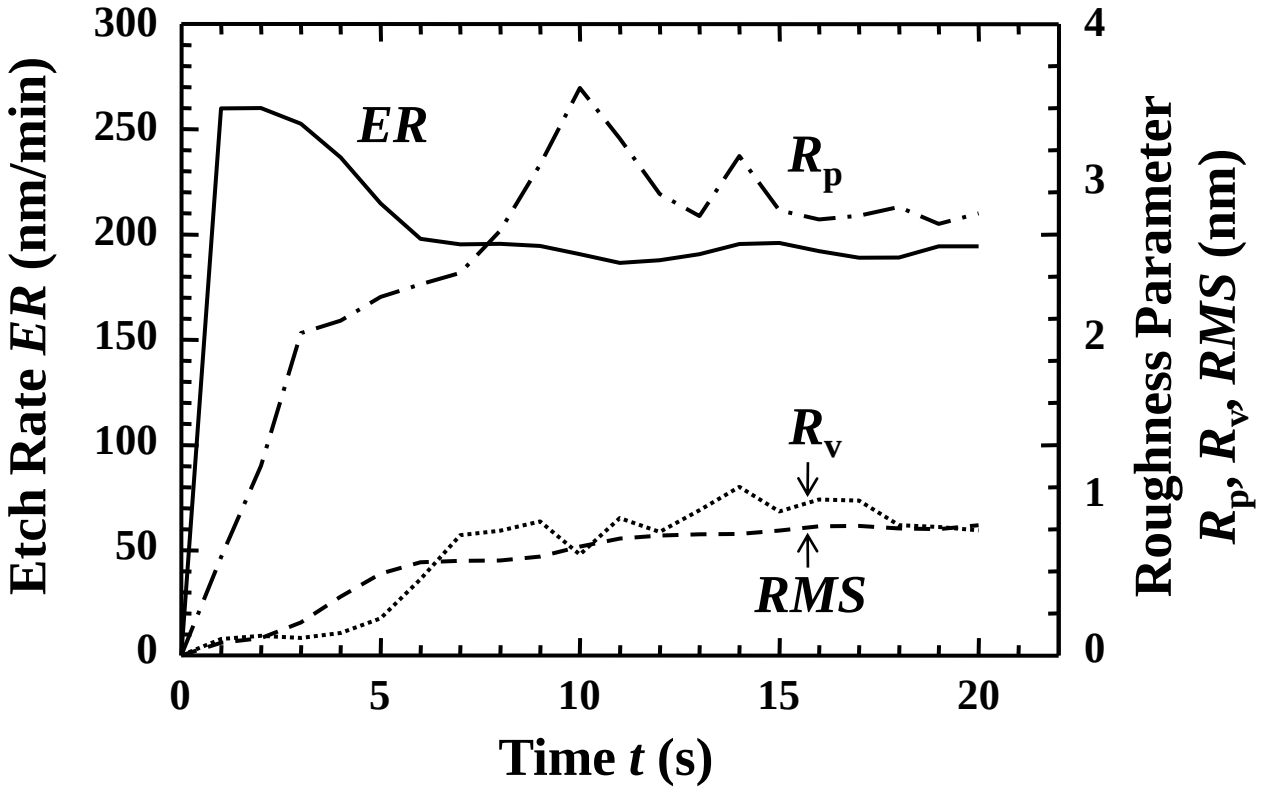

Fig. 5.6. Etch rate (*ER*) and surface roughness parameters (*RMS*, R_p, and R_v) as a function of etching or plasma exposure time, derived from the numerical simulations of Fig. 5.5. Note that *RMS* is the root mean square roughness, R_p is the maximum height of surface features measured from the mean height of etched surfaces, and R_v is the maximum depth of surface features from the mean height, where the mean height of etched surfaces is calculated from the location of the outermost Si atoms or substrate cells.

$$RMS = \sqrt{\frac{1}{N^2}\sum_{i=1}^{N}\sum_{j=1}^{M}\left[z(i,j) - \bar{z}\right]^2} \quad , \tag{5.3}$$

where (i, j) denotes the location of the outermost substrate cells in the (x, y) coordinate, $z(i, j)$ denotes the ordinate at the cell location (i, j), $\bar{z} = \left(1/N^2\right)\sum_{i=1}^{N}\sum_{j=1}^{N} z(i,j)$ is the arithmetic average of the z values within the surface area of 50×50 nm^2 concerned, and $N^2 = 184 \times 184$ is the number of cell locations or data points therein. R_p is the maximum height of surface features measured from the mean height of etched surfaces, and R_v is the maximum depth of surface features from the mean height. Here, the mean height of etched surfaces is calculated from the location of the outermost Si atoms or substrate cells. Here, the average etch rate ER is also calculated from the difference in the average or mean ordinate $\bar{z}$ between before and after etching, divided by the etching time, and is defined by

$$ER = \left(z_0 - \bar{z}\right)/t \quad , \tag{5.4}$$

where z_0 is the average of the ordinate of the initial outermost Si substrate cells before etching. The results indicate that the etch rate increases substantially to $ER \approx 260$ nm/min soon after the start of etching, and then decreases slightly to a constant $ER \approx 190$ nm/min after $t \approx 5$ s. In contrast, the roughness parameters continue to increase until $t \approx 5 - 10$ s, and then remain almost constant.

5.3.2 Evolution of Etch Yield and Ion Incident Angle Distribution

Figure 5.7 shows the etch yield as a function of time, together with that of the stoichiometry of etch products $SiCl_x$ ($x = 0 \sim 4$) desorbed from substrate surfaces, in the etching environments represented in Fig. 5.5. The etch yield increases substantially to $Y_{total} \approx 2.2$ soon after the start of etching, and then decreases slightly to a constant $Y_{total} \approx 1.7$ after $t \approx 5$ s, which is similar to the behavior of the etch rate ER in Fig. 5.6. It should be noted that the yield $Y_{total} \approx 2.2$ is nearly equal to that of Y_{SiCl4} for Cl^+ ions of $E_i = 100$ eV at normal incidence $\theta = 0°$ on saturated or fully chlorinated surfaces of Si, as can be seen in Fig. 5.3(a). This implies that the surfaces tend to be saturated or fully chlorinated soon after the start of etching. It is further noted that a substantial increase of the etch rate soon after the start of etching has been observed experimentally in Ar/XeF_2 plasma etching of polycrystalline silicon (poly-Si).[28)]

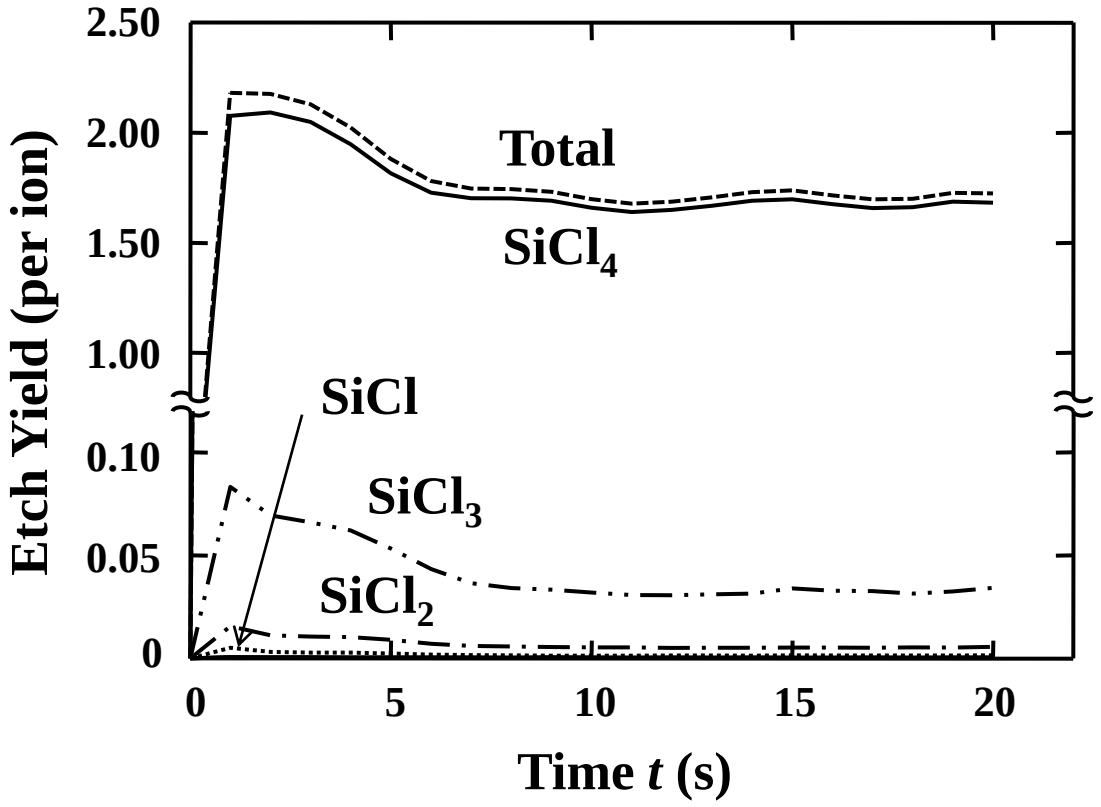

Fig. 5.7. Etch yield as a function of time, together with that of the stoichiometry of etch products $SiCl_x$ ($x = 0 \sim 4$) desorbed from substrate surfaces, in the etching environments of Fig. 5.5.

In the present ASCeM-3D model, more than 95% of desorbed products are $SiCl_4$ at high neutral-to-ion flux ratios, $\Gamma_n^0/\Gamma_i^0 = 100$, as the etch product stoichiometry indicates in Fig. 5.7. This is consistent with numerical and experimental studies that have been reported up to now: Mayer *et al.*[29] presumed $SiCl_4$ to be the end products of Si etching with Cl^+/Cl_2^+ ion beams, on the basis of quadrupole mass spectrometry measurments. Rossen and Sawin[30] identified both $SiCl_2$ and $SiCl_4$ as the primary etch products in Cl_2/Ar^+ beam etching of Si, and also observed that the amount of $SiCl_4$ is enhanced relative to that of $SiCl_2$ as the ion bombardment energy is reduced. Chang *et al.*[31] examined several experimental data and reported that the major product species is assumed to be $SiCl_4$ in Ar^+ ion-enhanced etching of Si with chlorine. Moreover, Humbird and Graves[32] indicated that $SiCl_4$ is the dominant etch product at a high Γ_n^0/Γ_i^0 of approximately 100 for Cl/Ar^+ by molecular dynamics simulation.

Figure 5.8 shows the angular distribution of ion fluxes incident to etched surfaces at different times, t = 0, 1, 3, 4, 5, and 10 s, after the start of etching. The distribution at $t = 0$ corresponds to that of ion fluxes incident on completely flat substrate surfaces, or to the Gaussian-like anisotropic distribution given at the top of the simulation domain. It is further noted that the incident angle θ after the start of etching is measured from the local surface normal on roughened surfaces upon incidence. Soon after the start of etching, the distribution becomes relaxed or broadened substantially with the incident angle of its peak being shifted to larger θ or an increasingly off-normal angle, and then remains almost unchanged with a broad distribution ranging from $\theta = 0$ to 120° after $t \approx 5$ s; this tendency is similar to the behavior of the roughness parameters *RMS*, R_p, and R_v (particularly the behavior of *RMS*) in Fig. 5.6. These imply that the surfaces tend to be roughened with increasing etching time, and the roughness tends to be saturated after several seconds; correspondingly, the angular distribution of ion fluxes incident on roughened surfaces tends to be broadened during etching, because the local surface normal has different directions thereon, and reaches a broad, saturated distribution after several seconds when the surface roughness is saturated. Similarly, the etch rate or yield tends to decrease with time after the surfaces are fully chlorinated, because the etch yield for ion-enhanced etching is lowered for ions of increasingly off-normal angle of incidence [as seen in Fig. 5.3(a)], and attains a constant value when the roughness and, in turn, the ion incident angle distribution is saturated.

5.3.3 Comparison of Numerical and Experimental Results

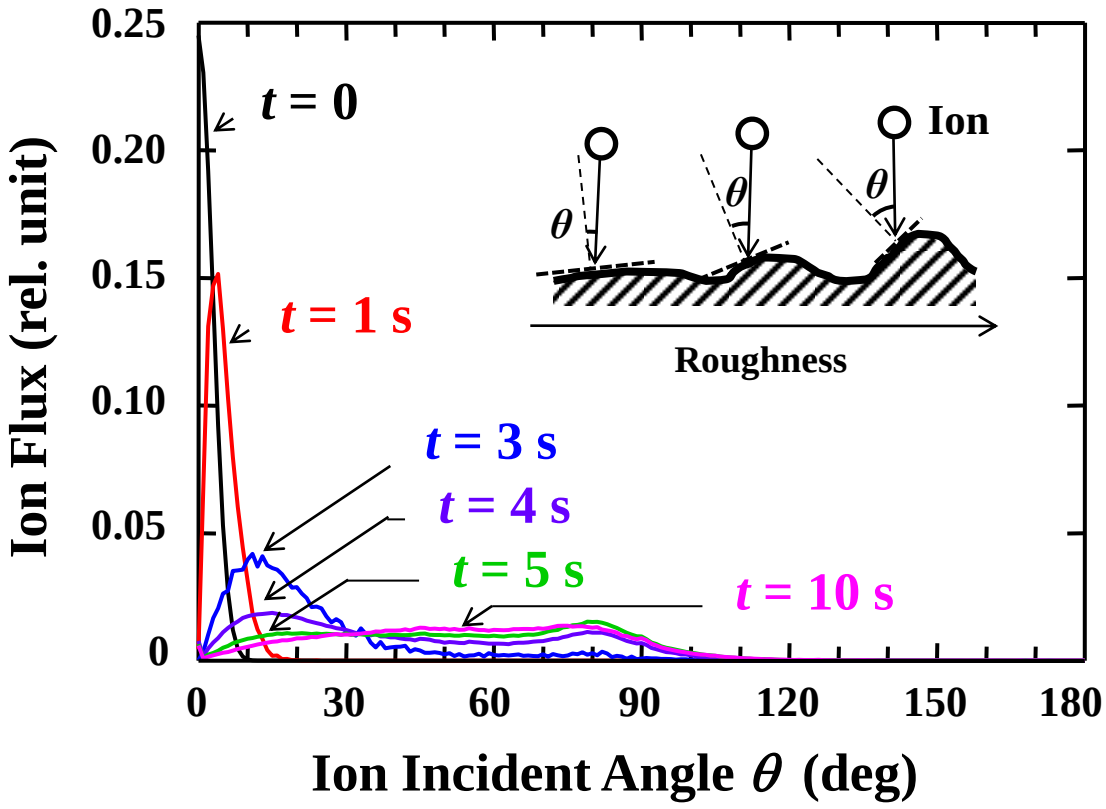

Fig. 5.8. Angular distribution of ion fluxes incident on etched surfaces at t = 0, 1, 3, 4, 5, and 10 s after the start of etching. Note that the distribution at t = 0 corresponds to that of ion fluxes incident on completely flat substrate surfaces, or to the Gaussian-like anisotropic distribution given at the top of the simulation domain, and that the incident angle θ after the start of etching is measured from the local surface normal on roughened surfaces upon incidence.

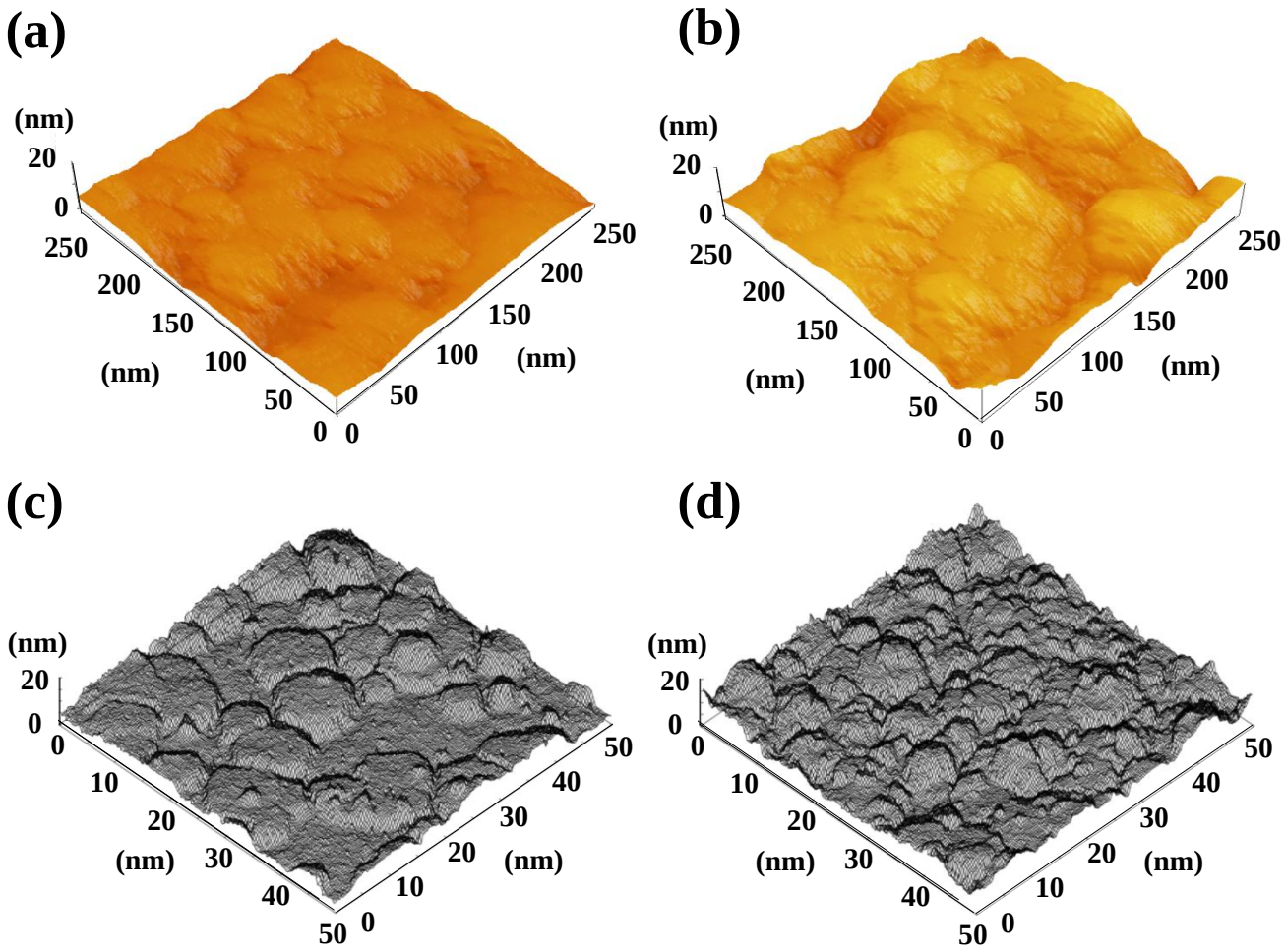

Fig. 5.9. Atomic force microscope (AFM) images of Si surfaces etched in Cl_2 plasmas with different rf bias powers of P_{rf} = (a) 20 and (b) 50 W, where the dc self-bias voltage and the peak-to-peak amplitude of the rf bias voltage at the wafer stage were measured to be V_{dc} = – 71 and – 138 V and V_{pp} = 184 and 344 V at P_{rf} = 20 and 50 W, respectively. Also shown are snapshots of Si surfaces at t = 10 s after the start of etching in Cl_2 plasmas, together with the respective values of *RMS*, R_p, and R_v, numerically simulated with E_i = (c) 75 and (d) 150 eV, where the other input parameters are the same as those in the case of Fig. 3. Roughness parameters are (a) *RMS* = 1.28, R_p = 4.51, and R_v = 5.12 nm, (b) *RMS* = 3.12, R_p = 9.09, and R_v = 11.1 nm, (c) *RMS* = 2.37, R_p = 8.33, and R_v = 2.05 nm, and (d) *RMS* = 2.42, R_p = 8.50, and R_v = 3.36 nm.

A comparison was made of the results of numerical simulation and etching experiments using an inductively coupled plasma (ICP) reactor, where Cl_2 gas was introduced at a flow rate of 20 sccm and a pressure of 20 mTorr. The ICP source power was P_{ICP} = 450 W at 13.56 MHz with different rf bias powers of P_{rf} = 20 and 50 W at 13.56 MHz. Under these conditions, Si(100) samples (*RMS* = 0.113, R_p = 0.643, and R_v = 0.586 nm) were exposed to the plasma for 2 min, where the dc self-bias voltage at the wafer stage, or a measure of the ion incident energy E_i, was measured to be V_{dc} = – 71 V at P_{rf} = 20W and V_{dc} = – 138 V at P_{rf} = 50 W.

Figures 5.9(a) and 5.9(b) show atomic force microscope (AFM) images of the Si surfaces etched in Cl_2 plasmas with P_{RF} = 20 and 50 W. The experiments show that sub-100-nm-scale roughness occurs on surfaces during etching, and the height of roughness tends to be larger at increased P_{rf}. The roughness parameters measured from AFM images are *RMS* = 1.28, R_p = 4.51, and R_v = 5.12 nm at P_{rf} = 20 W, and *RMS* = 3.12, R_p = 9.09, and R_v = 11.1 nm at P_{rf} = 50 W, indicating that the etched surfaces are roughened within a 10 nm scale height.

Figures 5.9(c) and 5.9(d) show snapshots of the Si surfaces at t = 10 s after the start of etching in Cl_2 plasmas, together with the respective values of *RMS*, R_p, and R_v, numerically simulated with E_i = 75 and 150 eV, where the other input parameters are the same as those in the case of Figs. 5.5. The results indicate that a number of 10-nm-scale roughened surfaces tend to occur during Si etching in Cl_2 plasmas, and that the *RMS*, R_p, and R_v simulated depending on E_i are in agreement with those obtained from AFM images. However, the present ASCeM-3D simulation domain is limited to 50 nm square, and hence it would be difficult to reproduce sub-100-nm-scale surface roughness seen in AFM images.

5.4 Conclusions

We have developed a three-dimensional atomic-scale cellular model (ASCeM-3D) and feature profile simulation to reproduce the three-dimensional structure of etched feature surfaces during Si etching in Cl_2 plasmas, together with the evolution of surface roughness soon after the start of etching. Numerical results indicated that nanometer-scale convex roughened surface features occur soon after the start of etching; then, the surfaces tend to be roughened with increasing etching or plasma exposure time, and the surface roughness tends to be saturated after several seconds. In effect, nanometer-scale convex features cause the formation of a higher surface roughness, because they increase in size with increasing time, and new nanoscale convex features continue to occur on top of enlarged convex ones during etching, thus resulting

in concavo-convex features superimposed on the roughened surface.

Moreover, experiments showed that sub-100-nm-scale roughness occurs on surfaces during Si etching in Cl_2 plasmas, and the height of roughness tends to be increased with increasing RF bias power or ion incident energy. The roughness parameters of *RMS*, R_p, and R_v obtained from AFM images are on a 10 nm scale of height, which is in agreement with numerical results, although the present ASCeM-3D reproduces only 10-nm-scale roughened surfaces owing to the limited scale of the simulation domain. Thus, it is concluded that the ASCeM-3D model would be useful for predicting and analyzing the nanometer-scale surface roughness that occurs during plasma etching.

References

1) H. Abe, M. Yoneda, and N. Fujiwara: Jpn. J. Appl. Phys. **47** (2008) 1435.
2) E. Pargon, M. Darnon, O. Joubert, T. Chevolleau, L. Vallier, L. Mollard, and T. Lill: J. Vac. Sci. Technol. B **23** (2005) 1913.
3) E. Pargon, M. Martin, J. Thiault, O. Joubert, J. Foucher, and T. Lill: J. Vac. Sci. Technol. B **26** (2008) 1011.
4) W. Guo and H. H. Sawin: J. Appl. Phys. D **42** (2009) 194014.
5) M. Tuda, K. Ono, and K. Nishikawa: J. Vac. Sci. Technol. B **14** (1996) 3291.
6) M. Tuda, K. Nishikawa, and K. Ono: J. Appl. Phys. **81** (1997) 960.
7) M. A. Vyvoda, M. Li, D. G. Graves, H. Lee, M. V. Malyshev, F. P. Klemens, J. T. C. Lee, and V. M. Donnelly: J. Vac. Sci. Technol. B **18** (2000) 820.
8) H. H. Hwang, M. Meyyappan, G. S. Mathad, and R. Ranade: J. Vac. Sci. Technol. B **20** (2002) 2199.
9) Y. Osano and K. Ono: Jpn. J. Appl. Phys. **44** (2005) 8650.
10) Y. Osano, M. Mori, N. Itabashi, K. Takahashi, K. Eriguchi, and K. Ono: Jpn. J. Appl. Phys. **45** (2006) 8157.
11) Y. Osano and K. Ono: J. Vac. Sci. Technol. B **26** (2008) 1425.
12) H. Tsuda, M. Mori, Y. Takao, K. Eriguchi, and K. Ono: Thin Solid Films **518** (2010) 3475.
13) H. Tsuda, M. Mori. Y. Takao, K. Eriguchi, and K. Ono: Jpn. J. Appl. Phys. **49** (2010) 08JE01.
14) K. Ono, H. Ohta, and K. Eriguchi: Thin Solid Films **518** (2010) 3461.
15) K. Ono, H. Ohta, and K. Eriguchi: Plasma Kakuyugo Gakkaishi **85** (2009) 163 [in Japanese].
16) R. A. Gottsho: J. Vac. Sci. Technol. B **11** (1993) 1884.
17) A. P. Mahorowala and H. H. Sawin: J. Vac. Sci. Technol. B **20** (2002) 1064.
18) E. A. Ogryzlo, D. E. Ibbotson, D. L. Flamm, and J. A. Mucha: J. Appl. Phys. **67** (1990) 3115.
19) W. Guo and H. H. Sawin: J. Vac. Sci. Technol. A **27** (2009) 1326.
20) W. Guo, B. Bai, and H. H. Sawin: J. Vac. Sci. Technol. A **27** (2009) 388.
21) W. Jin, S. A. Vitale, and H. H. Sawin: J. Vac. Sci. Technol. A **20** (2002) 2106.
22) J. P. Chang and H. H. Sawin: J. Vac. Sci. Technol. B **19** (2001) 1319.
23) K. Wittmaack: Phys. Rev. B **68** (2003) 235211.

24) J. Bohdansky, J. Roth, and H. L. Bay: J. Appl. Phys. **51** (1980) 2861.

25) H. L. Bay, J. Roth, and J. Bohdansky: J. Appl. Phys. **48** (1977) 4722.

26) J. F. Ziegler, J. Biersack, and U. Littmark: *The Stopping and Range of Ions in Matter* (Pergamon, New York, 1985).

27) J. F. Ziegler, J. P. Biersack, and M. D. Ziegler: *SRIM – The Stopping and Range of Ions in Matter* (SRIM, Chester, MD, 2008).

28) J. W. Coburn and H. F. Winters: J. Appl. Phys. **50** (1979) 3189.

29) T. M. Mayer, R. A. Barker, and L. J. Whitman: J. Vac. Sci. Technol. 18 (1981) 349.

30) R. A. Rossen and H. H. Sawin: J. Vac. Sci. Technol. A **5** (1987) 1595.

31) J. P. Chang, J. C. Arnold, G. C. H. Zau, H. S. Shin, and H. H. Sawin: J. Vac. Sci. Technol. A **15** (1997) 1853.

32) D. Humbird and D. B. Graves: J. Vac. Sci. Technol. A **23** (2005) 31.

Chapter 6
Modeling and Simulation of Nanoscale Surface Rippling

6.1 Introduction

As the dimensions of ultra-large-scale integrated (ULSI) circuit devices are scaled down, increasingly strict requirements are imposed on plasma etching technology, including the control or suppression of atomic-scale surface roughness on etched features. In the gate etch process, the surface roughness at the feature bottom affects the uniformity of bottom surfaces, which in turn leads to a recess and thus damage to transistors in gate fabrication; furthermore, the roughness of sidewalls causes the line edge roughness (LER) and line width roughness (LWR), which affect the gate or channel length and thus the transistor performance.[1)] Moreover, in advanced three-dimensional (3D) device structures such as fin-type field-effect transistors (FinFETs),[2,3)] the effects of the fin as well as the gate LER and LWR become significant,[4)] because LER and LWR occur also in the fin etch process,[5,6)] and the conducting channel of FinFETs is formed on the top and sidewall surfaces of the fin. However, the feature profiles are too small and/or too complex to measure the roughness on the top, bottom, and sidewall surfaces of the etched features; in addition, the formation of surface roughness is stochastic as well as 3D, being affected by a number of factors during processing including plasma etching. Therefore, modeling and simulation of the roughness formation during etching is becoming increasingly important for the fabrication of next-generation nanoscale devices,[7)] to predict the atomic-scale roughness on etched feature surfaces, and to gain a better understanding of the mechanisms underlying the phenomena observed.

Several numerical models or methods, such as the string model,[8–10)] ray-tracing model, [11)] cell removal model,[12–15)] level-set method,[16)] and molecular dynamics,[17,18)] have been developed to date, to analyze plasma-surface interactions and feature profile evolution during etching. However, there is still no definite method to analyze or reproduce the atomic- or nanometer-scale surface roughness formed during plasma etching. We have developed a Monte Carlo-based etching profile simulation with a semi-empirical cell removal model (called an atomic-scale cellular model, or ASCeM):[19–25)] a two-dimensional ASCeM (ASCeM-2D) reproduced the evolution of feature profile anomalies on the nanometer scale, including bowing, tapering, microtrenching, reactive ion etching (RIE) lag, inverse RIE lag, and micropillars, during Si trench etching in Cl_2 and Cl_2/O_2 plasmas.[19–25)] Moreover, a 3D ASCeM

(ASCeM-3D) has recently been developed to simulate the evolution of 3D feature profiles, including the nanometer-scale surface roughness, during Si etching in Cl_2 plasma with normal ion incidence onto planar substrates.[26] In this study, we present the ASCeM-3D simulation of the evolution of nanoscale surface features and roughness during Cl_2 plasma etching of Si with oblique ion incidence onto planar substrates, which corresponds to the situations that would occur on feature sidewalls. Emphasis is placed on the evolution of surface roughness and ripple structures that occur depending on the ion incident angle, which could not be reproduced by the ASCeM-2D and other conventional profile simulation models. In practice, the formation mechanisms for such surface ripples would be responsible for the formation of LER and LWR on feature sidewalls during etching for pattern definition.

6.2 Modeling and Simulation

Figure 6.1 shows a schematic of the ASCeM-3D for Si etching in Cl_2 plasma, together with the coordinate system (x, y, z) presently employed. The basic ASCeM-3D methodology and surface models have been described in a previous paper.[26] Briefly, the simulation domain is a square 50 nm on a side with a depth of 630 nm, which is divided into a number of small cubic cells of atomic size $L = \rho_{Si}^{-1/3} = 2.7$ Å, where $\rho_{Si} = 5.0 \times 10^{22}$ cm^{-3} is the atomic density of Si substrates, and Si atoms are allocated in the cells of substrates. In practice, the simulation domain consists of $184 \times 184 \times 2318$ atomic-scale cells (about 7.8×10^7 cells in total), and the substrates initially occupy a lower 620-nm-deep layer therein (or the substrate surfaces are initially flat, being located 10 nm downward from the top of the domain). In the calculation, energetic ions (Cl^+) and neutral reactants (Cl) are randomly allocated at the top of the simulation domain, being successively injected therefrom onto substrates with given energies, angular distributions, and fluxes; concretely, the incoming ions are taken to have a Gaussian-like anisotropic angular distribution around the incident angle θ_i,[19,20,27] while neutrals have an isotropic distribution. Moreover, etch and/or sputter products ($SiCl_x$) are taken to be desorbed from feature surfaces being etched, thermally or isotropically, with a so-called cosine distribution. The cells are assumed to be rigid, and Si atoms are removed from the outermost surface cells (or the outermost cells become empty) where the etching/sputtering causes the desorption of etch/sputter products; in contrast, Si atoms are newly allocated at the cells where the deposition of etch/sputter products occurs.

The transport of ions and neutrals in microstructures is analyzed using the 3D Monte Carlo

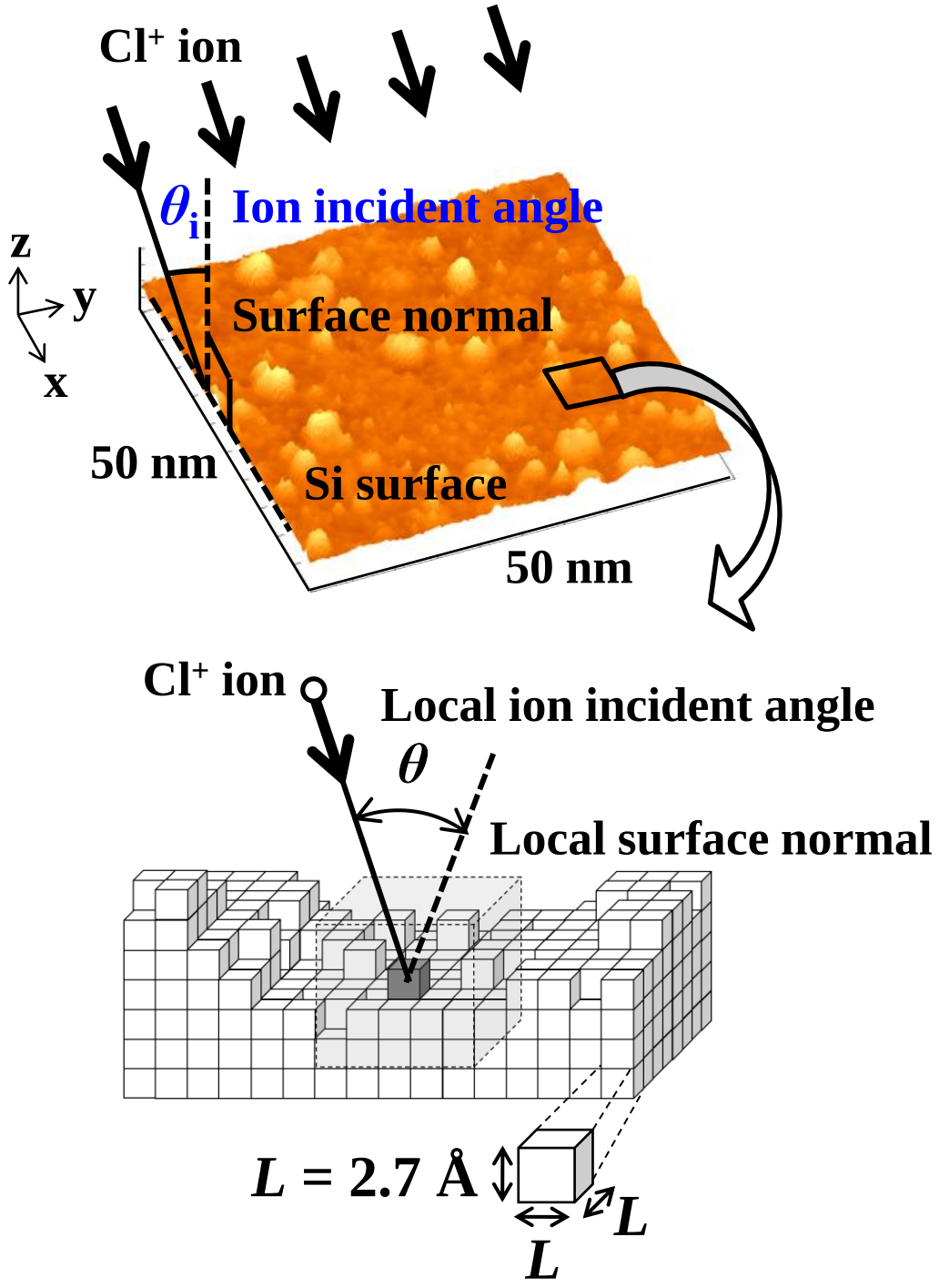

Fig. 6.1. Schematic of the ASCeM-3D and feature profile simulation, together with the coordinate system (x, y, z) presently employed. In the model, the local surface normal is calculated by the extended four-point technique for $5 \times 5 \times 5$ neighboring cells (125 cells in total) around the substrate surface cell that the ion reaches.

(MC) algorithm with periodical boundaries in the horizontal direction, based on single-particle trajectories with three velocity components (3-d/3-v). The transport is calculated at every movement of step L without collision with other particles therein, and the particle is assumed to reach the surface if there is a Si atom at any of the 26 cells neighboring the cell concerned. The local surface normal, and thus the local angle θ of incidence, is calculated by using the extended four-point technique[13] for $5 \times 5 \times 5$ neighboring cells (125 cells in total) around the substrate surface cell that the ion reaches, as shown in Fig. 1, which is the key procedure in the ASCeM-3D simulation. Feature surfaces are taken to be charge neutral during etching, because of the Auger process for energetic ions incident on surfaces.

The ASCeM-3D takes into account surface chemistries based on the MC algorithm,[26] presently including adsorption and reemission of neutrals,[20] chemical etching,[28] ion-enhanced etching,[29] physical sputtering,[14,30–34] and redeposition of etch and/or sputter products on feature surfaces.[20] The sticking probability of Cl neutrals was assumed to be $S_n = 1$ on unsaturated Si surfaces. The yield Y_{SiCl4} for ion-assisted etching through Cl^+ ions incident on saturated Si surfaces and the yield Y_{Si} for physical sputtering through Cl^+ on blank Si were taken from the empirical models, as shown in Figs. 6.2(a) and 6.2(b),[14,29,30] depending on the ion incident energy E_i and angle θ, where the incident angle θ is measured from the surface normal. The etch yield on unsaturated surfaces (x = 1–3) was assumed to be $Y_{SiClx} = (x/4)Y_{SiCl4}$. Moreover, two-body elastic collisions between incident ions and substrate atoms were taken into account to analyze the ion reflection from feature surfaces on incidence and penetration into substrates,[35,36] according to the MC calculation of ion trajectories based on the momentum and energy conservation through successive collisions. The interaction potential for Cl–Si employed was the Ziegler-Biersack-Littmark (ZBL) type.[37,38]

It is further noted that as this study considered the etching with a wafer stage being water-cooled, the substrate temperature was taken to be $T_s = 320$ K, and the sticking probability of etch and sputter products $SiCl_x$ (x = 0–4) desorbed from feature surfaces being etched was assumed to be constant at $S_q = 0.05$ on saturated as well as unsaturated substrate surfaces of Si.[20] The dopant concentration in substrates was taken to be $N_e = 1 \times 10^{18}$ cm^{-3}. In addition, the deposition of etch/sputter by-products coming from the plasma was not taken into account in this study, although the redeposition of etch/sputter products was assumed to come directly from feature surfaces. Surface migration of adsorbed neutrals, which would tend to smooth surfaces at higher temperatures, was also not taken into account in this study.

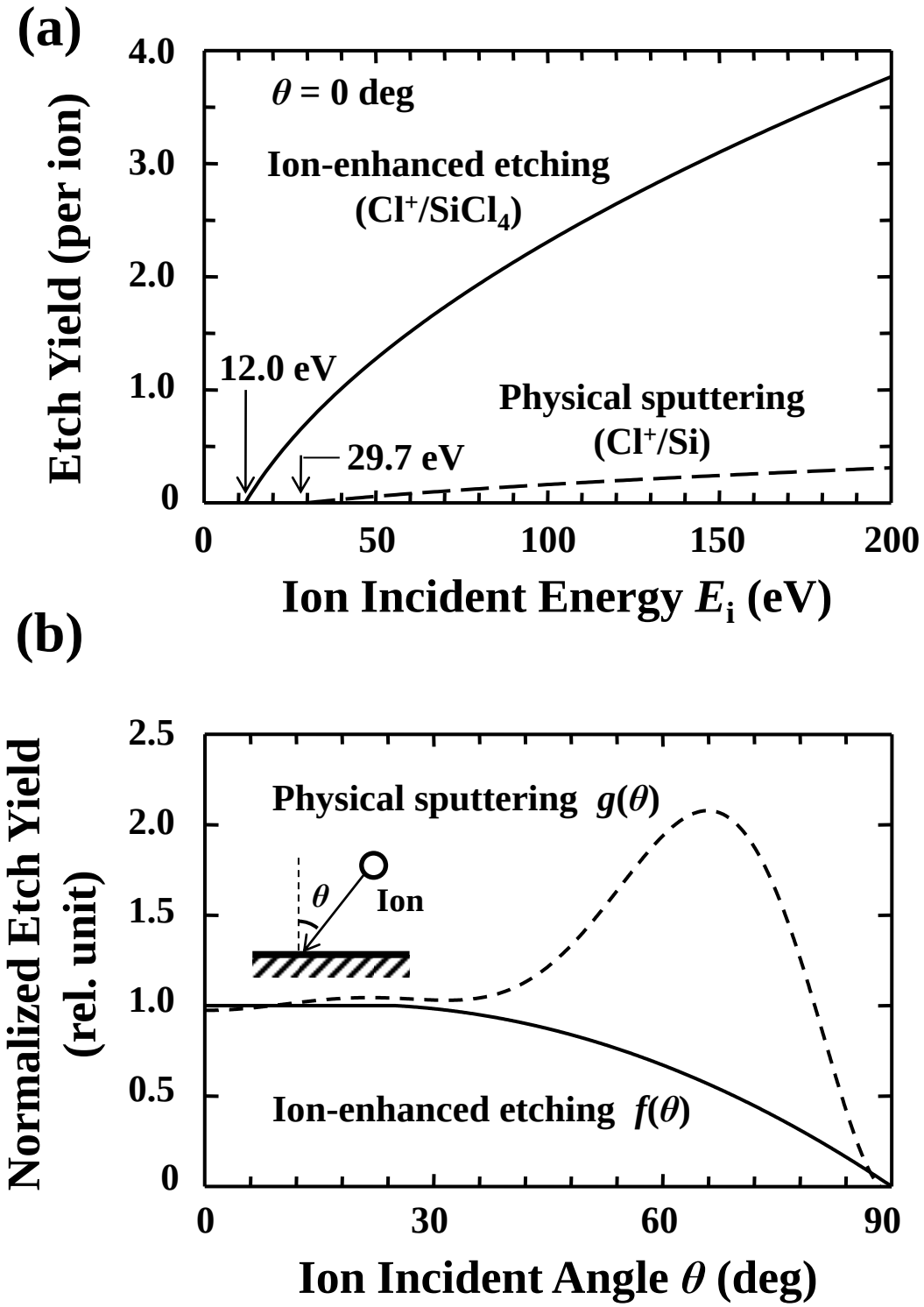

Fig. 6.2. Yield for ion-enhanced etching Y_{SiCl4} through Cl^+ ions incident on saturated Si surfaces and that for physical sputtering Y_{Si} through Cl^+ ions on blank Si surfaces, as a function of ion incident (a) energy E_i and (b) angle θ. These were employed in the ASCeM-3D with θ being the local angle θ of incidence measured from the local surface normal.

We simulated the evolution of surface features during t = 120 s after the start of etching, for different ion incident angles from θ_i = 0 to 85°, with an incident ion energy E_i = 100 eV, ion temperature kT_i = 0.5 eV, ion flux $\Gamma_i^0 = 1.0 \times 10^{16}$ cm^{-2} s^{-1}, neutral-to-ion flux ratio $\Gamma_n^0/\Gamma_i^0 = 100$, and neutral or gas temperature T_g = 500 K. These conditions are typical in low-pressure, high-density plasmas such as electron cyclotron resonance (ECR) and inductively coupled (ICP) plasmas,[8,9] where ion-enhanced etching is assumed to be the dominant mechanism for etching.

6.3 Results and Discussion

6.3.1 Comparison between Numerical and Experimental Results

Figure 6.3(a) shows a snapshot of the outermost surface features of Si (or a 3D plot of the location of the outermost Si substrate cells on etched surfaces) at t = 60 s after the start of etching in Cl_2 plasma, simulated for an ion incident angle θ_i = 0° or normal ion incidence. Numerical results indicate that nanometer-scale roughened features on the order of a few tens of nm occur randomly on surfaces during etching. To quantify the surface roughness, we introduce the root mean square (rms) surface roughness *RMS*, which is calculated from the rms average or standard deviation of the surface feature ordinates from their mean value:

$$RMS = \sqrt{\frac{1}{N^2}\sum_{i=1}^{N}\sum_{j=1}^{N}[z(i,j) - \bar{z}]^2} \ ,$$

where (i, j) denotes the location of the outermost substrate cells in the (x, y) coordinate, $z(i, j)$ denotes the ordinate at the cell location (i, j), $\bar{z} = (1/N^2)\sum_{i=1}^{N}\sum_{j=1}^{N} z(i,j)$ is the arithmetic average of the z values within the surface area of 50 × 50 nm^2 concerned, and N^2 = 185 × 185 is the number of cell locations or data points therein. Here, the average etch rate *ER* is also calculated from the difference in the average or mean ordinate $\bar{z}$ between before and after etching, divided by the etching time. The 3D contour of Fig. 6.3(a) gives *RMS* = 1.09 nm and *ER* = 280 nm/min. It should be noted that as surface smoothing mechanisms such as the surface migration of neutrals are not assumed in this study, the surface roughening tends to be caused primarily by locally different etch and/or sputter yields on surfaces, which would originate from locally different angles and fluxes of incident ions and neutrals thereon.

A comparison was made between numerical and experimental results, where the etching experiments employed an ICP plasma reactor with a Cl_2 gas flow rate of 20 sccm, a gas pressure of 20 mTorr, an ICP source power of P_{ICP} = 450 W at 13.56 MHz, and an rf bias power of P_{rf} = 0–100 W at 13.56 MHz. Under these conditions, 4-in.-diameter Si(100) samples (*RMS* = 0.11

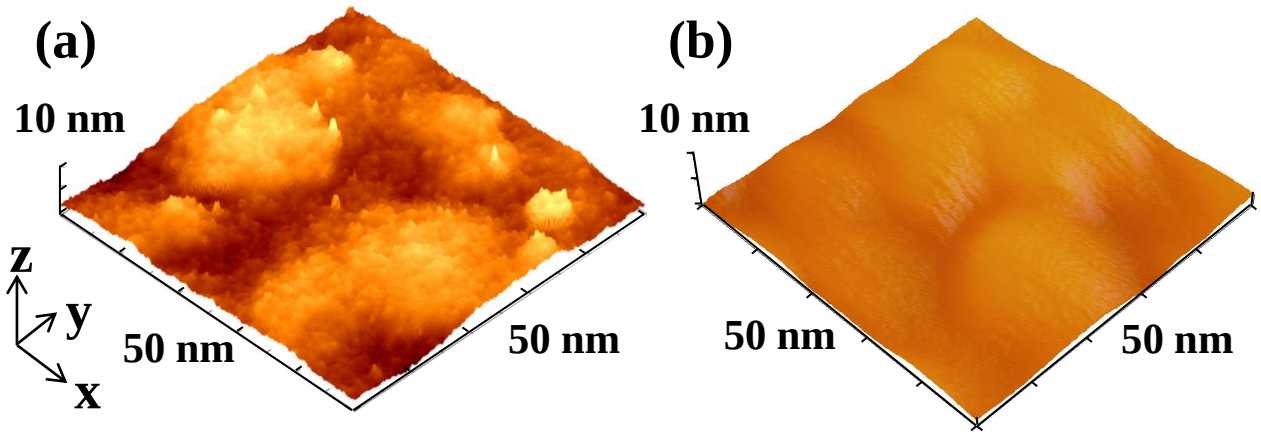

Fig. 6.3. Comparison between ASCeM-3D simulations and inductively coupled plasma (ICP) etching experiments for Si etching in Cl_2 plasmas. (a) A snapshot of the outermost surface features of Si at t = 60 s after the start of etching, simulated for an ion incident angle $\theta_i = 0°$ or normal ion incidence with an incident ion energy E_i = 100 eV, ion temperature kT_i = 0.5 eV, ion flux $\Gamma_i^0 = 1.0 \times 10^{16}$ cm^{-2} s^{-1}, and neutral-to-ion flux ratio $\Gamma_n^0/\Gamma_i^0 = 100$. The average etch rate and rms surface roughness were calculated as ER = 280 nm/min and RMS = 1.09 nm, respectively. (b) An AFM image of the Si surfaces etched in Cl_2 plasma, with a Cl_2 flow rate of 20 sccm, a gas pressure of 20 mTorr, an ICP source power of P_{ICP} = 450 W at 13.56 MHz, and an rf bias power of P_{rf} = 20 W at 13.56 MHz. Under these conditions, 4-in.-diameter Si(100) samples (RMS = 0.11 nm) were exposed to the plasma for 120 s, giving ER = 290 nm/min and RMS = 1.28 nm; in addition, the incident ion energy was measured to be $E_i = V_p - V_{dc}$ = 89 V, from the dc self-bias voltage V_{dc} at the wafer stage and the plasma potential V_p.

nm) were exposed to the plasma for 120 s, where the dc self-bias voltage V_{dc} at the wafer stage was measured using a voltage probe and the plasma potential V_p was measured using a cylindrical Langmuir probe. Figure 6.3(b) shows an atomic force microscopy (AFM) image of the Si surfaces etched in Cl_2 plasma with P_{rf} = 20 W, exhibiting several-10-nm-scale roughened features, where V_{dc} = –71 V and V_p = 18 V gave a measure of the incident ion energy as $E_i = V_p - V_{dc}$ = 89 V. The roughness parameter measured from the AFM image was *RMS* = 1.28 nm, and the etch rate was measured to be *ER* = 290 nm/min by stylus profilometry, which are in agreement with the numerical results.

6.3.2 Evolution of Surface Roughness and Ripple Structures

Figures 6.4 show the time evolution of surface features of Si during etching in Cl_2 plasma, simulated for different ion incident angles of θ_i = 0, 15, 45, 60, and 75°. The surface features shown are those at *t* = 5, 10, 15, 20, 30, and 60 s after the start of etching, exhibiting that as the angle θ_i is increased, the evolution of surface features and roughness drastically change, and ripple structures occur on etched surfaces. For θ_i = 0° or normal ion incidence, small concavo-convex features are formed randomly on surfaces by incident ions soon after the start of etching, and then large concavo-convex features are formed on etched surfaces. In contrast, for increased θ_i = 45° or oblique ion incidence, small concavo-convex features after the start of etching tend to merge with each other, and then ripple structures are formed on etched surfaces perpendicular to the direction of ion incidence. For further increased θ_i = 75°, small ripple structures or slit-like grooves are formed on surfaces parallel to the direction of ion incidence soon after the start of etching, and then some slit-like grooves tend to enlarge with time on etched surfaces.

The formation of such nanoscale ripple structures on Si by off-normal or oblique incident ions has attracted much attention in recent noble-gas ion-beam experiments (Ne^+, Ar^+, Kr^+, and Xe^+ ion beams of several hundred eV to a few tens of keV),[39–43] from the viewpoint of the fabrication of well-organized nanostructures. A transition from randomly roughened to regularly rippled surface structures and a transition of the ripples from perpendicular to parallel to the direction of ion incidence, which occur depending on ion incident angle, have also attracted attention in theoretical studies,[41,42,44–46] from the viewpoint of a fundamental interest in beam-surface interactions. In plasma environments, oblique incidence of ions occurs on feature sidewalls during etching, and so the formation mechanisms for such surface ripples

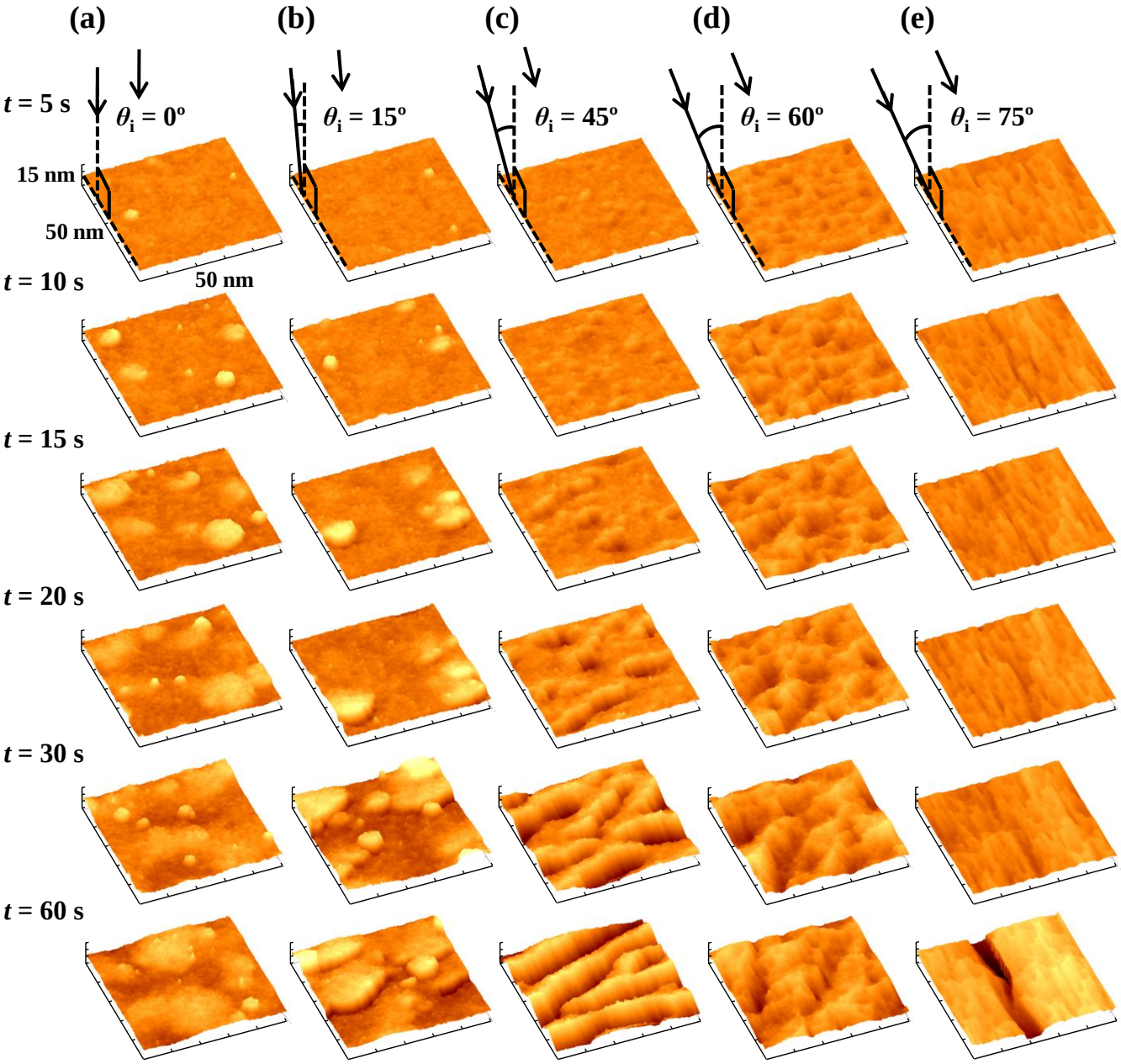

Fig. 6.4. Time evolution of surface features of Si during etching in Cl_2 plasma, simulated for different ion incident angles of θ_i = (a) 0, (b) 15, (c) 45, (d) 60, and (e) 75° under the same calculation conditions of Fig. 6.3.

would be responsible for LER and LWR formed thereon. However, it is difficult to carry out experiments to elucidate the effects of oblique ion incidence in plasma etching environments; in effect, the feature profiles are too small and/or too complex for nanoscale devices to diagnose plasma-surface interactions on patterned feature surfaces during etching. The experiments using planar substrates are also difficult, because the ion incidence is usually normal to substrate surfaces after being accelerated through the sheath on substrates immersed in plasma. Therefore, numerical approaches become important to predict the evolution of feature profiles and surface roughness during plasma etching for nanoscale pattern definition.

Figures 6.5 show the average etch rate *ER* and rms surface roughness *RMS* as a function of etching time *t* for different ion incident angles θ_i, derived from the simulations of Fig. 6.4. The *ER* exhibits a substantial increase immediately after the start of etching, and then maintains an almost constant value during etching; in practice, the steady-state *ER* ≈ 280 nm/s for θ_i = 0°, decreasing with increasing θ_i. On the other hand, the *RMS* exhibits a markedly different behavior: *RMS* increases gradually with time, and then tends to reach a steady state after about *t* = 40–60 s for $\theta_i \leq 60°$, while it continues to increase with time for θ_i = 75 and 80°. For further increased $\theta_i \geq 85°$, the surface roughness is reduced significantly, and the *RMS* value remains small.

Figures 6.6 show the average etch rate *ER* and rms surface roughness *RMS* at a steady state (*t* = 50 s) as a function of ion incident angles θ_i, derived from the data of Figs. 6.5. It is noted that for θ_i = 75–80°, the *RMS* increases with time during the simulation, and so the *RMS* data shown are those at around the end of the simulation (*t* = 120 s), which are over 5 nm owing in part to enlarged slit-like grooves, as seen in Figs. 6.4. The *ER* is maximum at θ_i = 0° or normal ion incidence, decreasing with increasing θ_i, which is similar to the angular dependence of the yield Y_{SiCl4} for ion-enhanced etching, as shown in Fig. 6.2(b). This implies that the ion-enhanced etching dominates Si etching in Cl_2 plasma under high Γ_n^0/Γ_i^0 = 100 conditions in this study. In contrast, the *RMS* exhibits a significant peak at $\theta_i \approx$ 75–80° or highly oblique ion incidence and a slight peak at $\theta_i \approx$ 30°, which is similar in some way to the angular dependence of the yield Y_{Si} for physical sputtering in Fig. 6.2(b). A similar angular dependence of the *RMS* or ripple wavelength (a substantial increase at highly oblique θ_i) has been observed in beam experiments[39,40] and theoretical studies.[44] This suggests that physical sputtering is responsible to some extent for the formation of surface roughness and ripples during plasma etching.

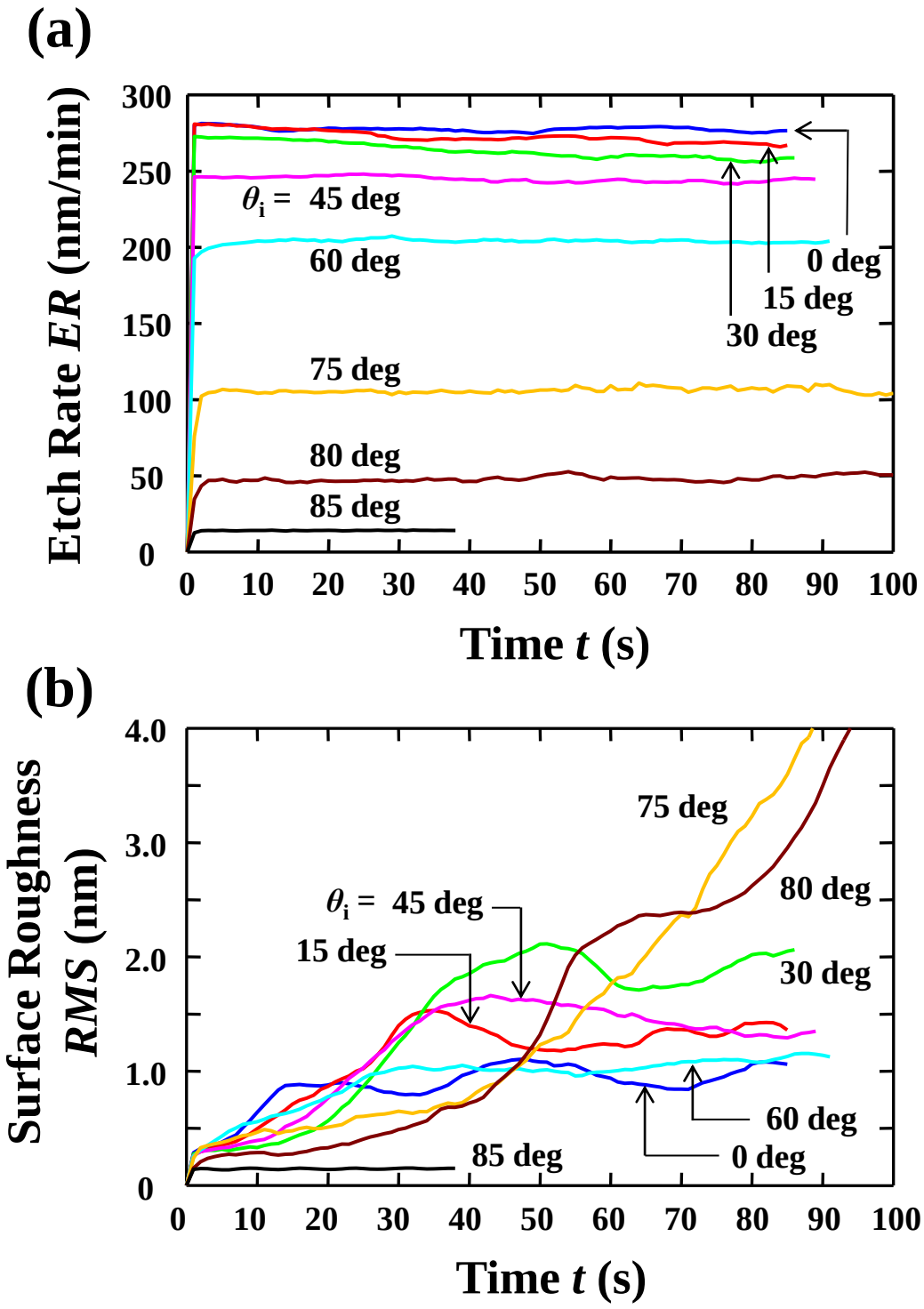

Fig. 6.5. (a) Average etch rate *ER* and (b) rms surface roughness *RMS* as a function of etching or plasma exposure time *t* for different ion incident angles θ_i, derived from the simulations of Fig. 6.4.

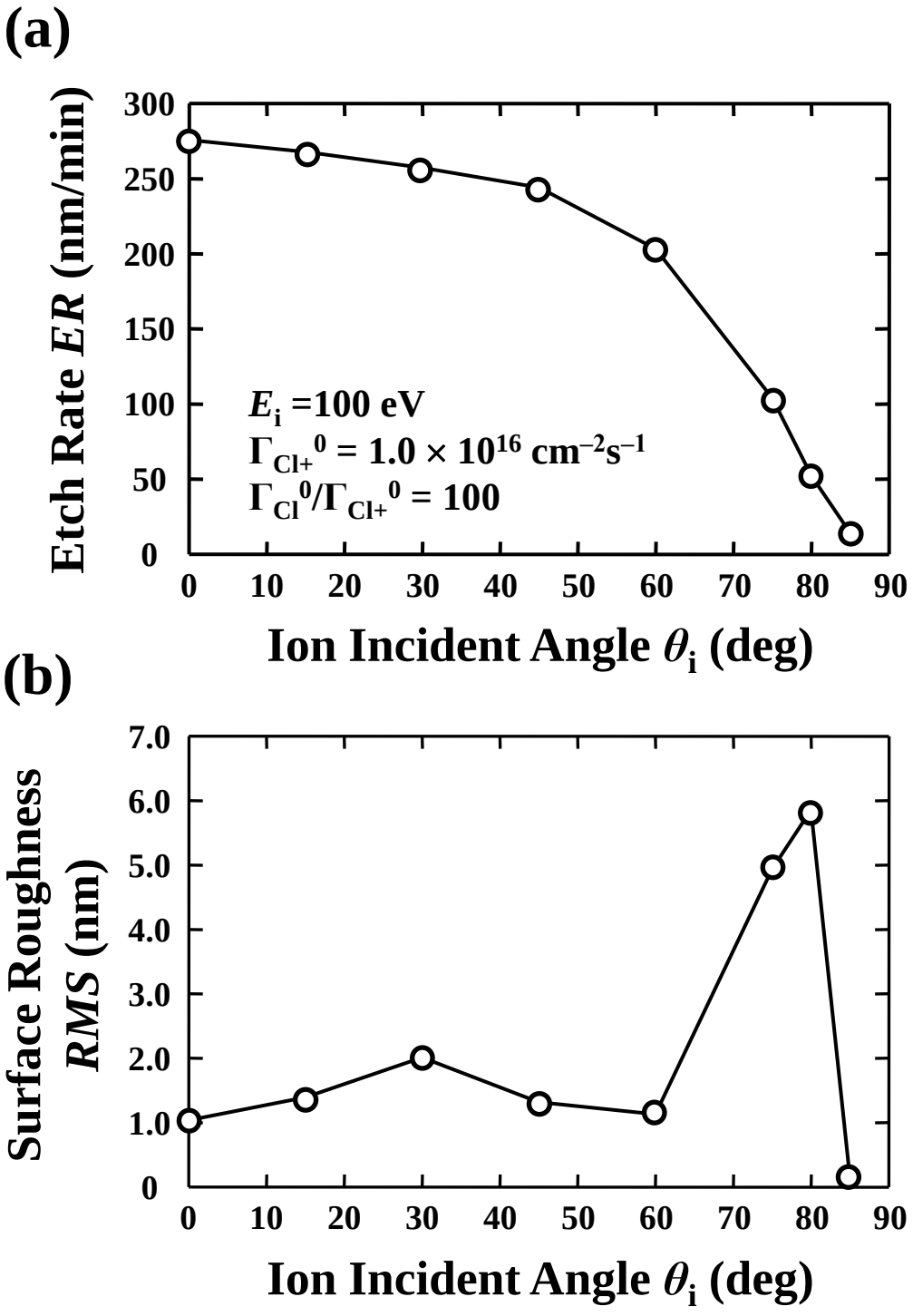

Fig. 6.6. (a) Average etch rate *ER* and (b) rms surface roughness *RMS* at a steady state (t = 50 s) as a function of ion incident angles θ_i, derived from the data of Fig. 6.5. Note that for highly oblique θ_i = 75–80°, the *RMS* increases with time during simulation, and so the *RMS* data shown are those at around the end of simulation (t = 120 s).

6.3.3 Formation Mechanisms of Ripple Structures

Figures 6.7 show side views of Si surfaces at t = 60 s after the start of etching, together with typical trajectories of energetic Cl^+ ions incident thereon, taken from the simulations of Figs. 6.4 for different ion incident angles of θ_i = 0 and 45°. It is noted here that the line of sight is perpendicular to the direction of ion incidence (or in the y direction; see Fig. 6.1), and that the simulation domain shown is 5 nm in width in the y direction at around the central x axis of the domain. Figure 6.7(a) exhibits that for θ_i = 0° or normal incidence, ions are incident almost vertically on substrate surfaces, and then penetrate into substrates. On the other hand, Fig. 6.7(b) exhibits that for θ_i = 45° or oblique incidence, ions incident on upstream slopes of the ripple have a small local angle θ of incidence, which penetrate locally into substrates; in contrast, ions incident on downstream slopes of the ripple have a large local angle θ of incidence, which tend to be reflected and/or scattered thereon and then reach near the bottom of the neighboring upstream slopes with a large local angle θ of incidence. In addition, the wavelength of the ripple is about 20 nm, and the ripple angle $\theta_{ripple} \approx 45°$, which is defined as the angle between the downstream slope of the ripple and the surface normal of substrates, correlates with the ion incident angle θ_i = 45°. The analysis of ion trajectories implies that the ion reflection and concentration on microscopically roughened surfaces largely affect the surface roughening and rippling during plasma etching.

Figure 6.8 shows top views of Si surfaces at an earlier point t = 15 s after the start of etching, together with the spatial distribution of a typical 1000 points on substrate surfaces where ions reach the surface and the following desorption of substrate atoms occurs as a result of etching and/or sputtering thereon in a time between t = 15 and 16 s. These are the data taken from the simulations of Figs. 6.4 for an ion incident angle of θ_i = 45°. The simulation domain shown is a square 25 nm on a side at around the center of the 50 nm square of domain, and the roughened surface features are 10 nm in height at maximum. It is further noted here that on substrate surfaces of the square 25 nm on a side, about 4.4×10^4 ions are incident in 1 s under the present conditions, and so the points shown in the figure are those randomly selected to see the spatial distribution of the points where ions reach the slightly roughened surfaces at the beginning of ripple formation. Figure 6.8(a) exhibits the points where ions reach the surface with a small local angle of incidence in the range θ = 0–30°, which are located on upstream slopes of the ripple, and Fig. 6.8(c) exhibits those where ions reach the surface with a large local angle of incidence in the range θ = 60–90°, which are located on downstream slopes

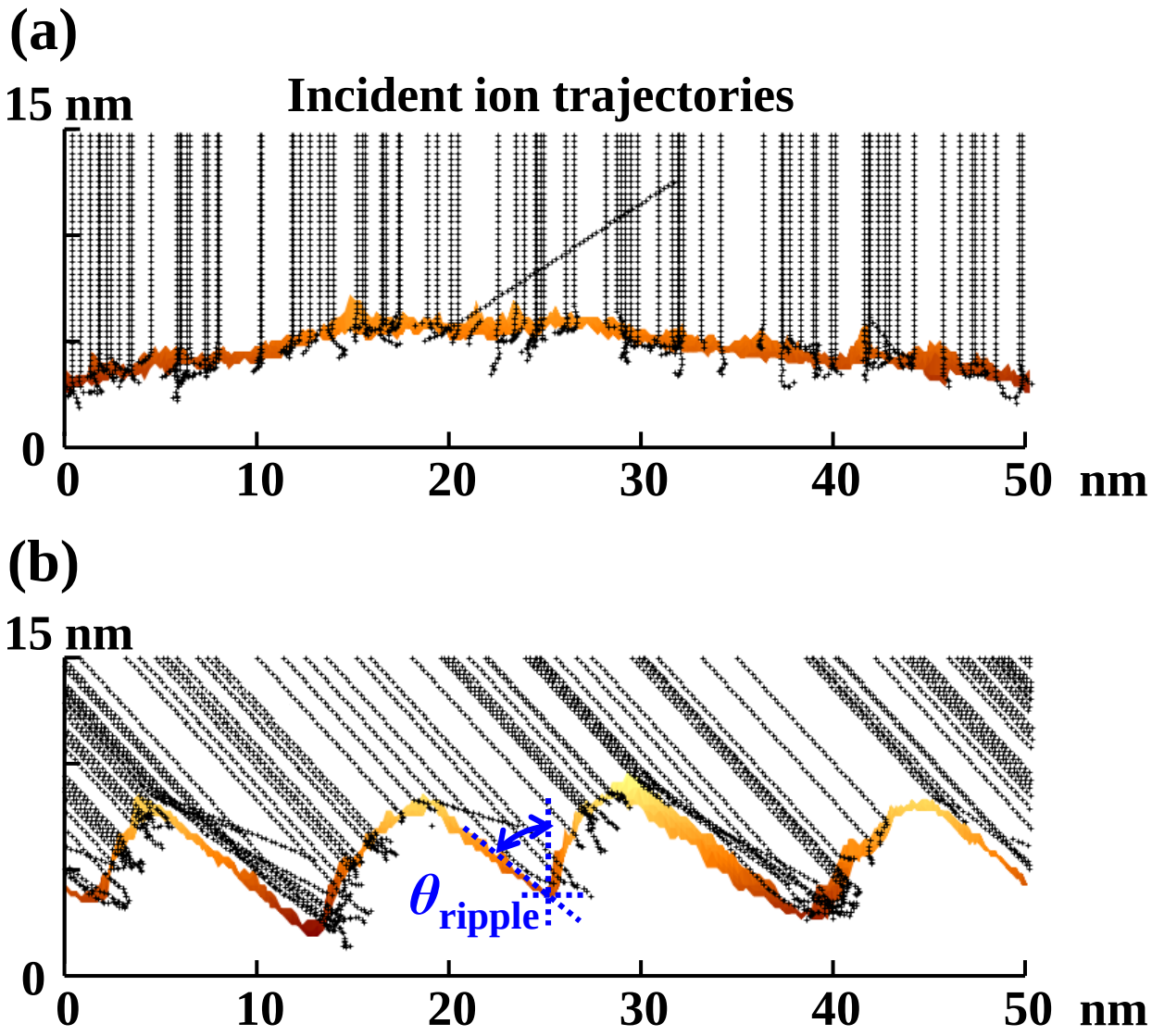

Fig. 6.7. Side views of Si surfaces at t = 60 s after the start of etching, together with typical trajectories of energetic Cl^+ ions incident thereon, taken from the simulations of Fig. 6.4 for different ion incident angles of θ_i = (a) 0 and (b) 45°. Note that the line of sight is perpendicular to the direction of ion incidence (or in the y direction; see Fig. 6.1), and that the simulation domain shown is 5 nm in width in the y direction at around the central x axis of the domain.

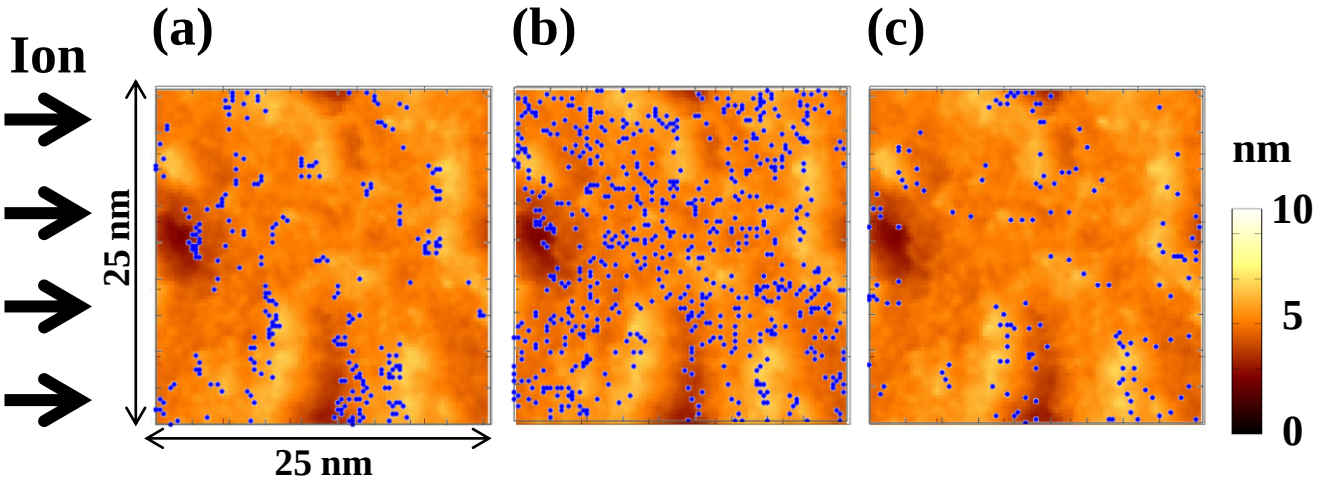

Fig. 6.8. Top views of Si surfaces at earlier t = 15 s after the start of etching, together with the spatial distribution of a typical 1000 points on substrate surfaces where ions reach the surface and the following desorption of substrate atoms occurs as a result of etching and/or sputtering thereon in a time between t = 15 and 16 s. These are the data taken from the simulations of Fig. 6.4 for an ion incident angle of θ_i = 45°, and the points are those where ions reach the surface with a local angle of incidence in the range θ = (a) 0–30°, (b) 30–60°, and (c) 60–90°. Note that the simulation domain shown is a square 25 nm on a side at around the center of the 50 nm square of domain, and the roughened surface features are 10 nm in height at maximum.

of the ripple. On the other hand, Fig. 6.8(b) exhibits the points where ions reach the surface with a medium local angle of incidence in the range θ = 30–60°, which tend to be located on top and bottom areas of roughened surface features. These give a separate view of the mechanisms: the local angle θ of ion incidence varies with the location on microscopically roughened surfaces, which triggers locally different etch yields or etch rates, and leads to the surface roughening and rippling during plasma etching.

6.4 Conclusions

We have developed a three-dimensional atomic-scale cellular model (ASCeM-3D) to simulate the evolution of 3D feature profiles on atomic or nanometer scale during Si etching in Cl_2 plasmas, with emphasis being placed on that of nanoscale surface features and roughness on etched surfaces. The transport of ions and neutrals in microstructures was analyzed using the 3D MC algorithm, where two-body elastic collisions between incident ions and substrate atoms were taken into account to analyze the ion reflection from feature surfaces on incidence and penetration into substrates. The model also took into account surface chemistries based on the MC algorithm, including adsorption and reemission of neutrals, chemical etching, ion-enhanced etching, physical sputtering, and redeposition of etch and/or sputter products on feature surfaces. Simulations were carried out for different ion incident angles from θ_i = 0° to 85°, with an ion incident energy E_i = 100 eV, flux $\Gamma_i^0 = 1.0 \times 10^{16}$ cm^{-2} s^{-1}, and neutral-to-ion flux ratio Γ_n^0/Γ_i^0 = 100, which are typical in high-density plasma etching environments.

Numerical results indicated that as the angle θ_i is increased, nanoscale concavo-convex features drastically change and ripple structures occur on etched surfaces. For θ_i = 0° or normal ion incidence, small concavo-convex features are formed randomly on surfaces soon after the start of etching, and then large concavo-convex features on the order of a few tens of nm are formed on etched surfaces; a comparison showed that the average etch rate and rms surface roughness numerically obtained are in agreement with ICP plasma etching experiments. In contrast, for increased θ_i = 45° or oblique ion incidence, small concavo-convex features after the start of etching tend to merge with each other, and then ripple structures with wavelengths on the order of a few tens of nm are formed on etched surfaces perpendicularly to the direction of ion incidence. For further increased θ_i = 75°, small ripple structures or slit-like grooves are formed on surfaces parallel to the direction of ion incidence soon after the start of etching, and then some slit-like grooves tend to enlarge with time on etched surfaces. Analysis of ion

trajectories implied that the ion reflection and concentration on microscopically roughened surfaces largely affects the surface roughening and rippling during plasma etching.

These numerical approaches would be useful for predicting and analyzing the evolution of nanoscale surface features and roughness (especially LER and LWR on feature sidewalls) during plasma etching for nanoscale pattern definition; in practice, experiments on the oblique incidence of ions on surfaces are difficult in plasma environments, because the ion incidence is usually normal to substrate surfaces after being accelerated through the sheath on substrates immersed in plasma.

References

1) X. Sun and T.-J. King Liu: IEEE Trans. Semicond. Manuf. **23** (2010) 311.
2) D. Hisamoto, W. C. Lee, J. Kedzierski, E. Anderson, H. Takeuchi, K. Asano, T. J. King, J. Bokor, and C. Hu: IEDM Tech. Dig., 1998, p. 1032.
3) H. S. P. Wong, D. J. Frank, and P. M. Solomon: IEDM Tech. Dig., 1998, p. 407.
4) K. Patel, T.-J. King Liu, and C. J. Spanos: IEEE Trans. Electron Devices **56** (2009) 3055.
5) E. Altamirano-Sánchez, V. Paraschiv, M. Demand, and W. Boullart: Microelectron. Eng. **88** (2011) 2871.
6) K. J. Kanarik, G. Kamarthy, and R. A. Gottscho: to be published in Solid State Technol. **55** (2012).
7) W. Guo and H. H. Sawin: J. Phys. D **42** (2009) 194014.
8) M. Tuda, K. Ono, and K. Nishikawa: J. Vac. Sci. Technol. B **14** (1996) 3291.
9) M. Tuda, K. Nishikawa, and K. Ono: J. Appl. Phys. **81** (1997) 960.
10) M. A. Vyvoda, M. Li, D. G. Graves, H. Lee, M. V. Malyshev, F. P. Klemens, J. T. C. Lee, and V. M. Donnelly: J. Vac. Sci. Technol. B **18** (2000) 820.
11) D. J. Cooperberg, V. Vahedi, and R. A. Gottscho: J. Vac. Sci. Technol. A **20** (2002) 1536.
12) G. S. Hwang, C. M. Anderson, M. J. Gordon, T. A. Moore, T. K. Minton, and K. P. Giapis: Phys. Rev. Lett. **77** (1996) 3049.
13) A. P. Mahorowala and H. H. Sawin: J. Vac. Sci. Technol. B **20** (2002) 1064.
14) W. Guo, B. Bai, and H. H. Sawin: J. Vac. Sci. Technol. A **27** (2009) 388.
15) M. Wang and M. J. Kushner: J. Vac. Sci. Technol. A **29** (2011) 051306-1.
16) H. H. Hwang, M. Meyyappan, G. S. Mathad, and R. Ranade: J. Vac. Sci. Technol. B **20** (2002) 2199.
17) H. Tsuda, K. Eriguchi, K. Ono, and H. Ohta: Appl. Phys. Express **2** (2009) 116501.
18) H. Tsuda, Y. Takao, K. Eriguchi, and K. Ono: Jpn. J. Appl. Phys. **50** (2011) 08KB02.
19) Y. Osano and K. Ono: Jpn. J. Appl. Phys. **44** (2005) 8650.
20) Y. Osano, M. Mori, N. Itabashi, K. Takahashi, K. Eriguchi, and K. Ono: Jpn. J. Appl. Phys. **45** (2006) 8157.
21) Y. Osano and K. Ono: J. Vac. Sci. Technol. B **26** (2008) 1425.
22) H. Tsuda, M. Mori, Y. Takao, K. Eriguchi, and K. Ono: Thin Solid Films **518** (2010) 3475.
23) H. Tsuda, M. Mori. Y. Takao, K. Eriguchi, and K. Ono: Jpn. J. Appl. Phys. **49** (2010) 08JE01.

24) K. Ono, H. Ohta, and K. Eriguchi: Thin Solid Films **518** (2010) 3461.
25) K. Ono, H. Ohta, and K. Eriguchi: Plasma Kakuyugo Gakkaishi **85** (2009) 163 [in Japanese].
26) H. Tsuda, H. Miyata, Y. Takao, K. Eriguchi, and K. Ono: Jpn. J. Appl. Phys. **50** (2011) 08JE06.
27) R. A. Gottsho: J. Vac. Sci. Technol. B **11** (1993) 1884.
28) E. A. Ogryzlo, D. E. Ibbotson, D. L. Flamm, and J. A. Mucha: J. Appl. Phys. **67** (1990) 3115.
29) W. Guo and H. H. Sawin: J. Vac. Sci. Technol. A **27** (2009) 1326.
30) W. Jin, S. A. Vitale, and H. H. Sawin: J. Vac. Sci. Technol. A **20** (2002) 2106.
31) J. P. Chang and H. H. Sawin: J. Vac. Sci. Technol. B **19** (2001) 1319.
32) K. Wittmaack: Phys. Rev. B **68** (2003) 235211.
33) J. Bohdansky, J. Roth, and H. L. Bay: J. Appl. Phys. **51** (1980) 2861.
34) H. L. Bay, J. Roth, and J. Bohdansky: J. Appl. Phys. **48** (1977) 4722.
35) J. P. Biersack and W. Eckstein: Appl. Phys. A **34** (1984) 73.
36) R. Behrisch: *Sputtering by Particle Bombardment I. Physical Sputtering of Single-Element Solids* (Springer, Berlin, 1981) p. 73.
37) J. F. Ziegler, J. Biersack, and U. Littmark: *The Stopping and Range of Ions in Matter* (Pergamon, New York, 1985) p. 14.
38) J. F. Ziegler, J. P. Biersack, and M. D. Ziegler: *SRIM – The Stopping and Range of Ions in Matter* (SRIM, Chester, MD, 2008) p. 2-1.
39) B. Ziberi, F. Frost, Th. Höche, and B. Rauschenbach: Phys. Rev. B **72** (2005) 235310.
40) B. Ziberi, M. Cornejo, F. Frost, and B. Rauschenbach: J. Phys.: Condens. Matter **21** (2009) 224003.
41) W. L. Chan and E. Chason: J. Appl. Phys. **101** (2007) 121301.
42) T. K. Chini, D. P. Datta, and S. R. Bhattacharyya: J. Phys.: Condens. Matter **21** (2009) 224004.
43) S. A. Pahlovy, S. F. Mahmud, K. Yanagimoto, and I. Miyamoto: J. Vac. Sci. Technol. A **29** (2011) 021015.
44) R. M. Bradley and J. M. E. Harper: J. Vac. Sci. Technol. A **6** (1988) 2390.
45) I. Koponen, M. Hautala, and O.-P. Sievänen: Phys. Rev. Lett. **78** (1997) 2612.
46) J. J. Végh and D. B. Graves: Plasma Sources Sci. Technol. **19** (2010) 045005.

Chapter 7
Conclusions

7.1 Concluding Remarks

This thesis presented a two-dimensional atomic-scale cellular model (ASCeM) of plasma-surface interactions and feature profile evolution during Si etching in Cl_2 and Cl_2/O_2 plasmas, to investigate the formation mechanisms of profile anomalies and microscopic uniformity. We also developed an extended ASCeM or a three-dimensional atomic-scale cellular model (ASCeM-3D) and simulated plasma-surface interactions and feature profile evolution during Si etching in Cl_2 plasma to analyze the formation mechanisms of atomic-scale surface roughening in 3D.

In Chapter 2, we focused on the analysis of formation mechanisms of profile anomalies and microscopic uniformity during plasma etching of Si in Cl_2 plasmas, using ASCeM and feature profile simulation. The ASCeM can reproduce the feature profile evolution experimentally observed, including microtrenches, tapered profiles, RIE lag, inverse RIE lag, and surface roughness. The numerical results indicated that high neutral-to-ion flux ratios resulted in microtrench formation. The effects of not only ion scattering on sidewalls but also neutral supply would be important in microtrench formation at the bottom corner of trenches. Moreover, RIE lag tended to occur at low neutral-to-ion flux ratios, whereas inverse RIE lag occurred at high neutral-to-ion flux ratios in typical low-pressure and high-density plasmas. Low neutral-to-ion flux ratio would cause RIE lag and ion-induced damage, while it would reduce microtrench and surface roughness. The numerical results also indicated that the etch rates for narrow patterns increased significantly with increasing neutral-to-ion flux ratio, because the etched surface in narrow space tended to be easily saturated with neutral species at high neutral-to-ion flux ratio. The synergistic effects between ion-enhanced etching and neutral shadowing in microstructural features play a significant role in the formation of profile anomalies.

In Chapter 3, we investigated the formation mechanisms for profile anomalies such as surface roughness and residue for Si etching in Cl_2/O_2 plasmas by numerical and experimental approaches. The ASCeM can reproduce the feature profile evolution experimentally observed during etching at increased O_2 concentrations, including the intricately-shaped surfaces on a nanometer scale. A comparison between numerical and experimental results indicated that the

local surface oxidation induced surface roughness at the bottom of the feature during etching. In practice, in roughened microstructural features, geometrical shadowing effects for neutral oxygen suppressed the surface oxidation at the local feature bottom, where the difference between etch rates through ion-assisted reactions on top surfaces (with significant oxidation) and bottom surfaces (with less oxidation) of the local feature further increased the roughness, and caused significant residues. Therefore, we concluded that synergistic effects between surface oxidation and ion scattering in microstructural features on roughened surfaces increase the surface roughness, which in turn cause a number of significant residues or micropillars on bottom surfaces of the feature.

As discussed in the previous chapter (Chapter 3), we focused on the formation mechanisms of micropillars/residues for Si etching in O_2-containing plasmas; however, the mechanisms of the initial-stage formation of micromasks soon after the start of etching were still poorly understood. In Chapter 4, we investigated the mechanisms of the initial-stage formation of roughened surfaces and micropillars during Si etching in Cl_2/O_2 plasmas by employing the MD approach. Numerical results indicated that there were several differences between the behavior of Cl and O atoms on and in surface reaction layers. The numerical results also indicated that O radicals tended to break Si–Si bonds and distort the Si lattice structure; thus, nanometer-scale micromasks tended to be formed on convex roughened surfaces, owing to the reactivity of O radicals with substrate Si atoms and Cl atoms. Moreover, experiments showed that over-100-nm-high micropillars were formed on the Si surface etched in Cl_2/O_2 plasmas, while only sub-10-nm-scale roughness occurred on the surface etched in pure Cl_2 plasma. These results also imply that the nanometer-scale micromasks caused by oxygen addition significantly affect the formation of roughened surfaces and evolution of micropillars.

In Chapter 5, we developed a three-dimensional model for feature profile simulation (ASCeM-3D) to reproduce the three-dimensional structure of etched feature surfaces during Si etching in Cl_2 plasmas. The ASCeM-3D indicated that nanometer-scale convex roughened features appeared on the surface soon after the start of etching, which caused the formation of a larger surface roughness, and that the surface roughness tended to be saturated after several seconds. Moreover, experiments also showed that sub-100-nm-scale roughness occurred on surfaces during Si etching in Cl_2 plasmas, and the height of roughness tended to be increased with increasing RF bias power or ion incident energy. The roughness parameters obtained from AFM images were on a 10 nm scale of height, which was in agreement with numerical

results. Therefore, it was concluded that the ASCeM-3D would be useful for predicting and analyzing the nanometer-scale surface roughness in 3D during plasma etching.

In Chapter 6, we investigated the evolution of nanoscale surface features and roughness during Si etching in Cl_2 plasmas, with further attention being given to that of ripple structures on etched surfaces by using the ASCeM-3D. Numerical results indicated that as the angle θ_i was increased, nanoscale concavo-convex features drastically changed and ripple structures occurred on etched surfaces. For $\theta_i = 0°$ or normal ion incidence, the surfaces were randomly roughened. For increased $\theta_i = 30–45°$ or oblique ion incidence, the ripples were formed perpendicular to the direction of ion incidence, while they were parallel to the direction of ion incidence for further increased $\theta_i = 75–80°$. Analysis of ion trajectories implied that the ion reflection and concentration on microscopically roughened surfaces largely affected the surface roughening and rippling during plasma etching. These numerical approaches would be useful for predicting and analyzing the evolution of nanoscale surface features and roughness (especially LER and LWR on feature sidewalls) during plasma etching for nanoscale pattern definition, because experiments of oblique incidence of ions on surfaces are difficult in plasma environments.

Finally, in this thesis, the formation mechanisms for profile anomalies and microscopic uniformity during plasma etching of Si in halogen plasmas have been analyzed using the ASCeM/ASCeM-3D and also using MD-based feature profile simulation. Analysis of the particle behavior of ions, neutral reactants, and etch products and by-products becomes more important to understand plasma-surface interactions and formation mechanisms for profile anomalies and microscopic uniformity. Thus, we would like to emphasize that the combination of different approaches of MC and MD become helpful for a better understanding of multi-scale phenomena such as plasma-surface interactions. Selecting the proper simulation model and comparing between numerical and experimental results would play a significant role in the analysis of nanometer-scale plasma-surface interactions for developing next-generation devices.

7.2 Future Works and Challenges

Although a number of numerical and experimental studies have been reported, fundamental cause-and-effect relationships for surface roughening and rippling are still poorly understood. It is still difficult for numerical and theoretical studies to reproduce roughening and rippling surfaces experimentally observed during plasma/beam etching. Especially, ripple formation

often exhibits a range of behavior that could not be described by theoretical model such as Bradley–Harper (BH) model,[1] because these phenomena are very sensitive and are affected by multiple factors, including ion incident energy and angle, ion fluence, exposure time, gas chemistry, substrate material, substrate temperature, and crystal orientation.[2–6] Further studies are now in progress to investigate the mechanisms of the initial-stage formation of surface rippling during plasma etching or beam etching, by using the analysis of spatial frequency and power spectral density (PSD) of ripple structures.[7–10]

From a perspective of numerical studies of surface roughening and rippling, fundamental problems about calculation domain dependence also still remain. In the periodic boundary conditions, the size or wavelength of surface roughness and ripple structures strongly depends on the size of calculation domain.[11,12] Therefore, it is necessary to select the proper simulation model and the size of calculation domain towards a better understanding of the formation mechanisms of surface roughening and rippling.

References

1) R. M. Bradley and J. M. E. Harper: J. Vac. Sci. Technol. A **6** (1988) 2390.
2) W. L. Chan and E. Chason: J. Appl. Phys. **101** (2007) 121301.
3) T. K. Chini, D. P. Datta, and S. R. Bhattacharyya: J. Phys.: Condens. Matter **21** (2009) 224004.
4) S. Habenicht, W. Bolse, K. P. Lieb, K. Reimann, and U. Geyer: Phys. Rev. B **60** (1999) R2200.
5) S. Habenicht, K. P. Lieb, J. Koch, and A. D. Wieck: Phys. Rev. B **65** (2002) 115327.
6) B. Ziberi, F. Frost, T. Höche, and B. Rauschenbach: Phys. Rev. B 72 (2005) 235310.
7) H. Tsuda, Y. Takao, K. Eriguchi, and K. Ono: Ext. Abstr. (73rd Autumn Meet., 2012); Japan Society of Applied Physics, 13a-E3-7 [in Japanese].
8) H. Tsuda, Y. Takao, K. Eriguchi, and K. Ono: Bull. Am. Phys. Soc. **57** (65th Annual Meet., 2012); Gaseous Electronics Conference, p. 45.
9) H. Tsuda, Y. Takao, K. Eriguchi, and K. Ono: Ext. Abstr. (59th Annual Meet., 2012); American Vacuum Society International Symposium, PS2-TuA12.
10) H. Tsuda, Y. Takao, K. Eriguchi, and K. Ono: Proc. (34th Annual Meet., 2012); Int. Symp. Dry Process, p. 7.
11) J. J. Végh and D. B. Graves: Plasma Sources Sci. Technol. 19 (2010) 045005.
12) H. Tsuda, H. Miyata, Y. Takao, K. Eriguchi, and K. Ono: Jpn. J. Appl. Phys. 50 (2011) 08JE06.

Appendix A
Atomic-Scale Cellular Model (2D Model)

A.1 Introduction

This appendix presents an atomic-scale cellular model (ASCeM) as shown in Chapter 2 and Chapter 3. The ASCeM is a Monte Carlo-based semi-empirical model at an intermediate scale between continuum models and the MD simulation, to simulate the feature profile evolution during etching of Si in Cl_2 and Cl_2/O_2 plasmas. The main scheme of the ASCeM has been developed by Osano *et al.*[1–3] The ASCeM has been also developed to describe the nanometer scale feature geometry, including the multilayer surface reactions and the ion scattering/reflection on the feature surface and penetration into substrates with a binary collision model.

A.2 Simulation Model

Figure A.1 shows a schematic of the ASCeM. We consider two-dimensional structures or infinitely long trenches being etched in Cl_2 and Cl_2/O_2 plasmas as illustrated in Fig. A.1(a). The simulation domain is a two-dimensional space (x, z), being divided into square lattices of $L = \rho_{Si}^{-1/3} = 2.7$ Å as shown in Fig. A.1(b) with $\Delta y = L$ taken in the y direction. Here, $\rho_{Si} = 5.0 \times 10^{22}$ cm^{-3} is the atomic density of Si substrates, and L correspond approximately to the interatomic distance in Si substrates. In this model, the Si atoms are allocated at the center (x, y, z) = $((n_x + 1/2)L, (1/2)L, (n_z + 1/2)L)$ of the respective square lattices, where n_x and n_z are integers; in addition, the solid-vacuum interfaces concerned are taken to be the edge of lattices filled with Si atoms. The lattice is assumed to be rigid, and Si atoms are taken to be removed from the outermost surfaces of the feature when the etching causes the desorption of reaction products $SiCl_x$ and the sputtering causes the removal of oxygen-containing products $SiCl_xO_y$; in contrast, Si atoms are newly allocated at the lattice when the deposition of etch products/by-products occurs thereat. Figure A.2(a) shows the adsorption and reflection of Cl neutrals on feature surfaces. If there is a Si atom at any of the four sites neighboring to the lattice where the neutral is located, the neutral is assumed to reach the surface; then, the neutral is adsorbed on the neighboring Si site, or is reemitted thermally or reflected randomly therefrom, depending on the site conditions concerned. Figure A.2(b) shows the deposition of etch products $SiCl_x$ and by-products $SiCl_xO_y$ on feature surfaces which is represented by the ballistic

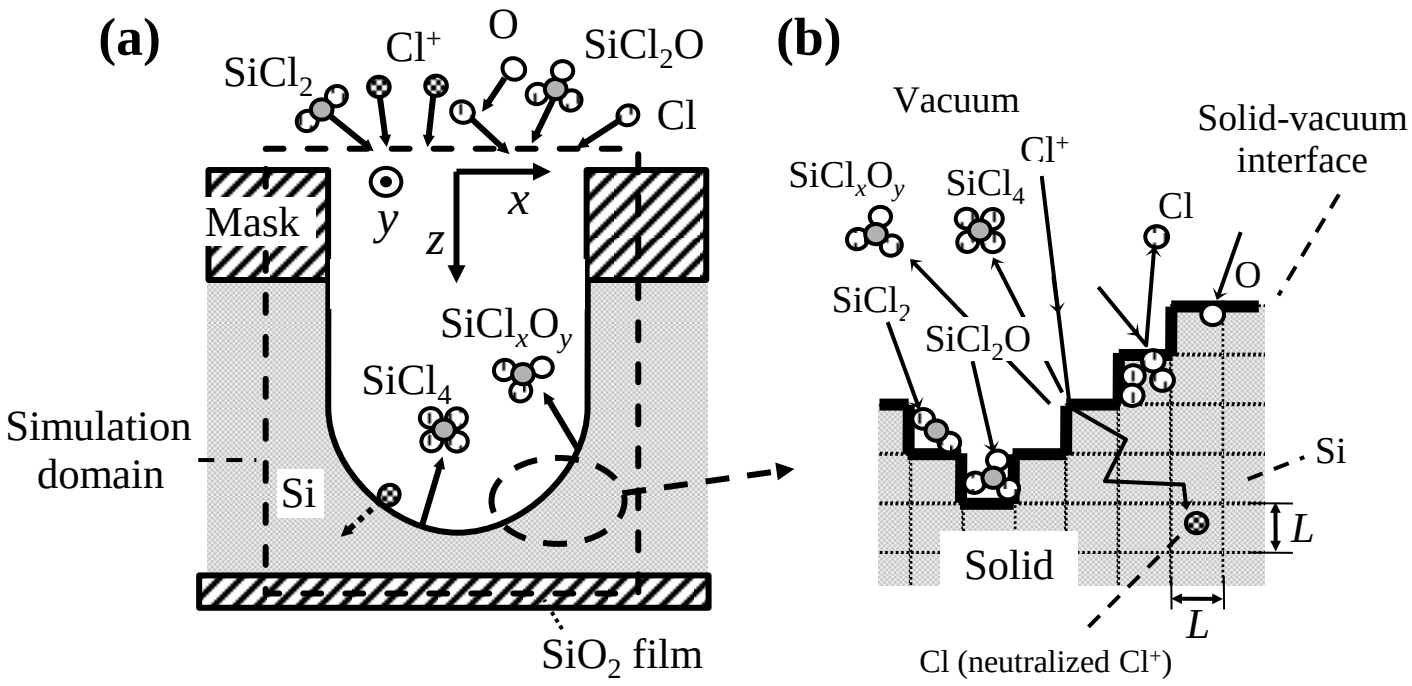

Fig. A.1. (a) Schematic illustration of the geometry of an infinitely long trench of Si being etched, together with the coordinate system presently employed. Here, Cl^+ ions, Cl neutrals, O neutrals, etch products $SiCl_x$, and etch by-products $SiCl_xO_y$ are injected from the top of the simulation domain with three velocity components (v_x, v_y, v_z); moreover, primary etch product species $SiCl_4$ are desorbed and etch by-product species $SiCl_xO_y$ are sputtered or removed from the feature surfaces during etching. Also shown is (b) the simulation domain in a two-dimensional space (x, z) divided into square lattices of $L = \rho_{Si}^{-1/3} = 2.7$ Å with $\Delta y = L$ in the y direction, where $\rho_{Si} = 5.0 \times 10^{22}$ cm^{-3} is the atomic density of Si substrates, and the Si atoms are allocated in the respective two-dimensional square lattices.

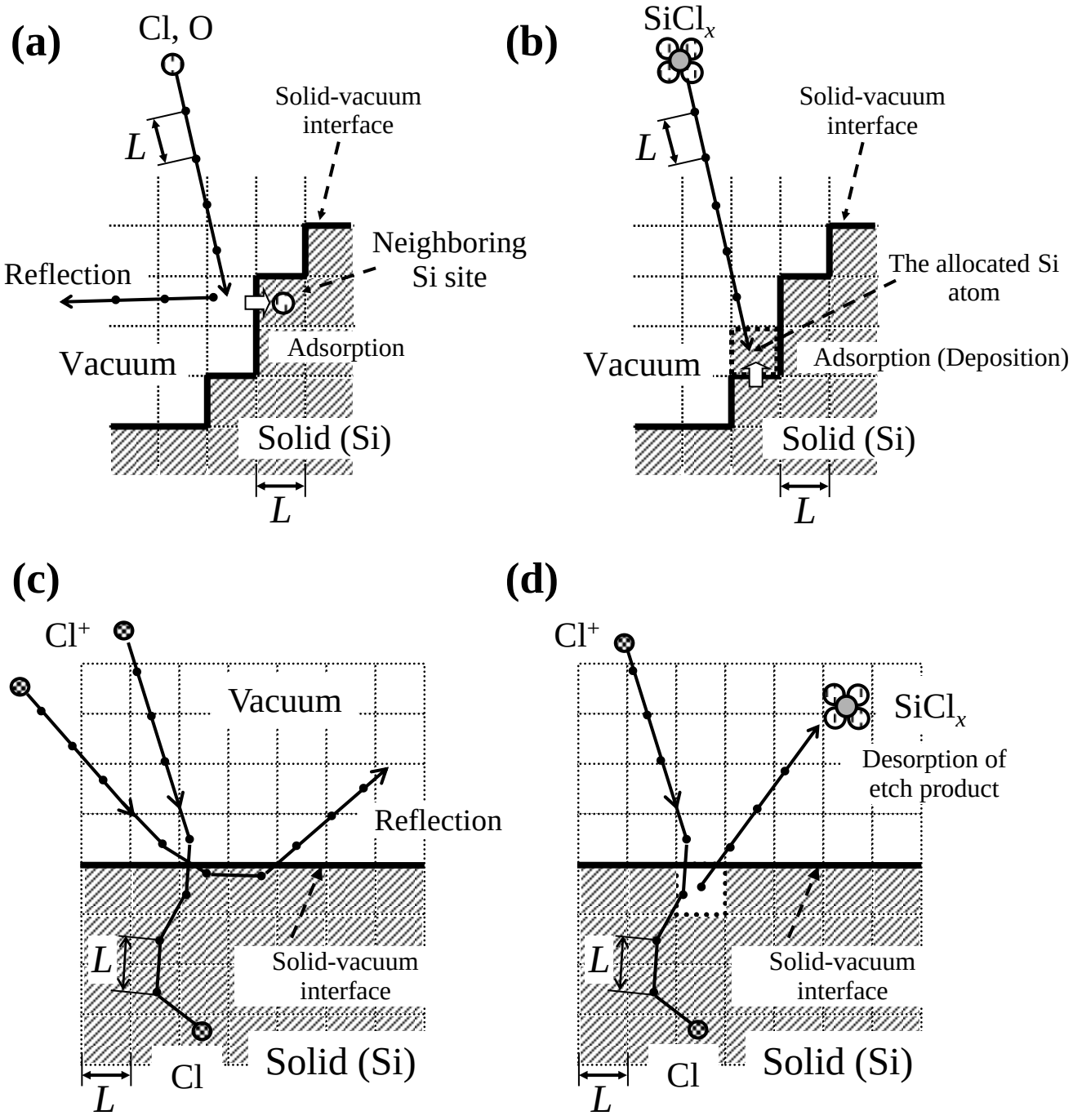

Fig. A.2. Schematic of surface reactions in ASCeM. The model takes into account surface chemistries based on the Monte Carlo (MC) algorithm: (a) adsorption and reflection of neutrals, (b) adsorption or deposition of etch products, (c) ion reflection on surfaces and penetration into Si substrate, (d) desorption of etch products by ion-enhanced etching.

deposition model.[4] A Si atom is newly allocated at a site neighboring to the surface site on incidence of etch products and by-products. Simultaneously, Cl and O atoms of $SiCl_x$ and $SiCl_xO_y$ are taken to adsorb on the same site.

The particle transport of energetic ions, neutrals, and etch products/by-products in microstructures is analyzed by using a two-dimensional particle simulation based on successively injected single-particle trajectories with three velocity components (v_x, v_y, v_z). In practice, the third velocity components v_y are also calculated, while the trajectories are projected to a two-dimensional space (x, z). In practice, the Cl^+, Cl, O, and $SiCl_xO_y$ are randomly allocated at the top boundary of the simulation domain, being successively injected therefrom with given energies and fluxes.

The incident angle of ions in given by randomly sampling from the angular distribution of ion fluxes through the sheath onto substrate surfaces as shown in Fig. A.3,

$$G_{\mathrm{i}}(\Theta)\cos\Theta = \frac{\exp(R)}{\sqrt{\pi}}\left[\frac{\sqrt{\pi}}{\cos\Theta}\exp\left(-\frac{R}{\cos^2\Theta}\right)+\frac{\sqrt{\pi}}{2}\mathrm{erfc}\left(\frac{\sqrt{\pi}}{\cos\Theta}\right)\right]\cos\Theta \quad , \qquad \text{(A.1)}$$

where

$$\mathrm{erfc}(x) = \frac{2}{\sqrt{\pi}}\int_x^{\infty}\exp\left(-t^2\right)dt \quad , \qquad \text{(A.2)}$$

Θ is the incident angle from the macroscopic substrate surface normal, and $R = eV_s/kT_i$ is the ratio of the incident ion energy $E_i = eV_s$ to the ion temperature kT_i (= 0.5 eV in this study).[5,6]

The neutrals and etch by-products are also randomly allocated at the top of the simulation domain, being injected thermally with an isotropic velocity distribution; the incident angle of neutrals is given by randomly sampling from the so-called cosine distribution,

$$G_{\mathrm{n}}(\Theta)\cos\Theta = \frac{1}{2}\cos\Theta \quad , \qquad \text{(A.3)}$$

which corresponds to $G_n(\Theta)\cos\Theta$ with $R = 0$.

The particles are assumed to move straight towards feature surfaces in microstructures without collision with other particles therein. In the ASCeM, the every movement of particles in the microstructural features is assumed to be rigid with the approximate atomic separation L = 2.7 Å. Energetic ions are taken to penetrate into substrates, atop at a finite depth, and react with substrate atoms thereat, as shown in Fig. A.2(c). The penetration of energetic Cl^+ ions into Si causes the multilayer adsorption of Cl, thus resulting in surface reaction multilayers of

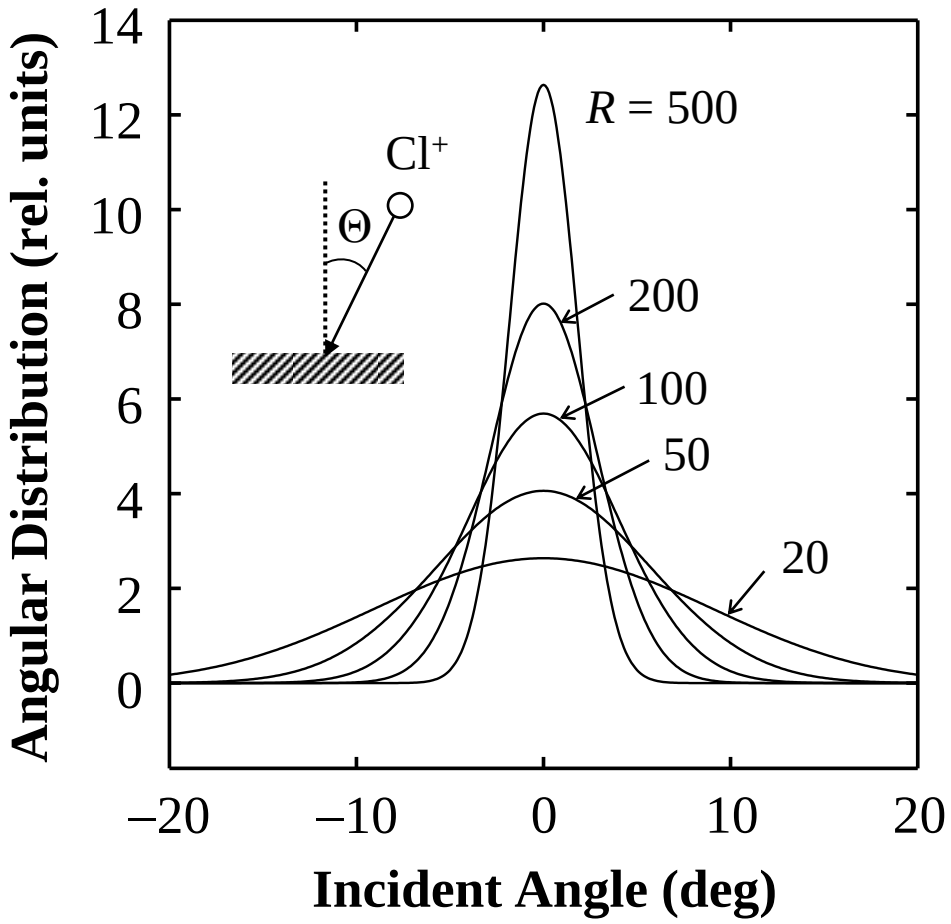

Fig. A.3. Angular distribution of ion fluxes incident on substrate surfaces, calculated for different ratios $R = eV_s / kT_i$ of the ion energy $E_i = eV_s$ gained in the sheath field to the ion temperature kT_i. Here, the ratio R = 20, 50, 100, 200, and 500 correspond to an ion energy E_i = 10, 25, 50, 100, and 250 eV, respectively, with an ion temperature kT_i = 0.5 eV.

Table IV. Surface Reactions during Si etching in Cl_2 and Cl_2/O_2 plasmas.

Reaction	Process [a]		Coefficient [b]
(1) Neutral adsorption	$Si(s) + xCl(s) + Cl(g) \rightarrow Si(s) + (x+1)Cl(s)$	(x = 0–3)	$S_n = 1 - x/4$
(2) Spontaneous chemical etching	$Si(s) + 3Cl(s) + Cl(g) \rightarrow SiCl_4(g)$		$\alpha_{chem}(T_s)$
(3) Ion-enhanced etching	$Si(s) + xCl(s) \xrightarrow{Cl^+} SiCl_x(g)$	(x = 1–4)	$(x/4)Y_{Si/Cl+}(E_i, \theta)$
(4) Surface oxidation	$Si(s) + xO(s) + O(g) \rightarrow Si(s) + (x+1)O(s)$	(x = 0, 1)	$S_o = 1 - x/2$
(5) Surface chlorination of oxidized surfaces	$Si(s) + O(s) + xCl(s) + Cl(g) \rightarrow Si(s) + O(s) + (x+1)Cl(s)$	(x = 0, 1)	$S_n = 0.5(1 - x/2)$
(6) Surface oxidation of chlorinated surfaces	$Si(s) + xCl(s) + O(g) \rightarrow Si(s) + xCl(s) + O(s)$ $Si(s) + xCl(s) + O(g) \rightarrow Si(s) + 2Cl(s) + O(s) + (x-2)Cl(g)$ $Si(s) + xCl(s) + O(s) + O(g) \rightarrow Si(s) + 2O(s) + xCl(g)$	(x = 1, 2) (x = 3, 4) (x = 1, 2)	S_o = 1, 1, 0.5
(7) Etching or removal of oxidized surfaces through sputtering	$Si(s) + xCl(s) + O(s) \xrightarrow{Cl^+} SiCl_xO(g)$ $Si(s) + xO(s) \xrightarrow{Cl^+} SiO(g) + (x-1)O(g)$	(x = 1, 2) (x = 1, 2)	$Y^{SP}_{Si/Cl+}(E_i, \theta)$
(8) Deposition of etch products from feature surfaces	$SiCl_x(g) \rightarrow Si(s) + xCl(s)$ $SiO_y(g) \rightarrow Si(s) + yO(s)$ $SiCl_xO_y(g) \rightarrow Si(s) + xCl(s) + yO(s)$	(x = 1–4) (y = 1) (x = 1, 2; y = 1)	S_n = 0.002 ~ 0.1
(9) Deposition of etch by-products form the plasma	$SiCl_2(g) \rightarrow Si(s) + 2Cl(s)$ $SiCl_2O(g) \rightarrow Si(s) + 2Cl(s) + O(s)$		S_n = 0.1 ~ 0.5

[a] (s) denotes species on the surface, while (g) denotes species in the gas phase (species incident on the surface from the gas phase, and species desorbed from the surface into the gas phase).

[b] S_j (j = n, o, q, p) denotes the sticking probability of neutrals, α_{chem} the reaction probability, $Y_{Si/Cl+}$ the etch yield, Y_n the desorption yield, and Y_{Si} the sputtering yield, where T_s is the surface temperature, and E_i and θ the ion incident energy and angle onto surfaces.

$SiCl_x$, as indicated by the molecular dynamics (MD) simulation. Note that the incident ions are known to be neutralized on the surfaces owing to the Auger process; in the present model, the feature surfaces are assumed to be kept charge neutral during etching. In contrast to ions, neutrals have too small energy to penetrate into substrates, thus the neutral adsorption occurs only on the outermost surfaces (or at sites of the outermost surface lattices). The neutrals is allowed the adsorption of four Cl atoms at a cell of Si, and are reemitted thermally at saturated surfaces, which then move towards another surface sites or go out of the simulation domain.

A.2.1 Surface Chemistry I: Adsorption and Chemical Etching

The ASCeM model takes into account surface chemistries by using the Monte Carlo (MC) algorithm,[3,7,8] including ion-enhanced etching, chemical etching, surface remission of neutrals, surface oxidation, deposition of etch products and by-products, and sputtering of deposited layers and oxidized surfaces, as shown in Table IV.

Neutral reactants of Cl incident on Si surfaces lead to spontaneous chemical etching, which is assumed to occur at the outermost surface sites being chlorine-saturated. In practice, Cl neutrals are assumed to adsorb or stick on unsaturated surfaces of Si with a probability $S_n = 1$:

$$\mathrm{Si}_{(s)} + x\mathrm{Cl}_{(s)} + \mathrm{Cl}_{(g)} \rightarrow \mathrm{Si}_{(s)} + (x+1)\mathrm{Cl}_{(s)} \qquad (x = 0 \sim 3)\,, \tag{A.4}$$

where (s) and (g) represent the solid and the gas phase, respectively. The etching reaction is taken to occur through an incidence of Cl neutrals as

$$\mathrm{Si}_{(s)} + 3\mathrm{Cl}_{(s)} + \mathrm{Cl}_{(g)} \rightarrow \mathrm{SiCl}_{4(g)}\,, \tag{A.5}$$

with the etch rate ER_{chem}, which is calculated from the experiments of Ogryzlo *et al.*[9,10] They measured the chemical etch rate ER_{chem} for Si in heated Cl_2 gases as a function of dopant concentration N_e, Cl concentration n_{Cl} in the gas phase, and substrate temperature T_s:

$$ER_{\mathrm{chem}} = \nu N_e^{\gamma} n_{\mathrm{Cl}} T_s^{1/2} \exp(-E/kT_s)\,, \tag{A.6}$$

where $\nu = 4.04 \times 10^{-18}$ Å $\mathrm{cm}^{3(1+\gamma)}\,\mathrm{min}^{-1}\,\mathrm{K}^{-1/2}$, $\gamma = 0.39$, and $E = 4.7$ kcal/mol are constants determined for P-doped poly-Si, and k is the Boltzmann constant.[9] The chemical etch yield Y_{chem} (the number of substrate atoms etched per incident reactant on saturated surfaces) is then given by

$$Y_{\text{chem}} = \frac{\rho_{\text{Si}}\, ER_{\text{chem}}}{\Gamma_{\text{Cl}}} = \frac{4\rho_{\text{Si}}\nu\, N_e^{\gamma} T_{\text{s}}^{1/2} \exp(-E/kT_{\text{s}})}{\bar{u}} \quad , \qquad \text{(A.7)}$$

where $\Gamma_{\text{Si}} = \rho_{\text{Si}} ER_{\text{chem}}$ is the flux of Si atoms desorbed from the surface through purely chemical etching, $\Gamma_{\text{Cl}} = (1/4) n_{\text{Cl}} \bar{u}$ is the flux of Cl atoms incident on substrate surfaces, and $\bar{u} = \sqrt{8kT_g / \pi m_{\text{Cl}}}$ is the average thermal velocity of Cl atoms with m_{Cl} being the atomic mass concerned.[11] The dopant concentration is taken to be $N_{\text{e}} = 1.0 \times 10^{18}$ cm^{-3} and $T_{\text{s}} = 300 \sim 320$ K in this study, along with a gas temperature of $T_{\text{g}} = 500$ K. The reaction probability of chemical etching is given by $\alpha_{\text{chem}} = Y_{\text{chem}}$, and the decision whether or not to chemical etching reaction is determined by random numbers from 0 to 1 in the MC algorithms.

A.2.2 Surface Chemistry II: Deposition of Etch Products

Silicon chlorides $SiCl_x$, oxides SiO_y, and oxychlorides $SiCl_xO_y$, which are desorbed from feature surfaces through the etching and sputtering processes, deposited on feature surfaces consist of etch products coming directly from the feature surfaces being etched and etch by-products coming from the plasma, as shown in Fig. A.2(b). These neutrals desorbed are assumed to move straight towards another surface site in microstructures without collision with other particles therein, and then to stick or redeposit on all feature surfaces of mask as well as Si with a probability S_{q}:

$$SiCl_{x(g)} \rightarrow Si_{(s)} + xCl_{(s)} \qquad (x = 1 \sim 4)\,, \qquad \text{(A.8)}$$

$$SiO_{y(g)} \rightarrow Si_{(s)} + yO_{(s)} \qquad (y = 1)\,, \qquad \text{(A.9)}$$

$$SiCl_xO_{y(g)} \rightarrow Si_{(s)} + xCl_{(s)} + yO_{(s)} \quad (x = 1, 2;\ y = 1)\,. \qquad \text{(A.10)}$$

Otherwise, they are reemitted thermally or reflected randomly with a probability $(1 - S_{\text{q}})$, which then move towards another surface sites or go out of the simulation domain into the plasma. It is noted that the sticking coefficient or probability concerned is still unclear, thus being varied from $S_{\text{q}} = 0.002$ to 0.1. In this study, the S_{q} were chosen to fit the numerical results to the etch rates and feature profiles measured in experiments, and we assumed $S_{\text{q}} = 0.05$.

In practice, the etch products coming into the plasma are dissociated by electron impact and also oxidized by reaction with O atoms, a part of which return back to substrates as etch

by-products and then are transported in microstructures onto feature surfaces. Regarding etch by-products of $SiCl_x$ coming from the plasma, $SiCl_2$ formed by electron-impact dissociation of primary etch products $SiCl_4$ is taken into account in this study, because a $SiCl_4$ molecule is known to have a small sticking coefficient or probability $S_p \sim 0.001$ on Si as compared to $S_p \sim 0.1$ for unsaturated $SiCl_x$. Etch by-products of SiO_y and $SiCl_xO_y$ are also formed by sputtering of oxidized surfaces of etch products deposited on chamber walls as well as by oxidized reaction of $SiCl_x$ in the plasma. We simply assume that oxygen-containing etch by-products coming from the plasma are $SiCl_2O$. The sticking probability concerned is also still unclear, thus being varied from $S_p = 0.1$ to 0.5, and the surface reemission or reflection occurs with a probability $(1 - S_p)$.

The removal of deposited surfaces also occurs by physical sputtering through energetic Cl^+ ion bombardment; in this study, deposited $SiCl_x$, SiO_y, and $SiCl_xO_y$ are assumed to be desorbed or removed from the surface. It should also be noted that the desorption angle of etch products from the surface being etched and the removal angle of etch products from the surface deposited are assumed to follow the cosine law for simplicity, as that for the surface reemission or reflection of neutrals.

A.2.3 Ion Reflection from Feature Surface

The injected energetic ions are assumed to reach the surface if there is a Si atom at any of the four sites neighboring to the lattice where the ions are located; then, we calculate the impact parameter p concerned with the neighboring Si atom. As shown in Fig. A.4(a), the scattering of an ion at a collision is calculated on the basis of kinetics of two-body elastic collision, when the impact parameter p is smaller than the cutoff radius r_{cutoff} = 3.5 Å ($p < r_{cutoff}$) of the Stillinger-Weber potential $V(r)$ of the Cl–Si system.[12,13] The impact parameter $p = |\boldsymbol{p}|$ is the distance from the colliding Si atom to the extension of the initial velocity vector $\boldsymbol{v}_0$ of the incident ion, given by solving the simultaneous vector equations

$$\boldsymbol{r}_{Cl+} + \lambda \boldsymbol{v}_0 = \boldsymbol{r}_{Si} + \boldsymbol{p} \quad , \tag{A.11}$$

$$\boldsymbol{v}_0 \cdot \boldsymbol{p} = 0 \quad , \tag{A.12}$$

for a parameter λ and the vector $\boldsymbol{p}$ perpendicular to $\boldsymbol{v}_0$, where $\boldsymbol{r}_{Cl+}$ is the position of the Cl^+ ion, $\boldsymbol{r}_{Si} = ((n_x + 1/2)L, (1/2)L, (n_z + 1/2)L)$ is the position of the Si atom, and the dot denotes an inner

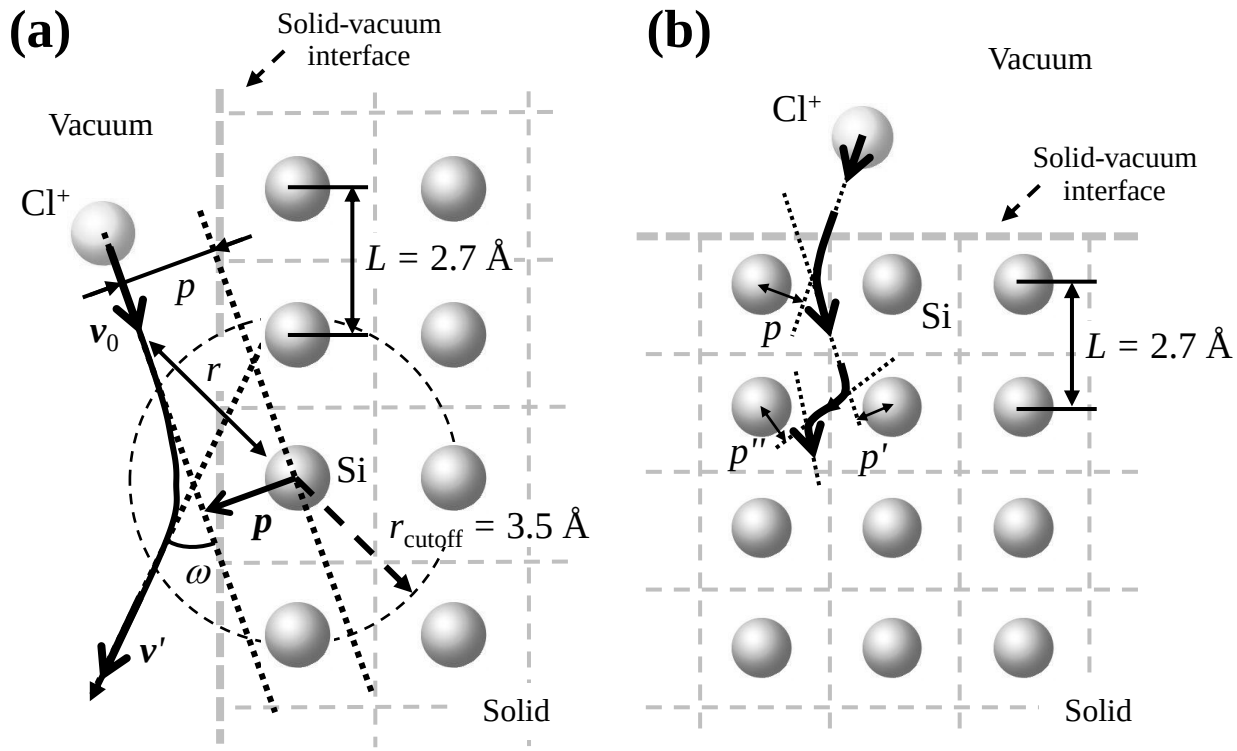

Fig. A.4. (a) Schematic illustration of the binary elastic collision between a Cl^+ ion and a Si atom (a) on substrate surfaces and (b) within solid, which is taken to occur when the impact parameter $p = |\boldsymbol{p}|$ is smaller than the cutoff radius r_{cutoff} = 3.5 Å ($p < r_{cutoff}$) of the Stillinger-Weber potential $V(r)$ of the Cl-Si system. Here, r is the distance between two colliding particles, ω the scattering angle, $\boldsymbol{v}_0$ the initial velocity vector, $\boldsymbol{v}'$ the velocity vector of the scattered ion and $\boldsymbol{p}$ the vector perpendicularly dropped from the Si atom to the extension of $\boldsymbol{v}_0$. After a collision between an ion and a Si atom on substrate surfaces, another collision is assumed to occur successively if the impact parameter p' concerned with the neighboring Si atom is smaller than r_{cutoff} ($p' < r_{cutoff}$). Within solids, successive collisions are assumed to occur only with the Si atom closest the ion, where the colliding Si atom is determined after every movement L.

product. Here, $r = |\boldsymbol{r}_{Cl+} - \boldsymbol{r}_{Si}|$ is the distance between two colliding particles. The energy loss and trajectory of the scattered ion at a single collision are determined from the momentum and energy conservation. The scattering angle Ω in the center-of-mass (CM) coordinate is calculated as follows:[14,15)]

$$\Omega = \pi - \int_{-\infty}^{\infty} \frac{p dr}{r^2 \left| 1 - \frac{V(r)}{E_c} - \frac{p^2}{r^2} \right|^{1/2}} \quad , \tag{A.13}$$

where E_c is the total energy of the system in the CM coordinate. Given the scattering angle Ω, the energy loss T of the ion and scattering angle ω in the laboratory coordinate are obtained from[14)]

$$T = \frac{4E_c M_{Si} M_{Cl}}{(M_{Si} + M_{Cl})^2} \sin^2 \frac{\Omega}{2} \quad , \tag{A.14}$$

$$\tan \omega = \frac{M_{Si} \sin \Omega}{M_{Cl} + M_{Si} \cos \Omega} \quad , \tag{A.15}$$

where M_{Si} and M_{Cl} are the masses of Si and Cl atoms, respectively. Because $\boldsymbol{v}_0$, $\boldsymbol{p}$, and the velocity vector $\boldsymbol{v}'$ of the scattered ion is on the same plane, $\boldsymbol{v}'$ is given by the linear combination of unit vectors $\boldsymbol{v}_0/|\boldsymbol{v}_0|$ and $\boldsymbol{p}/|\boldsymbol{p}|$:

$$\boldsymbol{v}' = \sqrt{|\boldsymbol{v}_0| - \frac{2T}{M_{Cl}}} \left(\frac{\boldsymbol{v}_0}{|\boldsymbol{v}_0|} \cos \omega + \frac{\boldsymbol{p}}{|\boldsymbol{p}|} \sin \omega \right) \quad . \tag{A.16}$$

Thus, the trajectory of an ion through collision with a Si atom is calculated without using a randomly chosen impact parameter and azimuthal scattering angle. As shown in Fig. A.4(b), another collision is assumed to occur successively if the impact parameter p' concerned with another neighboring Si atom and the velocity vector $\boldsymbol{v}'$ is smaller than r_{cutoff} ($p' < r_{cutoff}$). Consequently, the ASCeM model can represent the interaction between an ion and several substrate Si atoms on incidence.

A.2.4 Surface Chemistry III: Ion-Enhanced Etching

In the calculation, the ion-enhanced etching or the removal of substrate Si atoms is assumed to occur at the outermost surface sites chlorine-saturated; in practice, the saturated silicon chlorides $SiCl_4$ are taken to be desorbed from the surface through energetic ion bombardment, with the reaction being

$$\mathrm{Si}_{(s)} + 4\mathrm{Cl}_{(s)} \xrightarrow{\mathrm{Cl}^+} \mathrm{SiCl}_{4(g)} \ , \tag{A.17}$$

where Cl^+ above the arrow indicates that the reaction is induced by bombardment of energetic Cl^+ ions. In generally, physical and ion-enhanced etch yields are shown to be a liner function of the square root of the ion energy E_i. This agrees with the universal etching yield energy dependence model proposed by Steinbrüchel[16)]

$$Y = A\left(\sqrt{E_i} - \sqrt{E_{th}}\right) \ , \tag{A.18}$$

where A is a scaling factor and E_{th} is the threshold energy. The etch yield is considered to be smaller when the ion is reflected from surfaces than when it penetrates into substrates and stops therein, owing to increasing the etch or sputter yield, which is a function of the amount of energy deposited onto surfaces by an incident ion. According to this assumption, the etch yield $Y_{SiCl4/Cl+}$ (the number of substrate atoms etched per incident ion on saturated surfaces, which depends on the incident energy E_i and angle θ on surfaces)[17)] is taken to be

$$Y_{Si/Cl+} = A\left(\sqrt{E_i} - \sqrt{E_{th}}\right)\cdot f(\theta) = A\left(\sqrt{\Delta E} - \sqrt{E_{th}}\right) \ , \tag{A.19}$$

where $A = 0.353$ is a scaling factor, ΔE is the energy transfer from an ion to substrates, and E_{th} = 12 eV is the threshold energy for the reaction,[8)] and the angular dependence $f(\theta)$ of the ion-enhanced etching is obtained automatically in the MC-based calculation of ion reflection. Here, the energy transfer ΔE is taken to be equal to the total energy loss of an ion through successive collisions with substrate atoms, which is given by $\Delta E = E_i$ for the ion penetrating into substrates and $\Delta E = E_i - E_r$ for the ion reflected from surfaces, where E_r is reflected ion energy. Note that the local incident angle θ of ion is measured from the surface normal. The direction of the surface normal is represented by the four-point technique, where the surface normal is determined by the presence/absence of four neighboring cells, as shown in Figs. A.5.

In addition, the ion-enhanced etching is also taken to occur on the outermost surfaces unsaturated:

$$\mathrm{Si}_{(s)} + x\mathrm{Cl}_{(s)} \xrightarrow{\mathrm{Cl}^+} \mathrm{SiCl}_{x(g)} \ (x = 1 \sim 3) \ , \tag{A.20}$$

with a probability corresponding to the yield $Y'_{Si/Cl+} = (x/4)Y_{Si/Cl+}$. The sputtering of Si atoms through Cl^+ ion bombardment on unchlorinated surfaces is neglected in the two-dimensional ASCeM.

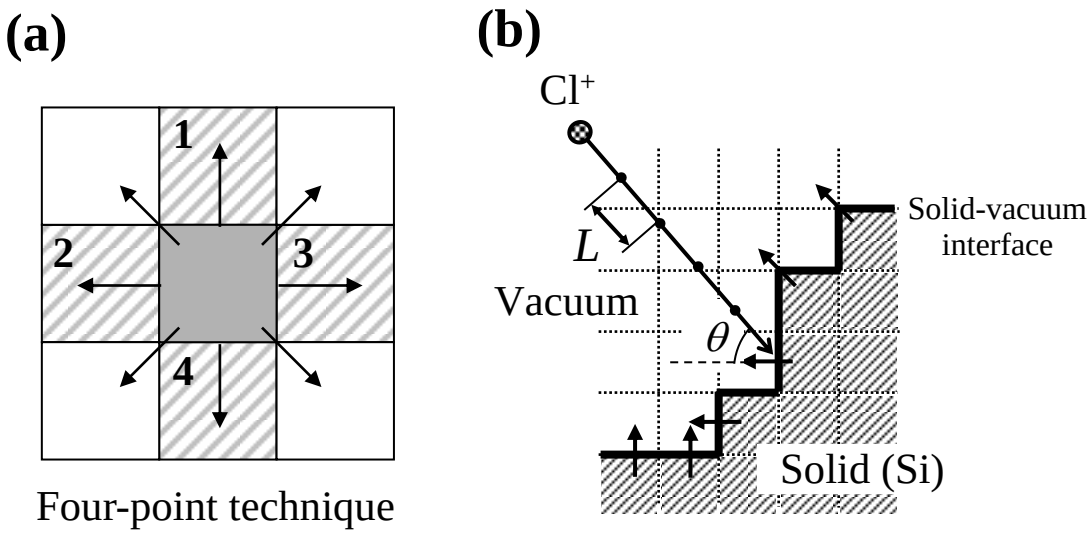

Fig. A.5. Schematic of the four-point techniques for calculating the direction of surface normal. Surface normal is determined by the presence/absence of four neighboring cells.

A.2.5 Surface Chemistry IV: Surface Oxidation

Surface oxidation is taken to be induced by adsorption of neutral O atoms on the outermost surfaces, where the injection and transport of O atoms in microstructures is treated similarly to that of Cl neutrals. The sticking coefficient or probability of O on Si is known to be $S_O = 1$;[18] in contrast, the dissociative adsorption of O_2 molecules is neglected owing to a small probability $S_{O2} < 0.01$.[19] It is noted that the adsorption of two O atoms at the maximum is allowed at a lattice of Si to form SiO_y surfaces:

$$\mathrm{Si}_{(s)} + x\mathrm{O}_{(s)} + \mathrm{O}_{(g)} \rightarrow \mathrm{Si}_{(s)} + (x+1)\mathrm{O}_{(s)} \qquad (x = 0, 1)\,, \qquad \text{(A.21)}$$

while O atoms are reemitted thermally or reflected randomly on saturated surfaces with O. Similarly, Cl atoms are taken to adsorb on unsaturated oxidized surfaces with a sticking probability $S_n = 1$:

$$\mathrm{Si}_{(s)} + \mathrm{O}_{(s)} + x\mathrm{Cl}_{(s)} + \mathrm{Cl}_{(g)} \rightarrow \mathrm{Si}_{(s)} + \mathrm{O}_{(s)} + (x+1)\mathrm{Cl}_{(s)} \qquad (x = 0, 1)\,. \qquad \text{(A.22)}$$

Moreover, strongly reactive O neutrals are assumed to oxidize $SiCl_x$ and $SiCl_xO_y$ surfaces ($x + 2y \leq 4$) with a probability of unity:[20,21]

$$\mathrm{Si}_{(s)} + x\mathrm{Cl}_{(s)} + \mathrm{O}_{(g)} \rightarrow \mathrm{Si}_{(s)} + x\mathrm{Cl}_{(s)} + \mathrm{O}_{(s)} \qquad (x = 1, 2)\,, \qquad \text{(A.23)}$$

$$\mathrm{Si}_{(s)} + x\mathrm{Cl}_{(s)} + \mathrm{O}_{(g)} \rightarrow \mathrm{Si}_{(s)} + 2\mathrm{Cl}_{(s)} + \mathrm{O}_{(s)} + (x-2)\mathrm{Cl}_{(g)} \qquad (x = 3, 4)\,, \qquad \text{(A.24)}$$

$$\mathrm{Si}_{(s)} + x\mathrm{Cl}_{(s)} + \mathrm{O}_{(s)} + \mathrm{O}_{(g)} \rightarrow \mathrm{Si}_{(s)} + 2\mathrm{O}_{(s)} + x\mathrm{Cl}_{(g)} \qquad (x = 1, 2)\,, \qquad \text{(A.25)}$$

where the latter two result in desorption or emission of displaced Cl atoms from the surface. It is further assumed that there is no reduction of O on oxidized SiO_y and $SiCl_xO_y$ surfaces by incidence of Cl neutrals or by the reverse reaction in Eq. (A.24) and (A.25), owing to the Si–O bond relatively strong as compared to that of Si–Cl; thus, Cl neutrals are usually reflected on saturated SiO_2 and $SiCl_2O$ surfaces on incidence. In addition, no spontaneous chemical etching is taken to be induced by Cl neutrals incident on oxidized surfaces.

The etching or removal of oxidized surfaces is given by

$$\mathrm{Si}_{(s)} + x\mathrm{Cl}_{(s)} + \mathrm{O}_{(s)} \xrightarrow{\mathrm{Cl}^+} \mathrm{SiCl}_x\mathrm{O}_{(g)} \qquad (x = 1, 2)\,, \qquad \text{(A.26)}$$

$$\mathrm{Si}_{(s)} + x\mathrm{O}_{(s)} \xrightarrow{\mathrm{Cl}^+} \mathrm{SiO}_{(g)} + (x-1)\mathrm{O}_{(g)} \qquad (x = 1, 2)\,, \qquad \text{(A.27)}$$

where silicon oxides SiO_y and oxychlorides $SiCl_xO_y$ are desorbed or removed from the surface by physical sputtering through energetic Cl^+ ion bombardment. The etch or sputter yield for a Cl^+ ion on oxidized surfaces is taken to be smaller than the yield $Y_{Si/Cl+}$ for the ion-enhanced etching as mentioned earlier; in practice,

$$Y_{\mathrm{Si/Cl+}}^{\mathrm{SP}} = \frac{1}{\beta} A\left(\sqrt{E_{\mathrm{i}}} - \sqrt{E_{\mathrm{th}}^{\mathrm{SP}}}\right) \cdot g(\theta) \qquad \text{(A.28)}$$

is employed in this study according to the Si/SiO_2 selectivity $\beta = Y_{Si}/Y_{SiO2} = 8.2$ experimentally obtained. Here, the constant $A = 0.353$ is the same as in $Y_{Si/Cl+}$, while the threshold energy is taken to be $E_{\mathrm{th}}^{\mathrm{SP}} = 30$ eV ($> E_{\mathrm{th}}$),[8,16] and the angular dependence

$$g(\theta) = \frac{5}{3}(18.7\cos\theta - 64.7\cos^2\theta + 145.2\cos^3\theta - 206\cos^4\theta + 147.3\cos^5\theta - 39.9\cos^6\theta) \qquad \text{(A.29)}$$

peaked at about $\theta = 65°$ is taken from a model for angle-dependent physical sputtering.[7] The ion-enhanced etching and sputtering yields for Cl^+ ions on Si and SiO_2 surfaces, as a function of incident energy and angle are shown in Figs. 3.2(a) and 3.2(b).

References

1) Y. Osano and K. Ono: Jpn. J. Appl. Phys. **44** (2005) 8650.
2) Y. Osano, M. Mori, N. Itabashi, K. Takahashi, K. Eriguchi, and K. Ono: Jpn. J. Appl. Phys. **45** (2006) 8157.
3) Y. Osano and K. Ono: Jpn. J. Vac. Sci. Technol. B **26** (2008) 1425.
4) R. N. Tait, T. Smy, and M. J. Brett: This Solid Films **187** (1990) 375.
5) M. Tuda, K. Ono, and K. Nishikawa: J. Vac. Sci. Technol. B **14** (1996) 3291.
6) R. A. Gottosho: J. Vac. Sci. Technol. B **11** (1993) 1884.
7) A. P. Mahorowala and H. H. Sawin: J. Vac. Sci. Technol. B **20** (2002) 1064.
8) W. Jin, S. A. Vitale, and H. H. Sawin: J. Vac. Sci. Technol. A **20** (2002) 2106.
9) E. A. Ogryzlo, D. E. Ibbotson, D. L. Flamm, and J. A. Mucha: J. Appl. Phys. **67** (1990) 3115.
10) Z. H. Walker and E. A. Ogryzlo: J. Appl. Phys. **69** (1991) 548.
11) M. A. Lieberman and A. J. Lichtenberg: *Principles of Plasma Discharges and Materials Processing, 2nd Edition* (Wiley, NewYork, 2005).
12) F. H. Stillinger and T. A. Weber: Phys. Rev. B **31** (1985) 5262.
13) H. Feil, J. Dieleman, and B. J. Garrison: J. Appl. Phys. **74** (1993) 15.
14) J. F. Ziegler, J. P. Biersack, and U. Littmark: *The Stopping and Range of Ions in Solids* (Pergamon Press, New York, 1985).
15) H. Goldstein: *Classical Mechanics* (Addison-Wesley, Reading, MA, 1990).
16) C. Steinbrüchel: Appl. Phys. Lett. **55** (1989) 1960.
17) J. P. Chang, A. P. Mahorowala, and H. H. Sawin: J. Vac. Sci. Technol. A **16** (1998) 217.
18) J. R. Engstrom, M. M. Nelson, and T. Engel: J. Vac. Sci. Technol. A **7** (1989) 1837.
19) J. R. Engstrom and T. Engel: Phys. Rev. B **41** (1990) 1038.
20) T. Morimoto: Jpn. J. Appl. Phys. **32** (1993) 1253.
21) L. Desvoivres, L. Vallier, and O. Joubert: J. Vac. Sci. Technol. B **19** (2001) 420.

Appendix B
Molecular Dynamics Simulation

B.1 Molecular Dynamics Simulation

Molecular dynamics (MD) simulations are more commonly used for analysis of such mechanisms of physical and chemical interactions of plasmas with surfaces. Dynamically surface reactions can be fruitfully explored using MD simulations, following the detailed motion of sets of interacting atoms by solving governing equations between the particles.[1)] The most straightforward way to simulate particle behavior is to simply follow the trajectories of a collection of molecules as they collide with each other. MD simulations follow the detailed motion of sets of interacting atoms through integration of atomic equations of motion, using interatomic potentials. In practice, it is noted that the particle-particle interactions need to be sufficiently accurately modeled by the chosen interatomic potential models to simulate collection of molecules and match experimental analysis.

Several interatomic potential models have been developed for MD simulations until now. Recently, in particular, there has been also development of first-principle MD (or *ab initio* MD),[2,3)] in which some form of electronic structure calculation is performed at each time step in the simulation, re-computing the interatomic potentials and therefore the interatomic forces. This method offers the obvious advantage, in principle, of greater accuracy than the other molecular dynamics simulations, but it comes at a considerable computational cost. To reduce computational burden, a classical MD simulation is widely used in practice. This model needs to be given empirical potentials in advance, whose parameters are fit by some combination of experimental data and separate *ab initio* calculations. A classical MD simulation is particularly useful for understanding interactions between a large number of atoms or molecules such as plasma-surface interactions.

B.2 Potential Model

To simulate Si etching in halogen-based chemistries, it is need to represent interatomic potentials between Si and halogen particles. The use of three body potentials is the simplest way to introduce many-body effects in MD simulations. In particular, three body potentials are often used for treating covalent bonds. One early attempt was formulated by Stillinger and Weber for describing silicon with two-body and three-body functions [i.e., Stillinger-Weber

(SW) potential].[4] They developed a potential model for Si/F systems.[5,6] Feil *et al.*[7] applied this functional form to Si/Cl systems by determining new parameter sets. Further improvements have been made by the Vashishta group for treating materials such as Si/O_2 [8] and Si/C.[9] Ohta and Hamaguchi [10] extended two sets of potential models for Si/O/F and Si/O/Cl systems based on previously reported potential models for Si/F, Si/Cl, and Si/O systems with additional *ab initio* data. Potential models for Si/O/C/F systems for performing the MD simulations of SiO_2 etching by fluorocarbon plasmas were reported by Smirnov *et al.*[11] After that, Smirnov *et al.*[12] further extended the SW models to Si/O/C/H systems for plasma etching simulations with low-k dielectric materials. Watanabe *et al*. proposed the novel Si/O mixed systems with introducing the bond0softening function to the two-body term.[13] Most recently, Ohta *et al.*[14] and Nagaoka *et al.*[15] determined the parameter set for Si/Br and Si/H/Br systems completely based on the *ab initio* calculations.

B.2.1 Many-Body Potential Function

Formally, any function $\boldsymbol{\Phi}$ describing the interactions between N particles can be cast in a sum of terms with 1, 2, 3, …, n bodies, according to

$$\boldsymbol{\Phi}(1.,...,N) = \sum_i \upsilon_1(i) + \sum_{i<j} \upsilon_2(i,j) + \sum_{i<j<k} \upsilon_3(i,j,k) + ... + \upsilon_n(i,...,n), \qquad \text{(B.1)}$$

The υ_1 term corresponds to interaction with a wall or external potentials. It is often omitted and thus the potentials are written as a combination of two-body and three-body potentials υ_2 and υ_3 functions:

$$\boldsymbol{\Phi} = \sum_{i<j} \upsilon_2(i,j) + \sum_{i<j<k} \upsilon_3(i,j,k). \qquad \text{(B.2)}$$

In this study, the interatomic potential used for Si/Cl/O systems is a newly developed model based on the SW-type potential function for covalent bonds, where the total potential energy is expressed by the summation of the two- and three-body potential functions. Moreover, the SW potential with a known parameter set is used for Si/Cl,[7] Si/O,[13] and Si/Cl/O,[10] as shown in Table V (two-body potentials) and VI (three-body potentials). It is noted here that all these potentials employ an improved potential form of the SW model for Si/halogen systems, which involves a correction term or more accurately without an overestimation of the repulsive interaction in the original SW model.[16]

B.2.2 Two-Body Potential Function

The pair-like interaction $\upsilon_2(i, j)$ between the ith and the jth atoms takes the following form:

$$\upsilon_2(i,j) \equiv \upsilon_{ij}(r_{ij}) = g(i,j)A_{ij}(B_{ij}r_{ij}^{-p_{ij}} - r_{ij}^{-q_{ij}})\exp\left[\frac{C_{ij}}{r_{ij}-a_{ij}}\right], \qquad \text{(B.3)}$$

if $r_{ij} < a_{ij}$, and $\upsilon_2(i, j) = 0$, otherwise.

Here, $r_{ij} = |\boldsymbol{r}_j - \boldsymbol{r}_i|$ denotes the distance between the ith and jth atoms located at $\boldsymbol{r}_i$ and $\boldsymbol{r}_j$, respectively. The parameters A_{ij}, B_{ij}, C_{ij}, p_{ij}, q_{ij}, and a_{ij} depend on the nature of the ith and jth elements. a_{ij} is the cutoff distance. $g(i, j)$ is the *bond-softening function* that controls the contribution of the two-body term.[13] The system symmetry requires that the parameters become invariant when indices i and j are interchanged, i.e., $A_{ij} = A_{ji}$, $g(i, j) = g(j, i)$, …, etc.

$g(i, j)$ is effective only for Si–O or Cl–O pairs. Namely,

$$g(i,j)\begin{cases} = g(z_i) & \text{for } i = \text{O and } j = \text{Si or halogen (Cl)}, \\ = g(z_j) & \text{for } i = \text{O and } j = \text{Si or halogen (Cl)}, \\ = 1 & \text{otherwise}, \end{cases} \qquad \text{(B.4)}$$

where z_i and z_j are the *coordination number* functions of O atoms. With the coordination numbers thus defined, we use function

$$g(z_i) = \frac{0.097}{\exp\left(\dfrac{1.6 - z_i}{0.3654}\right)+1} \cdot \exp\left(0.1344(z_i - 6.4176)^2\right), \qquad \text{(B.5)}$$

to define $g(i, j)$.

The coordination number z_i is defined by

$$z_i = \sum f_C^{ij}(r_{ij}) \ , \qquad \text{(B.6)}$$

where f_C^{ij} is the cutoff function and the sum is taken over all atoms except for the ith atom. Function f_C^{ij} is defined by

$$f_C^{ij}(r_{ij})\begin{cases} = 1 & (r_{ij} < R_{ij} - D_{ij}), \\ = 1 - \dfrac{r_{ij} - R_{ij} + D_{ij}}{2D_{ij}} + \dfrac{\sin\left[\dfrac{\pi(r_{ij} - R_{ij} + D_{ij})}{D_{ij}}\right]}{2\pi} & (R_{ij} - D_{ij} \le r_{ij} < R_{ij} + D_{ij}), \\ = 0 & (r_{ij} \ge R_{ij} + D_{ij}), \end{cases} \qquad \text{(B.7)}$$

where R_{ij} and D_{ij} are parameters satisfying $R_{ij} = R_{ji}$ and $D_{ij} = D_{ji}$. This is a modified form of

Tersoff's cutoff function.[17] Tersoff's function has discontinuity in its second derivations at $r_{ij} = R_{ij} - D_{ij}$ and $r_{ij} = R_{ij} + D_{ij}$, which lowers the preservation accuracy of the Hamiltonian throughout molecular dynamics calculations.

B.2.3 Three-Body Potential Function

The three-body functions is given by

$$\upsilon_3(i, j, k) \equiv \upsilon_{ijk}(\boldsymbol{r}_i, \boldsymbol{r}_j, \boldsymbol{r}_k) = h_{jik}(r_{ij}, r_{ik}, \theta_{jik}) + h_{ijk}(r_{ji}, r_{jk}, \theta_{ijk}) + h_{ikj}(r_{ki}, r_{kj}, \theta_{ikj}) \quad \text{(B.8)}$$

with θ_{jik} being the angle spanned by vectors $r_{ij} \equiv \boldsymbol{r}_j - \boldsymbol{r}_i$ and $r_{ik} \equiv \boldsymbol{r}_k - \boldsymbol{r}_i$ at the vertex $\boldsymbol{r}_i$. And if $r_{ij} < a^j_{jik}$ and $r_{ik} < a^k_{jik}$, we employ the functional form for h_{ijk} given by either

$$h_{jik}(r_{ij}, r_{ik}, \theta_{jik}) = \lambda_{jik} \exp\left[\frac{\gamma^j_{jik}}{r_{ij} - a^j_{jik}} - \frac{\gamma^k_{jik}}{r_{ik} - a^k_{jik}}\right], \quad \text{(B.9)}$$

for $i \in$ halogen (= Cl),

or

$$h_{jik}(r_{ij}, r_{ik}, \theta_{jik}) = \lambda_{jik} \exp\left[\frac{\gamma^j_{jik}}{r_{ij} - a^j_{jik}} - \frac{\gamma^k_{jik}}{r_{ik} - a^k_{jik}}\right] \cdot \left|\cos\theta_{jik} - \cos\theta^0_{jik}\right|^{2\alpha_{jik}}, \quad \text{(B.10)}$$

for $i \in$ not halogen (= Si, O).

Eq. (B.9) is used to cancel the extra attractive interactions resulting from the simple summation of two-body potentials υ_{ij}. Eq. (B.10) is used to restrict the angles between two covalent bonds. The parameters of $\lambda_{jik}, \gamma^j_{jik}, \gamma^k_{jik}, a^j_{jik}, a^k_{jik}$, and θ^0_{jik} depend on the species of the (i, j, k) triplet. a^j_{jik} and a^k_{jik} are cutoff distances for the three-body interaction. θ^0_{jik} is the equilibrium angle of j-i-k.

Recently, Humbird *et al*. clarified that the halogen atom could not be mixed into Si under the SW-type Si/F systems and repulsive interactions ultimately dictated that halogen atom remain on a vacuum-facing surface.[18] Furthermore, Ohta *et al*. found that the original SW model has a flaw in the three-body function, which is an overestimation of the repulsive force caused by the simple summation of the three-body functions, where a halogen atom is surrounded by more than three atoms.[16]

In this study, an improved SW potential functions are introduced to prevent such overestimation of the repulsive force, and are given by

$$\Phi = \sum_{i<j} \upsilon_2(i) + \sum_{i<j<k} \varepsilon_i(b_i) \cdot \upsilon_3(i, j, k), \tag{B.11}$$

$$\varepsilon_i(b_i) \begin{cases} = 1 & \\ = h(b_i)\dfrac{2}{b_i} + (1 - h(b_i)) \cdot 1 & \text{for} \quad i \in \text{halogen}, \\ = \dfrac{2}{b_i} & \end{cases} \tag{B.12}$$

$$\varepsilon_i(b_i) = 1 \qquad \text{for} \quad i \notin \text{halogen},$$

where b_i is the bonding number of the ith atom. Here, $h(x) = \dfrac{1}{1 + \exp(-10(x - 2.5))}$ is a smoothing function. This parameter $\varepsilon_i(b_i)$ prevents the overestimation of the penetration energy of ions into lattice, and would be a key factor to predict the surface reaction dynamics.

B.2.4 Equation of Motion

MD simulation involves numerically solving equation of motion of a set of N interatomic atoms or molecules. The trajectories of atoms and molecules are determined by numerically solving the Newton's equations of motion for a system of interacting particles:

$$m_i \frac{d^2 \mathbf{r}_i}{d t^2} = \mathbf{F}_i, \tag{B.13}$$

where m_i is mass of the ith atom. The forces between the particles and potential energy are defined by molecular mechanics force fields, and are given by

$$\mathbf{F}_i = -\nabla_i \boldsymbol{\Phi}(\vec{r}_1(t), \vec{r}_2(t), ..., \vec{r}_N(t)). \tag{B.14}$$

In Hamiltonian systems, the criterion of quality is generally energy conservation. Conservation of this quantity is ensured by a proper value of time step Δt. A variable time step integration algorithm for carrying out MD simulations of atomic collision cascades have been proposed which evaluates the interaction forces only once per time step until now. In this study, Smith's *Two Step A algorithm* is used for solving equations of motion and interatomic forces.[19)]

B.3 Calculation Condition

To describe interactions between ions and surfaces, bonding require correctly treating the energy exchanges between incoming atoms (or ions) and the surface atoms. In the case of ions impacting surfaces, it is generally assumed that ions recombine via Auger neutralization.[20)]

Auger neutralization of the ions near the surface can be applied to interactions between low energy ions and surfaces, and potential models can assume the charge-neutral condition. Therefore, these potential models assume a charge-neutral condition for any clusters in this study.

The ions are injected vertically onto the surface from randomly selected horizontal locations onto the space pattern. Every after injection of a single energetic particle, we allowed the system evolve for 0.7 ps with the total energy being constant, and then artificially cooled the system for 0.3 ps down to the initial temperature (T_s = 300 K) of target atoms.[21] The target atoms in the bottom layer are fixed during the simulation, while additional Si layers are automatically added when the incoming species reach the bottom layer.

Table V. Parameters of the two-body potentials for Si/Cl/O systems.[a)]

υ_{SiSi} [b)]	A_{SiSi}	7.049556277	υ_{SiO} [c)]	A_{SiO}	115.364065913	υ_{ClO} [d)]	A_{ClO}	71.0
	B_{SiSi}	0.6022245584		B_{SiO}	0.9094442793		B_{ClO}	0.471
	C_{SiSi}	1.0		C_{SiO}	1.0		C_{ClO}	3.55
	p_{SiSi}	4.0		p_{SiO}	2.58759		p_{ClO}	3.13
	q_{SiSi}	0		q_{SiO}	2.39370		q_{ClO}	1.53
	a_{SiSi}	1.8		a_{SiO}	1.4		a_{ClO}	1.8
				R_{SiO}	1.3		R_{ClO}	1.0
υ_{SiCl} [b)]	A_{SiCl}	28.0		D_{SiO}	0.1		D_{ClO}	0.1
	B_{SiCl}	0.67						
	C_{SiCl}	1.3	υ_{OO} [c)]	A_{OO}	−12.292427744			
	p_{SiCl}	2.2		B_{OO}	0			
	q_{SiCl}	0.9		C_{OO}	1.0			
	a_{SiCl}	0.8		p_{OO}	0			
				q_{OO}	2.24432			
υ_{ClCl} [b)]	A_{ClCl}	8.611		a_{OO}	1.25			
	B_{ClCl}	0.789						
	C_{ClCl}	0.5795						
	p_{ClCl}	6.0						
	q_{ClCl}	5.0						
	a_{ClCl}	2.0862						

[a)] The energy and length units are 50.0 kcal/mol (2.17 eV) and 2.0951 Å, respectively.
[b)] Ref. 7.
[c)] Ref. 13.
[d)] Ref. 10.

Table VI. Parameters of the three-body potentials for Si/Cl/O systems.[a)]

h_{SiSiSi} [b)]	λ_{SiSiSi}	16.404	h_{SiSiO} [c)]	λ_{SiSiO}	10.667	h_{ClClO} [d)]	λ_{ClClO}	1170.0
	γ^{Si}_{SiSiSi}	1.0473		γ^{Si}_{SiSiO}	1.93973		γ^{Cl}_{ClClO}	3.97
	a^{Si}_{SiSiSi}	1.8		a^{Si}_{SiSiO}	1.9		a^{Cl}_{ClClO}	2.0862
	$\cos\theta^0_{SiSiSi}$	−1/3		γ^{O}_{SiSiO}	0.25		γ^{O}_{ClClO}	3.24
	α_{SiSiSi}	1.0		a^{O}_{SiSiO}	1.4		a^{O}_{ClClO}	1.8
				$\cos\theta^0_{SiSiO}$	−1/3			
h_{SiSiCl} [b)]	λ_{SiSiCl}	15.0		α_{SiSiO}	1.0	h_{ClOCl} [d)]	λ_{ClOCl}	78.3
	γ^{Si}_{SiSiCl}	1.0					γ^{Si}_{ClOCl}	1.83
	a^{Si}_{SiSiCl}	1.8	h_{SiOSi} [c)]	λ_{SiOSi}	2.9572		a^{Si}_{ClOCl}	1.8
	γ^{Cl}_{SiSiCl}	1.0		γ^{Si}_{SiOSi}	0.71773		$\cos\theta^0_{ClOCl}$	−0.221
	a^{Cl}_{SiSiCl}	1.8		a^{Si}_{SiOSi}	1.4		α_{ClOCl}	1.0
	$\cos\theta^0_{SiSiCl}$	−1/3		$\cos\theta^0_{SiOSi}$	−0.6155238			
	α_{SiSiCl}	1.0		α_{SiOSi}	1.0	h_{ClOO} [d)]		0
h_{SiClSi} [b)]	λ_{SiClSi}	50.0	h_{SiOO} [c)]		0	h_{OClO} [d)]	λ_{OClO}	166000.0
	γ^{Si}_{SiClSi}	1.0					γ^{O}_{OClO}	5.78
	a^{Si}_{SiClSi}	1.8	h_{OSiO} [c)]	λ_{OSiO}	3.1892		a^{O}_{OClO}	1.8
				γ^{O}_{OSiO}	0.3220			
h_{SiClCl} [b)]	λ_{SiClCl}	15.0		a^{O}_{OSiO}	1.65	h_{SiClO} [d)]	λ_{SiClO}	214.0
	γ^{Si}_{SiClCl}	1.0		$\cos\theta^0_{OSiO}$	−1/3		γ^{Si}_{SiClO}	1.12
	a^{Si}_{SiClCl}	1.8		α_{OSiO}	1.0		a^{Si}_{SiClO}	1.8
	γ^{Cl}_{SiClCl}	1.0					γ^{O}_{SiClO}	3.24
	a^{Cl}_{SiClCl}	1.8	h_{OOO} [c)]		0		a^{O}_{SiClO}	1.8
h_{ClSiCl} [e)]						h_{ClSiO} [d)]	λ_{ClSiO}	33.5
							γ^{Cl}_{ClSiO}	0.295
h_{ClClCl} [f)]							a^{Cl}_{ClSiO}	1.4
							γ^{O}_{ClSiO}	1.63
							a^{O}_{ClSiO}	1.4
							$\cos\theta^0_{ClSiO}$	0.0575
							α_{ClSiO}	2.31
						h_{SiOCl} [d)]	λ_{SiOCl}	10.3
							γ^{Si}_{SiOCl}	0.723
							a^{Si}_{SiOCl}	1.4
							γ^{Cl}_{SiOCl}	0.564
							a^{Cl}_{SiOCl}	1.4
							$\cos\theta^0_{SiOCl}$	−0.438
							α_{SiOCl}	1.05

[a)] The energy and length units are 50.0 kcal/mol (2.17 eV) and 2.0951 Å, respectively.
[b)] Ref. 7.
[c)] Ref. 13.
[d)] Ref. 10.
[e)] $h_{ClSiCl}(r_{ij}, r_{ik}, \theta_{jik}) = \left[30.0\left(\cos\theta_{jik} - \cos 103°\right)^2 - 0.5\right] \exp\left[\frac{1.0}{r_{ij} - 1.8} + \frac{1.0}{r_{ik} - 1.8}\right]$

[f)] $h_{ClClCl}(r_{ij}, r_{ik}, \theta_{jik}) = 3.0\,(r_{ij} \cdot r_{ik})^{-2.056} \exp\left[\frac{0.5795}{r_{ij} - 2.0862} + \frac{0.5795}{r_{ik} - 2.0862}\right]$

$$+ 23.778(2.0 - \cos^2\theta_{jik}) \exp\left[\frac{1.7386}{r_{ij} - 1.6226} + \frac{1.7386}{r_{ik} - 1.6226}\right]$$

References

1) R. Smith: *Atomic and Ion Collisions in Solid and at Surfaces* (Cambridge University Press, UK, 1997).
2) R. Car and M. Parrinello: Phys. Rev. Lett. **55** (1985) 2471.
3) R. Car and M Parrinelo: Phys. Rev. Lett. **60** (1988) 204.
4) F. H. Stillinger and T. A. Weber: Phys. Rev. B **31** (1985) 5262.
5) F. H. Stillinger and T. A. Weber: J. Chem. Phys. **88** (1988) 5123.
6) F. H. Stillinger and T. A. Weber: Phys. Rev. Lett. **62** (1989) 2144.
7) H. Feil, J. Dieleman, and B. J. Garrison: J. Appl. Phys. **74** (1993) 1303.
8) P. Vashishta, R. K. Kalia, J. P. Rino, and I. Ebbsjö: Phys. Rev. B **41** (1990) 12197.
9) F. Shimojo, I. Ebbsjö, R. K. Kalia, A. Nakano, J. P. Rino, and P. Vashishta: Phys. Rev. Lett. **84** (2000) 3338.
10) H. Ohta and S. Hamaguchi: J. Chem. Phys. **115** (2001) 6679.
11) V. V. Smirnov, A. V. Stengach, K. G. Gaynullin, V. A Pavlovsky, S. Rauf, P. J. Stout, and P. L. G. Ventzek: J. Appl. Phys. **97** (2005) 093302.
12) V. V. Smirnov, A. V. Stengach, K. G. Gaynullin, V. A Pavlovsky, S. Rauf, and P. L. G. Ventzek: J. Appl. Phys. **101** (2007) 053307.
13) T. Watanabe, H. Fujiwara, H. Noguchi, T. Hoshino, and I. Ohdomari: Jpn. J. Appl. Phys. **38** (1999) 366.
14) H. Ohta, A. Iwakawa, K. Eriguchi, and K. Ono: J. Appl. Phys. **104** (2008) 073302.
15) T. Nagaoka, K.Eriguchi, K. Ono, and H. Ohta: J. Appl. Phys. **105** (2009) 023302.
16) H. Ohta, T. Nagaoka, K. Eriguchi, and K. Ono: Jpn. J. Appl. Phys. **48** (2009) 020225.
17) J. Tersoff: Phys. Rev. B **37** (1988) 6991.
18) D. Humbird and D. B. Graves: Plasma Source Sci. Technol. **13** (2004) 548.
19) R. Smith and D. E. Harrison: Jr., Comput. Phys. **3** (1989) 68.
20) H. D. Hagstrum: Phys. Rev. **122** (1961) 83.
21) H. J. Berendsen J. P. M. Postma, W. F. van Gunstern, A. DiNola, and J. R. Haak: J. Chem. Phys. **81** (1984) 3684.

Publication List

Journal Papers

1. **Hirotaka Tsuda**, Koji Eriguchi, Kouichi Ono, and Hiroaki Ohta: "*Molecular-Dynamics-Based Profile Evolution Simulation for Sub-10-nm Si Processing Technology*", Appl. Phys. Express **2** (2009) 116501-1~3.

2. **Hirotaka Tsuda**, Masahiko Mori, Yoshinori Takao, Koji Eriguchi and Kouichi Ono: "*Atomic-scale cellular model and profile simulation of Si etching: Formation of surface roughness and residue*", Thin Solid Films **518** (2010) 3475-3480.

3. **Hirotaka Tsuda**, Masahiko Mori, Yoshinori Takao, Koji Eriguchi, and Kouichi Ono: "*Atomic-Scale Cellular Model and Profile Simulation of Si Etching: Analysis of Profile Anomalies and Microscopic Uniformity*", Jpn. J. Appl. Phys. **49** (2010) 08JE01-1~4.

4. **Hirotaka Tsuda**, Hiroki Miyata, Yoshinori Takao, Koji Eriguchi, and Kouichi Ono: "*Three-dimensional Atomic-scale Cellular Model and Feature Profile Evolution during Si Etching in Chlorine-based Plasmas: Analysis of Profile Anomalies and Surface Roughness*", Jpn. J. Appl. Phys. **50** (2011) 08JE06-1~6.

5. **Hirotaka Tsuda**, Yoshinori Takao, Koji Eriguchi, and Kouichi Ono: "*Molecular Dynamics Analysis of the Formation of Surface Roughness during Si Etching in Chlorine-based Plasmas*", Jpn. J. Appl. Phys. **50** (2011) 08KB02-1~5.

6. **Hirotaka Tsuda**, Yoshinori Takao, Koji Eriguchi, and Kouichi Ono: "*Modeling and Simulation of Nanoscale Surface Rippling during Plasma Etching of Si under Oblique Ion Incidence*", Jpn. J. Appl. Phys. **51** (2012) 08HC01-1~7.

International Conference Papers

1. **Hirotaka Tsuda**, Shoki Irie, Masahito Mori, Hiroaki Ohta, Koji Eriguchi, and Kouichi Ono: "*Atomic-scale cellular model and profile simulation of Si etching in chlorine- and*

bromine-containing plasmas: Effects of surface oxidation on evolution of feature profiles", 61st Annual Gaseous Electronics Conference (GEC 61), DT1.00003, Bull. Am. Phys. Soc. **53**(10) (2008) 18 (1 page), October 13-17, 2008, Marriott Dallas/Addison Quorum by the Galleria in Dallas, Texas, USA.

2. **Hirotaka Tsuda**, Masahito Mori, Koji Eriguchi, and Kouichi Ono: "*Atomic-scale cellular model and profile simulation of Si etching: Analysis of profile anomalies and microscopic uniformity*", 31st International Symposium on Dry Process (DPS 2009), 2-P19 (2 pages), September 24-25, 2009, Busan Exhibition & Convention Center, Busan, Korea.

3. **Hirotaka Tsuda**, Tatsuya Nagaoka, Hiroki Miyata, Yoshinori Takao, Koji Eriguchi, and Kouichi Ono: "*Plasma-surface interactions during Si etching in Cl- and Br-based plasmas: An empirical and atomistic study*", 62nd Annual Gaseous Electronics Conference (GEC 62), SR3.00004 (1 page), Bull. Am. Phys. Soc. **54**(12) (2009) 70, October 20-23, 2009, Saratoga Springs, NY, USA.

4. **Hirotaka Tsuda**, Tatsuya Nagaoka, Koji Eriguchi, Kouichi Ono, and Hiroaki Ohta: "*Fully Atomistic Profile Evolution Simulation of Nanometer-scale Si Trench Etching by Energetic F, Cl, and Br Beams*", American Vacuum Society 56th International Symposium & Exhibition (AVS 56), PS1-ThA8 (1 page), November 8-13, 2009, San Jose Convention Center, San Jose, CA, USA.

5. **Hirotaka Tsuda**, Yoshinori Takao, Koji Eriguchi, and Kouichi Ono: "*Profile simulation of silicon etching in halogen-based plasmas: Monte Carlo and molecular dynamics approaches*", 1st International Workshop on Plasma Nano-interfaces, FS06 (2 pages), January 10, 2010, Nagasaki University, Nagasaki, Japan.

6. **Hirotaka Tsuda**, Tatsuya Nagaoka, Yoshinori Takao, Koji Eriguchi, and Kouichi Ono: "*Atomic-scale analysis of plasma-surface interactions and feature profile evolution by molecular dynamics approaches*", 3rd International Conference on Plasma-Nanotechnology & Science (IC-PLANTS 2010), P-22 (2 pages), March 11-12, 2010, Meijyo University, Nagoya, Japan.

7. **Hirotaka Tsuda**, Yoshinori Takao, Koji Eriguchi, and Kouichi Ono: "*Atomic-scale analysis of plasma-surface interactions and feature profile evolution during Si etching in halogen-based plasmas: Monte Carlo and molecular dynamics approaches*", 10th Asia Pacific Conference on Plasma Science and Technology (APCPST 10) / 23th Symposium on Plasma Science for Materials (SPSM 23), PP442 2010-401 (1 page), July 8, 2010, Lotte Hotel Jeju, Jeju, Korea.

8. **Hirotaka Tsuda**, Hiroki Miyata, Yoshinori Takao, Koji Eriguchi, and Kouichi Ono: "*3-dimensional atomics-scale cellular model and feature profile evolution during Si etching in chlorine-based plasmas: Analysis of profile anomalies and surface roughness*", 63rd Gaseous Electronics Conference (GEC 63) / 7th International Conference on Reactive Plasmas (ICRP 7) / 28th Symposium on Plasma Processing (SPP 28), KWP.00063, Bull. Am. Phys. Soc. **55**(7) (2010) 119 (1 page for GEC and 2 pages for ICRP&SPP), October 4-8, 2010, Maison de la Chimie, Paris, France.

9. **Hirotaka Tsuda**, Yoshinori Takao, Koji Eriguchi, and Kouichi Ono: "*Molecular Dynamics Analysis of Surface Roughness during Si Etching in Chlorine-Based Plasmas*", 32nd International Symposium on Dry Process (DPS 2010), H-2 (2 pages), November 11-12, 2010, Tokyo Institute of Technology, Japan.

10. [Invited] **Hirotaka Tsuda**, Yoshinori Takao, Koji Eriguchi, and Kouichi Ono: "*Surface Roughness Formation during Si Etching in Chlorine-based Plasmas: Atomic-scale Analysis of Three-dimensional Feature Profile Evolution*", 2nd International Workshop on Plasma Nano-Interfaces and Plasma Characterization (2WPNI), (2 pages), March 1-4, 2011, Hotel Raj, Cerklje, Slovenia.

11. **Hirotaka Tsuda**, Yoshinori Takao, Koji Eriguchi, and Kouichi Ono: "*Surface Roughness Formation during Si Etching in Cl_2 and Cl_2/O_2 Plasmas: Atomic-scale Analysis of Three-dimensional Feature Profile Evolution*", 4th International Conference on Plasma Nano-Technology & Science (IC-PLANTS 2011), O-07 (2 pages), March 10-12, 2011, Takayama Public Cultural Hall, Takayama, Gifu, Japan.

12. **Hirotaka Tsuda**, Yoshinori Takao, Koji Eriguchi, and Kouichi Ono: "*Three-Dimensional Modeling and Formation Mechanisms of Atomic-Scale Surface Roughness during Si Etching in Chlorine-Based Plasmas*", American Vacuum Society 58th International Symposium & Exhibition (AVS 58), PS-FrM9 (1 page), October 30 - November 4, 2011, Nashville Convention Center, Nashville, TN, USA.

13. **Hirotaka Tsuda**, Yoshinori Takao, Koji Eriguchi, and Kouichi Ono: "*Modeling and Simulation of Nanoscale Surface Rippling during Plasma Etching of Si under Oblique Ion Incidence*", 33rd International Symposium on Dry Process (DPS 2011), B-2 (2 pages), November 10-11, 2011, Kyoto Garden Palace Hotel, Kyoto, Japan. (DPS 2011 Young Researcher Award)

14. [Invited] **Hirotaka Tsuda**, Yoshinori Takao, Koji Eriguchi, and Kouichi Ono: "*Model Analysis of Nanoscale Surface Roughness and Rippling during Plasma Etching of Si under Oblique Ion Incidence: Effects of Oxygen Addition*", 5th International Conference on Plasma-Nanotechnology & Science (IC-PLANTS 2012), S-2 (2 pages), March 9-10, 2012, Freude, Inuyama International Sightseeing Center, Aichi, Japan.

15. **Hirotaka Tsuda**, Yoshinori Takao, Koji Eriguchi, and Kouichi Ono: "*Rippling Mechanism of Nanoscale Surface during Plasma Etching of Si under Oblique Ion Incidence*", 11th Asia Pacific Conference on Plasma Science and Technology (APCPST 11) / 25th Symposium on Plasma Science for Materials (SPSM 25), 1-P60 (1 pages), October 2-5, 2012, Kyoto University ROHM Plaza, Kyoto, Japan.

16. **Hirotaka Tsuda**, Yoshinori Takao, Koji Eriguchi, and Kouichi Ono: "*Formation Mechanisms of Surface Roughening and Rippling during Plasma Etching and Sputtering of Silicon*", 65th Annual Gaseous Electronics Conference (GEC 65), HW2-2, Bull. Am. Phys. Soc. **57**(8) (2012) 45 (1 page), October 22-26, 2012, the AT&T Conference Center on The University of Texas at Austin campus in Austin, Texas, USA.

17. **Hirotaka Tsuda**, Yoshinori Takao, Koji Eriguchi, and Kouichi Ono: "*Formation*

Mechanisms of Nanoscale Surface Roughness and Rippling during Plasma Etching and Sputtering of Si under Oblique Ion Incidence", American Vacuum Society 59th International Symposium & Exhibition (AVS 59), PS2-TuA12 (1 pages), October 28-November 2, 2012, Tampa Convention Center, Florida, USA.

18. **Hirotaka Tsuda**, Yoshinori Takao, Koji Eriguchi, and Kouichi Ono: "*Modeling and Simulation of Nanoscale Surface Roughness during Plasma Etching of Si: Mechanism and Reduction*", 34th International Symposium on Dry Process (DPS 2012), A-3 (2 pages), November 15-16, 2012, Takeda Hall, Takeda Sentanchi Building, The University of Tokyo, Tokyo, Japan.

19 [Invited] **Hirotaka Tsuda**, Nobuya Nakazaki, Daisuke Fukushima, Yoshinori Takao, Koji Eriguchi, and Kouichi Ono: "*Surface roughening during Si etching in inductively coupled Cl_2 plasmas: Experimental investigations and a comparison with numerical simulations*", 6th International Conference on Plasma-Nanotechnology & Science (IC-PLANTS 2013), S-1 (2 pages), Feburary 2-3, 2013, Gero Synergy Center, Gero, Gifu, Japan.

Domestic Conference Papers

1. **Hirotaka Tsuda**, Shoki Irie, Masahito Mori, Koji Eriguchi, and Kouichi Ono: 「塩素系・臭素系プラズマによる Si エッチングにおける形状進展のモデル解析 (Model analysis of the profile evolution during Si etching in chlorine- and bromine-containing plasmas)」, 第 25 回プラズマプロセシング研究会 (SPP 25), B4-02 (2 pages), 2008 年 1 月 23 日～25 日, 山口県教育会館・ゆ～あいプラザ山口県社会福祉会館.

2. **津田博隆**, 森政士, 太田裕朗, 江利口浩二, 斧高一: 「原子スケールセルモデルによる Si エッチング形状シミュレーション：微細パターン内での表面酸化と粒子挙動の解析 (Atomic-scale cellular model and profile simulation of Si etching: Analysis of particle trajectory and surface oxidation)」, 2008 年秋季 第 69 回応用物理学会学術講演会, 3a-ZC-9 (1 page), 2008 年 9 月 2 日～5 日, 中部大学.

3. **津田博隆**, 森政士, 太田裕朗, 江利口浩二, 斧高一: 「原子スケールセルモデルに

よるSiエッチング形状シミュレーション: Si微細パターン内での表面酸化と粒子挙動の解析」, 第2回プラズマエレクトロニクス インキュベーションホール, 2008年9月24日～26日, マキノパークホテル&セミナーハウス. （最優秀ポスター賞, 優秀質問者賞 受賞）

4. **津田博隆**、入江祥己、森政士、太田裕朗、江利口浩二、斧高一: 「原子スケールセルモデルによる Si エッチング形状シミュレーション：形状進展における表面酸化の影響 (Atomic-scale Cellular Model and Profile Simulation of Si Etching: Effects of Surface Oxidation on Feature Profile Evolution)」, プラズマ科学シンポジウム 2009 (PSS 2009) / 第26回プラズマプロセシング研究会 (SPP 26), P3-03 (2 pages), 2009年2月2日～4日, 名古屋大学 豊田講堂・シンポジオン.

5. **津田博隆**, 森政士, 太田裕朗, 江利口浩二, 斧高一: 「原子スケールセルモデルによる Si エッチング形状シミュレーション: パターン底面部の表面あらさの定量化 (Atomic-scale Cellular Model and Profile Simulation of Si Etching: Quantification of Bottom Surface Roughness)」, 2009 年春季 第 56 回応用物理学関係連合講演会, 1p-ZW-15 (1 page), 2009年3月30日～4月2日, 筑波大学.

6. **Hirotaka Tsuda**, Masahito Mori, Koji Eriguchi and Kouichi Ono: “Atomic-scale cellular model and profile simulation of Si etching: Formation of surface roughness and residues”, 第22回プラズマ材料科学シンポジウム (SPSM 22), P-5 (1 page), 2009年6月15日～16日, 東京大学 山上会館.

7. **津田博隆**, 森政士, 鷹尾祥典, 江利口浩二, 斧高一 : 「原子スケールセルモデルによる Si エッチング形状進展シミュレーション: 残渣の発現メカニズム (Atomic-scale cellular model and profile simulation of Si etching: Formation mechanism of surface roughness and residues)」, 2009 年秋季 第 70 回応用物理学会学術講演会, 9a-ZG-12 (1 page), 2009年9月8日～11日, 富山大学.

8. **津田博隆**, 森政士, 鷹尾祥典, 江利口浩二, 斧高一 : 「原子スケールモデルによる Si エッチング形状進展シミュレーション: 形状異常の予測とその制御 (Atomic-scale cellular model and profile simulation of Si etching in chlorine-containing

plasmas: Control and prediction of profile anomalies)」, 第 27 回プラズマプロセシング研究会 (SPP 27), A2-03 (2 pages), 2010 年 2 月 1 日～3 日, 横浜市開港記念会館.

9. **津田博隆**, 森政士, 鷹尾祥典, 江利口浩二, 斧高一: 「原子スケールモデルによる Si エッチング形状シミュレーション: 微視的不均一性に関する解析 (Atomic-scale Cellular Model and Profile Simulation of Si Etching in Chlorine-based Plasmas: Analysis of Mechanisms for Microscopic Uniformity)」, 2010 年春季 第 57 回応用物理学関係連合講演会, 18p-ZD-12 (1 page), 2010 年 3 月 17 日～20 日, 東海大学湘南キャンパス.

10. **津田博隆**, 宮田浩貴, 鷹尾祥典, 江利口浩二, 斧高一: 「3 次元原子スケールセルモデルによる Si エッチング形状進展シミュレーション: 表面ラフネスの構造解析 (3-Dimensional Atomic-scale Cellular Model and Feature Profile Evolution during Si Etching in Chlorine-based Plasmas: Analysis of Surface Roughness)」, 2010 年秋季 第 71 回応用物理学会学術講演会, 16a-ZA-5 (1 page), 2010 年 9 月 14 日～17 日, 長崎大学文教キャンパス.

11. **津田博隆**, 宮田浩貴, 鷹尾祥典, 江利口浩二, 斧高一: 「3 次元原子スケールセルモデルによる Si エッチング形状進展: シミュレーション:ナノスケール表面ラフネス形成機構の解明 (3-dimensional Atomic-scale Cellular Model and Feature Profile Evolution during Si Etching in Chlorine-based Plasmas: Nanoscale Surface Roughness Formation)」, 2011 年春季 第 58 回応用物理学関係連合講演会（講演会中止）, (1 page), 2011 年 3 月 24 日～27 日, 神奈川工科大学.

12. **Hirotaka Tsuda**, Yoshinori Takao, Koji Eriguchi and Kouichi Ono:
"Atomic-scale surface roughness depending on the ion incident angle during Si etching in chlorine-based plasmas", 第 24 回プラズマ材料科学シンポジウム (SPSM 24), B4-4 (1 page), 2011 年 7 月 19 日～20 日, 大阪大学 銀杏会館.

13. **津田博隆**, 鷹尾祥典, 江利口浩二, 斧高一: 「3 次元原子スケールセルモデルによる表面ラフネス形成機構の解明: イオンの入射エネルギー・角度依存性 (Atomic-Scale Surface Roughness Depending on the Energy and Angle of Incident Ions during Si Etching in Chlorine-Based Plasmas)」, 2011 年秋季 第 72 回応用物理学会学術

講演会, 30a-M-9 (1 page), 2011 年 8 月 29 日～9 月 2 日, 山形大学小白川キャンパス.

14 [Invited] **津田博隆**, 鷹尾祥典, 江利口浩二, 斧高一:「エッチング加工形状進展と表面ラフネスのモデリング･シミュレーション」, 第 8 回プラズマ新領域研究会「プラズマプロセスと先端数値解析」, (1 page), 2011 年 10 月 26 日, 慶應義塾大学日吉キャンパス 来往舎.

15. **津田博隆**, 鷹尾祥典, 江利口浩二, 斧高一: 「プラズマエッチング時における表面ラフネス形成メカニズムとイオン入射角度依存性 (Model Analysis of Nanoscale Surface Roughness and Rippling during Plasma Etching of Si under Oblique Ion Incidence)」, プラズマ・核融合学会第 28 回年会 / 応用物理学会第 29 回プラズマプロセシング研究会 (SPP 29) / 日本物理学会（領域 2）2011 年秋季大会 / Plasma Conference 2011 (PLASMA 2011), 23P007-O (2 pages), 2011 年 11 月 22 日～25 日, 石川県立音楽堂.

16. [Invited] **津田博隆**, 鷹尾祥典, 江利口浩二, 斧高一: 「Si エッチング形状進展シミュレーションと表面反応解析」, ICAN Kyou Sou Seminar【第 5 回】ナノデバイスにおける微細加工技術についてのオープンセミナー, 2012 年 3 月 5 日, 産業技術総合研究所 西-7A SCR.

17. **津田博隆**, 鷹尾祥典, 江利口浩二, 斧高一: 「3 次元原子スケールセルモデルによる表面ラフネス形成機構の解明：酸素添加依存性 (Three-Dimensional Atomic-Scale Cellular Model and Mechanism of Surface Roughness: Effects of Oxygen Addition)」, 2012 年春季 第 59 回応用物理学関係連合講演会, 17p-A7-18 (1 page), 2012 年 3 月 15 日～18 日, 早稲田大学 早稲田キャンパス. （2012 年春季 第 32 回応用物理学会講演奨励賞 受賞）

18. [Invited] **津田博隆**, 鷹尾祥典, 江利口浩二, 斧高一: 「3 次元原子スケールセルモデルによる表面ラフネス形成機構の解明:酸素添加依存性 II. –イオン斜め入射時のリップル形成メカニズム–」, 2012 年秋季 第 73 回応用物理学会学術講演会, 13a-E3-7 (1 page), 2012 年 9 月 11 日～14 日, 愛媛大学 城北キャンパス. （2012 年春季 第 32 回応用物理学会講演奨励賞受賞記念講演）

19. [Invited] **津田博隆**, 鷹尾祥典, 江利口浩二, 斧高一: 「Si エッチングにおけるプラズマ・表面相互作用のモデリングと形状進展シミュレーション」, 第 156 回応用物理学会シリコンテクノロジー分科会研究会, (9 pages), 2013 年 2 月 15 日, 東京大学本郷キャンパス工学部 9 号館 1 階大会議室.